Development and Validation of a COMSOL Version of the Copper Corrosion Model

NWMO-TR-2022-08

March 2023

Fraser King[1] and Scott Briggs[2]

[1] Integrity Corrosion Consulting Ltd., [2] Nuclear Waste Management Organization

NUCLEAR WASTE MANAGEMENT ORGANIZATION
SOCIÉTÉ DE GESTION DES DÉCHETS NUCLÉAIRES

Nuclear Waste Management Organization
22 St. Clair Avenue East, 4th Floor
Toronto, Ontario
M4T 2S3
Canada

Tel: 416-934-9814
Web: www.nwmo.ca

Development and Validation of a COMSOL Version of the Copper Corrosion Model

NWMO TR-2022-08

March 2023

Fraser King[1] and Scott Briggs[2]
[1] Integrity Corrosion Consulting Ltd.
[2] Nuclear Waste Management Organization

Document History

Title:	Development and Validation of a COMSOL Version of the Copper Corrosion Model		
Report Number:	NWMO TR-2022-08		
Revision:	R000	Date:	March 2023
Author Company(s)			
Authored by:	Fraser King, Integrity Corrosion Consulting Ltd. Scott Briggs, Nuclear Waste Management Organization		
Nuclear Waste Management Organization			
Reviewed by:	Mehran Behazin, Peter Keech		
Accepted by:	Paul Gierszewski		

ABSTRACT

Title: **Development and Validation of a COMSOL Version of the Copper Corrosion Model**
Author(s): Fraser King[1], Scott Briggs[2]
Company: [1]Integrity Corrosion Consulting Ltd., [2]NWMO
Date: March 2023

Abstract

This report describes the conceptual basis for the Copper Corrosion Model (CCM) and defines a stepwise approach to the implementation of the conceptual model using the COMSOL Multiphysics software platform. The conceptual model is based on Version 1.1 of the existing custom-designed CCM code previously developed by King and Kolář (2000). The overall aim is to develop a validated COMSOL version of the existing CCM Version 1.1 custom-designed code as a basis for further development of NWMO's mixed-potential modelling capabilities for copper-coated used fuel containers.

The stepwise approach involves increasing degrees of mechanistic, geometric, and/or physico-chemical complexity in each incremental version of the model. Each successive development is validated against the results of a previously published study in which the corrosion potential E_{CORR} of a copper electrode in contact with a layer of NaCl-saturated compacted bentonite was measured as the dissolved O_2 content in the external solution was progressively decreased. Steady-state and transient versions of the COMSOL CCM are validated against the observed steady-state values and transient behaviour of E_{CORR}, respectively. Experimental measurements are available for both 1-mm-thick and 10-mm-thick clay layers.

The majority of the model development is conducted using a 1-D linear version of the code, in which the layer of compacted clay is represented by an equivalent porous medium bounded by the copper electrode on one side and the bulk O_2-containing NaCl solution on the other. Except for adjustment of the value of the tortuosity factor of the compacted clay found necessary to account for the time-dependence of E_{CORR}, all other input parameter values are taken from independent electrochemical measurements. A 2-D axisymmetric version of the COMSOL model was also developed to investigate the effect of multidimensional diffusion effects, which were found to be particularly important in the case of the 10-mm-thick clay layer. The 1-D linear version of the COMSOL model was also validated against the custom-designed (conventional) CCM code.

Overall, good agreement was found between the predicted steady-state and transient values of E_{CORR} and those measured experimentally. The steady-state E_{CORR} values agreed within a few mV and, following the adjustment in the value of the tortuosity factor, the COMSOL model was capable of predicting the transient behaviour of E_{CORR} as the O_2 concentration was progressively decreased. The agreement between measured and predicted E_{CORR} values was better for the 1-mm-thick clay layer than for the 10-mm electrode. Good agreement between the COMSOL and conventional versions of the CCM was also found for the 1-mm clay electrode. The one aspect of the reaction mechanism that proved difficult to simulate was the adsorption and desorption of Cu(II) by the bentonite. Finally, although the 1-mm clay electrode approximated a 1-D linear diffusion regime, interesting multi-dimensional effects were revealed using the 2-D axisymmetric model of the 10-mm-thick clay electrode. The validated COMSOL version of the CCM developed here is formally identified as the Copper Corrosion Model – COMSOL (CCMC) Version 1.0. Interim, incremental versions are referred to as Step 1, Step 2, Step 3a, etc.

TABLE OF CONTENTS

LIST OF TABLES

Page

LIST OF FIGURES

Page

1. INTRODUCTION

As with other components of the disposal system, it is necessary to make predictions of the long-term corrosion behaviour of the used fuel container (UFC). There are various approaches to UFC lifetime prediction (King 2014), including relatively simple mass-balance or mass-transport calculations or, for some container materials, the extrapolation of empirical corrosion rates. Macdonald (2003) argues that long-term predictions can only be justified on the basis of determinism rather than empiricism. Deterministic models are mechanistically based, such as Macdonald's Point Defect Model (Macdonald 1999) or the reactive-transport model described here.

The Copper Corrosion Model (CCM) predicts the uniform (general) corrosion behaviour of copper-coated UFC in a deep geological repository (DGR). The model is generally applicable and is capable of describing the corrosion behaviour of copper in any O_2-containing Cl^- environment in which mass transport of species to and from the corroding surface occurs by diffusion. In its current form, the model is one-dimensional (1-D) which makes it robust and applicable to a range of container and DGR designs. The strength of the CCM is that it is mechanistically based and was developed in conjunction with an expensive experimental program of electrochemical and corrosion studies (King and Kolář 2000, 2006a). As such, the CCM has been extended to include the effect of microbial processes (CCM-MIC, King and Kolář 2006b; King et al. 2002, 2003, 2004) and of sulfide (Copper Sulfide Model, CSM) (King and Kolář 20019a,b; King et al. 2011a,b, 2020), and to predict the likelihood of stress corrosion cracking (CCM-SCC) (King and Kolář 2004, 2005).

However, the CCM does have limitations. The model has been developed as a custom-designed code based on the TRANSIENT solver for partial differential equations (PDEs) (Kolář 2020). As such the code does not have the same extensive quality assurance (QA) basis of more widely used commercial codes, nor the documentation or user-community that would make it easy for other users to learn and develop. In addition, although great use has been made of the code despite the fact that it is limited to 1-D, there are certain aspects of the DGR design that are best simulated in 3-D. For these reasons, the custom-designed CCM is converted here for use with the commercial software package COMSOL Multiphysics (www.comsol.com).

This report describes the initial stages of the step-wise conversion of the custom-designed CCM to the COMSOL software platform. Chapter 2 provides an historical overview of the development of the CCM and introduces the underlying reaction mechanisms on which the model is based. The stepwise approach to the development of the COMSOL version of the model described in Chapter 3 is based on progressively increasing the functionality, mechanistic complexity, and dimensionality of the code. At each step in the development, the model predictions are validated against an experimental data set. The results of the simulations with each interim version of the code are described in Chapter 4. The main text is supported by an appendix giving a detailed description of the reaction-diffusion equations for each step (Appendix A). Appendix B lists all of the default input parameter values and their sources. In Appendix C, there is a discussion of the literature on the adsorption (and desorption) of copper on bentonite, a process that is found to have significant effects on the predictions from the model. The validated COMSOL version of the CCM developed here is formally identified as the Copper Corrosion Model – COMSOL (CCMC) Version 1.0. Interim, incremental versions are referred to as Step 1, Step 2, Step 3a, etc.

2. HISTORICAL DEVELOPMENT OF THE “COPPER CORROSION MODEL”

The Copper Corrosion Model (CCM) has been developed over the past 20 years (King 2008a; King and Kolář 1995, 1996a, 1996b, 1997a, 1997b, 2000, 2006a; King et al. 2008; Kolář and King 1996). Various changes and improvements to the reaction scheme and numerical implementation were made over this period, resulting in a number of distinct versions of the model. The most recent, and current, version of the model is the CCM Version 1.1, as described by King (2008a), King and Kolář (2006a), King et al. (2008). All versions of the code have been based on custom-designed software (written in C) that use the TRANSIENT solver (Kolář 2020) to solve sparse matrices resulting from the discretized finite-difference scheme.

The basic underlying reaction scheme has been extended to include the effects of sulfide (Copper Sulfide Model, CSM) (King 2008b; King et al. 2011a,b, 2019 a,b), microbial activity (CCM-MIC) (King and Kolář 2006b; King et al. 2002, 2003, 2004), and the likelihood of stress corrosion cracking (CCM-SCC) (King and Kolář 2004, 2005). These variants of the CCM are not considered further here.

A number of different versions of the model have been developed since 1995 (Table 1). These different versions are defined largely by the reaction scheme on which the code was based and on the treatment of the spatial and temporal variation in temperature and saturation. Figure 1 shows the reaction scheme for the initial version of the model (King and Kolář 1995, 1997a), which at that time was not referred to as the CCM. This version of the model was based on the solution of a set of six mass-balance equations or partial differential equations (PDEs), one for each of the six species specifically included in the model, namely: dissolved O_2, dissolved $CuCl_2^-$, precipitated Cu_2O, a dissolved Cu(II) species (exact speciation not defined), Cu(II) adsorbed on the bentonite, and a precipitated Cu(II) species (referred to as either CuO or $CuCl_2 \cdot 3Cu(OH)_2$). It is important to note that the CCM (and its predecessors) is a kinetically based code and does not incorporate a full equilibrium speciation code to account for the spatial and temporal changes in the pore-water chemistry. (The k’s noted in the figure are the corresponding rate constants, and the wavy lines denote diffusive mass transport). Thus, the precise nature of the dissolved Cu(II) species (Cu^{2+}, $CuOH^+$, $CuCl^+$, $Cu(OH)_2$, etc.) is not determined. Similarly, the nature of the precipitated Cu(II) phase is not determined, but is implicitly identified by the user-defined solubility.

This reaction mechanism was derived based on the results of a series of electrochemical and corrosion experiments (King and Kolář 2000). Electrochemical studies were used to define the nature of the interfacial anodic (the dissolution of copper as $CuCl_2^-$ species) and cathodic (the reduction of O_2) reactions. Corrosion experiments in the presence of compacted buffer material and synthetic saline ground water were used to determine the nature of the precipitated phases on the corroding copper and the extent of adsorption and transport of dissolved copper. As for all versions of the model, the reaction mechanism in Figure 1 is based on the assumption of a Cl^- dominated pore water, and in this early version of the model the $[Cl^-]$ was assumed to be constant in time and space. Redox reactions between dissolved Fe(II) and both O_2 and dissolved Cu(II) are also included in the reaction scheme and, similarly, the [Fe(II)] was assumed to be constant, rather than being treated as a spatial and temporal variable like the six primary species.

Table 1: Summary of the Historical Development of the "Copper Corrosion Model".

Step	Reaction scheme	Features	Application	Reference
Initial Version	Figure 1	6 species 1 anodic/1 cathodic reactions Isothermal Constant saturation Constant [Cl^-] and [Fe(II)] 2 layers	Effect of unsaturated conditions	King and Kolář 1995, 1997a
Central Case	Figure 2	10 species 1 anodic/2 cathodic reactions Isothermal Fully saturated 4 layers	AECL 2nd Case Study In-room configuration	King and Kolář 1996a Kolář and King 1996
Central Case + T (CCM Version 1.0)	Figure 2	As above, but spatially and temporally variable temperature	Effect of geosphere conditions AECL 2nd Case Study In-room configuration	King and Kolář 1997b, 2000 King 1996 Johnson et al. 1996
CCM Version 1.1	Figure 3	10 species 1 anodic/2 cathodic reactions Temperature f(x,t) Saturation f(x,t) Up to 11 layers	O_2 consumption for *in situ* tests and NWMO 3rd Case Study (in-room design)	King and Kolář 2006 King et al. 2008
CCMC Version 1.0 (Copper Corrosion Model – COMSOL Version 1.0)	Figure 3	Validated COMSOL version of CCM Version 1.1	Prediction of corrosion potentials in a DGR environment including current densities for prediction of corrosion rates. Developed in a stepwise approach (Steps 1 to 3f) detailed in this report.	This report

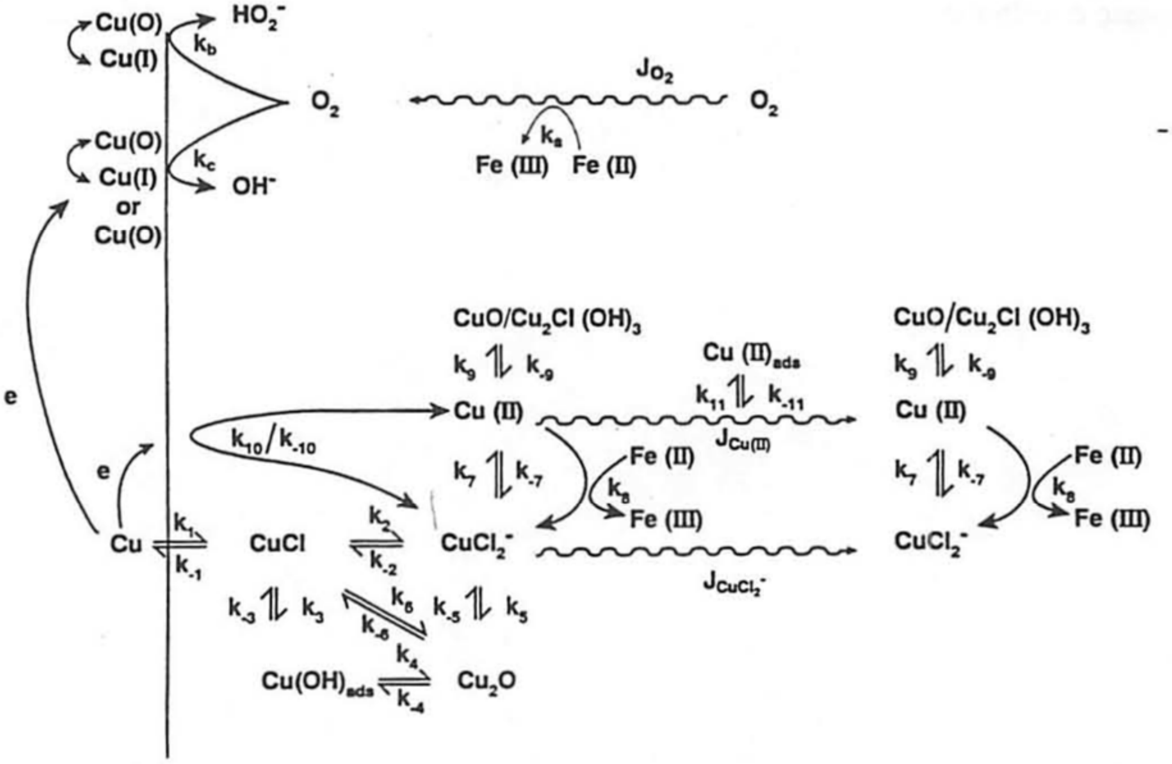

Figure 1: Reaction Scheme for Initial Copper Container Reactive-transport Model (King and Kolář 1995, 1997a).

An important aspect of this, and subsequent, versions of the reaction mechanism is the assumption of a Cl^- dominated pore solution. As a consequence, copper dissolves exclusively as Cu(I) (as the dissolved $CuCl_2^-$ species), with Cu(II) formed by the homogeneous oxidation of Cu(I) by dissolved O_2. Direct dissolution of copper as Cu(II) was shown to be a minor contributor to the overall copper dissolution reaction (King and Tang 1998). For this reason, SO_4^{2-} was assumed to play no role in the interfacial kinetics and was not included in the reaction scheme. This assumption of a Cl^- dominated system is common to all versions of the CCM.

Another important aspect of the model is the coupling of the electrochemically-based interfacial corrosion reactions to the homogeneous processes and mass transport of species in the environment away from the corroding surface. The anodic and cathodic Butler-Volmer expressions serve as mathematical boundary conditions for the solution of the PDEs of the species involved (in this case, dissolved O_2 and $CuCl_2^-$). By using the equality of the magnitude of the anodic and cathodic currents as an additional boundary condition, the model represents a mixed-potential model for the UFC surface coupled to processes in the near-field. Thus, one of the more important capabilities of the CCM is the prediction of the corrosion potential (E_{CORR}) of the corroding surface. For this initial version of the model, a single anodic reaction was coupled to a single cathodic reaction. Disproportionation of Cu(II) on the copper surface was included in the reaction scheme (as described by rate constants k_{10}/k_{-10} in Figure 1)

$$Cu^{2+} + Cu(0) + 4Cl^- = 2CuCl_2^- \qquad (1)$$

but was assumed not to be potential-determining.

In addition to predicting the time-dependent evolution of E_{CORR}, the other basic output of the model is the spatial and temporal variation of the concentration of each of the species included in the model as described by a PDE. The rate of each of the individual reactions can also be determined in space and time from which the extent of a specific process can be determined as a function of time or location based on suitable integration of the reaction rates.

A fundamental feature, and limitation, of this and subsequent versions of the CCM is that the precipitated corrosion products are assumed to only act as a sink (or source) of dissolved copper. Precipitation of Cu_2O and $CuO/CuCl_2{\cdot}3Cu(OH)_2$ is assumed not to modify the rates of the interfacial reactions, either by the formation of a protective or passive surface film or by modification of the mechanism of the anodic and cathodic processes. This is not the case for the related CSM (King 2008b; King and Kolář 2019 a,b; King et al. 2011a,b), in which the precipitated Cu_2S corrosion product is treated as a porous layer that not only blocks a fraction of the copper surface but also restricts the rate of transport of species to and from the underlying corroding interface.

Other features of this initial version of the model and reaction scheme include (King and Kolář 1995):

- Isothermal conditions, although different temperatures could be simulated in different runs by suitable modification of the values of temperature-dependent parameters.
- Constant saturation, although different degrees of saturation could be simulated in different runs by suitable modification of the effective diffusivity of O_2 to represent the faster diffusion of gaseous O_2 though unsaturated pores. No other effects of unsaturated conditions were simulated.
- Two porous mass-transport barriers representing the bentonite-based buffer material and host rock. The width of the buffer layer was defined by the ratio of the volume of buffer in the DGR to the container surface area in order to properly account for the initial O_2 inventory in the DGR.
- The left-hand boundary of the model represented by the UFC surface and the right-hand boundary by a groundwater-bearing fracture that maintained constant chemical conditions.
- For simulations of a fully saturated system, the initial concentration of dissolved O_2 was adjusted to represent both the dissolved and gaseous O_2 initially present in the as-placed, partially saturated buffer.
- As noted above, the pore-water [Cl^-] and [Fe(II)] were assumed to be constant in space and time.
- Assumption of near-neutral pH conditions at the copper surface and in the pore water at all times. This assumption is consistent with pH buffering by calcite and the experimental observation of $CuCl_2{\cdot}3Cu(OH)_2$ rather than CuO, the latter only being thermodynamically stable at pH > 7.5 in 1 mol/L Cl^- at 25°C (King and Kolář 1995).
- The precipitation of Cu_2O by either the hydrolysis of $CuCl_2^-$ or the loss of H_2O from adsorbed $Cu(OH)_{ads}$ intermediate species (Figure 1). In general, the anodic reaction involved the possible interaction between the adsorbed intermediates $Cu(OH)_{ads}$ and $CuCl_{ads}$, as well as Cu_2O and dissolved $CuCl_2^-$.

- Two possible pathways for the interfacial reduction of O_2, involving either the 2-electron reduction to peroxide (HO_2^-) or the 4-electron reduction to OH^-. In both cases, electron transfer was considered to be catalyzed by Cu(0)/Cu(I) surface states, as identified experimentally (King et al. 1995a,b).

This initial version of the code was used for the preliminary simulations of King and Kolář (1995) and to assess various impacts of geosphere properties on the corrosion of the UFC (King and Kolář 1997a).

Figure 2 shows the reaction scheme for what was referred to as the Central Case model (Table 1) and for what was to become the first version of the Copper Corrosion Model, subsequently referred to as CCM Version 1.0 (King and Kolář 1996, 1997b, 2000). This version of the model was developed in support of AECL's 2nd Case Study (Johnson et al. 1996). The most significant changes to the reaction scheme and model from the initial version described above were:

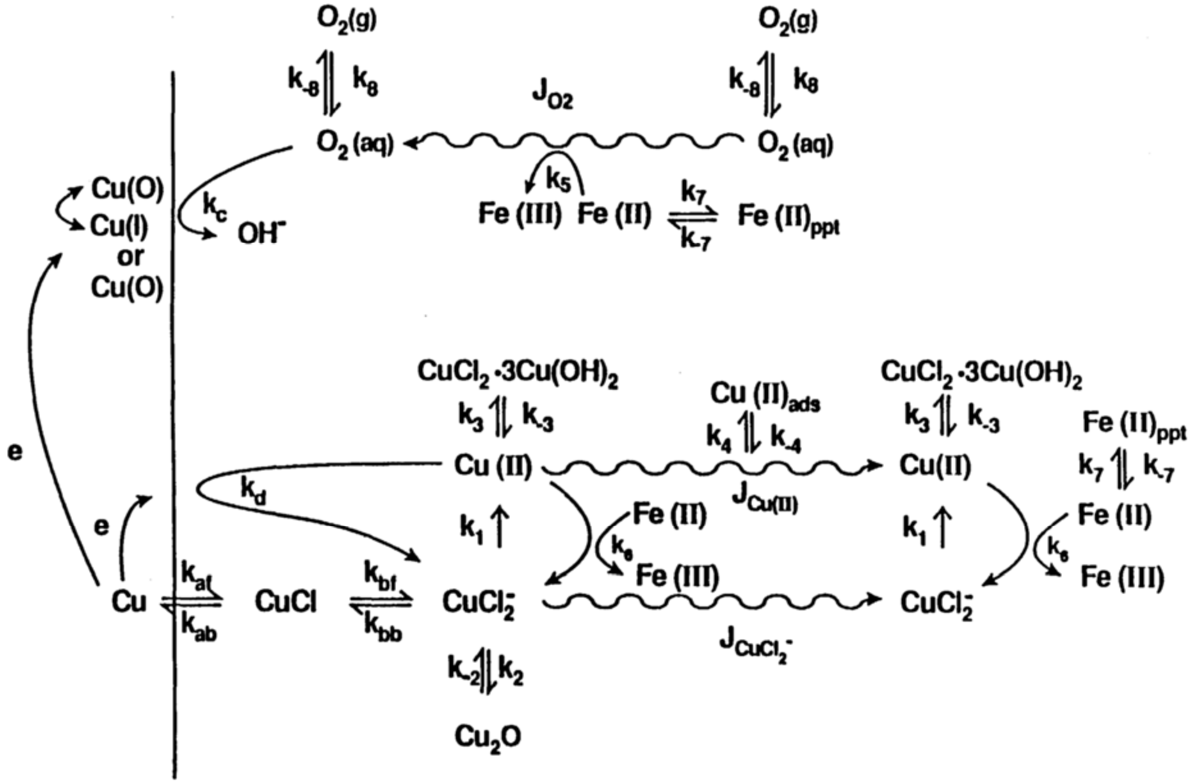

Figure 2: Reaction Scheme for the Central Case and Copper Corrosion Model Version 1.0 (King and Kolář 1996, 1997b, 2000).

- Replacement of the disproportionation of Cu(II) by the interfacial reduction of Cu(II) as a second cathodic process.
- Addition of three additional species (and three additional PDEs), namely; Cl^-, dissolved Fe(II), and a secondary Fe(II) precipitated phase. Gaseous O_2 is also shown in the reaction scheme, but was never implemented in any of the simulations.
- Dissolution of biotite, or other Fe(II)-containing solid, as the original source of dissolved Fe(II). Dissolved Fe(II) could subsequently precipitate if the concentration exceeded the solubility of this secondary solid Fe(II) phase. Biotite dissolution was treated using a shrinking-core kinetic model.
- Extension of the model geometry to include four mass-transport layers, generally taken to represent the buffer and backfill materials, an excavation-damaged zone (EDZ) of rock, and the host rock. The width of the layer representing backfill was based on the backfill volume:container surface area ratio in order to account for all of the initially trapped O_2. The widths of the EDZ and host rock layers were defined according to the characteristics of the DGR and site properties.

As with the initial version of the code, fully saturated conditions were assumed in the simulations, requiring the artificial increase in the initial dissolved $[O_2]$ in the buffer and backfill layers to properly conserve the amount of trapped O_2.

Early simulations using the Central Case model were conducted assuming isothermal conditions and included preliminary simulations of the in-room DGR design used for AECL's 2nd Case Study (King and Kolář 1996a, Kolář and King 1996), as well as of copper concentration profiles observed for a Bronze Cannon natural analogue study (King and Kolář 1996b).

A major improvement was made to the Central Case model for the actual analyses for 2nd Case Study through the introduction of the effects of the spatial and temporal variation in temperature. This improvement involved the incorporation of Arrhenius-type temperature-dependent expressions for all of the rate constants, diffusion coefficients, solubilities, etc. and the addition of a heat-conduction PDE. This version of the model was the first to be referred to as the Copper Corrosion Model and represents the CCM Version 1.0 (Table 1, King and Kolář 2000).

Figure 3 shows the reaction scheme for the latest version of the model, referred to as CCM Version 1.1, and the version to be used for the development of the COMSOL model (King and Kolář 2006, King et al. 2008). The major development from the previous Version 1.0 model is the incorporation of the spatial and temporal variation of the degree of saturation (S) of the different mass-transport layers. Instead of trying to solve coupled thermal-hydraulic-chemical (THC) expressions, the saturation behaviour was treated as a user-defined external input in the form of a set of time-dependent S(t) profiles for each of the mass-transport layers. To better spatially discretize the saturation behaviour, the layers representing the buffer and backfill materials were sub-divided. An arbitrary number of layers, up to a maximum of 11, could be specified in the CCM Version 1.1. From a mechanistic point of view, the incorporation of the time (t)- and spatial (x)-dependence of the saturation (S(x,t)) required the addition of one more species, gaseous O_2. Gaseous O_2 was assumed to dissolve (and exsolve) in the pore solution and could diffuse through the unsaturated pores, but otherwise was assumed not to react. One additional first-order process was added to the reaction scheme to represent the consumption of dissolved O_2 by aerobic microbes (Figure 3).

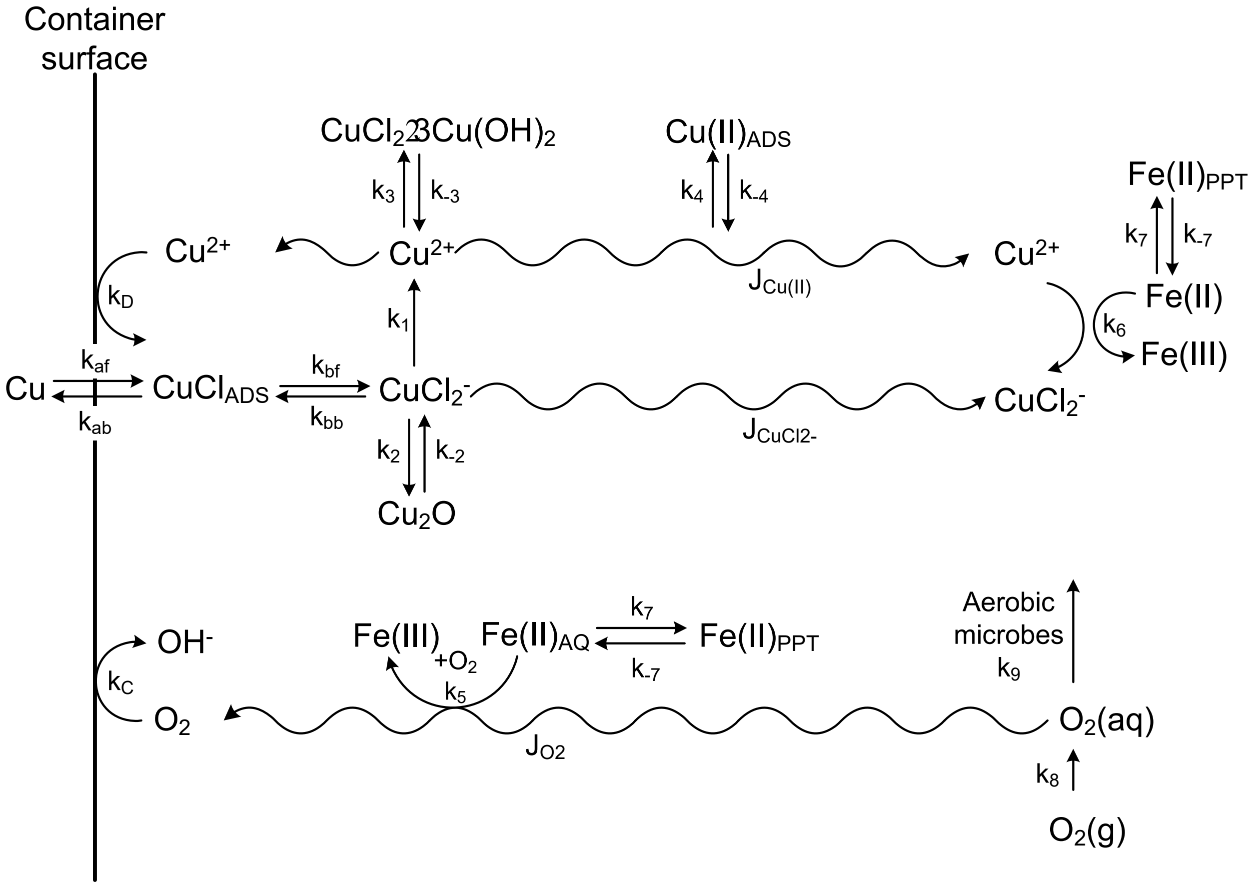

Figure 3: Reaction Scheme for the Copper Corrosion Model Version 1.1 (King and Kolář 2006, King et al. 2008).

A number of additional saturation-dependent processes were included in CCM Version 1.1, namely:

- Separate diffusion terms for gaseous and dissolved O_2, to replace the saturation-dependent effective diffusivity of O_2 used to approximate the transport of gaseous O_2 used in previous versions of the model.
- Modification of diffusivity of dissolved species based on the degree of saturation.
- Adjustment of the concentration of dissolved species in response to changes in the spatially and temporally varying moisture levels.
- Introduction of a minimum degree of saturation for the interfacial reactions, to simulate the drying of the surface and the cessation of the corrosion reaction at low relative humidity.
- Saturation-dependence of the specific heat and thermal conductivity of the buffer, backfill, and rock.
- Use of a threshold degree of saturation for the microbial consumption of O_2 to simulate the dependence of microbial activity on the availability of water.

A benefit of the separate treatment of gaseous and dissolved O_2 was the removal of the previous requirement to increase the initial concentration of dissolved O_2 in order to properly account for all of the trapped oxygen.

The CCM Version 1.1 was used to describe the corrosion behaviour of copper UFC for the conceptual DGR designs considered in OPG's 3rd Case Study (Russell and Simmons 2013) and to predict the consumption of O_2 in the DGR and various large-scale *in situ* experimental studies (King and Kolář 2006, King et al. 2008).

The CCM Version 1.1 is the latest version of the model and is the basis for the conversion of the custom-designed code to the COMSOL software platform. This conversion will involve a series of interim versions of the code of increasing mechanistic complexity, functionality, and dimensionality. The designation Copper Corrosion Model – COMSOL (CCMC) Version 1.0 (Table 1) is used here for the final, validated version of the COMSOL model, the initial development stages of which are described in this report. Interim, incremental versions of the CCMC code are identified as Step 1, Step 2, Step 3a, etc.

3. DEVELOPMENT OF COMSOL MODEL

Conversion of the custom-designed CCM to the COMSOL software platform is based on a stepwise approach, with each interim step representing an increase in mechanistic complexity, functionality, or dimensionality of the code. These steps are briefly outlined in Section 3.1, with the changes to the underlying structure of the code described in detail for each step in Appendix A. The basic features of the model common to both the custom-designed and COMSOL versions of the code are described in Section 3.2, including the PDEs that represent the reaction-diffusion (mass-balance) equations of the different chemical species, the model geometry, boundary and initial conditions, and the treatments of saturation and temperature effects. The basis for the COMSOL model is described in Section 3.3, including the software version used, the nature of the finite-element mesh, and the modifications required to accommodate the PDEs in the format prescribed by the COMSOL module used. Each interim version of the COMSOL model has been validated against a set of experimental data, with the validation procedure described in Section 3.4. As a second validation check, the results of the COMSOL model were compared with the results of identical simulations using the custom-designed code.

3.1 STEPWISE APPROACH

Table 2 summarizes the different steps for the development of the COMSOL model. Each successive step introduces additional complexity in terms of the solution type (steady-state or transient), the complexity of the reaction scheme, the model dimensionality, or the treatment of thermal and saturation effects. The general approach can be described as follows:

Step 1:	steady-state solution using a simplified reaction scheme
Step 2:	transient solution for the simplified reaction scheme
Steps 3a-3f:	transient solution with progressively more-complex reaction scheme
Step 4:	non-isothermal effects
Step 5:	effects of variable saturation
Step 6:	2D/3D simulation of DGR

The work reported here describes the development of the COMSOL model up to Step 3, although some 2-D axisymmetric modelling of the experimental set-up used for validation is also described. The further development to include variable temperature and saturation effects (Steps 4 and 5, respectively) and to extend the model to describe the geometry of the Mark II DGR (Step 6) will be described in a subsequent publication.

Table 2: Summary of Steps in the Development of the COMSOL Copper Corrosion Model.

Step	Dimensionality	Solution type	Incremental species/processes	Temperature	Saturation
1	1-D	Steady-state	O_2, Cl^-, $CuCl_2^-$	Isothermal	Saturated
2	1-D, 2-D	Transient	O_2, Cl^-, $CuCl_2^-$	Isothermal	Saturated
3a	1-D, 2-D	Transient	Cu^{2+}, homogeneous oxidation of $CuCl_2^-$ (k_1), interfacial reduction of Cu^{2+} (k_D)	Isothermal	Saturated
3b	1-D	Transient	$CuCl_2 \cdot 3Cu(OH)_2$, precipitation/dissolution of solid Cu(II) (k_3/k_{-3})	Isothermal	Saturated
3c	1-D	Transient	Cu_2O, precipitation/dissolution of solid Cu_2O (k_2/k_{-2})	Isothermal	Saturated
3d	1-D	Transient	$Cu(II)_{ADS}$, adsorption/desorption of Cu^{2+} (k_4/k_{-4})	Isothermal	Saturated
3e	1-D	Transient	Aerobic respiration (k_9)	Isothermal	Saturated
3f	1-D	Transient	$Fe(II)_{AQ}$, $Fe(II)_{PPT}$, reactions involving dissolved and precipitated Fe(II) (k_5, k_6, k_7/k_{-7})	Isothermal	Saturated
4	1-D	Transient	Spatial and temporal variation in temperature (T), T-dependence of rate constants, diffusion coefficients, and other input data	Non-isothermal	Saturated
5	1-D	Transient	Gaseous O_2, oxygen dissolution (k_8), spatial and temporal variation in saturation, effects of saturation on interfacial reactions, effective diffusion coefficients, and solute concentration	Non-isothermal	Variable saturation
6	2-D/3-D	Transient	2D/3D dimensionality of Mark II DGR	Non-isothermal	Variable saturation

3.2 PROGRAM DESIGN OF CCM

The basic features of the model described in this section are applicable to both the custom-designed and the COMSOL versions of the code. The model is based on the reaction scheme shown in Figure 3. For the purposes of software documentation, Table 3 summarises the program design and theory requirements.

Table 3: Program Design and Theory Summary Table

Requirement	Section
Identification of Algorithms	3.2.1
Program Structure	3.2, Appendix A, Appendix B
Additional Program Requirements	3.3.1

3.2.1 Reaction-diffusion Equations

The model is based on a series of PDEs that describe the transport and reaction of each of the chemical species in the model, plus a heat-conduction equation.

$$\frac{\partial\left[(1-S)\varepsilon_a c_A\right]}{\partial t} = \frac{\partial}{\partial x}\left(\tau_f(1-S)^3\varepsilon_e D_A\frac{\partial c_A}{\partial x}\right) - \varepsilon_a S k_8 (c_0^{sat} - c_0)(1-S)c_A \tag{2}$$

$$\begin{aligned}\varepsilon_a\frac{\partial(Sc_0)}{\partial t} = \frac{\partial}{\partial x}\left(\tau_f\varepsilon_e S D_0\frac{\partial c_0}{\partial x}\right) - \varepsilon_a S\left[\frac{k_1}{4}c_0c_1 + k_5c_0c_7 + k_9c_0\theta(S - S_{MIC})\right] \\ + \varepsilon_a S k_8(c_0^{sat} - c_0)(1-S)c_A\end{aligned} \tag{3}$$

$$\varepsilon_a\frac{\partial(Sc_1)}{\partial t} = \frac{\partial}{\partial x}\left(\tau_f\varepsilon_e S D_1\frac{\partial c_1}{\partial x}\right) + \varepsilon_a S\left[-k_1c_0c_1 + k_6c_3c_7 - k_2\max(0, c_1 - c_1^{sat})\right] + 2k_{-2}c_2 \tag{4}$$

$$\frac{\partial c_2}{\partial t} = \varepsilon_a S\frac{k_2}{2}\max(0, c_1 - c_1^{sat}) - k_{-2}c_2 \tag{5}$$

$$\begin{aligned}\varepsilon_a\frac{\partial(Sc_3)}{\partial t} = \frac{\partial}{\partial x}\left(\tau_f\varepsilon_e S D_3\frac{\partial c_3}{\partial x}\right) + \varepsilon_a S\left[k_1c_0c_1 - k_6c_3c_7 - k_3\max(0, c_3 - c_3^{sat}) - k_4c_3(c_5^{max} - c_5)\rho_d\right] \\ +4k_{-3}c_4 + k_{-4}c_5\rho_d\end{aligned} \tag{6}$$

$$\frac{\partial c_4}{\partial t} = \varepsilon_a S \frac{k_3}{4} \max(0, c_3 - c_3^{sat}) - k_{-3} c_4 \tag{7}$$

$$\rho_d \frac{\partial c_5}{\partial t} = \varepsilon_a S k_4 c_3 (c_5^{max} - c_5)\rho_d - k_{-4} c_5 \rho_d \qquad c_5 < c_5^{max} \tag{8}$$

$$\varepsilon_a \frac{\partial (S c_6)}{\partial t} = \frac{\partial}{\partial x}\left(\tau_f \varepsilon_e S f_{D6} D_6 \frac{\partial c_6}{\partial x}\right) + \varepsilon_a S\left[2k_1 c_0 c_1 - 2k_6 c_3 c_7 + 2k_2 \max(0, c_1 - c_1^{sat}) - \frac{k_3}{2}\max(0, c_3 - c_3^{sat})\right]$$
$$+2k_{-3} c_4 - 4k_{-2} c_2 \tag{9}$$

$$\varepsilon_a \frac{\partial (S c_7)}{\partial t} = \frac{\partial}{\partial x}\left(\tau_f \varepsilon_e S D_7 \frac{\partial c_7}{\partial x}\right) + \varepsilon_a S A_F [R_0 e^{-\alpha_F t} + R_1]$$
$$-\varepsilon_a S[4k_5 c_0 c_7 + k_6 c_3 c_7 + k_7 \max(0, c_7 - c_7^{sat})] + k_{-7} c_8 \tag{10}$$

$$\frac{\partial c_8}{\partial t} = \varepsilon_a S k_7 \max(0, c_7 - c_7^{sat}) - k_{-7} c_8 \tag{10}$$

where the notation for the concentrations of the ten species (A, 0, 1 ….. 8) is given in Table 4 and the other symbols are defined in Table 5. The heat-conduction equation is given by

$$\rho C \frac{\partial T}{\partial t} = \frac{\partial}{\partial x}\left(K \frac{\partial T}{\partial x}\right) \tag{11}$$

Table 4: Notation for the Concentration of Each of the Chemical Species and Temperature Used in the Copper Corrosion Model for Uniform Corrosion (CCM-UC.1.1)

Species	Notation
Gaseous O_2	c_A
Dissolved O_2	c_0
Dissolved $CuCl_2^-$	c_1
Precipitated Cu_2O	c_2
Dissolved Cu^{2+}	c_3
Precipitated $CuCl_2 \cdot 3Cu(OH)_2$	c_4
Adsorbed Cu(II)	c_5
Dissolved Cl^-	c_6
Dissolved Fe(II)	c_7
Precipitated Fe(II)	c_8
Temperature	T

Table 5: Definition of Symbols for Chemical Species, Rate Constants, Mass-transport, and Thermal Properties in CCM-UC.1.1

Symbol	Definition
c_A	bulk-volume concentration of gaseous O_2 in reservoir
c_0	pore-solution concentration of dissolved O_2
c_1	pore-solution concentration of dissolved $CuCl_2^-$
c_2	bulk-volume concentration of precipitated Cu_2O
c_3	pore-solution concentration of dissolved Cu^{2+}
c_4	bulk-volume concentration of precipitated $CuCl_2{\cdot}3Cu(OH)_2$
c_5	mass-concentration of adsorbed Cu^{2+}
c_6	pore-solution concentration of Cl^-
c_7	pore-solution concentration of dissolved Fe(II)
c_8	bulk-volume concentration of precipitated Fe(II) secondary phase
c_0^{sat}	Saturated concentration of dissolved O_2
c_1^{sat}	Saturated concentration of dissolved $CuCl_2^-$
c_3^{sat}	Saturated concentration of dissolved Cu^{2+}
c_7^{sat}	Saturated concentration of dissolved Fe(II)
c_5^{max}	Maximum concentration of adsorbed Cu^{2+}
f_{D6}	Enhancement factor for the diffusion coefficient of Cl^-
k_1	Homogeneous rate constant for the oxidation of $CuCl_2^-$ by O_2
k_2	Homogeneous rate constant for the precipitation of Cu_2O
k_{-2}	Homogeneous rate constant for the dissolution of Cu_2O
k_3	Homogeneous rate constant for the precipitation of $CuCl_2{\cdot}3Cu(OH)_2$
k_{-3}	Homogeneous rate constant for the dissolution of $CuCl_2{\cdot}3Cu(OH)_2$
k_4	Homogeneous rate constant for the adsorption of Cu^{2+}
k_{-4}	Homogeneous rate constant for the desorption of Cu^{2+}
k_5	Homogeneous rate constant for the oxidation of Fe(II) by O_2
k_6	Homogeneous rate constant for the reduction of Cu^{2+} by Fe(II)
k_7	Homogeneous rate constant for the precipitation of a secondary-phase Fe(II) solid
k_{-7}	Homogeneous rate constant for the dissolution of a secondary-phase Fe(II) solid
k_8	Homogeneous rate constant for the dissolution of gaseous O_2
k_9	First-order rate constant for the consumption of O_2 by microbes
t	Time
x	Distance
A_F	Surface area of exposed biotite
C	Specific heat
D_A	Effective diffusion coefficient of gaseous O_2
D_0	Pore-solution diffusion coefficient of dissolved O_2
D_1	Pore-solution diffusion coefficient of dissolved $CuCl_2^-$
D_3	Pore-solution diffusion coefficient of dissolved Cu^{2+}
D_6	Pore-solution diffusion coefficient of dissolved Cl^-
D_7	Pore-solution diffusion coefficient of dissolved Fe(II)

…. continued

Table 6: Definition of Symbols for Chemical Species, Rate Constants, Mass-transport, and Thermal Properties in CCM-UC.1.1 (concluded)

Symbol	Definition
K	Thermal conductivity
R_0	Instantaneous rate of release of Fe(II) from biotite dissolution
R_1	Steady-state rate of release of Fe(II) from biotite dissolution
S	Degree of saturation
T	Temperature
α_F	Time constant for the dissolution of biotite
ε_a	Accessible porosity
ε_e	Effective porosity for mass transport
$\theta(x)$	Theta function having a value of 1 for $x \geq 0$ and a value of 0 for $x < 0$
ρ	Dry density
τ_f	Tortuosity factor

3.2.2 Model Geometry

The PDEs in the previous section are written on the assumption of 1-D linear geometry, but can in principle be reformulated to describe other geometries, such as 1-D radial, 2-D, or 3-D. As shown in Table 2, the COMSOL models described here are largely based on 1-D linear geometry, with higher dimensionalities to be used in Step 6. However, a 2-D axisymmetric model has also been developed to assist validation of the Step 2 and Step 3a models, as described in more detail below.

Because of the coupled nature of these PDEs, the model is best solved using either finite-difference or finite-element methods. The custom-designed code was solved using finite-difference methods and the TRANSIENT numerical solver of Kolář (2020). COMSOL Multiphysics uses a finite-element scheme to solve the PDEs (COMSOL 2020) as described in more detail in Section 3.3.2.

3.2.3 Boundary Conditions

Regardless of the method of solution, boundary conditions are required to solve the PDEs for mobile species. The two boundaries for the 1-D linear model are the corroding copper surface on the left and a location in the DGR or, in this case, the experimental set-up in which the chemical conditions are controlled or well-defined.

From a corrosion point of view, the most important boundary conditions are those for species participating in the anodic and cathodic reactions on the copper surface; namely: dissolved O_2, $CuCl_2^-$, Cl^-, and Cu^{2+}. Butler-Volmer expressions are used to describe the rates of the electrochemical reactions, along with the condition that the sum of the anodic (i_a) and cathodic (i_c, i_d) currents (or current densities, in this case) equals zero:

$$i_a + i_c + i_d = 0 \tag{12}$$

The formulations of the anodic and cathodic Butler-Volmer expressions are given in Appendix A. The important point here is that these electrochemical boundary conditions represent a mixed-potential model and allow the corrosion potential E_{CORR} of the copper surface to be determined. For dissolved species that do not react on the copper surface, such as gaseous O_2 or Fe(II), it is usual to use a zero-flux boundary condition.

As noted above, the right-hand boundary conditions are determined by the properties of the system being modelled. For species that do not leave or enter the modelled domain, a zero-flux boundary condition is commonly used. For species for which the concentration is determined by the properties of the medium at the boundary, it is usual to use either a constant or a time-dependent concentration boundary condition.

For temperature, the boundary condition is either constant at both left-hand and right-hand boundaries for isothermal systems, or a specific time-dependent value in the case of non-isothermal simulations.

3.2.4 Initial Conditions

Initial conditions are required for all ten chemical species and for temperature for all domains defined by the model geometry. These initial conditions define the properties of the system being modelled; for example, whether it is initially aerated or initially free of dissolved species other than O_2 and Cl^-. The specific initial conditions used for the different species in the step-wise development of the COMSOL model are defined in Appendix A.

3.2.5 Treatment of Saturation

The effects of spatially and temporally variable saturation are introduced in Step 5 of the step-wise development (Table 2) and will not be discussed in detail here. As described in Section 2, a number of effects of variable saturation are simulated in the CCM Version 1.1 (King and Kolář 2006). It should be noted that the reaction-diffusion equations defined in Section 3.2.1 are written to take into account the effects of variable saturation S.

For all versions of the model described in this report, fully saturated conditions are assumed.

3.2.6 Treatment of Temperature Effects

The effects of spatially and temporally variable saturation are introduced in Step 4 of the step-wise development (Table 2) and will not be discussed in detail here. Briefly, all of the rate constants, diffusion coefficients, solubilities, and standard electrochemical potentials used as model inputs are temperature dependent. In the majority of cases, the effect of the spatial and temporal variation in temperature, as determined by solution of the heat-conduction equation, is accounted for using an Arrhenius-type relationship defined by the parameter value at a specified temperature and a corresponding activation energy (King and Kolář 2006).

For all versions of the model described in this report, isothermal conditions are assumed.

3.3 REQUIREMENT SPECIFICATION – COMSOL MODEL

In this section, certain aspects of the implementation of the Copper Corrosion Model – COMSOL (CCMC) Version 1.0 using the COMSOL Multiphysics software are described, including: the version of the software package and modules used for the current study, modifications to the reaction-diffusion equations to ensure consistency with the treatment of transport in COMSOL, and a description of the finite-element mesh and model geometry. For the purposes of software documentation, Table 6 summarises the requirement specifications for CCMC Version 1.0.

Table 7: Requirement Specification Summary Table

Requirement	Section
Name and Version	3.3
Function	3.2
Software and Hardware	3.3.1
User Interface	Standard COMSOL interface, See also Section 3.2 and Appendix A
Input Requirements	Appendix B
Output Requirements	Current density and corrosion potential
Physical Model	3.2.1
Error and Accuracy	3.3.3
Validation and Verification Activities	3.4

3.3.1 Software and Hardware

All the simulations described here were performed using version 5.6 of the COMSOL Multiphysics platform, including the Corrosion Module and specifically the Electroanalysis physics interface (see www.comsol.com). Simulations were executed on a Dell Precision 7920 workstation running on Intel Xeon x86 processors. Model runtime varied from 4 minutes to 10 hours depending on the dimensionality of the problem (i.e., 1-D and 2-D axisymmetric) and the model Step (i.e., Step 2 through Step 3f), while computer memory requirements similarly ranged between 4 GB and 24 GB.

The number of CPU cores used was 18. While the workstation has two physical CPU sockets (each with 18 cores), it was found that using both physical CPUs together (total 36 cores) resulted in longer runtimes due to the overhead of using multiple CPU sockets. Core counts are based on physical cores as COMSOL does not benefit from the use of virtual cores. The overhead is a result of the communication latency and bandwidth limitations between CPU sockets. In general, COMSOL Multiphysics can scale to an arbitrary number of CPUs but parallel performance in practice is dependent on the specific physics and implementation details of a simulation. A simulation may benefit from parallel performance improvements based on the amount of code that can be run in parallel but limited by code that must run in serial. While 18 cores (1 CPU socket) were used to run simulations, additional testing of the CCM using

COMSOL for parallel performance improvements with increasing (or decreasing) core count was not conducted.

3.3.2 Modification to PDEs

The CCM requires reaction-diffusion PDEs be solved (see Section 3.2.1) to model the chemical reactions and diffusion through clay, a porous medium. However, the COMSOL implementation of the CCM used the physics interface Electroanalysis which, in version 5.6, includes reaction-diffusion PDEs by default but not specific to porous media. To account for the desired transport physics, in addition to the reaction-diffusion PDEs, diffusive transport in porous media includes the effects of porosity and tortuosity. In the case of the CCM the porosity term, ε_a, is not time or space dependent (for a given domain) and can be moved out of the differential equation. For example, Equation (2) from Section 3.2.1 becomes:

$$\varepsilon_a \frac{\partial[(1-S)c_A]}{\partial t} = \varepsilon_e \frac{\partial}{\partial x}\left(\tau_f (1-S)^3 D_A \frac{\partial c_A}{\partial x} \right) - \varepsilon_a S k_8 (c_0^{sat} - c_0)(1-S)c_A \qquad (13a)$$

Dividing through the equation by ε_a gives:

$$\frac{\partial[(1-S)c_A]}{\partial t} = \frac{\partial}{\partial x}\left(\tau_f (1-S)^3 \frac{\varepsilon_e}{\varepsilon_a} D_A \frac{\partial c_A}{\partial x} \right) - S k_8 (c_0^{sat} - c_0)(1-S)c_A \qquad (13b)$$

Up to Step 5, the model is fully saturated (S=1), so we can rearrange the equation and define:

$$\tau\varepsilon = \frac{\varepsilon_e}{\varepsilon_a}\tau_f \qquad (14)$$

$$\frac{\partial c_A}{\partial t} - \frac{\partial}{\partial x}\left(\tau\varepsilon D_A \frac{\partial c_A}{\partial x} \right) = -k_8 (c_0^{sat} - c_0) c_A \qquad (15)$$

Equation 15 is now in the form used by the Electroanalysis physics interface in COMSOL with the diffusion physics on the left-hand side of the equation and the reaction physics on the right-hand side. Similar manipulations were made for all species in the CCM for implementation in COMSOL Multiphysics using the Electroanalysis interface.

$$\frac{\partial c_0}{\partial t} - \frac{\partial}{\partial x}\left(\tau\varepsilon D_0 \frac{\partial c_0}{\partial x} \right) = -\frac{1}{4} k_1 c_0 c_1 - k_5 c_0 c_7 - k_9 c_0 \max(0, 1 - S_{MIC}) \qquad (16)$$

$$\frac{\partial c_1}{\partial t} - \frac{\partial}{\partial x}\left(\tau\varepsilon D_1 \frac{\partial c_1}{\partial x} \right) = -k_1 c_0 c_1 + k_6 c_3 c_7 - k_2 \max(0, c_1 - c_1^{sat}) + \frac{2}{\varepsilon_a} k_{-2} c_2 \qquad (17)$$

$$\frac{\partial c_2}{\partial t} = \varepsilon_a \frac{k_2}{2} \max(0, c_1 - c_1^{sat}) - k_{-2} c_2 \qquad (18)$$

$$\begin{aligned}\frac{\partial c_3}{\partial t}-\frac{\partial}{\partial x}\left(\tau\varepsilon D_3\frac{\partial c_3}{\partial x}\right)&=k_1c_0c_1-k_6c_3c_7-k_3\max(0,c_3-c_3^{sat})-k_4c_3(c_5^{max}-c_5)\rho_d\\&\quad+\frac{1}{\varepsilon_a}\left[4k_{-3}c_4+k_{-4}c_5\right]\end{aligned}\tag{19}$$

$$\frac{\partial c_4}{\partial t}=\varepsilon_a\frac{k_3}{4}\max(0,c_3-c_3^{sat})-k_{-3}c_4\tag{20}$$

$$\frac{\partial c_5}{\partial t}=\varepsilon_a k_4c_3(c_5^{max}-c_5)-k_{-4}c_5\tag{21}$$

$$\begin{aligned}\frac{\partial c_6}{\partial t}-\frac{\partial}{\partial x}\left(\tau\varepsilon D_6\frac{\partial c_6}{\partial x}\right)&=2k_1c_0c_1-2k_6c_3c_7+2k_2\max(0,c_1-c_1^{sat})-\frac{k_3}{2}\max(0,c_3-c_3^{sat})\\&\quad+\frac{1}{\varepsilon_a}\left[2k_{-3}c_4-4k_{-2}c_2\right]\end{aligned}\tag{22}$$

$$\begin{aligned}\frac{\partial c_7}{\partial t}-\frac{\partial}{\partial x}\left(\tau\varepsilon D_7\frac{\partial c_7}{\partial x}\right)&=A_F[R_0e^{-\alpha_F t}+R_1]-4k_5c_0c_7-k_6c_3c_7\\&\quad-k_7\max(0,c_7-c_7^{sat})+\frac{1}{\varepsilon_a}k_{-7}c_8\end{aligned}\tag{23}$$

$$\frac{\partial c_8}{\partial t}=\varepsilon_a k_7\max(0,c_7-c_7^{sat})-k_{-7}c_8\tag{24}$$

COMSOL Multiphysics includes many physics interfaces for ease of use to end-users but is at its core a graphical interface for a finite element solver of any combination of PDEs or ODEs. The PDEs listed above are just one of many ways that COMSOL Multiphysics can be used to solve the desired physics. The presented implementation used the Electroanalysis physics interface and was adjusted to include the porosity in the PDEs as discussed above. Adjustments were also made to the anodic and cathodic reaction kinetics and post-processing of current density calculations to account for the accessible porosity term.

3.3.3 Finite-element Mesh, Time Stepping and Model Geometry

The CCM as implemented in COMSOL Multiphysics is a finite element model of reaction and diffusion physics. As such it includes up to 8 species and their associated reactions and transport mechanisms. Each species is considered a dependent variable within COMSOL which allows for the transport and reaction of each species in the model. The large number of dependent variables significantly increases the degrees of freedom of the finite element system and results in a larger system of equations to solve numerically. The system of equations are solved across the discretization of space using a finite element mesh.

COMSOL Multiphysics includes an automatic mesh generation algorithm for single and multi-dimensional models. The 1-D implementation of CCM uses constant mesh spacing across the

1 mm and 10 mm model geometry. In the 2-D asymmetric implementation, COMSOL has the capability to use triangular and rectangular elements. For the work presented here, only triangular elements were selected. Sensitivity to the mesh was determined by testing element spacing over many orders of magnitude and is discussed further below.

Time discretization was also specified in the COMSOL solver settings. In this model, a dynamic time-stepping algorithm was used to determine time discretization where the selection of each successive time step is determined based on a calculation of relative error. While many time discretization settings are available to the user in COMSOL, most were left as default within the COMSOL interface. Others, including the initial time step and the relative tolerance were adjusted to minimize errors within the simulation. By default, COMSOL selects an initial time step as a small fraction of the total simulation time, but the selection of an initial time step is a feature of the COMSOL solver available to the user. It was found that negative concentrations, due to numerical error, resulted when the initial time step was large, and an initial time step of, at most, 1×10^{-7} hrs was needed to maintain positive species concentrations. Similarly, the relative tolerance is a COMSOL feature that allows the user to reduce the relative error tolerance while solving the finite element model. Typically, a lower relative tolerance results in more time steps taken during a simulation resulting in longer solve times and more-accurate solutions. The default value in COMSOL is 0.005 (unitless) but a lower value of 1×10^{-4} was used in the COMSOL version of the CCM. Relative tolerance values of 1×10^{-3}, 1×10^{-4} and 1×10^{-5} were tested and no variation between the tested values was apparent when comparing species concentrations (see oxygen concentrations as a representative example in Figure 4) or the corrosion potential, E_{corr} (see Figure 5).

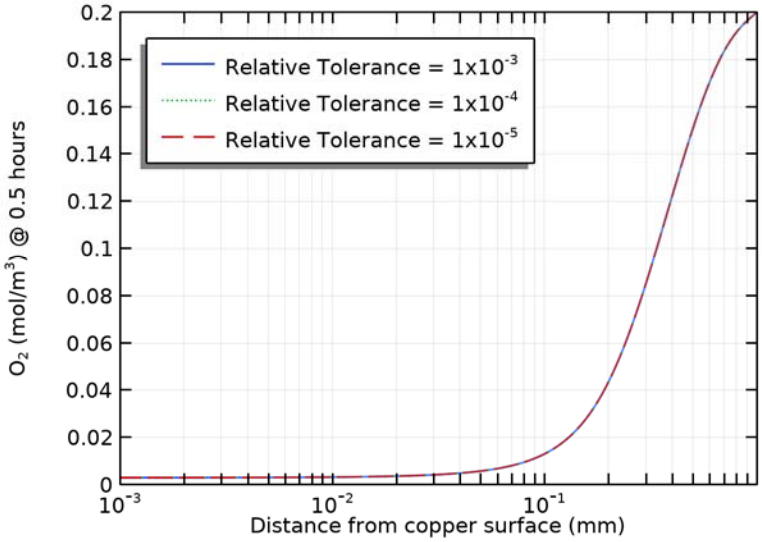

Figure 4: Time Discretization Sensitivity Analysis Comparing Oxygen Concentration at 0.5 hours for a 1-D, 1 mm Model Geometry.

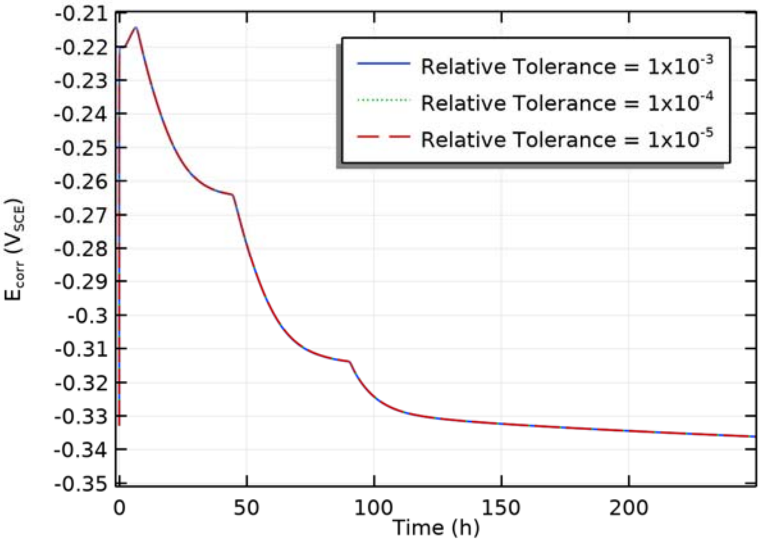

Figure 5: Time Discretization Sensitivity Analysis Comparing E_{corr} Values for a 1-D, 1 mm Model Geometry.

Differences in time discretization do emerge when comparing the sum of all current densities. The COMSOL implementation of the CCM is a mixed-potential model that solves for corrosion potentials when the sum of the current densities is equal to zero. In practice, the numerical solution is close to, but not exactly, zero. As long as the deviation from zero is much less than any individual current density then the error is considered negligible. Therefore, the targeted accuracy can be stated as: $\sum |i_i| \ll |i_i|$ where i_i is the current density for each surface reaction i. For a 1 mm model geometry in 1-D, Figure 6 shows the results from the time discretization study and the sensitivity of the model to the relative tolerance parameter. Current densities are plotted using the absolute values in Figure 6 and results can be summarized by:

1. A relative tolerance of 1x10^{-3} results in the sum of current densities larger than i_d at early time (Figure 6a) and the accuracy target is not met.
2. A relative tolerance of 1x10^{-4} results in a sum of current densities closer to zero and less than any individual current density for most of the simulation (Figure 6b). The accuracy target is met for values of time > 1x10^{-7} hrs.
3. A relative tolerance of 1x10^{-5} results in a sum of current densities smaller again and much less than i_d (Figure 6c). The accuracy target is met for time > 1x10^{-10} hrs.

Computation requirements increased significantly with the finest time discretization and a final relative tolerance of 1x10^{-4} was selected for the COMSOL model presented in this report. This value gives sufficient accuracy with balanced computational requirements.

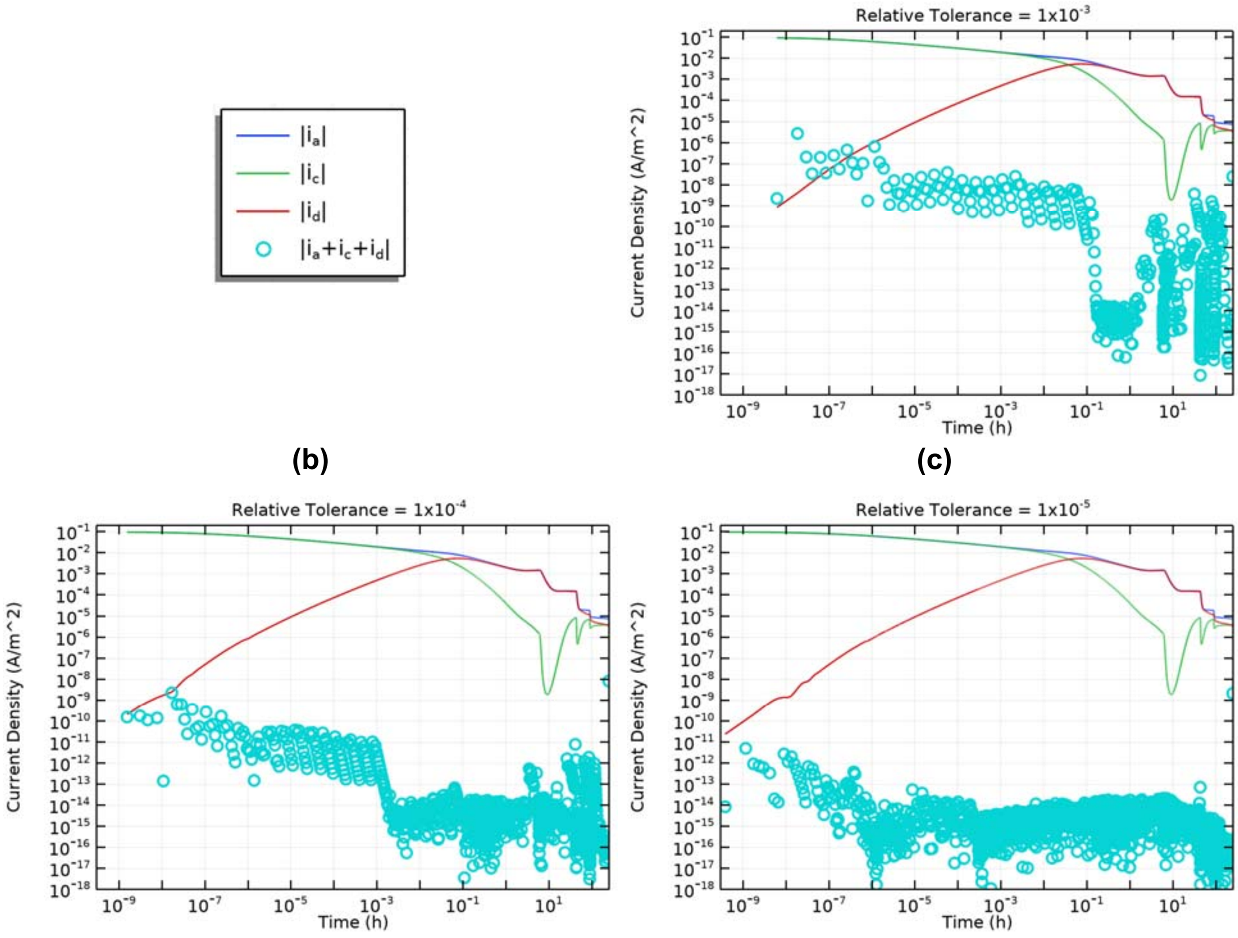

Figure 6: Time Discretization Sensitivity Analysis of Current Density for a 1-D, 1 mm Model Geometry.

The spatial discretization of a finite element model is required to numerically solve the system of equations. A finer element size typically requires more computational resources (CPU and memory requirements), but results in a more accurate solution. To reduce computational requirements, it is desirable to find the largest finite element size, or mesh size, that accurately computes the solution. This can be accomplished by reducing the mesh size until the solution converges to within a desired tolerance. For the purpose of this model a qualitative comparison of simulation outputs (e.g., concentrations, E_{corr} and current densities) are used to select an appropriate mesh size. Element sizes between 6.7x10^{-4} m and 6.7x10^{-9} m were tested where both the 1 mm and 10 mm model geometries used a constant grid spacing across the domain. Similar to the time discretization study, the oxygen concentration across the model domain is used as a representative result (Figure 7) to illustrate that all but the coarsest mesh tested converge to the same solution. Note that the coarsest mesh also results in negative concentrations and, in general, a poorly resolved model. Similar results are found when comparing the corrosion potential in Figure 8.

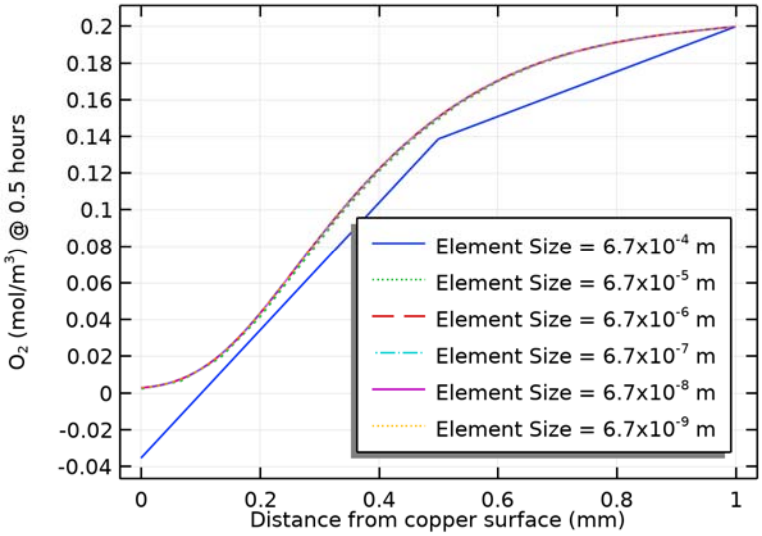

Figure 7: Spatial Discretization Sensitivity Analysis Comparing Oxygen Concentration at 0.5 hours for a 1-D, 1mm Model Geometry.

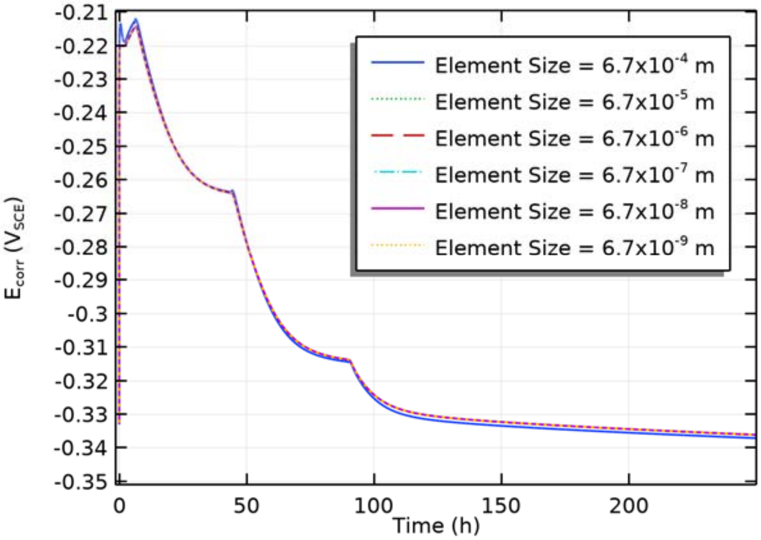

Figure 8: Spatial Discretization Sensitivity Analysis Comparing E_{corr} Values for a 1-D, 1 mm Model Geometry.

However, when comparing current densities at very early time, a clear distinction emerges from the discretization study. In Figure 9 the anodic dissolution of copper (i_a) and the cathodic reduction of Cu^{2+} (i_d) are compared at varying elements sizes. All but the coarsest mesh are convergent after 0.1 hrs through the final simulated 250 hrs. At earlier times, down to $1x10^{-7}$ hrs, only the two finest meshes converge on a common solution and is, in part, explained by Figure 10. Figure 10 shows the absolute values of the current density for the three surface reactions as well as the sum of the current densities (where the sum of the current densities should be zero or numerically close to zero as discussed above). From Figure 10, as the mesh spacing is reduced, the sum of the current densities approaches zero at earlier time resulting in converging solutions at earlier time. It was desirable to have convergent solutions down to $1x10^{-7}$ hrs for comparison and validation purposes with the previous implementation of the CCM. For this reason, a mesh spacing of $6.7x10^{-8}$ m was chosen for all 1-D model geometries. At this resolution the accuracy targets are met and 1-D computational requirements remained reasonable with solve times between 4 minutes and 6 hours depending on the CCM Step being simulated.

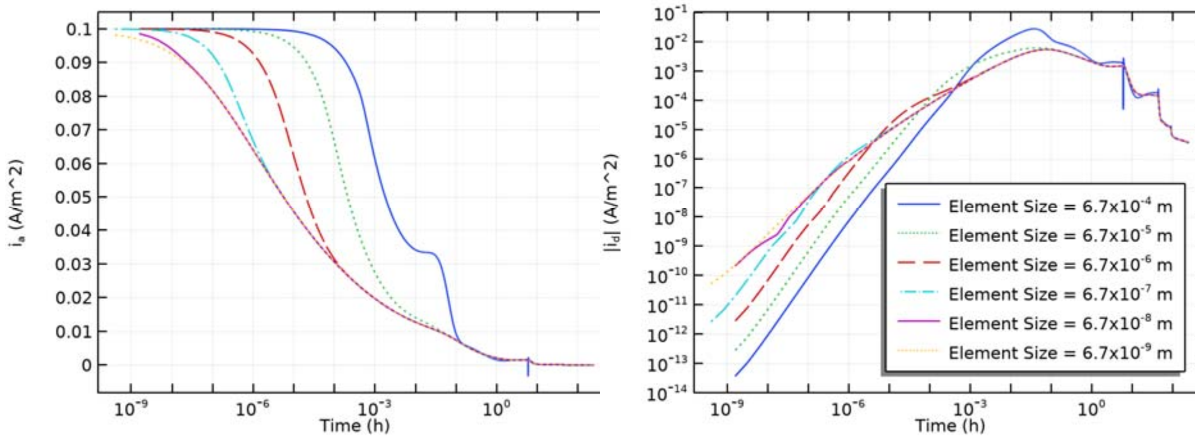

(a) **(b)**

Figure 9: Spatial Discretization Sensitivity Analysis Comparing (a) the Anodic Dissolution of Copper (i_a) and (b) the Absolute Value of the Cathodic Reduction of Cu^{2+} (i_d) for a 1-D, 1 mm Model Geometry. Note: Legend Applies to both (a) and (b).

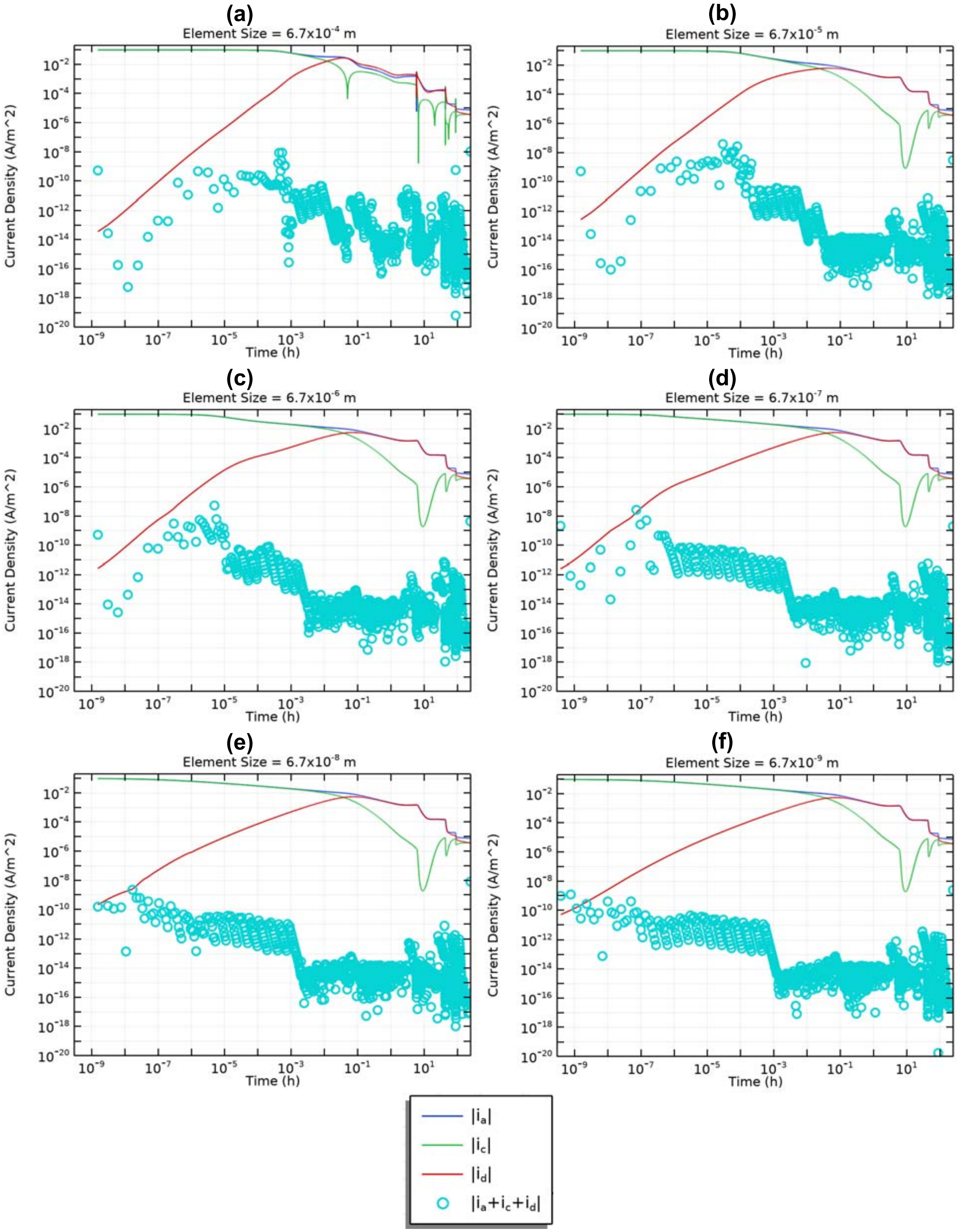

Figure 10: Spatial Discretization Sensitivity Analysis of Current Density for a 1-D, 1 mm Model Geometry.

For all 2-D axisymmetric models, a maximum finite element size of $1.5\text{x}10^{-5}$ m and a minimum element size of $1\text{x}10^{-7}$ was specified with an average element size of approximately $1.45\text{x}10^{-5}$ m. The time discretization relative tolerance parameter was specified at $1\text{x}10^{-4}$. While the finite element size is larger than that specified for the 1-D models it was desirable to maintain a simulation time under 10 hours for model development purposes. Figure 11 shows the radial comparison between the three surface reactions current density and the sum of all current densities. For the model at 6 hours, the cathodic reaction i_c (blue dashed line) is smaller than the sum of the current densities (blue circles) indicating sufficient time and spatial discretization was not achieved (accuracy target not met). The current densities averaged across the entire electrode surface and plotted against time are shown in Figure 12 and indicate that the sum of current densities are not always less than any individual current density for early time (< 55 hrs).

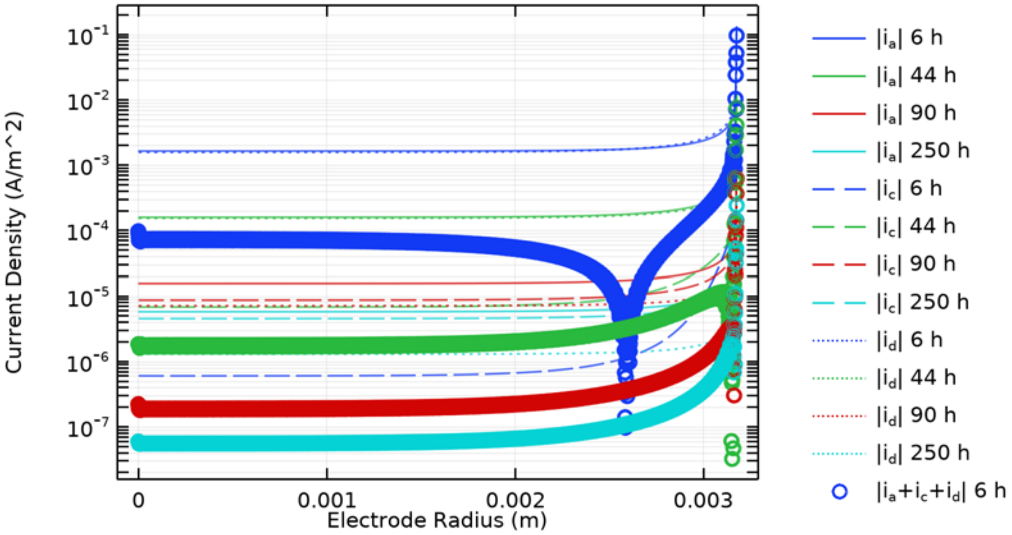

Figure 11: 2-D Axisymmetric Model Radial Current Density Comparison for a 1 mm Model Geometry.

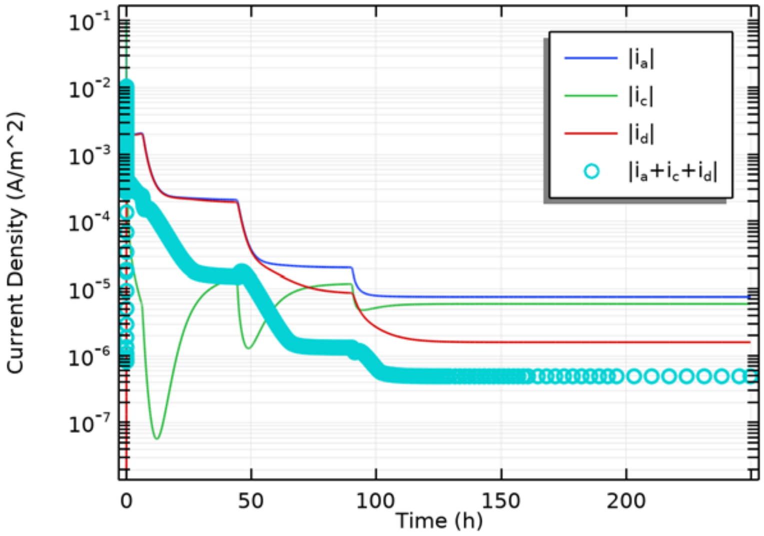

Figure 12: 2-D Axisymmetric Model Averaged Current Density Comparison for a 1 mm Model Geometry.

3.3.4 Nomenclature for Interim COMSOL Versions

The interim versions of the COMSOL model are identified by the respective steps (Table 7).

Table 8: Nomenclature for the Interim Versions of the COMSOL-based CCMC Version 1.0.

Model	Basis
Step 1	Steady-state, simplified reaction scheme
Step 2	Transient, simplified reaction scheme
Step 3a	As for Step 2, with addition of formation and cathodic reduction of Cu^{2+}
Step 3b	As for Step 3a, with addition of precipitation/dissolution $CuCl_2{\cdot}3Cu(OH)_2$
Step 3c	As for Step 3b, with addition of precipitation/dissolution of Cu_2O
Step 3d	As for Step 3c, with addition adsorption/desorption Cu(II)
Step 3e	As for Step 3d, with addition of aerobic respiration
Step 3f	As for Step 3e, with addition of reactions involving Fe(II)
Step 4	As for Step 3f, with addition variable temperature
Step 5	As for Step 4, with addition variable saturation
Step 6	As for Step 5, in 2-D/3-D

3.4 VALIDATION AND VERIFICATION PROCEDURES

Two procedures were used to validate the COMSOL version of the CCM. The primary validation was comparison of the predicted E_{CORR} to experimental values reported by King et al. (1995c), against which each incremental version of the COMSOL model (i.e., each of the versions in Table 7) was validated. The secondary method of validation was a comparison between certain versions of the COMSOL model and an equivalent version of the custom-designed code. Various quality assurance checks were applied to the output of the model in order to verify the code.

3.4.1 Validation Against Experimental E_{CORR} Values

3.4.1.1 Description of Experiment and Data Available

King et al. (1995c) published an extensive set of E_{CORR} measurements of copper in O_2-containing NaCl environments for a range of mass-transport conditions. Three different electrode configurations were used, including (i) a rotating disc electrode (RDE) in bulk solution (characterized by a steady-state mass-transfer coefficient $k_M = D/\delta$ in the approximate range 10^{-2} to 10^{-3} cm/s, where D is the diffusion coefficient and δ is the diffusion layer thickness), (ii) a copper disc electrode covered by a porous nylon membrane fabricated from a nucleopore filter (characterized by a k_M of approximately 10^{-4} cm/s), and (iii) a copper disc electrode covered by a layer of compacted bentonite with a thickness of either 1 mm or 10 mm (characterized by k_M in the approximate range 10^{-6} to 10^{-7} cm/s). Thus, the set of three electrodes covered a range of k_M of approximately five orders of magnitude. Measurements were made in aerated solution and in solutions equilibrated with either 2 vol.% O_2/N_2, 0.2 vol.% O_2/N_2, or were nominally deaerated. Thus, the dissolved O_2 concentration was varied by approximately four orders of magnitude. Finally, although the majority of measurements were made using 1 mol/L NaCl solution, a few experiments were conducted in 0.1 mol/L NaCl. The overall aim of the experiments was to determine the relative importance of mass transport and of the interfacial kinetics on the corrosion behaviour of copper in environments representative of the initial aerobic phase in the evolution of the DGR (King 1987).

A custom-manufactured copper RDE of conventional design was used in the experiments. The design of the membrane-covered electrode is described in detail by King et al. (1995c) and Figure 13 shows the design of the clay-covered electrode. In all three cases, the electrodes were designed so that mass-transport conditions were approximately 1-D in nature. However, there could be significant 3-D effects for the clay-covered electrode since the diameters of the copper disc and clay layer (and of the opening to the bulk solution) are not the same. The relevant dimensions for this electrode are: diameter of the copper disc 6.35 mm, diameter of the disc of compacted clay 20 mm, and diameter of the opening in the plexiglass electrode mount exposed to the bulk solution 16 mm.

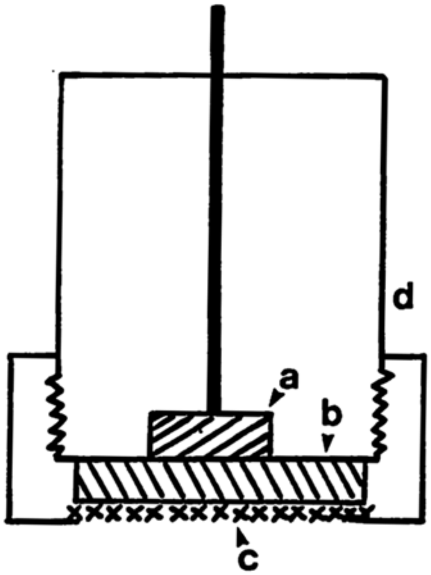

Figure 13: Design of the Clay-Covered Copper Electrode Used in the Experiments of King et al. (1995c,d). (a) copper disc electrode, (b) layer of compacted clay, (c) Pt-gauze support for the clay layer, (d) plexiglass electrode mount.

A combination of steady-state and transient E_{CORR} measurements were reported by King et al. (1995c). Steady-state E_{CORR} measurements were made using the RDE and membrane-covered electrodes in bulk NaCl solutions equilibrated with the various purging gases and, in the case of the RDE, as a function of rotation rate. For the clay-covered electrode experiments, sufficient aerated NaCl solution was added to dry Na-bentonite (Bearspaw, Saskatchewan) and compacted to produce a fully saturated 1-mm-thick disc with a bulk density of ~1.8 g/cm^3 (dry density ~1.2 g/cm^3, total porosity 0.52). The assembled electrode (Figure 13) was immersed in a solution of the same aerated NaCl solution and the sealed vessel purged with air. Transient E_{CORR} measurements were made until the potential had stabilized, at which point the purge gas was changed to 2 vol.% O_2/N_2 as E_{CORR} was continued to be monitored (Figure 14). Following the establishment of an apparently constant potential, the purge gas was changed to 0.2 vol.% O_2/N_2 and eventually to 100 vol.% N_2 at the times indicated in the figure. A similar experiment was performed using a 10-mm-thick clay layer (not shown) which lasted approximately ten times the duration of that shown in Figure 14. Table 8 summarizes the time intervals for each of the purge gases for the two experiments. These transient E_{CORR} measurements are the main source of data used to validate the individual COMSOL models, as described below.

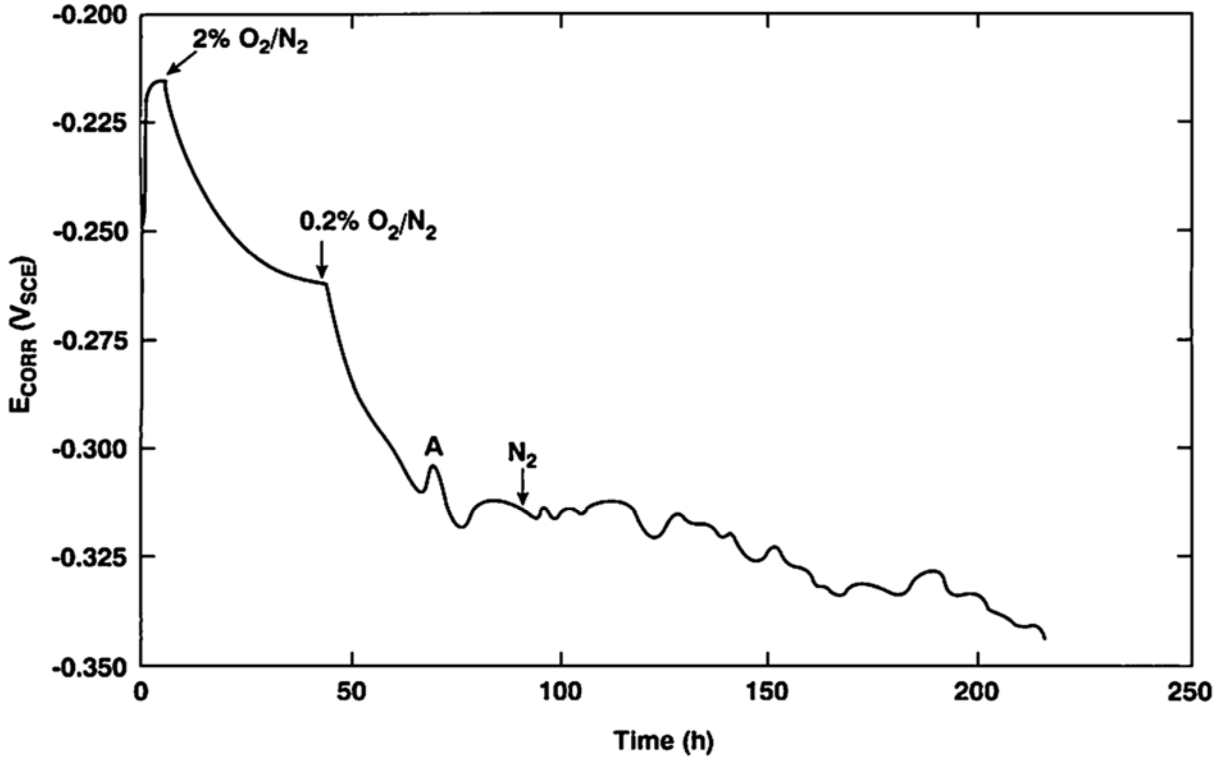

Figure 14: Transient Corrosion Potential (E_{CORR}) Measurements for a Copper Electrode Covered by a 1-mm-thick Compacted Clay Layer and Immersed in Initially Aerated 1 mol/L NaCl Solution as the Purge Gas Composition was Changed at the Times Indicated (King et al. 1995c). Point A indicates the time at which a small volume of aerated solution was added to the cell.

Table 9: Experimental Time Intervals Corresponding to the Different Purge Gases Used in the Compacted Clay Electrode Experiments

Purge Gas	Time Interval (hrs) 1-mm clay layer	Time Interval (hrs) 10-mm clay layer
Air	0-6.0	0-107.4
2 vol.% O_2/N_2	6.0-44.0	107.4-673.0
0.2 vol.% O_2/N_2	44.0-90.0	673.0- end
100 vol.% N_2	90.0- end	n/a

In order to interpret the steady-state E_{CORR} measurements, King et al. (1995c) developed a simple mixed-potential model based on the coupling of the anodic dissolution of copper as $CuCl_2^-$

$$\begin{aligned} Cu + Cl^- &\underset{k_{ab}}{\overset{k_{af}}{\rightleftharpoons}} CuCl_{ADS} + e^- \\ CuCl_{ADS} + Cl^- &\underset{k_{bb}}{\overset{k_{bf}}{\rightleftharpoons}} CuCl_2^- \end{aligned} \tag{14}$$

to the cathodic reduction of O_2

$$O_2 + 2H_2O + 4e^- \xrightarrow{k_C} 4OH^- \tag{15}$$

This simple model is equivalent to that considered here in Steps 1 and 2 (Table 2, Appendix A.1 and A.2).

All electrodes were fabricated from oxygen-free electronic copper (UNC C10100) and were successively ground and polished to a 1 μm finish before use. All experiments were conducted in unbuffered environments and under isothermal conditions at ambient temperature (23±1°C).

3.4.1.2 Validation Procedure

Validation was based on a visual comparison of predicted and measured E_{CORR} values and the use of expert judgement to determine the "goodness-of-fit".

With two exceptions, no attempt was made to fit the predicted E_{CORR} values to the experimental data by adjusting the values of selected input parameters. The two exceptions were:

- Selection of the optimum values for the cathodic transfer coefficient α_C and of the activity coefficient of Cl^- in 1 mol/L NaCl solution (based on a comparison of steady-state E_{CORR} values and the Step 1 COMSOL model).
- Selection of the optimum value of the combined parameter $\tau_f\varepsilon_e$ (based on a comparison of the time-dependence of E_{CORR} for the Step 2 transient version of the COMSOL model)

It was also apparent that the E_{CORR} predicted using the default values for the Cu(II) adsorption and desorption rate constants k_4 and k_{-4} (Figure 3) was inconsistent with the experimental observations. Therefore, a sensitivity analysis was performed with the Step 3d model in order to select appropriate values for k_4/k_{-4} for further development of the model. In addition, an equilibrium approach to adsorption was also used based on the built-in functionality of the COMSOL software. Appendix C presents a brief review of the literature on the adsorption and desorption behaviour of Cu(II) for montmorillonite clays.

Apart from these specific cases, all other input parameter values were taken directly from the literature. A complete set of input parameter values and their sources is given in Appendix B.

3.4.2 Validation Against the Custom-designed CCM Code

A limited number of comparisons were made between the results from Steps 2 and 3a of the COMSOL model and an equivalent version of the custom-designed CCM. This "code-to-code" validation is a test of the implementation and solution of the reaction-diffusion equations and, in particular, is a useful comparison of the use of finite-element and finite-difference solution methods for the COMSOL and custom-designed codes, respectively.

This inter-model comparison exercise was conducted at an earlier stage of the model development and some of the input parameter values differ from those used in the complete stepwise COMSOL model validation described above. The results of the inter-model validation exercise are described in Section 4.2

3.4.3 Quality Assurance and Code Verification

Different quality checks were applied to the output from the COMSOL model as a means of verifying the code. The results of these quality checks are discussed below in the context of the stepwise development of the model, but included comparisons of:

- Sum of the anodic and cathodic current densities, which should equal zero
- The total quantity of copper species in the clay layer versus the difference in time integrated copper fluxes between the left-hand and right-hand
- Mass balances for O_2 and dissolved copper for Steps 2 and 3a

Examples of these code verification quality checks are given in Section 4.1

4. DEVELOPMENT AND VALIDATION OF THE COMSOL CCM CODE

4.1 STEPWISE MODEL DEVELOPMENT AND VALIDATION AGAINST EXPERIMENTAL DATA FOR THE 1-mm CLAY ELECTRODE

4.1.1 Step 1 Simplified Reaction Scheme, Steady-state

The Step 1 model is based on the simplest possible reaction scheme involving only three species ($CuCl_2^-$, O_2, and Cl^-) and a single anodic reaction (dissolution of $CuCl_2^-$) coupled to a single cathodic reaction (O_2 reduction). A steady-state solution was developed in COMSOL for comparison with the steady-state E_{CORR} measurements using the copper RDE and 1- and 10-mm clay electrodes. Step 1 is identical to the steady-state mixed-potential model developed by King et al. (1995c). Details of the model and the underlying reaction scheme are given in Appendix A.1.

4.1.1.1 Selection of Values for Cathodic Transfer Coefficient and Chloride Activity

As noted above, the Step 1 validation process was used to select the optimum values for the cathodic transfer coefficient α_C and for the activity coefficient of Cl^- in 1 mol/L NaCl solution. An assumed value for α_C of 0.5 was used in the original study of King et al. (1995c), although subsequent studies of the O_2 reduction reaction suggested a value of 0.37 (King et al. 1995a,b). Simulations with the Step 1 model were performed for both values of α_C.

King et al. (1995c) also used an activity coefficient for Cl^- of 0.657 in 1 mol/L NaCl. Theoretically, E_{CORR} is inversely related to the square of the logarithm of the Cl^- activity (on the assumption that the dichloro-copper complex $CuCl_2^-$ is the predominant form of dissolved copper), and the selection of an appropriate value for the Cl^- activity is important for the subsequent development of the model. A parametric sweep was performed using the COMSOL software for Cl^- activities of 0.6, 0.657, 0.7, 0.8, 0.9, and 1.0 mol/L.

Table 10 shows a comparison of measured and predicted E_{CORR} values in the case of a copper RDE (at a single rotation rate of 2 Hz) and the clay-covered copper electrode (clay layer thicknesses of 1 mm and 10 mm). The difference between the predicted and measured values varies from as high as 44 mV to as little as 0 mV. In general, the COMSOL model predictions are closer to the measured values in the case of the two clay-covered electrode experiments, although the exact match between measured and predicted values indicated above was for the RDE.

The table also shows the sum of the differences between measured and predicted E_{CORR} values ($\sum\left(E_{CORR}^{COMSOL} - E_{CORR}^{Expt}\right)$), which is used here as one of the criteria to select the optimum values of α_C and Cl^- activity. The main selection criterion is consistency of the selected value with the underlying mechanism of the corroding system. In terms of the sum of the differences, there are eight combinations of α_C and Cl^- activity that produce a total difference of <20 mV (highlighted in red font in the table), all of which refer to the clay-covered electrode experiments. Given that the ultimate use of the model is to predict E_{CORR} of the in the DGR, greater emphasis is placed here on the results of the comparison with the clay-covered electrodes than with the RDE.

Table 10: Comparison of Experimental and Predicted Steady-state Corrosion Potentials for Various Copper Electrodes in O_2-containing 1 mol/L Sodium Chloride Solution.*

Table 10(a): Copper RDE, rotation frequency 2 Hz, $\delta = 45\ \mu m$, k_M □ 2.2×10^{-3} cm/s

$[O_2]$ (mol/L)	Expt.	$\alpha_C = 0.37$						$\alpha_C = 0.50$					
		0.60	0.657	0.70	0.80	0.90	1.0	0.60	0.657	0.70	0.80	0.90	1.0
7×10^{-7} (N_2)	-0.426	-0.4368	-0.4402	-0.4426	-0.4477	-0.4521	-0.4561	-0.3877	-0.3910	-0.3933	-0.3981	-0.4025	-0.4063
1.9×10^{-6} (0.2% O_2)	-0.413	-0.4180	-0.4214	-0.4238	-0.4288	-0.4333	-0.4372	-0.3697	-0.3730	-0.3752	-0.3800	-0.3843	-0.3881
1.9×10^{-5} (2% O_2)	-0.356	-0.3746	-0.3780	-0.3804	-0.3855	-0.3899	-0.3939	-0.3291	-0.3323	-0.3345	-0.3392	-0.3434	-0.3471
2.0×10^{-4} (air)	-0.306	-0.3304	-0.3338	-0.3362	-0.3412	-0.3456	-0.3496	-0.2883	-0.2914	-0.2936	-0.2982	-0.3023	-0.3060
$\sum\left(E_{CORR}^{COMSOL} - E_{CORR}^{Expt}\right)$ (V)**		-0.0588	-0.0725	-0.0820	-0.1022	-0.1199	-0.1358	0.1262	0.1133	0.1043	0.0854	0.0686	0.0536
$\frac{dE_{CORR}}{d\log_{10}[O_2]}$ (V)**	0.0503	0.0433	0.0433	0.0433	0.0433	0.0434	0.0434	0.0405	0.0405	0.0406	0.0407	0.0408	0.0408
R^2	0.9954	1.0000	1.0000	1.0000	1.0000	1.0000	1.0000	1.0000	1.0000	1.0000	1.0000	0.9999	0.9999

* All potentials given in V_{SCE}. COMSOL predicted E_{CORR} values are given as a function of the cathodic transfer coefficient α_C (values of 0.37 and 0.50) and Cl^- activity (values from 0.60 to 1.0 mol/L).

** $\sum\left(E_{CORR}^{COMSOL} - E_{CORR}^{Expt}\right)$ is the sum of the differences between the predicted and experimental E_{CORR} values summed for the various $[O_2]$. $dE_{CORR}/d\log_{10}[O_2]$ is the slope of the dependence of E_{CORR} on O_2 concentration and can be indicative of the nature of the rate-determining steps for the anodic and cathodic reactions (see text).

Table 10(b): Clay-covered Copper Electrode, δ = 1 mm, k_M □ 10^{-6} cm/s

$[O_2]$ (mol/L)	**Expt.**	**α_C = 0.37**						**α_C = 0.50**					
		0.60	**0.657**	**0.70**	**0.80**	**0.90**	**1.0**	**0.60**	**0.657**	**0.70**	**0.80**	**0.90**	**1.0**
7 × 10^{-7} (N_2)	-0.3390	-0.3461	-0.3506	-0.3538	-0.3604	-0.3662	-0.3715	-0.3433	-0.3479	-0.3511	-0.3580	-0.3640	-0.3693
1.9 × 10^{-6} (0.2% O_2)	-0.3110	-0.3217	-0.3261	-0.3292	-0.3358	-0.3416	-0.3467	-0.3178	-0.3224	-0.3257	-0.3325	-0.3385	-0.3439
1.9 × 10^{-5} (2% O_2)	-0.2690	-0.2670	-0.2712	-0.2742	-0.2804	-0.2860	-0.2909	-0.2595	-0.2641	-0.2673	-0.2740	-0.2799	-0.2853
2.0 × 10^{-4} (air)	-0.2220	-0.2139	-0.2179	-0.2207	-0.2266	-0.2318	-0.2366	-0.2016	-0.2060	-0.2090	-0.2155	-0.2213	-0.2264
$\sum\left(E_{CORR}^{COMSOL} - E_{CORR}^{Expt}\right)$ (V)**		*-0.0077*	-0.0249	-0.0369	-0.0622	-0.0846	-0.1046	*0.0188*	*0.0006*	*-0.0120*	-0.0390	-0.0627	-0.0839
$\frac{dE_{CORR}}{d\log_{10}[O_2]}$ (V) **	0.0465	0.0538	0.0541	0.0542	0.0545	0.0547	0.0550	0.0577	0.0578	0.0579	0.0580	0.0581	0.0582
R^2	0.9960	0.9998	0.9998	0.9998	0.9998	0.9998	0.9998	0.9999	0.9999	1.0000	1.0000	1.0000	1.0000

* All potentials given in V_{SCE}. COMSOL predicted E_{CORR} values are given as a function of the cathodic transfer coefficient α_C (values of 0.37 and 0.50) and Cl^- activity (values from 0.60 to 1.0 mol/L).

** $\sum\left(E_{CORR}^{COMSOL} - E_{CORR}^{Expt}\right)$ is the sum of the differences between the predicted and experimental E_{CORR} values summed for the various $[O_2]$. *Italic font* indicates combinations of α_C and Cl^- activity that give a sum of differences <20 mV. $dE_{CORR}/d\log_{10}[O_2]$ is the slope of the dependence of E_{CORR} on O_2 concentration and can be indicative of the nature of the rate-determining steps for the anodic and cathodic reactions (see text).

Table 10(c): Clay-covered Copper Electrode, δ = 10 mm, k_M □ 10^{-7} cm/s

$[O_2]$ (mol/L)	Expt.	α_C = 0.37						α_C = 0.50					
		0.60	**0.657**	**0.70**	**0.80**	**0.90**	**1.0**	**0.60**	**0.657**	**0.70**	**0.80**	**0.90**	**1.0**
7 × 10^{-7} (N_2)		-0.3433	-0.3479	-0.3511	-0.3581	-0.3641	-0.3693	-0.3430	-0.3477	-0.3509	-0.3578	-0.3638	-0.3692
1.9 × 10^{-6} (0.2% O_2)	-0.3390	-0.3178	-0.3225	-0.3257	-0.3325	-0.3386	-0.3439	-0.3174	-0.3220	-0.3253	-0.3322	-0.3382	-0.3436
1.9 × 10^{-5} (2% O_2)	-0.2910	-0.2593	-0.2639	-0.2671	-0.2739	-0.2799	-0.2852	-0.2583	-0.2630	-0.2662	-0.2731	-0.2791	-0.2845
2.0 × 10^{-4} (air)	-0.2220	-0.2002	-0.2047	-0.2079	-0.2146	-0.2205	-0.2257	-0.1981	-0.2027	-0.2059	-0.2128	-0.2188	-0.2242
$\sum\left(E_{CORR}^{COMSOL} - E_{CORR}^{Expt}\right)$ (V)**		0.0746	0.0609	0.0513	0.0310	*0.0131*	*-0.0029*	0.0782	0.0643	0.0545	0.0340	*0.0159*	*-0.0003*
$\frac{dE_{CORR}}{d\log_{10}[O_2]}$ (V) **	0.0579	0.0583	0.0583	0.0583	0.0584	0.0585	0.0585	0.0590	0.0590	0.0590	0.0591	0.0591	0.0591
R^2	0.9906	1.0000	1.0000	1.0000	1.0000	1.0000	1.0000	1.0000	1.0000	1.0000	1.0000	1.0000	1.0000

* All potentials given in V_{SCE}. COMSOL predicted E_{CORR} values are given as a function of the cathodic transfer coefficient α_C (values of 0.37 and 0.50) and Cl^- activity (values from 0.60 to 1.0 mol/L).

** $\sum\left(E_{CORR}^{COMSOL} - E_{CORR}^{Expt}\right)$ is the sum of the differences between the predicted and experimental E_{CORR} values summed for the various $[O_2]$. *Italic font* indicates combinations of α_C and Cl^- activity that give a sum of differences <20 mV. $dE_{CORR}/d\log_{10}[O_2]$ is the slope of the dependence of E_{CORR} on O_2 concentration and can be indicative of the nature of the rate-determining steps for the anodic and cathodic reactions (see text).

Of the eight combinations with a sum of differences <20 mV, three are for an α_C value of 0.37 and five for a value of 0.5 (Table 9(b) and (c)). The optimum choice of α_C is only important if the cathodic reaction is under kinetic or joint kinetic-transport control, which is the case in aerated bulk solution (King et al. 1995c,d). With decreasing k_M and $[O_2]$, however, the cathodic reaction becomes transport limited and the value of α_C has no effect on the predicted E_{CORR}. Since we are most interested in conditions of restrictive mass transport and limited O_2, the choice of the value of α_C is relatively unimportant and a value of 0.5 is selected for further development of the COMSOL model to be consistent with the value used by King et al. (1995c).

The selection of the value for the Cl^- activity (or, more correctly, the activity coefficient γ_{Cl}) is more important. King et al. (1995c) specified γ_{Cl} values of 0.657 and 0.779 for 1.0 mol/L and 0.1 mol/L NaCl solutions, respectively. Based on the sum of the differences, higher values of γ_{Cl} fit the measured E_{CORR} values for the 10-mm-thick clay layer (Table 9(c)), whereas lower values fit better for the 1-mm clay layer (Table 9(b)). Therefore, the sum of the differences does not clearly identify the optimum value for γ_{Cl} for further development of the COMSOL model, so here a value of 0.657 is selected in order to again be consistent with the value used by King et al. (1995c).

4.1.1.2 Nature of the Anodic and Cathodic Rate-determining Steps

In addition to supporting the selection of the optimum values of α_C and Cl^- activity, the results of the Step 1 simulations can be used to provide mechanistic insight into the corrosion behaviour of copper in O_2-containing Cl^- environments. In particular, the dependence of E_{CORR} on $[O_2]$ depends on the rate-determining steps (rds) for the anodic and cathodic reactions (King 1987, King et al. 1995c, Power and Ritchie 1981). The rate of the anodic reaction (Reaction (25)) is controlled by the rate of transport of $CuCl_2^-$ away from the corroding surface (Kear et al. 2004; King et al. 1995c,d), whereas the rate of the cathodic reduction of O_2 can be under kinetic or transport control depending on the value of k_M and of the $[O_2]$. For a combination of anodic: transport control/cathodic: kinetic control, the dependence of E_{CORR} on $[O_2]$ is given by (King 1987)

$$\frac{dE_{CORR}}{d\log[O_2]} = \frac{2.3RT}{(n_a + \alpha_C)F} \tag{16}$$

and if both anodic and cathodic reactions are transport limited, the dependence is given by

$$\frac{dE_{CORR}}{d\log[O_2]} = \frac{2.3RT}{n_a F} \tag{17}$$

where R, T, and F are the gas constant, absolute temperature, and the Faraday constant, respectively, and n_a is the number of electrons transferred in the anodic reaction ($n_a = 1$). Thus, at a temperature of 23°C, E_{CORR} will increase by 39 mV or 43 mV for $\alpha_C = 0.5$ or 0.37, respectively, for each decade increase in $[O_2]$ if the cathodic reaction is under kinetic control and by 59 mV if both reactions are transport limited.

Comparison of these theoretical dependences with the measured and predicted values in Table 9 suggests the cathodic rds changes from kinetic control in bulk solution to transport control in the presence of compacted clay. Based on the predicted E_{CORR} dependences, the $dE_{CORR}/d\log[O_2]$ values in Table 9(a) suggest that the cathodic reaction is almost entirely kinetically limited for the RDE since the predicted slopes are close to the theoretical dependences of 39 mV or 43 mV given above, depending on the value of α_C. In the case of the clay-covered electrode with a 10-mm thick clay layer (Table 9(c)), the cathodic reaction becomes almost completely transport limited as the $dE_{CORR}/d\log[O_2]$ is close to the theoretical value of 59 mV and is independent of the value of α_C. The situation for the 1-mm-thick clay layer (Table 9(b)) appears to lie in between, with $dE_{CORR}/d\log[O_2]$ slightly less than that for full cathodic transport control and with some slight dependence on α_C, suggesting joint kinetic-transport control of the cathodic reaction. While there is some uncertainty regarding the appropriate value of α_C, the values of all other input parameters (such as the interfacial rate constants for the anodic and cathodic reactions and the effective diffusivities in bulk solution and compacted clay) have been taken from individual studies of the anodic and cathodic reactions or taken from the literature. Thus, the predicted switch in the nature of the rds of the cathodic reaction is entirely a consequence of the relative kinetics of the interfacial and mass-transport processes based on these independently measured values of the different input parameters.

It is also interesting to compare the theoretical and measured dependences. For the 10-mm-thick clay layer, the experimental dependence of 58 mV is close to the theoretical value of 59 mV for transport control of both anodic and cathodic reactions (Table 9(c)). Smaller dependences are observed for the RDE (Table 9(a)) and 1-mm-thick clay layer (Table 9(b)), indicative of joint kinetic-transport control of the cathodic reaction.

As well as the dependence of E_{CORR} on $[O_2]$, the dependence of E_{CORR} on k_M can also provide evidence for the nature of the anodic and cathodic rds. However, as discussed in the next section, there is some uncertainty in the value of the effective diffusivity in compacted clay (and, hence of the value of k_M) and the dependence of E_{CORR} on k_M is not investigated further here.

The impact of the relative rates of the interfacial and transport processes can be understood through the use of Evans diagrams. Figure 15 shows quantitative Evans diagrams for the three electrodes described above; namely, a copper RDE with a rotation frequency of 2 Hz, and clay-covered copper electrodes with clay layer thickness of 1 mm and 10 mm. These quantitative diagrams were derived using the values of rate constants and other parameters given by King et al. (1995c), which were determined from electrochemical studies of the individual anodic (Reaction (25)) and cathodic (Reaction (26)) processes. For estimation of the rate of mass-transport of species through the clay layers, a combined $\tau_f\varepsilon_e$ value of 0.01 was assumed.

As can be seen from the Evans diagrams, the system becomes progressively mass-transport limited with decreasing k_M and decreasing $[O_2]$. The anodic reaction is mass-transport limited under all conditions, with the dependence of the anodic current density on potential the result of the fact that the concentration of the diffusing species (i.e., $CuCl_2^-$) is itself a function of potential. In contrast, the cathodic reactions shifts from being under kinetic (interfacial) control at E_{CORR} for the RDE (Figure 15(a)), to being under transport control in the presence of a clay layer (Figure 15(b) and (c)). Even in nominally deaerated bulk solution, there is sufficient residual O_2 that the cathodic reaction is largely kinetically controlled at E_{CORR} for the RDE (cf. N_2 curve in Figure 15(a)). For the aerated, 1-mm-clay layer experiment (which represents the experiment with the highest O_2 flux in the presence of bentonite), the E_{CORR} value just falls into the transport-limited region for the O_2 reduction process (cf. air curve in Figure 15(b)). For decreasing $[O_2]$ or for a thicker clay layer, however, E_{CORR} lies completely within the transport-limited region and both anodic and cathodic reactions are diffusion limited.

(a) RDE

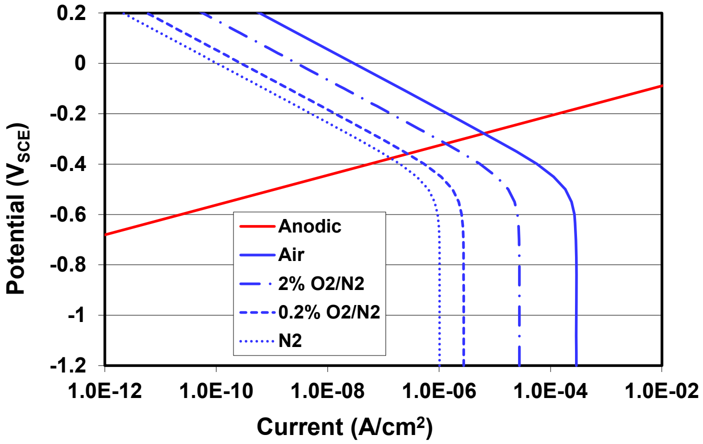

(b) 1 mm clay layer

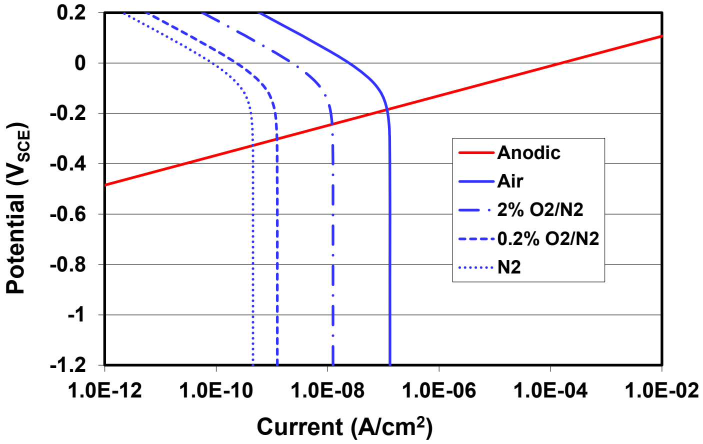

(c) 10 mm clay layer

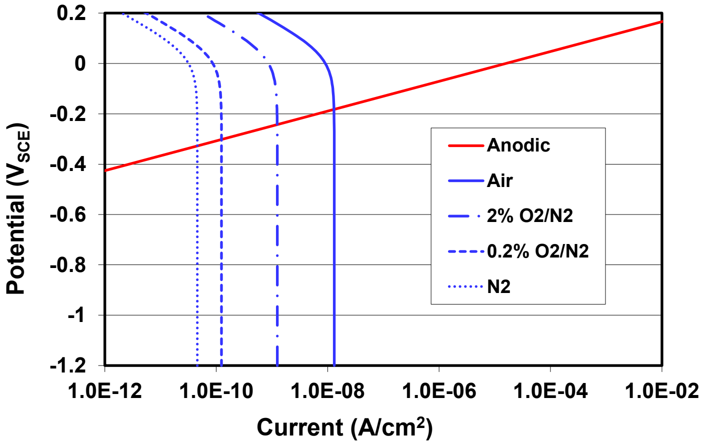

Figure 15: Evans Diagrams for the Corrosion of Copper in O_2-containing 1 mol/L NaCl Solution for Electrodes of Different Mass Transfer Characteristics. (a) Copper RDE, rotation frequency 2 Hz, (b) copper electrode with 1-mm-thick clay layer, (c) copper electrode with 10-mm-thick clay layer. Purge gases of air, 2% O_2/N_2, 0.2% O_2/N_2, and N_2 produce dissolved $[O_2]$ of 2×10^{-4}, 1.9×10^{-5}, 1.9×10^{-6}, and an estimated 7×10^{-7} mol/L, respectively. Cathodic transfer coefficient of 0.5 and chloride ion activity coefficient of 0.657.

These Evans diagrams also illustrate other interesting features of the dependence of E_{CORR} on the rate of mass transport. As the rds for the cathodic reaction changes from interfacial control (for the RDE) to transport control (for the clay-covered electrodes), E_{CORR} shifts to more-positive values (Figure 15). This effect is demonstrated by the experimental data for the different electrodes in Table 9. The shift is of the order of 100 mV and is not sufficient to drive the potential into a region where the surface might be susceptible to localized corrosion were it to be in the passive state. Furthermore, if both anodic and cathodic reactions are transport limited, then E_{CORR} becomes independent of the value of k_M (as shown by the identical E_{CORR} values in Figure 15(b) and (c). Thus, E_{CORR} is independent of the thickness of the layer of compacted bentonite (both in the laboratory and in the DGR), although the corrosion rate (corrosion current density) decreases with decreasing k_M.

4.1.2 Step 2 Simplified Reaction Scheme, Transient

The Step 2 model (Table 7) is based on the same mechanism as the Step 1 code but involves a transient solution, permitting the prediction of the time dependence of E_{CORR} rather than simply the steady-state values. Validation of the model predictions was performed by visual comparison with the time-dependence of the E_{CORR} for the 1-mm-thick clay layer experiment (Figure 14), during which the $[O_2]$ was progressively decreased as indicated in Table 8. Because the results of preliminary simulations indicated that the default values for the effective diffusivities of O_2 and $CuCl_2^-$ (and Cl^-) could not account for the observed time dependence of E_{CORR}, the Step 2 model simulations were used to optimize the value for $\tau_f\varepsilon_e$ (denoted tauEps in the COMSOL code) which is used to modify the values of the bulk solution diffusion coefficients to account for the porous and tortuous nature of the diffusion paths in compacted bentonite.

4.1.2.1 Optimization of the Values of $\tau_f\varepsilon_e$ (tauEps)

Figure 16 shows a comparison between the experimental E_{CORR} values and the Step 2 COMSOL model predictions for various values of tauEps. It is apparent that the default value of 0.01 (blue curve) predicts a slower response of E_{CORR} to changes in $[O_2]$ than was observed experimentally and that a value of 0.025 provides an improved fit to the experimental data. Consequently, this value of tauEps is used for all subsequent COMSOL simulations.

The CCM is based on a multi-porosity model of the bentonite pore structure (Bradbury and Baeyens 2003, King et al. 2017, Wersin 2003). Historically, the total porosity in the model was divided into accessible and non-accessible porosities, with the former divided between the effective porosity for diffusive transport and a storage porosity associated with dead-end pores (Choi and Oscarson 1996, Johnson et al. 1994, King et al. 1996). For the reference 50:50 bentonite:sand buffer material specified by AECL (Johnson et al. 1994, 1996), the total porosity of approximately 0.4 was equally divided between accessible and non-accessible porosity and the accessible porosity was equally divided between effective and storage porosities, leading to an ε_e value of 0.1 (Choi and Oscarson 1996, Johnson et al. 1994). The tortuosity factor τ_f accounts for both the tortuousness of the pore network and the variation in the throat size of the pores (the constrictivity) and was found experimentally to have a value of ~0.1 (Choi and Oscarson 1996).

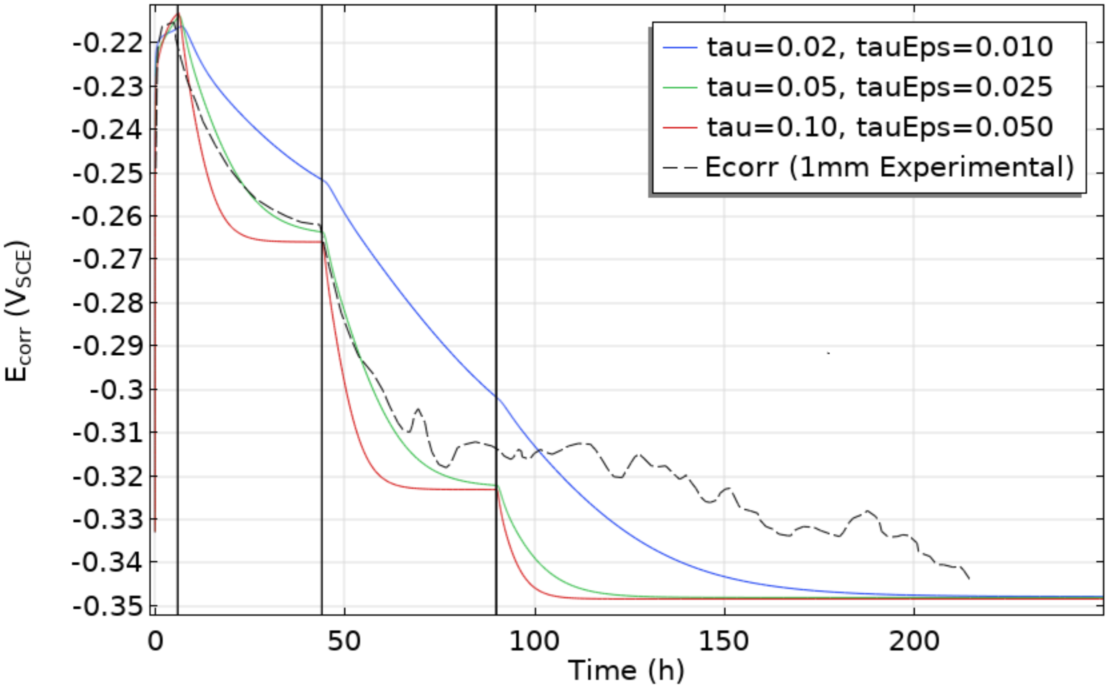

Figure 16: Comparison of the Experimental Time-dependent Corrosion Potential for the 1-mm-thick Clay Electrode with Simulations from the Step 2 COMSOL Model for Various Values of tauEps.

Since the CCM was first developed, there have been many studies of the pore structure of compacted bentonites. The multi-porosity model is still the most widely used conceptual model, although the single porosity model of Birgersson and Karnland (2009) in which all of the porosity is available for diffusive transport also has its proponents.

For the COMSOL version of the CCM, we use a multi-porosity model in which all of the porosity is accessible to solutes. Of the total porosity, 50% is taken to be associated with through-pores associated with diffusive transport (i.e., ε_e), with the remaining 50% associated with storage porosity. The important distinction is that reactions can occur in either type of pore, but diffusion only occurs in the effective porosity. For the 100% bentonite clay layers used by King et al. (1995c), the estimated dry density is 1.28 g/cm^3 and the total porosity is 0.52, resulting in effective and storage porosities of 0.26. Because of the manner in which transport through porous media is treated in COMSOL (see Section 3.3.2), the “EPS” term in tauEPS is given by the ratio of the effective porosity ε_e divided by the total porosity (EPS = 0.26/0.52 = 0.5). Thus, the optimum tauEPS value of 0.025 implies a value for the tortuosity factor of 0.05.

To understand the relative importance of transport and kinetics, it is useful to define a characteristic diffusion time, defined here as $\delta^2/4D_{eff}$. The effective diffusivities ($D_{eff} = \varepsilon_e\tau_f D_0$) of the three species in the model (O_2, $CuCl_2^-$, and Cl^-) differ because different values are used for the bulk-solution diffusion coefficient D_0. For the 1-mm thick clay layer (δ = 0.1 cm), the characteristic diffusion times vary from 5.6 hrs for Cl^-, 6.5 hrs for O_2, and 19 hrs for $CuCl_2^-$.

Figure 17 shows the predicted time dependence of the anodic and cathodic current densities. Whereas the E_{CORR} takes up to 50 hrs to reach a stable value after each progressive decrease in the purge gas composition, the current densities achieve constant values within approximately 5 hrs of a change in purge gas. The current density stabilization period is consistent with the characteristic diffusion time for O_2. The response of E_{CORR} is slower because the corrosion potential is sensitive to changes in the <u>relative</u> rates of the anodic and cathodic reactions and even small changes in the absolute current densities can lead to significant changes in potential.

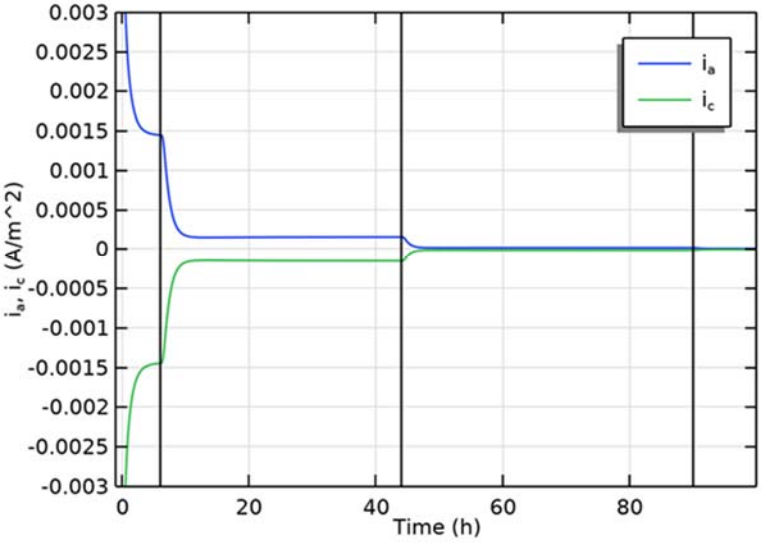

Figure 17: Predicted Time Dependence of the Anodic and Cathodic Current Densities for the 1-mm-thick Clay Electrode. The vertical lines indicate the times at which the purge gas was changed.

4.1.2.2 Quality Checks

Figure 18 shows the results of two checks on the quality of the output from the COMSOL model. Figure 18(a) shows the time dependence of the sum of the anodic and cathodic current densities which should be equal to zero (Equation (12)). Compared with individual anodic and cathodic current densities of the order of 10^{-3} A/m^2 (Figure 17), the sum of the currents is $<10^{-12}$ A/m^2, suggesting a highly accurate mixed-potential treatment.

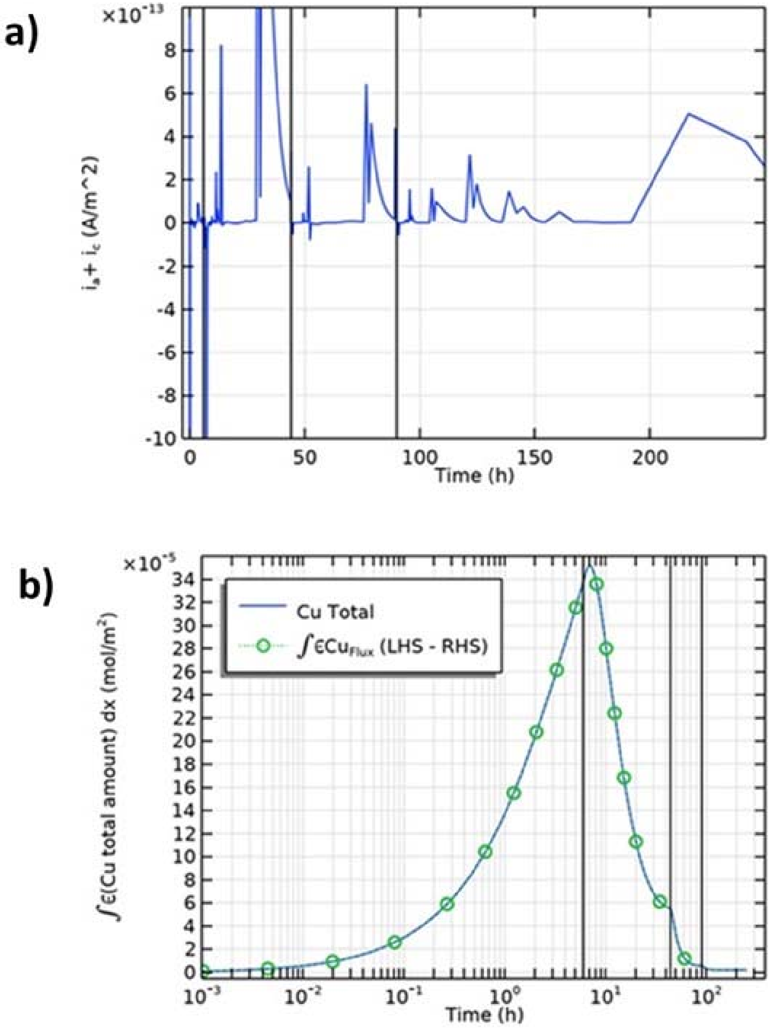

Figure 18: Quality Checks on the Results of the Step 2 COMSOL Model. (a) Time dependence of the sum of the anodic and cathodic current densities, (b) comparison of the time dependence of the total amount of copper in the clay layer with the difference of the copper fluxes at the left-hand and right-hand boundaries. The vertical lines indicate the times at which the purge gas was changed.

Figure 18(b) illustrates the accuracy of the model in terms of the mass-balance of copper species. The solid line in the figure is the time dependence of the integrated amount of dissolved $CuCl_2^-$ in the 1-mm clay layer determined by summing the amounts in each of the elements based on the concentrations and total porosity. The individual points (denoted by the green open circles) are the differences between the flux of copper at the left-hand boundary (i.e., the copper surface) and the right-hand boundary in contact with the bulk solution. The exact correspondence of these two independent measures of the copper inventory provide further evidence for the accuracy of the model output.

4.1.2.3 Mechanistic Insights

The output from the model can be used to investigate the mechanism of the reaction and of the nature of the rds for the individual reactions and for the overall corrosion process. The maximum steady-state corrosion rate is equal to the steady-state flux of O_2 across the clay layer. For the case of aerated conditions, Figure 17 indicates a corrosion current density (equal to the anodic current density) of 2.5×10^{-3} A/m^2, equivalent to a flux of copper ions of 2.6×10^{-8} mol·m^{-2}·s^{-1}. In contrast, the steady-state flux of O_2 across the clay layer assuming the cathodic reaction is transport limited (i.e., a zero interfacial [O_2]) is 3.4×10^{-8} mol·m^{-2}·s^{-1} (based on $\varepsilon_e\tau_f D_0$ for O_2 of $0.025 \times 1.7 \times 10^{-9}$ m^2/s = 4.25×10^{-11} m^2/s). Thus, the cathodic reaction is not completely transport limited, despite the suggestion from the Evans diagram in Figure 15(b)). Figure 19(a) shows the O_2 concentration profiles for selected times during the experiment, which confirms that, at a time of 5 hrs just prior to the switch from air to 2 vol.%O_2/N_2 purge gas, the interfacial [O_2] is non-zero, consistent with joint interfacial-transport control of the cathodic reaction. The time-dependence of the interfacial [O_2] further illustrates this point (Figure 20(a)), with complete transport control of the cathodic reaction (as indicated by a zero interfacial concentration) only achieved once the purge gas is switched to 0.2 vol.%O_2/N_2.

Figure 19(b) and Figure 20(b) show the $CuCl_2^-$ concentration profiles for selected times and the time dependence of the interfacial [$CuCl_2^-$], respectively. The concentration profiles and interfacial concentrations change in concert with the changes in E_{CORR}. The question is whether these changes are in response to the change in E_{CORR}, or the cause? Figure 21 shows a comparison of the measured and predicted E_{CORR} values and of the equilibrium potentials for the anodic and cathodic reactions calculated from the predicted interfacial concentrations of $CuCl_2^-$, Cl^-, and O_2 (constant pH 7 assumed). The E_{CORR} values are close to the equilibrium potential for the anodic reaction and far from that for the O_2 reduction reaction, suggesting rate control by the cathodic reaction (Shoesmith 2003).

Chloride ions also participate in the interfacial reactions but, unlike O_2 and $CuCl_2^-$, are present in a large excess in the system. Thus, although the interfacial concentration (or, more correctly, activity) decreases slightly as Cl^- is consumed in the formation of $CuCl_2^-$, the extent of chloride depletion is minimal (Figure 19(c), Figure 20(c)). Interestingly, although the characteristic diffusion time for Cl^- is 5.6 hrs, the interfacial [Cl^-] never fully recovers to the initial value until the interfacial [$CuCl_2^-$] is close to zero after the switch to the N_2 purge (Figure 20(c)).

An interesting feature of the experimental measurements was that E_{CORR} responded immediately to a change in the purge gas, even though the characteristic time for the diffusion of O_2 across the clay layer is 6.5 hrs. This immediate response is because the interfacial [O_2] responds immediately to any change in the [O_2] gradient across the clay layer. For example, the [O_2] profiles for 5 hr and 7 hr in Figure 19(a) correspond to 1 hr prior to and 1 hr after the switch from of purge gas from air 2 vol.%/N_2. Even within this short time period, the flux of O_2 to the electrode surface (as indicated by the slope of the profiles) has changed significantly. The rapid decrease in the interfacial [O_2] upon the change in purge gas is more clearly illustrated in Figure 20(a).

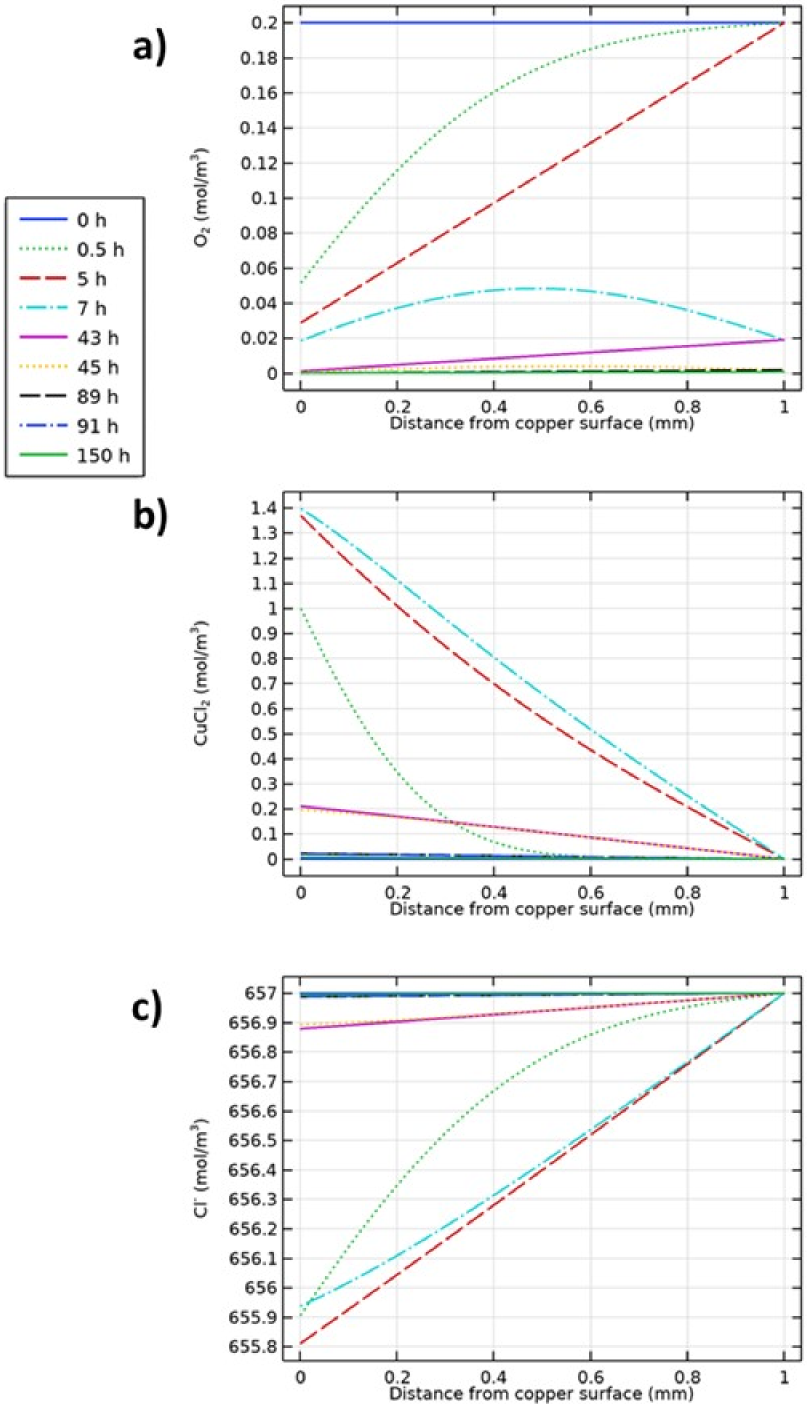

Figure 19: Concentration Profiles in the 1-mm Clay Layer for (a) O_2, (b) $CuCl_2^-$, and (c) Cl^- ions at Selected Times for the Step 2 COMSOL Model.

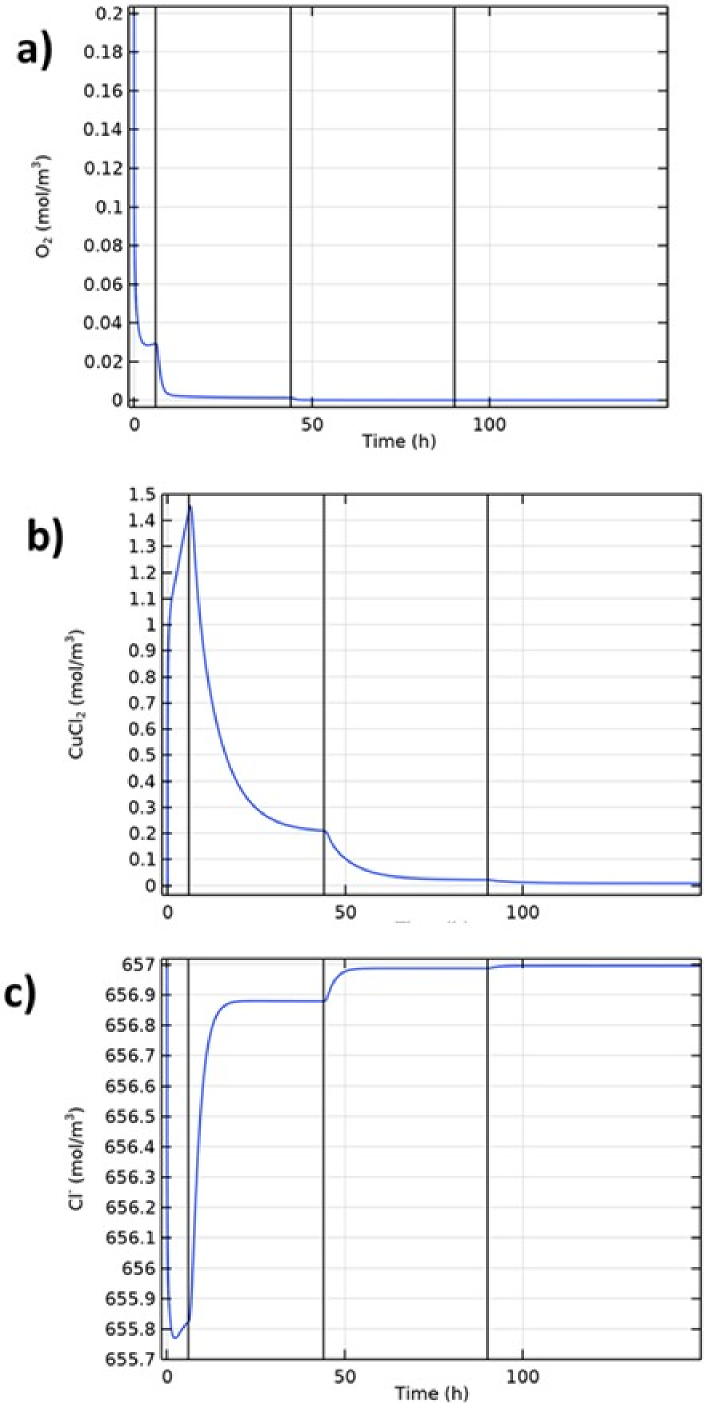

Figure 20: Time Dependence of the Interfacial Concentrations of (a) O_2, (b) $CuCl_2^-$, and (c) Cl^- ions at Selected Times for the Step 2 COMSOL Model. The vertical lines indicate the times at which the purge gas was changed.

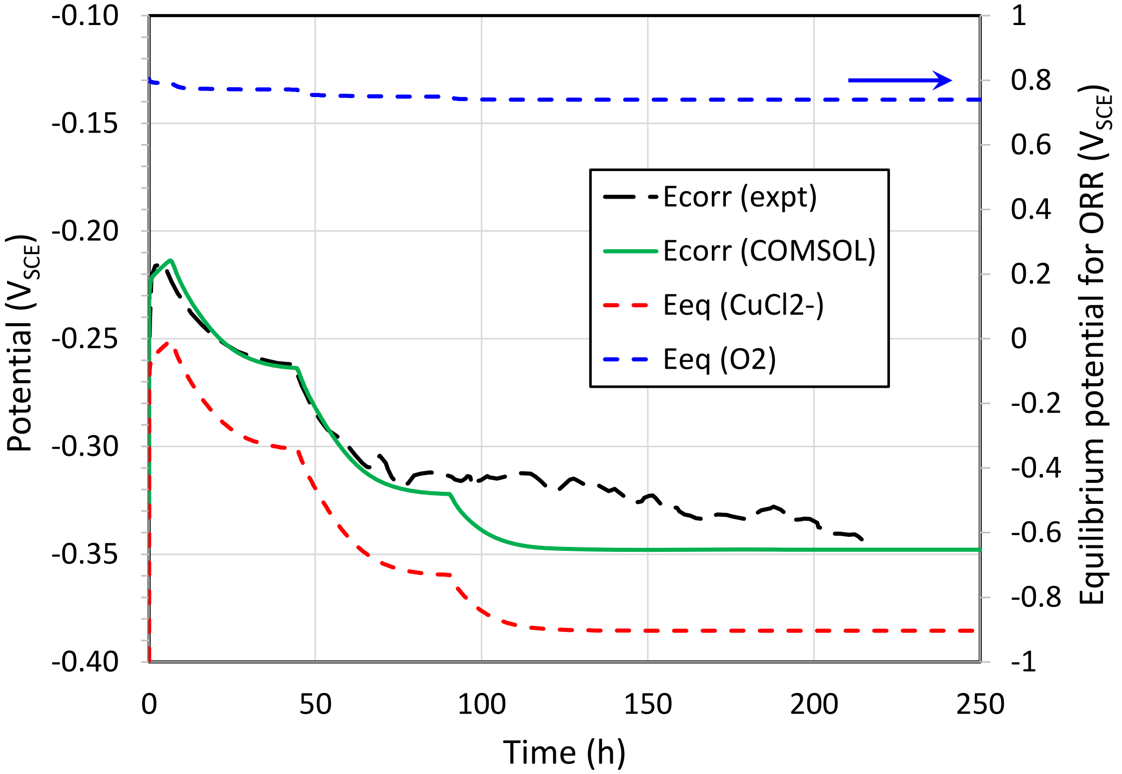

Figure 21: Comparison of the Time Dependence of the Measured and Predicted Corrosion Potentials with the Equilibrium Potentials for the Anodic and Cathodic Reactions Based on the Predicted Interfacial Concentrations of $CuCl_2^-$, Cl^-, and O_2. A constant pH 7 was assumed to determine the equilibrium potential for the O_2 reduction reaction, which is plotted on the right-hand y-axis.

Although E_{CORR} may respond immediately to changes in the purge gas composition, the overall time-dependence of the corrosion potential and the period required to reach steady state appears to be determined by the diffusivity of the slowest potential-determining species. The rate of response of the interfacial concentrations of O_2, $CuCl_2^-$, and Cl^- decreases with decreasing diffusivity (Figure 20), with the $[O_2]$ responding fastest and $[CuCl_2^-]$ the most slowly. Comparison of the time dependences in Figure 20 with that of E_{CORR} in Figure 16 suggests that it is the diffusivity of $CuCl_2^-$ that determines the length of time for E_{CORR} to reach steady state.

4.1.2.4 Cause of Initial Ennoblement of E_{CORR}

Another feature of both the experimental and predicted E_{CORR} values is the increase during the initial 6-hour aerated phase (Figure 16). In corroding systems, a positive shift (ennoblement) of E_{CORR} is commonly associated with either passivation or catalysis of the cathodic reaction. In this case, however, neither explanation is plausible, as (a) the COMSOL model is based on an actively corroding system and (b) far from increasing, the rate of the cathodic reaction is decreasing with time due to O_2 consumption.

Initially, the [O_2] in the clay layer is uniform and equal to the value in the bulk solution (Figure 19(a)). However, as soon as corrosion starts, the interfacial [O_2] decreases and a concentration gradient develops in the clay layer. According to the Evans diagram in Figure 15(b), this consumption of O_2 leads to a negative shift in E_{CORR}, rather than ennoblement. However, at the same time, the interfacial [$CuCl_2^-$] increases because of dissolution and slow transport away from the surface (Figure 19(b), Figure 20(b)). This results in a positive shift in the equilibrium potential for the anodic reaction and a corresponding increase in E_{CORR} (Figure 21).

Thus, far from being an indication of passivation, this initial ennoblement of E_{CORR} is in fact due to the increase in the interfacial concentration of $CuCl_2^-$ and an actively corroding system under cathodic control. The close agreement between predicted and observed behaviour implies that copper corrodes actively in the presence of compacted buffer.

4.1.3 Step 3a Homogeneous Oxidation of Cu(I) and Second Cathodic Reaction

Step 3a represents a significant change to the reaction mechanism and the potential-determining interfacial reactions (Table 2). In addition to the simplified mechanism used for Steps 1 and 2, the irreversible homogeneous oxidation of $CuCl_2^-$ to Cu^{2+} by O_2 is added to the reaction scheme (Appendix A.3):

$$CuCl_2^- + \tfrac{1}{4}O_2 + \tfrac{1}{2}H_2O \xrightarrow{k_1} Cu^{2+} + 2Cl^- + OH^- \qquad (18)$$

where k_1 is the second-order rate constant, the value of which is calculated within the code as it depends on the spatially and temporally variable [Cl^-]. (The pH throughout the model is assumed to be constant and buffered at pH 7, so the OH^- species is not tracked in the code). This change not only introduces another diffusing species to the model (in the form of Cu^{2+}), but also an additional cathodic reaction

$$Cu^{2+} + 2Cl^- + e^- \xrightarrow{k_d} CuCl_2^- \qquad (19)$$

where k_d denotes the interfacial rate constant.

4.1.3.1 Predicted E_{CORR} and the Nature of the Cathodic Reaction

Despite the addition of a second cathodic reaction to the mechanism for Step 3, there is relatively little effect on the predicted time dependence of E_{CORR}. Figure 22 compares the experimental and predicted E_{CORR} values, in the latter case for the Step 2 and Step 3a models. The only difference of including the reduction of Cu^{2+} as a second cathodic reaction is a slightly more-positive E_{CORR} (by 4-5 mV) with air and 2% O_2/N_2 purge gases, a difference that disappears once the solution is nominally deaerated.

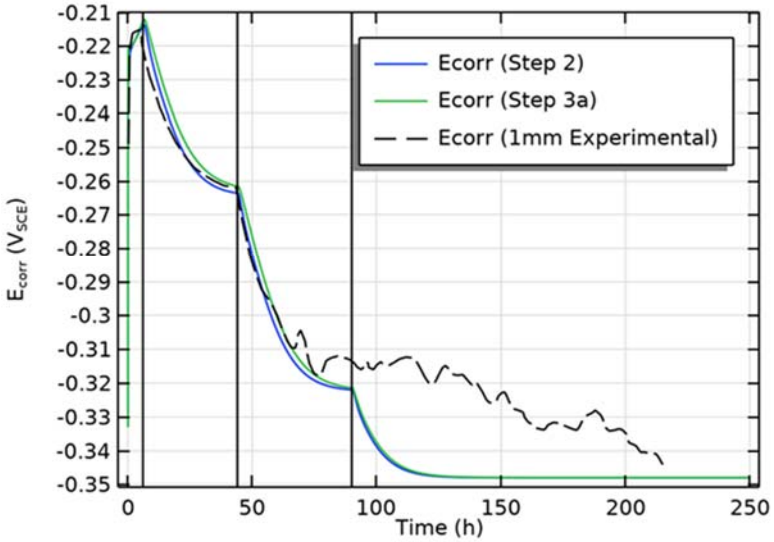

Figure 22: Comparison of the Time-dependent Corrosion Potential for the 1-mm Clay Electrode Experiments and the Predicted E_{CORR} with the Step 2 and Step 3a COMSOL Models.

This relatively minor effect of including the second cathodic reaction is not because O_2 remains the predominant oxidant; in fact, quite the opposite is the case. Figure 23(a) shows the time dependence of the anodic current density (i_a) and those for the reduction of O_2 (i_c) and of Cu^{2+} (i_d). The reduction of Cu^{2+} is the predominant cathodic reaction for times greater than approximately 0.03 hrs (>100 s). Figure 23(b) shows the time dependence of the ratio i_c/i_d, which confirms this predominance of the Cu^{2+} reduction reaction. Interestingly, this predominance continues until the purge gas is changed to 100% N_2 after 90 hrs, at which point the O_2 reduction reaction predominates. This switch in cathodic reaction under nominally deaerated conditions is presumably because of the low concentration of Cu^{2+} under these conditions. Another interesting feature of Figure 23(b) is that the ratio i_c/i_d exhibits a (downwards) spike immediately following a change in purge gas composition. This increase in the relative importance of the Cu^{2+} reduction reaction is a result of the decrease in the interfacial [O_2] that follows a change in the purge gas and a decrease in the rate of the cathodic reduction of O_2.

The clay layer is initially free of Cu^{2+} but there is sufficient present at the copper surface at the first time step in the COMSOL simulation (corresponding to 10^{-10} hrs) that the equilibrium potential for Reaction (30) exceeds that for the dissolution of copper. Thus, the reduction of Cu^{2+} is a thermodynamically viable cathodic reaction (insofar as the criterion for spontaneous corrosion E_{eq}(anodic) < E_{CORR} < E_{eq}(cathodic) is met) at all times, but only becomes kinetically favoured after 0.03 hrs. Figure 24 shows a comparison of the time dependence of the measured and predicted E_{CORR} values and of the equilibrium potentials for the three electrochemical processes, confirming that the reduction of Cu^{2+} is a viable cathodic reaction.

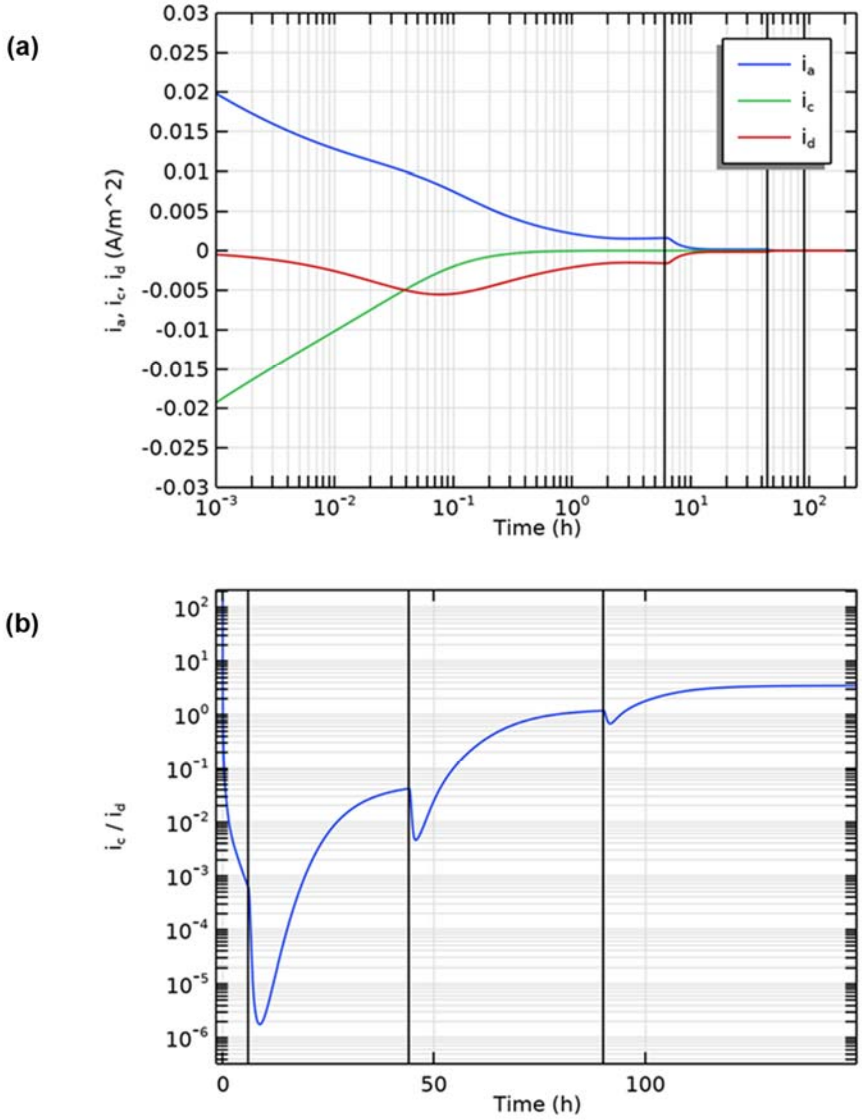

Figure 23: Nature of the Cathodic Reaction as a Function of Time for the Step 3a COMSOL Model. (a) Time dependence of the anodic and two cathodic current densities (log time scale), (b) ratio of the rate of O_2 reduction to the reduction of Cu^{2+} (linear time scale). The vertical lines indicate the times at which the purge gas composition was changed.

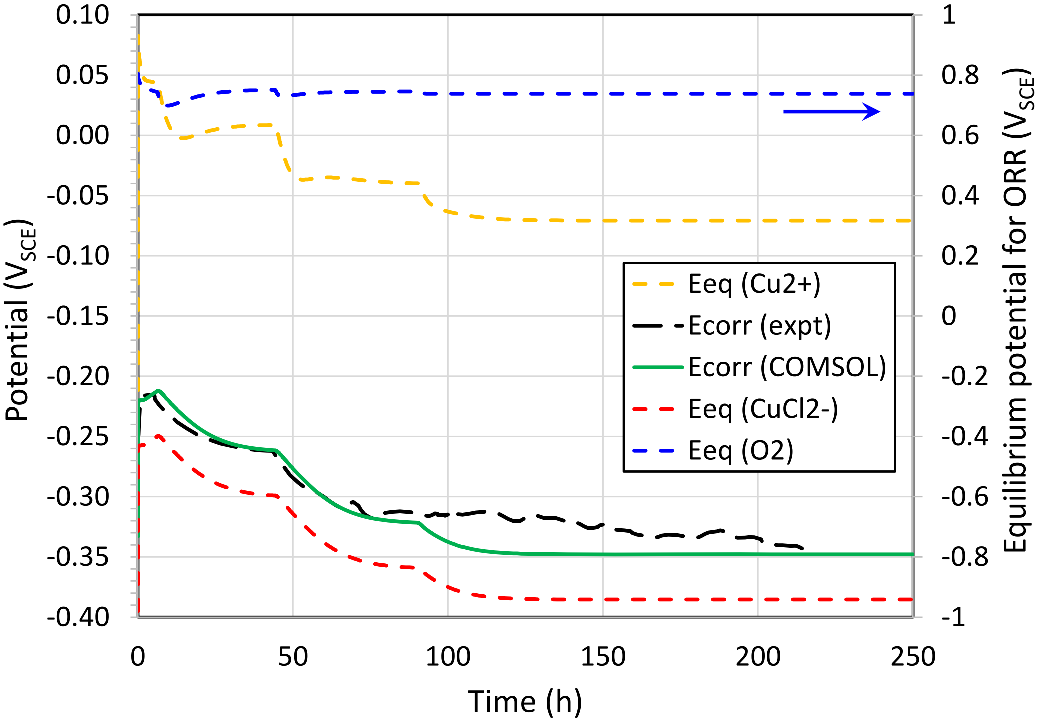

Figure 24: Comparison of the Experimental and Predicted Corrosion Potentials and of the Equilibrium Potentials for the Anodic and Two Cathodic Reactions for the Step 3 COMSOL Model Based on the Predicted Interfacial Concentrations of $CuCl_2^-$, Cl^-, Cu^{2+}, and O_2. A constant pH 7 was assumed to determine the equilibrium potential for the O_2 reduction reaction, which is plotted on the right-hand y-axis.

The observation that the nature of the cathodic reaction has little influence of the value of E_{CORR} is a consequence of the corrosion process being under cathodic transport control. The ultimate controlling process is the supply of O_2 from the right-hand boundary (i.e., from the bulk solution in the experiment), which determines the rate of the cathodic reaction regardless of whether that process involves the reduction of O_2 or of Cu^{2+}. As noted above, if the cathodic reaction is transport limited, E_{CORR} lies close to the equilibrium potential for the anodic reaction (Shoesmith 2003), as illustrated in Figure 24.

4.1.3.2 Quality Checks

Similar quality checks on the output of the Step 3a model were done as were done for Step 2. Except for very short times, the sum of the current densities for the three interfacial reactions was identically equal to zero (Figure 25(a)). Similarly, the time-dependent inventory of Cu in the clay layer was identical to the difference in copper fluxes across the left-hand and right-hand boundaries (Figure 25(b)). In this latter case, the flux across the right-hand boundary is simply equal to the diffusive fluxes of the two copper species $CuCl_2^-$ and Cu^{2+}. However, the flux across the left-hand boundary represents the difference between the dissolution of Cu as $CuCl_2^-$ and the reduction of Cu^{2+} representing a flux in the opposite direction.

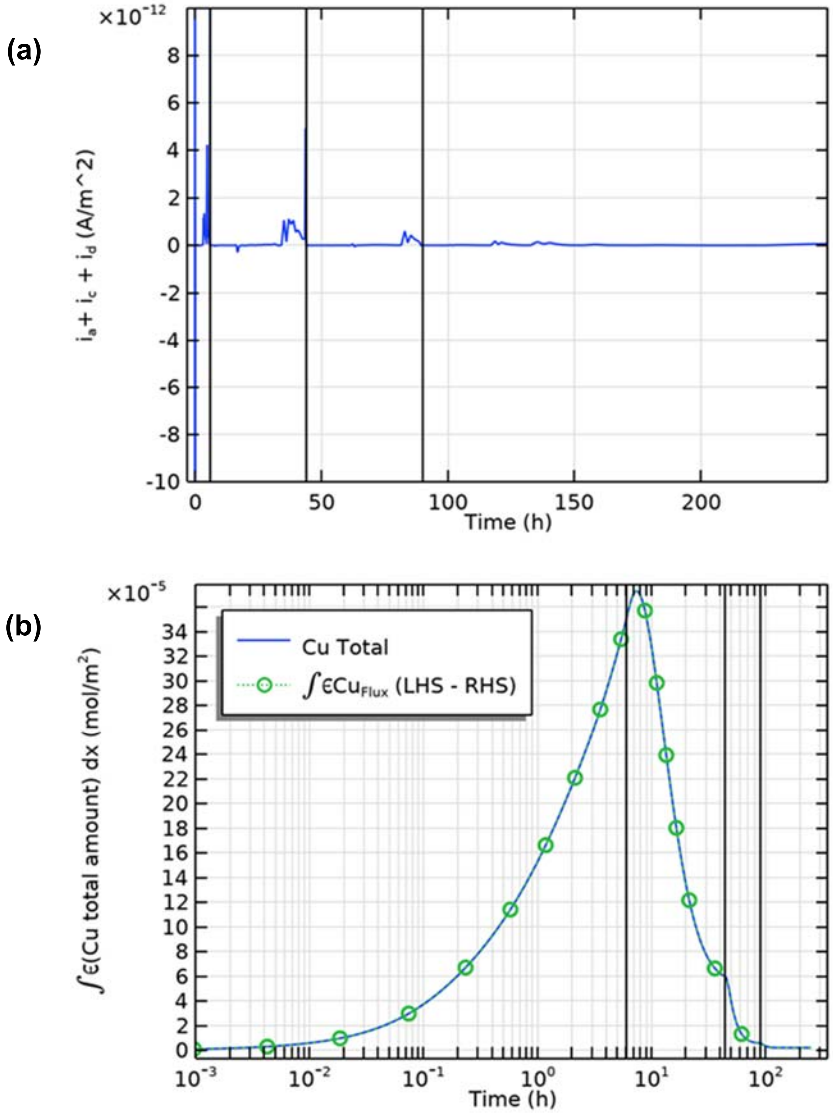

Figure 25: Quality Checks on the Results of the Step 3a COMSOL Model. (a) Time dependence of the sum of the anodic and cathodic current densities, (b) comparison of the time dependence of the total amount of copper (in the form of both $CuCl_2^-$ and Cu^{2+}) in the clay layer with the difference of the copper fluxes at the left-hand and right-and boundaries. The vertical lines indicate the times at which the purge gas was changed.

4.1.3.3 Mechanistic Insights

As for Step 2, examination of the concentration profiles and time-dependent interfacial concentrations of the reactants and products provides mechanistic insight into the corrosion process.

Figure 26 shows the concentration profiles for O_2, $CuCl_2^-$, and Cu^{2+} in the 1-mm clay layer at various selected times for the Step 3a simulations. The first point of interest is that, compared with the Step 2 model (Figure 19(a)), the O_2 is quickly consumed close to the copper surface in the Step 3a model, with the concentration dropping to zero within an hour or so (Figure 26(a)). In contrast, a zero-concentration condition for O_2 at the copper surface was not established in the Step 2 model until after the purge gas had been changed to 0.2% O_2/N_2 (Figure 20(a)). The depletion of O_2 near the copper surface is the result of not only the interfacial reduction process but also the homogeneous oxidation of $CuCl_2^-$ to Cu^{2+} by O_2. A significant concentration of Cu^{2+} develops close to the copper surface (Figure 26(c)), although the interfacial concentration remains zero because the Cu^{2+} is itself cathodically reduced on the electrode surface. It is interesting to note that while neither the concentration profiles for $CuCl_2^-$ nor Cu^{2+} exhibit any tendency towards steady state (Figure 26(b) and (c)), the profile for the total copper concentration does (Figure 27).

Figure 28 shows the spatial dependence of the time-integrated extent of the homogeneous oxidation reaction. While this reaction primarily occurs near the copper surface at short times, the location of the oxidation reaction moves progressively towards the right-hand boundary with increasing time. Oxidation of $CuCl_2^-$ almost ceases after 43 hrs, which is close to the end of the period with a purge gas composition of 2 vol.% O_2/N_2. By this time, in addition to the early oxidation near the copper surface, there are two maxima in the integrated oxidation curve centred at around 0.3 mm and 0.7 mm from the copper surface. The highest rates of oxidation will occur at locations where the product of the O_2 and $CuCl_2^-$ concentrations is highest. The maximum centred at 0.3 mm is associated with the early aerobic period, whereas that at 0.7 mm occurs later once the $CuCl_2^-$ produced at the copper surface has diffused towards the right-hand boundary.

The time-dependent interfacial concentrations of O_2, $CuCl_2^-$, and Cu^{2+} are shown in Figure 29. By the end of the first hour, the interfacial $[O_2]$ has dropped from the initially aerated conditions (0.2 mol/m^3, 2×10^{-4} mol/L) to a value of 8.9×10^{-7} mol/L (28 ppb), a level associated here with nominally deaerated solution (Figure 29(a)). The time dependence of the interfacial $[CuCl_2^-]$ for Step 3a (Figure 29(b)) is similar to that for Step 2 (Figure 20(b)). The interfacial concentration of Cu^{2+} (Figure 29(c)) is approximately 100 times lower than that of $CuCl_2^-$, but is not zero, suggesting that although the cathodic reduction of Cu^{2+} is fast, it is not entirely transport limited. Interestingly, Cu^{2+} starts to accumulate at the surface from mid-way through the initial aerobic phase, resulting in a secondary peak in the concentration after 6 hrs. Why Cu^{2+} should accumulate at the interface during this period is not entirely clear, unless this corresponds to Cu^{2+} formed further away from the surface which then diffuses towards the left-hand boundary. This time corresponds to the period of maximum $[Cu^{2+}]$ in the system (Figure 26(c)), with a peak concentration at a distance of 0.4 mm from the copper surface.

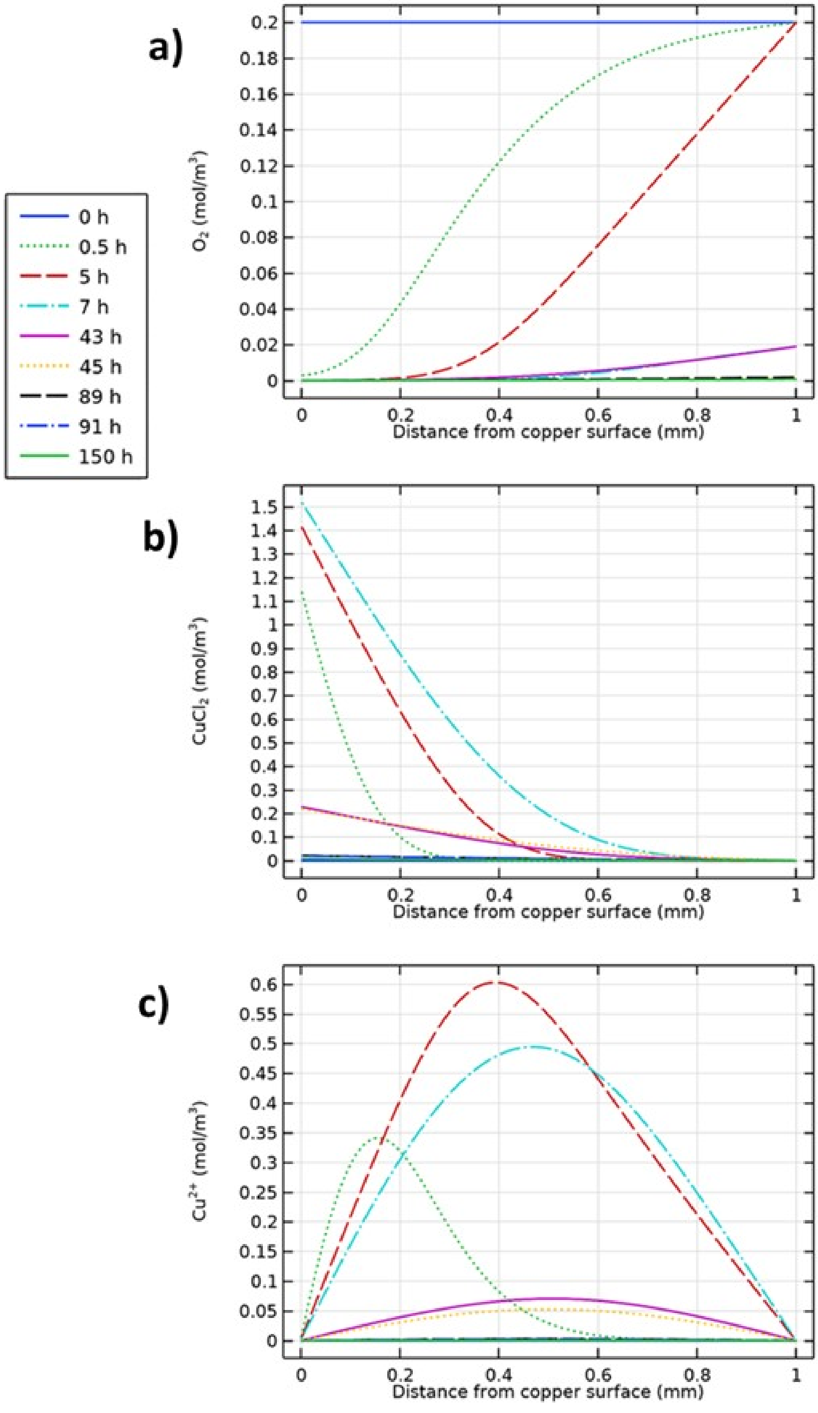

Figure 26: Concentration Profiles in the 1-mm Clay Layer for (a) O_2, (b) $CuCl_2^-$, and (c) Cu^{2+} Ions at Selected Times for the Step 3a COMSOL Model.

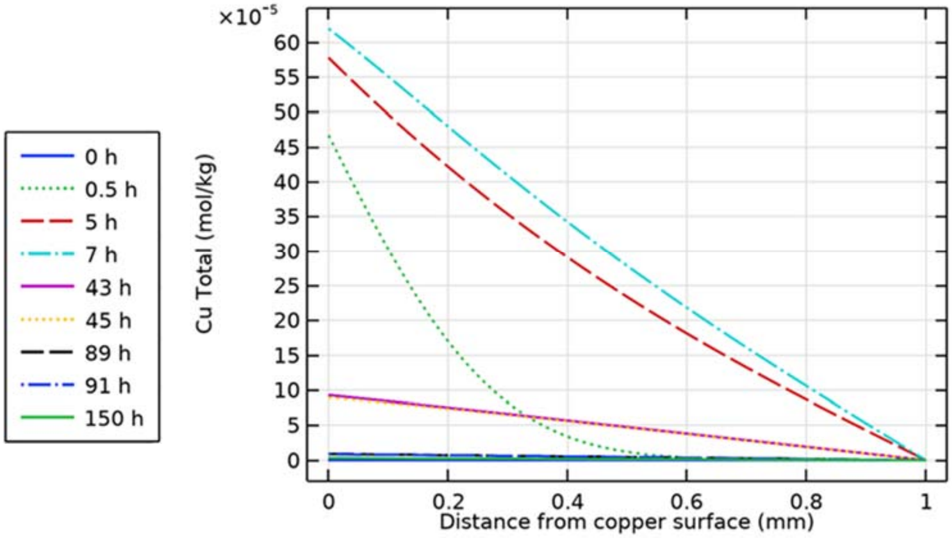

Figure 27: Total Copper (as $CuCl_2^-$ and Cu^{2+}) Concentration Profiles in the 1-mm Clay Layer at Selected Times for the Step 3a COMSOL Model.

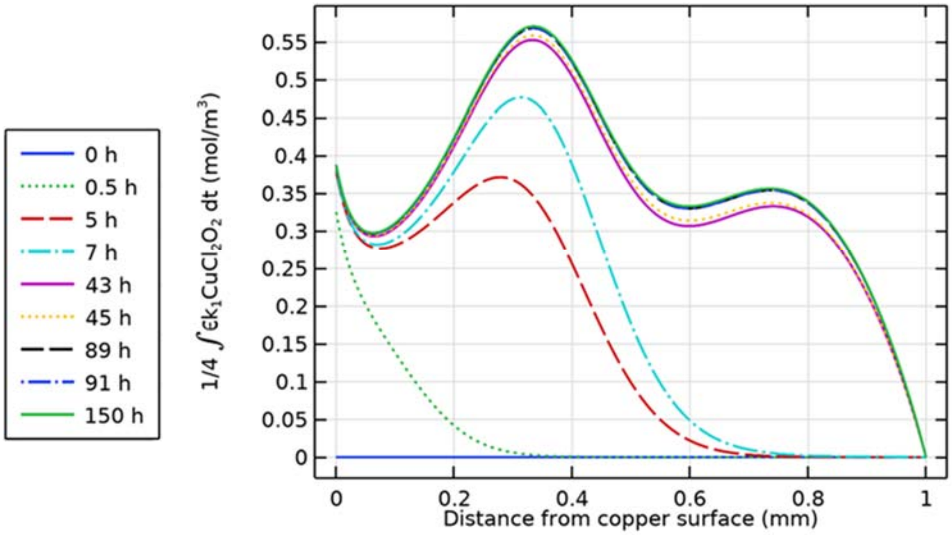

Figure 28: Spatial Variation of the Cumulative Extent of Copper(I) Oxidation by Oxygen for Selected Times for the Step 3a COMSOL Model.

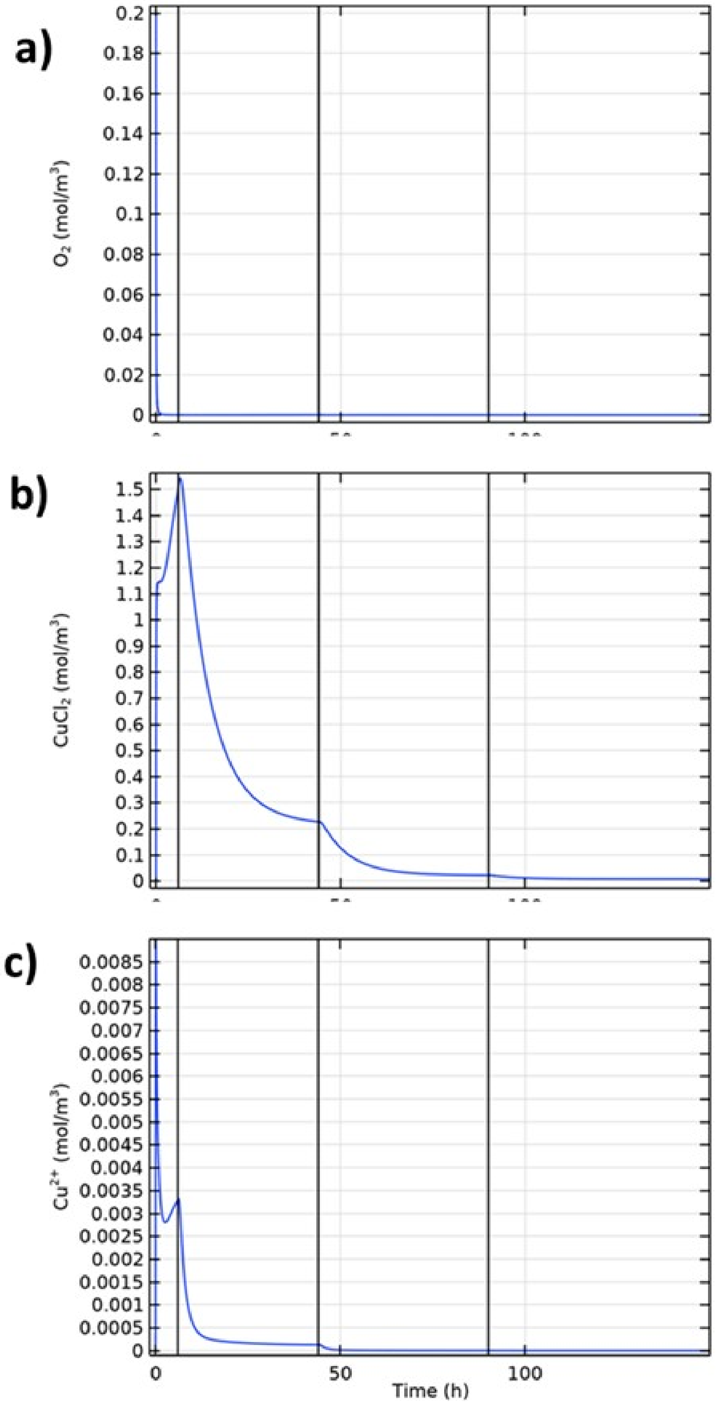

Figure 29: Time Dependence of the Interfacial Concentrations of (a) O_2, (b) $CuCl_2^-$, and (c) Cu^{2+} ions at Selected Times for the Step 3a COMSOL Model. The vertical lines indicate the times at which the purge gas was changed.

4.1.3.4 Extent of Corrosion

Marginally more corrosion is predicted to occur by the Step 3a model than by the simpler Step 2 version (Figure 30). If O_2 reduction is the only cathodic reaction, the total amount of corrosion by the end of the 250-hr simulation is predicted to be approximately 75.6 C/m^2 or 0.0056 μm (Figure 30(b)). If Cu^{2+} reduction is also included, not only does the predominant cathodic reaction change from O_2 reduction to Cu^{2+} reduction (Figure 30(a)), but the total amount of corrosion increases slightly to approximately 84.6 C/m^2 or 0.0062 μm.

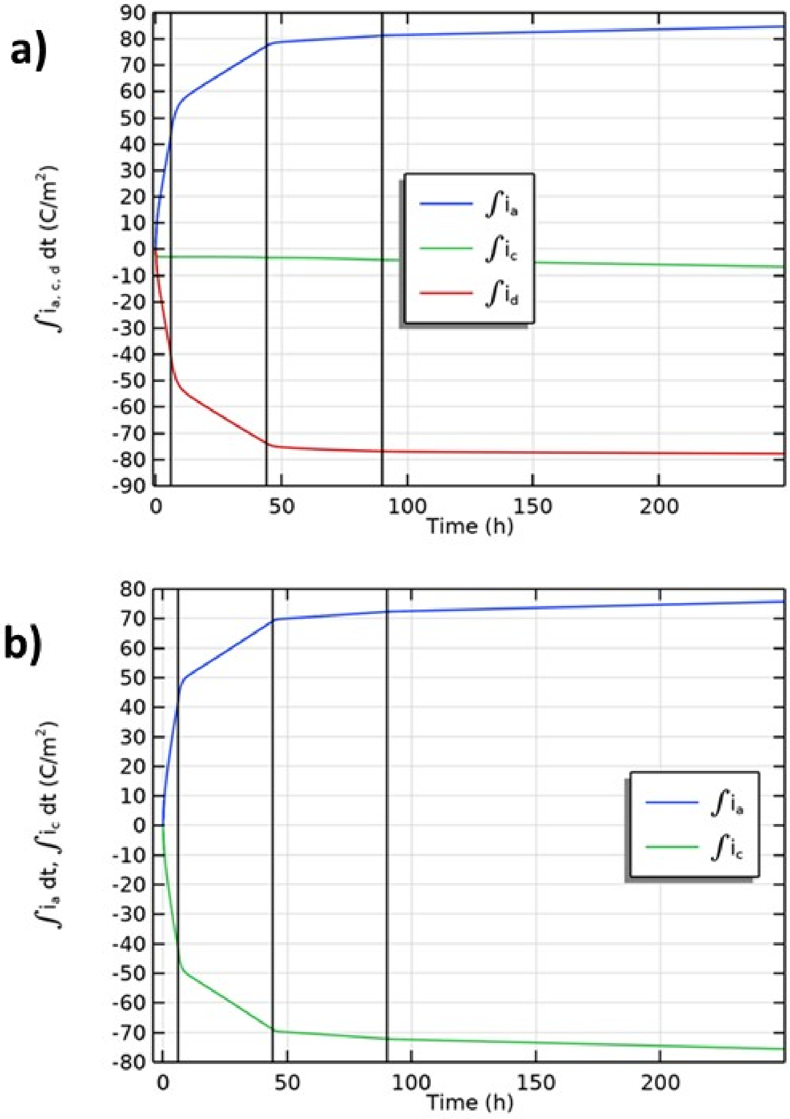

Figure 30: Comparison of the Time Dependence of the Integrated Current Densities for (a) the Step 3a and (b) the Step 2 COMSOL Models. The vertical lines indicate the times at which the purge gas was changed.

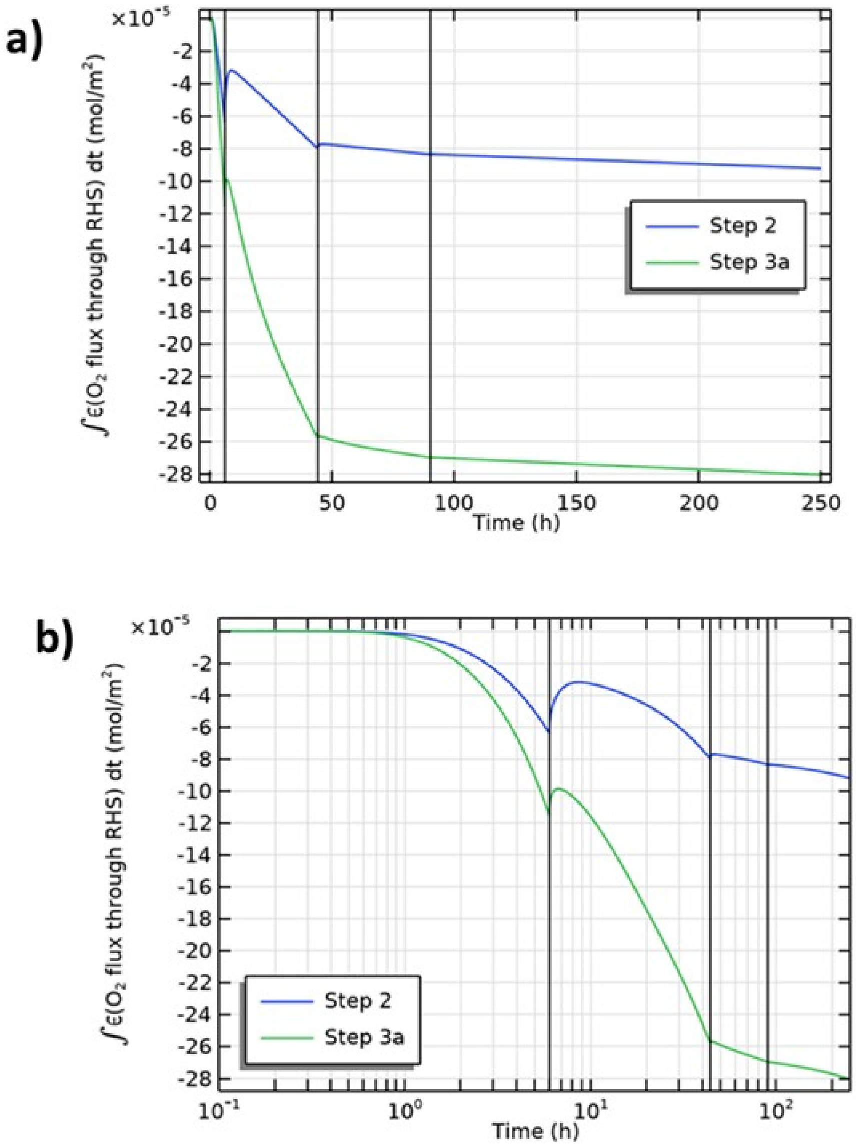

Figure 31: Comparison of the Time-integrated Fluxes of Oxygen Across the Right-hand Boundary for the Steps 2 and 3a COMSOL Models Plotted on (a) Linear and (b) Logarithmic Time Scales. A negative flux indicates O_2 enters the clay layer.

Regardless of the nature of the cathodic reaction, the ultimate source of oxidant is O_2, either that initially present in the saturated clay layer or that which enters from the bulk solution during the course of the experiment. The initial inventory of O_2 in the clay layer is 1.04×10^{-4} mol/m^2, corresponding to 40.1 C/m^2. Additional O_2 enters the clay layer during the 6-hr aerated phase (Figure 31). Once the purge gas is changed to 2% O_2/N_2, some of the O_2 in the clay layer diffuses back out into the bulk solution, especially if O_2 reduction is the only cathodic reaction (see Step 2 in Figure 31(b)). However, once the clay layer has equilibrated with the new purge gas, O_2 re-enters the clay layer in the period 6-44 hrs, with smaller amounts diffusing in from the bulk solution during the later periods with either 0.2% O_2/N_2 or 100% N_2 as purge gases.

The greater influx of O_2 into the clay layer from the bulk solution for Step 3a compared with Step 2 (Figure 31(a)) is a consequence of the steeper O_2 concentration gradient at the clay/solution interface. Consumption of O_2 by the oxidation of Cu(I) results in lower [O_2] in the clay layer for Step 3(a) (compare the [O_2] profiles for Step 3a in Figure 26(a) and Step 2 in Figure 19(a)), and hence a larger diffusive driving force for O_2 to enter the clay layer from the bulk solution. Of the total amount of corrosion (corresponding to 75.6 C/m^2 and 84.6 C/m^2 for Steps 2 and 3a, respectively), approximately 50% (40.1 C/m^2) can be accounted for by the O_2 initially in the clay layer, with the remainder due to O_2 entering form the bulk solution during the course of the experiment.

4.1.3.5 Mass Balances for Oxygen and Copper

Mass-balance estimates for O_2 and for the various Cu species provides another opportunity to check on the quality of the simulations. Table 10 summarises the initial and final inventories, as well as the gains and losses (consumption) for O_2 and for the various Cu species for the Step 2 and Step 3a simulations.

The mass-balance for O_2 is given by:

(Initial O_2 inventory + net O_2 flux into clay layer) = (final O_2 inventory + amount O_2 reacted) (31)

where the amount of O_2 reacted includes both that reduced electrochemically ($\int$ic dt) and, for Step 3a only, that consumed in oxidation of Cu(I) to Cu(II).

Table 11: Inputs for the Calculation of the Mass Balances for Oxygen and Copper for Step 2 and Step 3a COMSOL Simulations.

Parameter		Step 2	Step 3a
Electrochemical reactions	$\int i_a dt\ (C/m^2)$	75.6	84.6
	$\int i_c dt\ (C/m^2)$	-75.6	-6.8
	$\int i_d dt\ (C/m^2)$	-	-77.9
O_2 inventory	Initial (mol/m^2)	1.04×10^{-4}	1.04×10^{-4}
	Final (mol/m^2)	0	0
Net O_2 flux into clay layer	mol/m^2	9.22×10^{-5}	2.81×10^{-4}
O_2 consumption due to Cu(I) oxidation	mol/m^2	0	3.67×10^{-4}
Final copper inventories	mol/m^2	0	0
Flux of $CuCl_2^-$ and Cu^{2+} out of clay layer	mol/m^2	7.82×10^{-4}	8.75×10^{-4}

Table 12: Mass-balance Calculations for Oxygen and Copper for Step 2 and Step 3a COMSOL Simulations.

		Step 2	**Step 3a**
O_2 mass balance	Initial inventory + net flux	1.962×10^{-4} mol/m^2	3.850×10^{-4} mol/m^2
	Final inventory + amount reacted	1.960×10^{-4} mol/m^2	3.845×10^{-4} mol/m^2
	Relative error	0.09%	0.05%
Cu mass balance	Amount produced	7.84×10^{-4} mol/m^2	8.77×10^{-4} mol/m^2
	Final inventory + amount exited	7.82×10^{-4} mol/m^2	8.75×10^{-4} mol/m^2
	Relative error	0.26%	0.23%

Similarly, the mass-balance for copper is given by:

Amount of produced = (final Cu inventory + amount Cu exiting clay layer) (32)

where the amount produced is simply the integrated anodic current density.

Table 12 summarises the mass-balance calculations for Steps 2 and 3a based on the data in Table 11. In both cases the O_2 mass-balance is excellent, with a relative error of <0.1%. The relative error is somewhat higher for the copper mass balance, but is still <0.3%.

4.1.4 Step 3b Precipitation/dissolution of Atacamite

Step 3b involves the addition of the reversible precipitation of atacamite ($CuCl_2{\cdot}3Cu(OH)_2$) to the reaction scheme (Appendix A.3.2), based on the following reaction:

$$4Cu^{2+} + 2Cl^{-} + 6OH^{-} \underset{k_{-3}}{\overset{k_3}{\rightleftharpoons}} CuCl_2{\bullet}3Cu(OH)_2 \qquad (33)$$

where the forward (precipitation) and reverse (dissolution) 1st-order rate constants k_3 and k_{-3} have assumed values of 10^{-5} s^{-1} and 10^{-6} s^{-1}, respectively. The rate of precipitation is assumed to be proportional to the difference between the dissolved Cu^{2+} concentration and the equilibrium [Cu^{2+}] in the presence of atacamite, i.e., to the degree of under-saturation of the solution. The precipitation and dissolution rate constants correspond to “half-lives” for Cu^{2+} and for the precipitated phase of 19 hrs and 193 hrs, respectively. Again the OH^- species is not tracked in the model and the pH is assumed to be a constant pH 7.

4.1.4.1 Predicted E_{CORR} and the Nature of the Cathodic Reaction

Figure 32 shows a comparison of the measured E_{CORR} and of the predicted time dependence for the Steps 2, 3a, and 3b models. There is little difference between the predicted E_{CORR} values for the aerated and 2 vol.% O_2/N_2 phases (up 44 hrs), but the Step 3b model predicts more-positive values for the 0.2 vol.% O_2/N_2 and 100% N_2 purge gases that are closer to the experimental values than those predicted by the prior versions of the code.

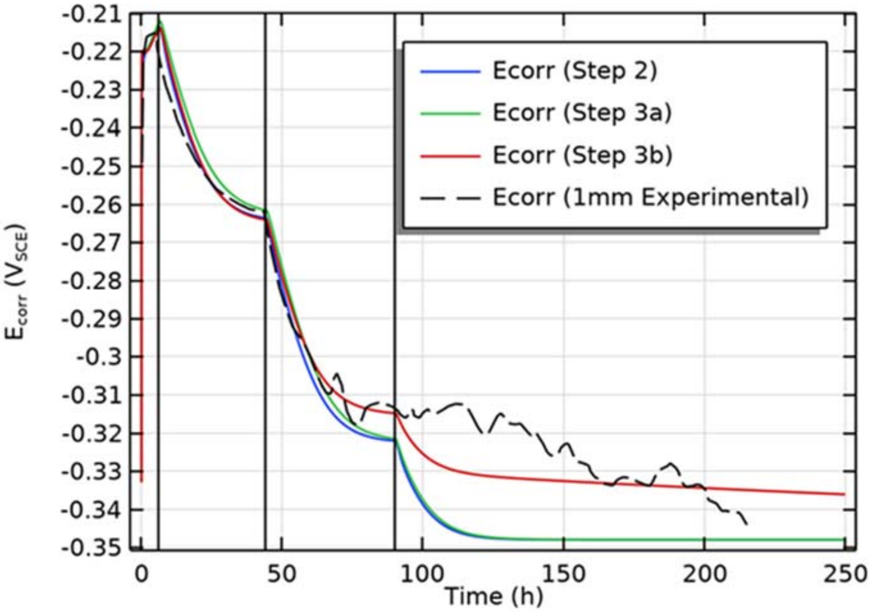

Figure 32: Comparison of the Experimental Corrosion Potential and the Predicted Values for the Step 2, Step 3a, and Step 3b COMSOL Models. The vertical lines indicate the times at which the purge gas was changed.

This improved agreement between observed and predicted E_{CORR} values for Step 3b is a consequence of a subtle change in the nature of the cathodic reaction. Figure 33(a) shows the time dependence of the anodic and cathodic current densities for Step 3b, which are visually indistinguishable from those for Step 3a shown in Figure 23(a). However, whereas the reduction of O_2 becomes the predominant cathodic reaction at low $[O_2]$ for Step 3a (Figure 23(b)), the ratio i_c/i_d remains less than one at all times for Step 3b (Figure 33(b)), indicating that the reduction of Cu^{2+} is the main cathodic reaction regardless of the dissolved $[O_2]$. As will be shown below, this persistence of the Cu^{2+} reduction reaction is believed to be because the slow dissolution of atacamite ("half-life" of 193 hrs) acts as a source of dissolved Cu^{2+} throughout the simulated time period.

4.1.4.2 Quality Checks

The same quality checks were conducted for the Step 3b code as for Step 3a, i.e., the sum of the currents and the comparison of the total Cu inventory to the integrated gain (from the left-hand boundary) and loss (from the right-hand) boundary of dissolved copper (cf. Figure 25). Excellent agreement was again found in both cases, providing confidence in the quality of the model output.

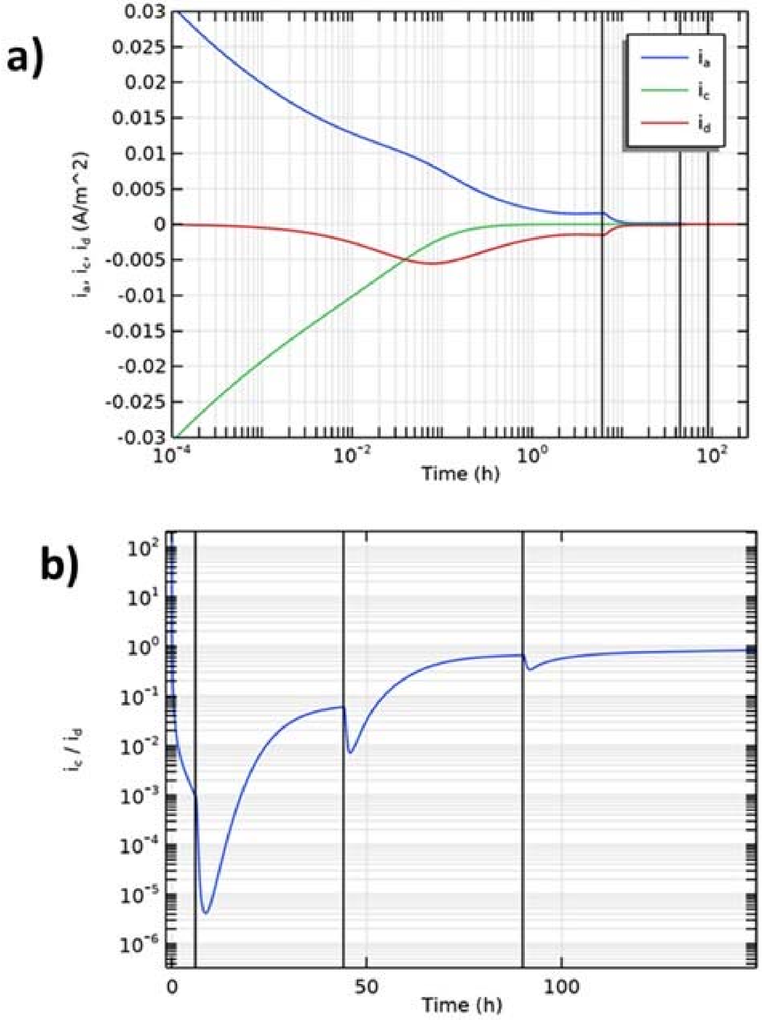

Figure 33: Nature of the Cathodic Reaction as a Function of Time for the Step 3b COMSOL Model. (a) Time dependence of the anodic and two cathodic current densities (log time scale), (b) ratio of the rate of O_2 reduction to the reduction of Cu^{2+} (linear time scale). The vertical lines indicate the times at which the purge gas composition was changed.

4.1.4.3 Mechanistic Insights

The spatial distribution of precipitated atacamite is similar to the distribution of dissolved Cu^{2+}, exhibiting a maximum some distance away from the copper surface (Figure 34). In terms of the copper speciation, dissolved $CuCl_2^-$ and Cu^{2+} predominate at short times (see concentration profiles for times up to approximately 7 hrs in Figure 34), but $CuCl_2 \cdot 3Cu(OH)_2$ predominates at long times (see profiles for times of 89 hrs and longer). This change in dominant speciation with time is a consequence of the relatively slow rate of precipitation and the even slower rate of dissolution of the solid phase.

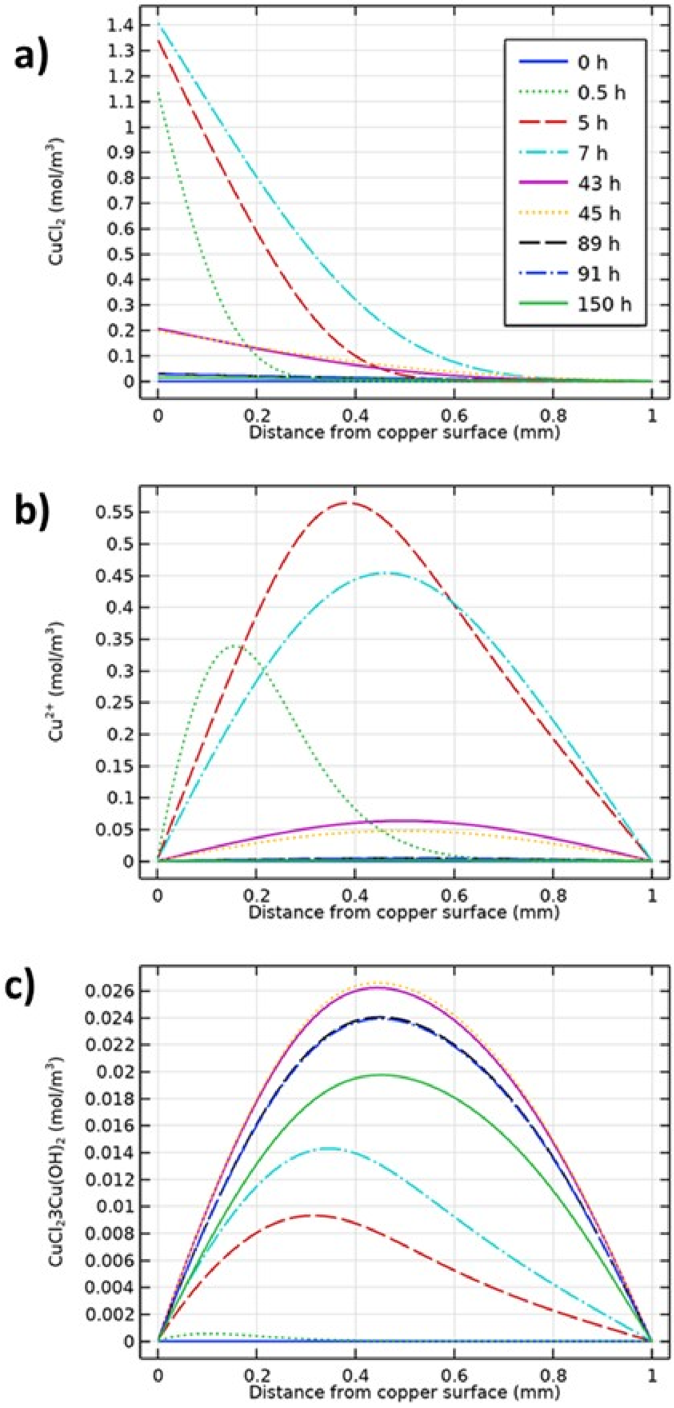

Figure 34: Concentration Profiles in the 1-mm Clay Layer for (a) $CuCl_2^-$, (b) Cu^{2+} and (c) $CuCl_2 \cdot 3Cu(OH)_2$ at Selected Times for the Step 3b COMSOL Model.

Unlike the complex spatial distribution of the extent of copper(I) oxidation (Figure 28), the integrated extents of atacamite precipitation (Figure 35(a)) and dissolution (Figure 35(b)) mirror the distribution of dissolved Cu^{2+} species. Atacamite precipitation and dissolution are both 1st-order processes depending on the concentration of only a single species, whereas the rate of copper(I) oxidation is 2nd-order and depends on the concentrations of both $CuCl_2^-$ and O_2, resulting in a more-complex spatial distribution of reaction rates.

Figure 35 also demonstrates the relative kinetics of precipitation and dissolution, with the former virtually ceasing after 90 hrs, but dissolution continuing throughout the duration of the simulation.

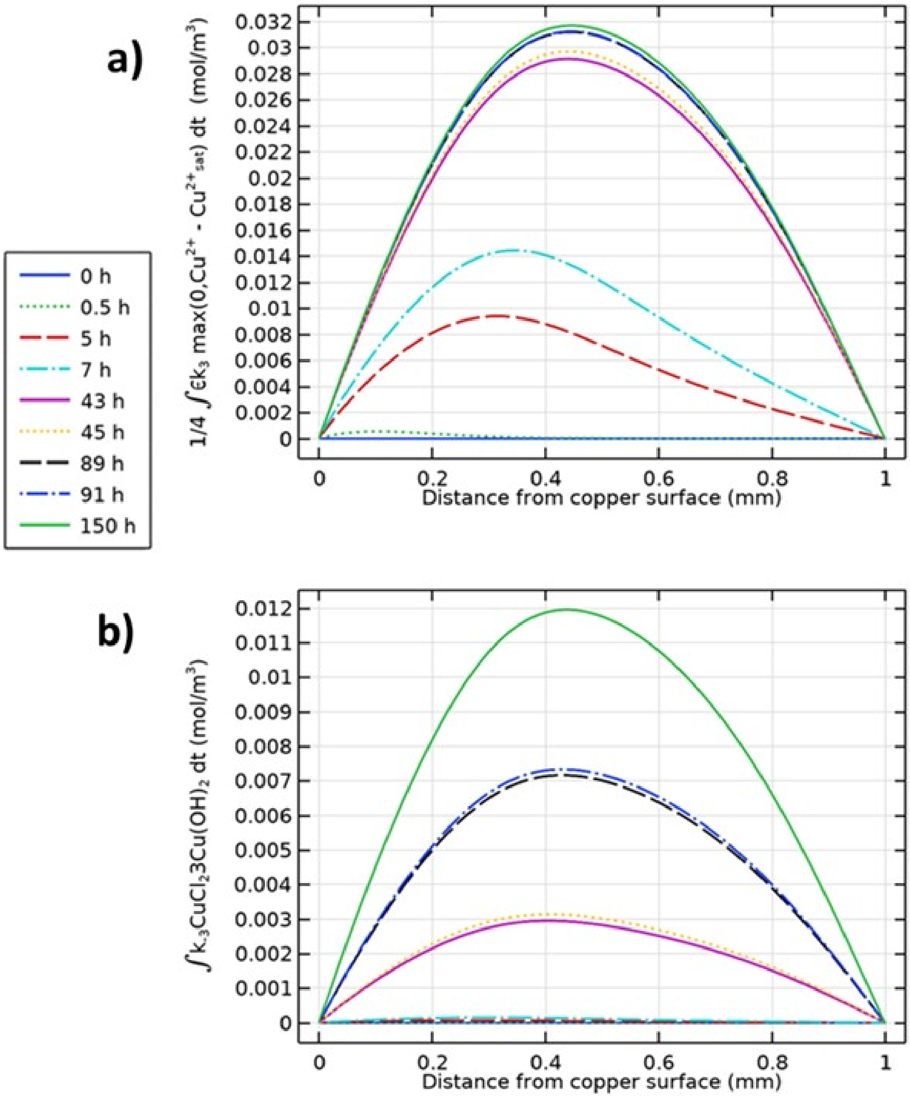

Figure 35: Spatial Variation of the Cumulative Extent of (a) Atacamite Precipitation and (b) Atacamite Dissolution for Selected Times for the Step 3a COMSOL Model.

The predicted time dependences of the inventories of the various copper species also demonstrate the persistence of the precipitated phase. Figure 36(a) and (b) show the inventories of $CuCl_2^-$ and of Cu^{2+} (i.e., the total amount in the 1-mm clay layer) for the Step 3b model. The amounts of these species closely follows the time dependence of E_{CORR}, which in turn responds to the changing redox conditions in the experiment. Thus, by the end of the period of purging with 0.2 vol.% O_2/N_2 (i.e., after 90 hrs), most of the dissolved copper has diffused out of the clay layer. In contrast, the inventory of atacamite reaches a maximum after about 50 hrs and then only slowly decreases as the $CuCl_2{\cdot}3Cu(OH)_2$ dissolves (Figure 36(c)). By the end of the experiment, more than half of the atacamite remains in the clay layer. It is this persistence of the precipitated phase, and the slow release of Cu^{2+} as it dissolves, that maintains the reduction of Cu^{2+} as the predominant cathodic reaction (Figure 33(b)), which is responsible for the slight ennoblement of E_{CORR} for Step 3b compared with the Step 2 and 3a models (Figure 32).

4.1.5 Step 3c Precipitation/dissolution of Cuprite

For Step 3c, the reaction mechanism was extended to include the precipitation and dissolution of cuprite Cu_2O (Appendix A.3.3), based on the following reversible reaction:

$$2CuCl_2^- + H_2O \underset{k_{-2}}{\overset{k_2}{\rightleftarrows}} Cu_2O + 4Cl^- + 2H^+ \tag{34}$$

where the forward (precipitation) and reverse (dissolution) 1st-order rate constants k_3 and k_{-3} have assumed values of 1 s^{-1} and 0.1 s^{-1}, respectively. Thus, precipitation and dissolution are both treated as kinetically fast reactions, and as a consequence $CuCl_2^-$ and Cu_2O are essentially in equilibrium.

Figure 37 shows the predicted and measured time-dependent E_{CORR} values for the 1-mm clay electrode experiment, with predicted profiles shown for Steps 2, 3a, 3b, and 3c. The E_{CORR} predicted using the Step 3c model is identical to that for the Step 3b model, suggesting that the precipitation and dissolution of Cu_2O has no effect on the potential-determining reactions. (The E_{CORR} profiles for Steps 3b and 3c are coincident and only the curve for the latter is visible in Figure 37). The interfacial concentration of $CuCl_2^-$ (of the order of 10^{-3} mol/L) is sufficiently high that it exceeds the equilibrium solubility for Cu_2O in 1 mol/L Cl^- solution (equivalent to 3.4×10^{-6} mol/L), suggesting that Cu_2O precipitation is possible. However, Cu_2O is predicted not to accumulate in the clay layer because of the assumption of fast dissolution kinetics.

In all other respects, the results of the Step 3c simulations are identical to those from the Step 3b model.

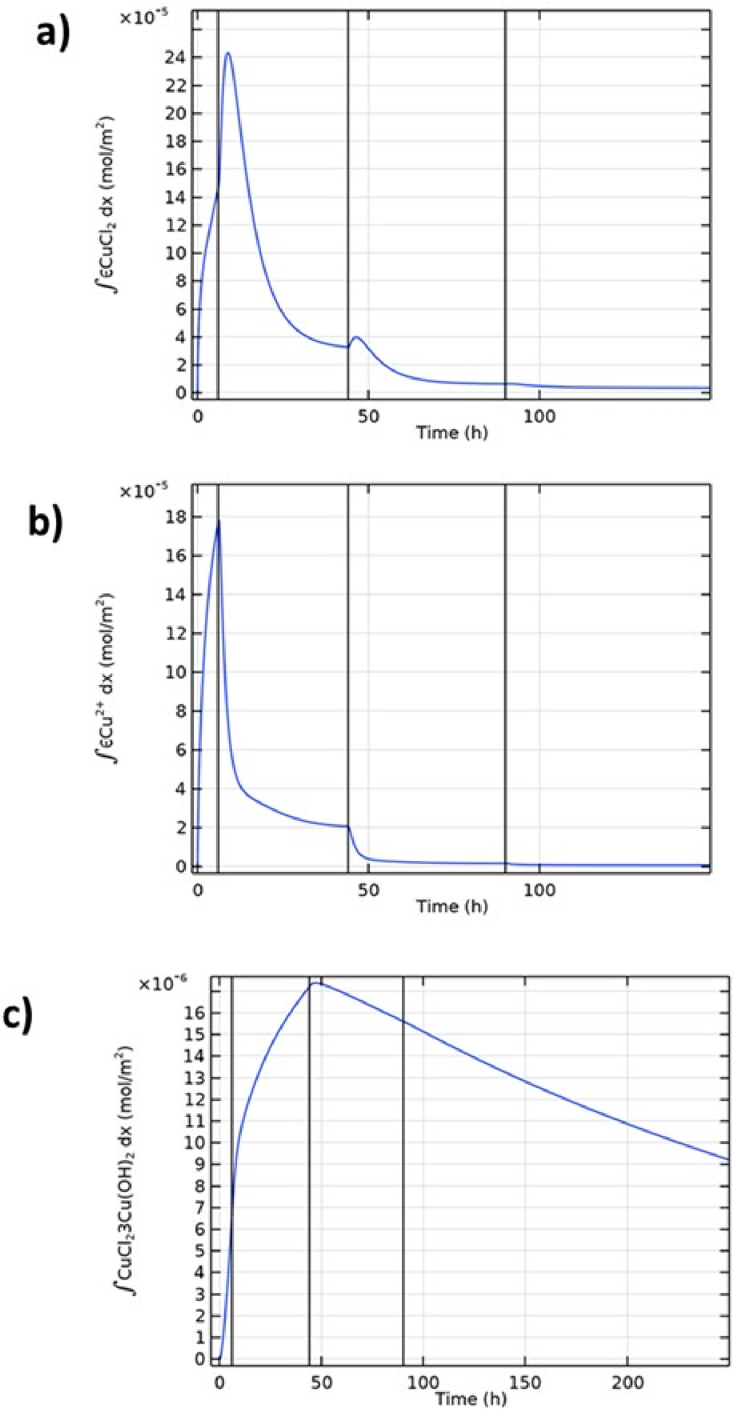

Figure 36: Time-dependent Inventories of (a) $CuCl_2^-$ (b) Cu^{2+}, and (c) $CuCl_2{\cdot}3Cu(OH)_2$ for the Step 3b Model.

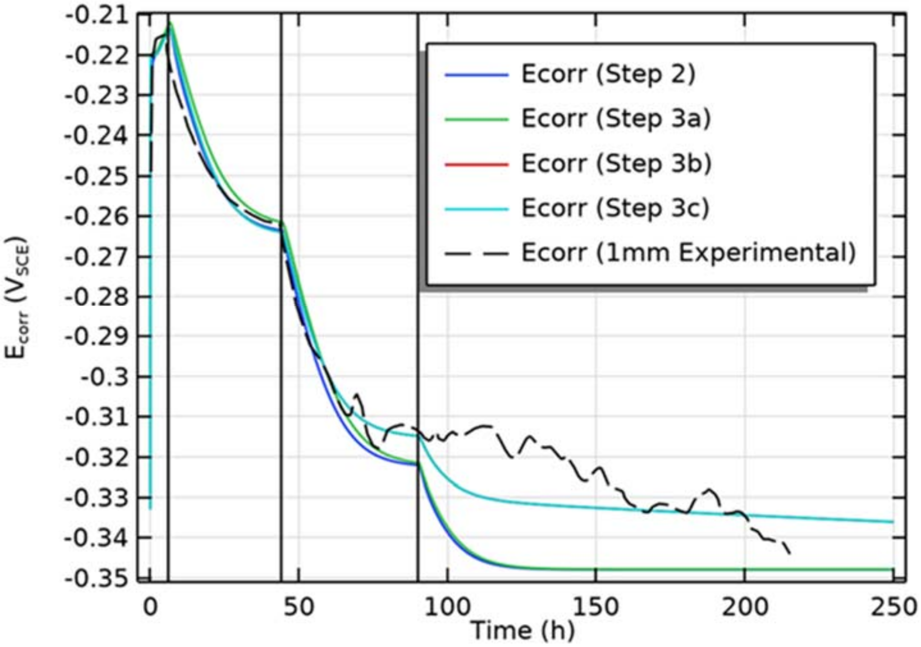

Figure 37: Comparison of the Measured and Predicted (Steps 2, 3a, 3b, and 3c) Time-dependent Corrosion Potentials for the 1-mm Clay Layer Experiment. The E_{CORR} profiles for Steps 3b and 3c are coincident. The vertical lines indicate the times at which the purge gas was changed.

4.1.6 Step 3d Adsorption/desorption of Copper(II)

In line with the treatment of other processes in the CCM, the adsorption and desorption of Cu^{2+} by the bentonite is treated kinetically (Appendix A.3.4). Because of the observation from copper corrosion experiments in compacted buffer that the total copper concentration in the clay closest to the copper surface was equivalent to the cation-exchange capacity (CEC) of the clay (King et al. 1992, Litke et al. 1992), a Langmuir adsorption isotherm was assumed. In the kinetic treatment of adsorption via a Langmuir isotherm, the rate of adsorption is proportional to the fraction of free adsorption sites, with the adsorbed concentration exhibiting a maximum that, based on the experimental evidence, is equivalent to the CEC of the clay for divalent Cu(II) species. The rate of adsorption (which also depends on the adsorbate concentration) is given by

$$\frac{\partial c_5}{\partial t} = k_4 c_3 (c_5^{max} - c_5) \qquad \text{for } c_5 < c_5^{max} \qquad (35)$$

where, c_3 is the concentration of dissolved Cu^{2+}, c_5 is the concentration of adsorbed Cu, and c_5^{max} is the maximum surface coverage of adsorbed copper. In the original CCM, the value for the second-order adsorption rate constant k_4 was uncertain and was selected on the basis of expert judgement and the observation that adsorption of Cu^{2+} on loose bentonite is rapid (Ryan and King 1994). The rate of desorption is proportional to the concentration of adsorbed Cu(II)

$$-\frac{\partial c_5}{\partial t} = k_{-4} c_5 \qquad (36)$$

where k_{-4} is the desorption rate constant, the value of which was again selected based on expert judgement and the experimental observation that the rate of desorption is slow (Ryan and King 1994). The default values of k_{-4} (1×10^{-6} s^{-1}) corresponds to a "half-life" for adsorbed Cu(II) of 193 hrs.

Figure 38 shows a comparison of the experimental and predicted time-dependence of E_{CORR} values for the Step 3d model using the default values for k_4 and k_{-4}, as well as for the preceding model steps. Compared with both the experimental time dependence and that predicted by the preceding models, the inclusion of Cu(II) adsorption/desorption in Step 3d leads to faster evolution of E_{CORR} between changes in O_2 concentration, as well as more-positive steady-state potential values. The more-rapid decrease in E_{CORR} is due to the relatively rapid Cu(II) adsorption step, which has the effect of removing oxidant from the system (Figure 39). In the long-term, the slow desorption of Cu(II) from the clay acts as a "reservoir" of oxidant slowly releasing Cu^{2+} to be reduced at the copper surface, in much the same way as the slow dissolution of $CuCl_2{\cdot}3Cu(OH)_2$ in Step 3b (Figure 36(c)).

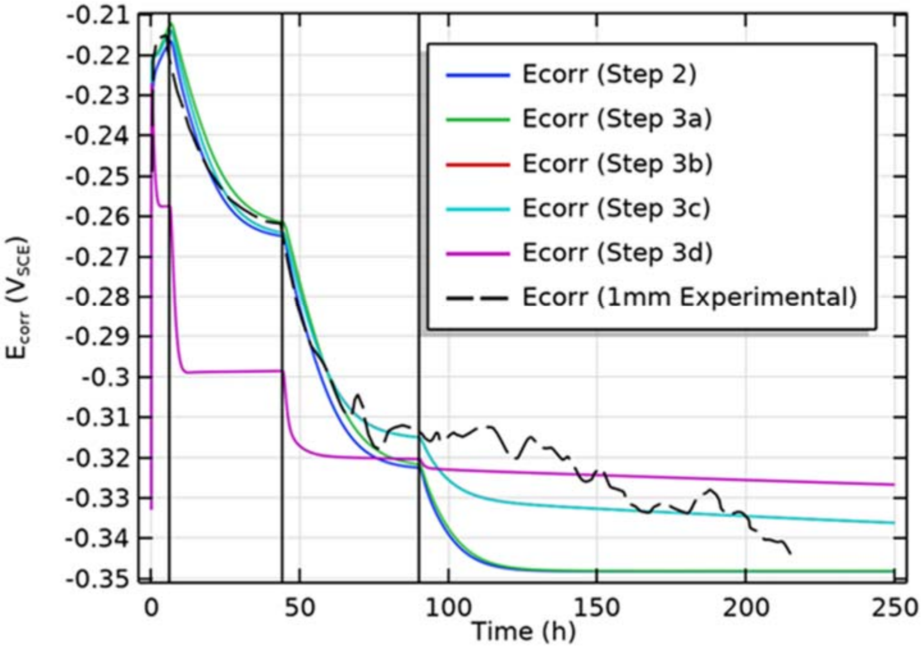

Figure 38: Comparison of the Experimental Corrosion Potential and the Predicted Values for the Step 2, Step 3a, Step 3b, Step 3c, and Step 3d COMSOL Models. The Step 3d model was run using the default values for the adsorption and desorption rate constants of $k_4 = 2\times10^{-6}$ $m^3{\cdot}mol^{-1}{\cdot}s^{-1}$ and $k_{-4} = 1\times10^{-6}$ s^{-1}, respectively. The vertical lines indicate the times at which the purge gas was changed.

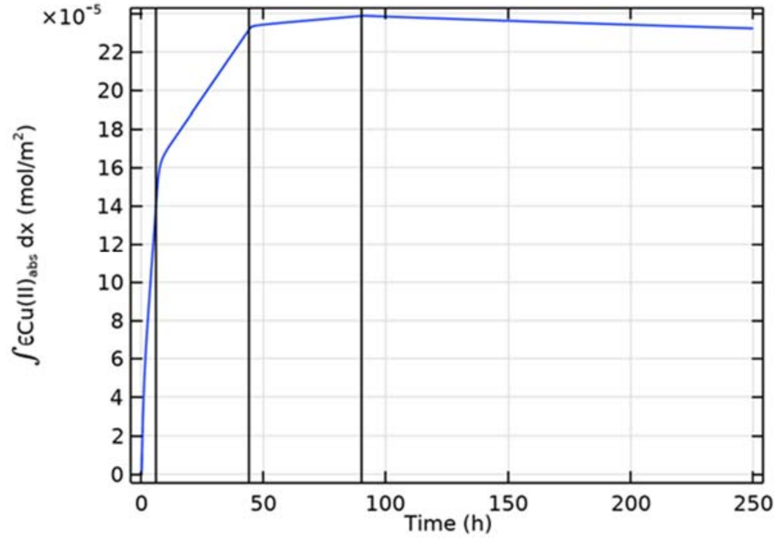

Figure 39: Predicted Time Dependence of the Inventory of Adsorbed Cu(II) for the Step 3d Model for the Default Values of k_4 and k_{-4}. The vertical lines indicate the times at which the purge gas was changed.

The availability of Cu(II) depends on the relative rates of adsorption and desorption. It is apparent that the default adsorption kinetics over estimate the rate of Cu^{2+} adsorption, as evidenced by the rapid decrease in E_{CORR}. Therefore, a sensitivity analysis was performed in which the adsorption and desorption rate constants were varied by 6-10 orders of magnitude (and, in the case of k_{-4}, was set to zero to simulate an irreversible sorption process). The results of the sensitivity were again judged by the visual goodness-of-fit of the time dependence of the predicted and measured E_{CORR} values. The details of the sensitivity analysis are given in Appendix C. Fits to the experimental E_{CORR} data that were judged to be "very good" were obtained for either:

- A value for the adsorption rate constant k_4 of 2×10^{-9} $m^3 \cdot mol^{-1} \cdot s^{-1}$, corresponding to a value of 1000× slower than the default value, or
- A ratio of k_4/k_{-4} of ≤ 0.0002 $m^3 \cdot mol^{-1}$, corresponding to a factor of 10,000× lower than the ratio for the default values of 2 $m^3 \cdot mol^{-1}$.

Figure 40 shows the predicted time dependence for E_{CORR} for the "best-fit" values of k_4 and k_{-4} from the sensitivity analysis compared with the experimental time dependence and for the Steps 2-3c COMSOL models. The time-dependence of the best-fit Step 3d model is similar to that for Steps 3b and 3c. This agreement with these earlier models is not surprising as decreasing the value of k_4 or of the ratio k_4/k_{-4} both have the effect of suppressing the extent of Cu(II) adsorption. This is apparent from a comparison Figure 41 and Figure 39 which shows a factor of 100× lower adsorbed Cu(II) concentration for the best-fit rate constant. In effect, we can only get a good agreement between observed and experimental E_{CORR} values for the kinetic adsorption treatment if we essentially suppress Cu(II) adsorption.

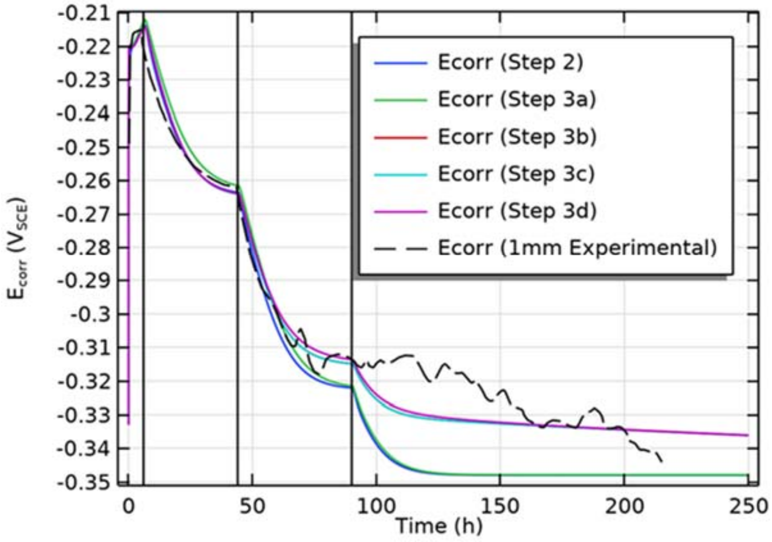

Figure 40: Comparison of the Experimental Corrosion Potential and the Predicted Values for the Step 2, Step 3a, Step 3b, Step 3c, and Step 3d COMSOL Models. The Step 3d model was run using the best-fit values for the adsorption and desorption rate constants based on the sensitivity analysis described in Appendix C of $k_4 = 2\times10^{-9}$ $m^3{\cdot}mol^{-1}{\cdot}s^{-1}$ and $k_{-4} = 1\times10^{-5}$ s^{-1}, respectively. The vertical lines indicate the times at which the purge gas was changed.

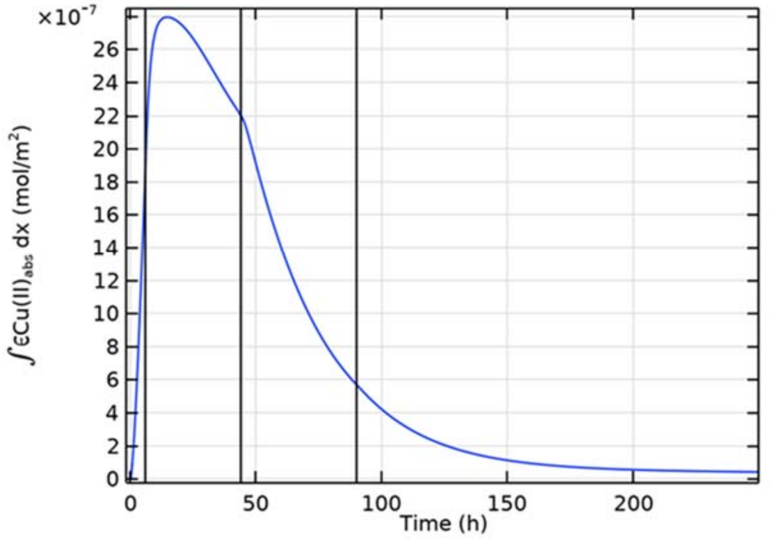

Figure 41: Predicted Time Dependence of the Inventory of Adsorbed Cu(II) for the Step 3d Model for the Best-fit of k_4 and k_{-4} (2×10^{-9} $m^3{\cdot}mol^{-1}{\cdot}s^{-1}$ and 1×10^{-5} s^{-1}, respectively). The vertical lines indicate the times at which the purge gas was changed.

The COMSOL software allows for the use of built-in expressions for various standard or user-defined types of equilibrium adsorption isotherm. Ryan and King (1994) measured the equilibrium adsorption isotherms for Cu(II) on loose and compacted bentonite as a function of temperature in the presence of a saline synthetic groundwater solution ([Cl$^-$] = 0.97 mol/L). The bentonite came from the same batch as that used by King et al. (1995c) for the E_{CORR} measurements being simulated here. A Langmuir isotherm was found to best fit the adsorption behaviour for loose clay and a Freundlich isotherm fitted the data for compacted clay (see Appendix C for more details).

Figure 42 and Figure 43 compare the experimental E_{CORR} values with those predicted using the Step 3d COMSOL model for Langmuir and Freundlich isotherms, respectively. While the Langmuir isotherm produces a poor fit to the experimental data (Figure 42), the Freundlich isotherm results in a significantly better fit (Figure 43).

It is not clear why the Freundlich isotherm should produce a better fit to the experimental E_{CORR} values than the Langmuir isotherm. Figure 44 shows the predicted porewater Cu^{2+} and adsorbed Cu(II) concentration profiles for the Langmuir, from which it is apparent that only a small fraction of the total available adsorption sites are occupied. Under such conditions, the Langmuir isotherm should approximate a linear isotherm, in which the adsorbed concentration is proportional to the dissolved (porewater) Cu^{2+} concentration. The Langmuir isotherm is given by (Shaw 1970)

$$\frac{s}{s_{max}} = \frac{K_L c}{1 + K_L c} \tag{37}$$

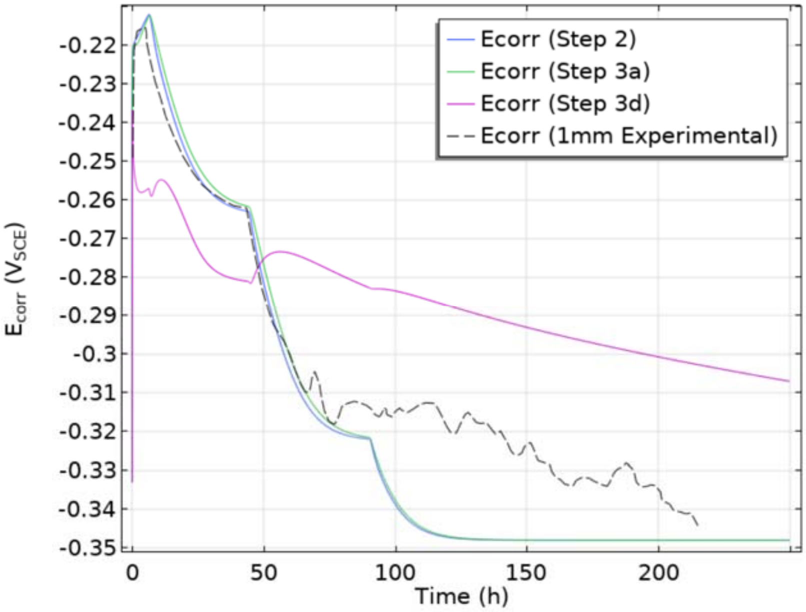

Figure 42: Comparison of the Experimental Corrosion Potential and the Predicted Values for the Step 2, Step 3a, and Step 3d COMSOL Models. The Step 3d model was run using an equilibrium Langmuir isotherm to describe Cu(II) sorption.

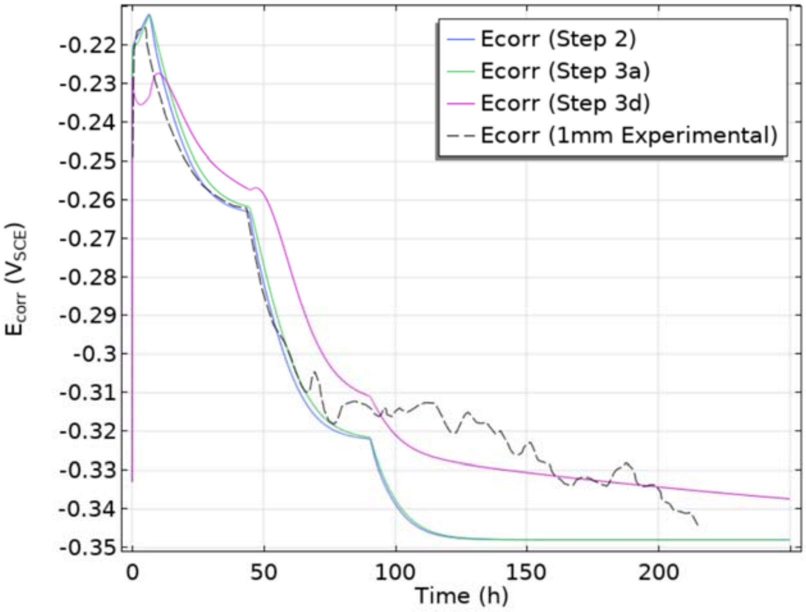

Figure 43: Comparison of the Experimental Corrosion Potential and the Predicted Values for the Step 2, Step 3a, and Step 3d COMSOL Models. The Step 3d model was run using an equilibrium Freundlich isotherm to describe Cu(II) sorption.

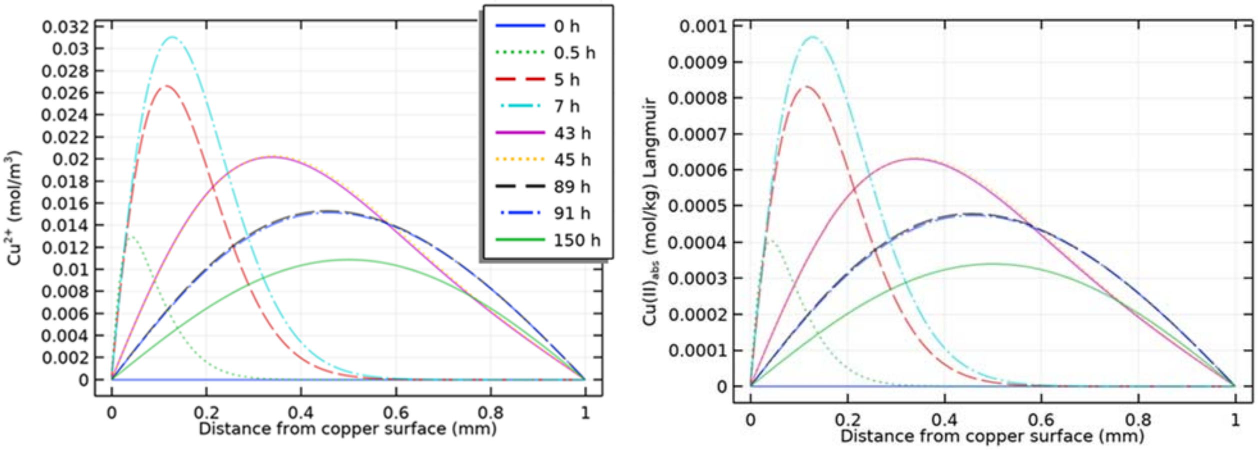

(a) Dissolved Cu^{2+} **(b) Adsorbed Cu(II)**

Figure 44: Comparison of the Predicted Concentration Profiles for Dissolved and Adsorbed Cu(II) for the Step 3d Model with a Langmuir Adsorption Isotherm. Profile times apply to both figures.

where s and s_{max} are the sorbed and maximum sorbed concentrations, respectively, c is the concentration of dissolved adsorbate, and K_L is the Langmuir constant. At low adsorbate concentrations

$$\frac{s}{c} = K_L s_{max} \tag{38}$$

and the adsorption isotherm is linear. The linear nature of the predicted sorption behaviour is evident from the identical shapes of the dissolved and adsorbed copper concentrations in Figure 44.

The Freundlich isotherm is given by

$$S = K_F c^{1/n} \tag{39}$$

where K_F is the Freundlich constant and n is a constant. The Freundlich isotherm was originally developed as an empirical fit to adsorption data, but it can be shown to have a theoretical basis if the heat of adsorption varies with surface coverage. Alternatively, the Freundlich isotherm can be considered to be the sum of a number of Langmuir isotherms (Shaw 1970).

Figure 45 shows the predicted porewater and adsorbed Cu(II) concentrations for the Step 3d model with a Freundlich isotherm. Unlike the similarity of the shape of the corresponding plots for the Langmuir isotherm (Figure 44), the shapes of the two sets of curves are not the same for the Freundlich isotherm, indicating that the adsorption behaviour is not linear, even at these low surface coverages.

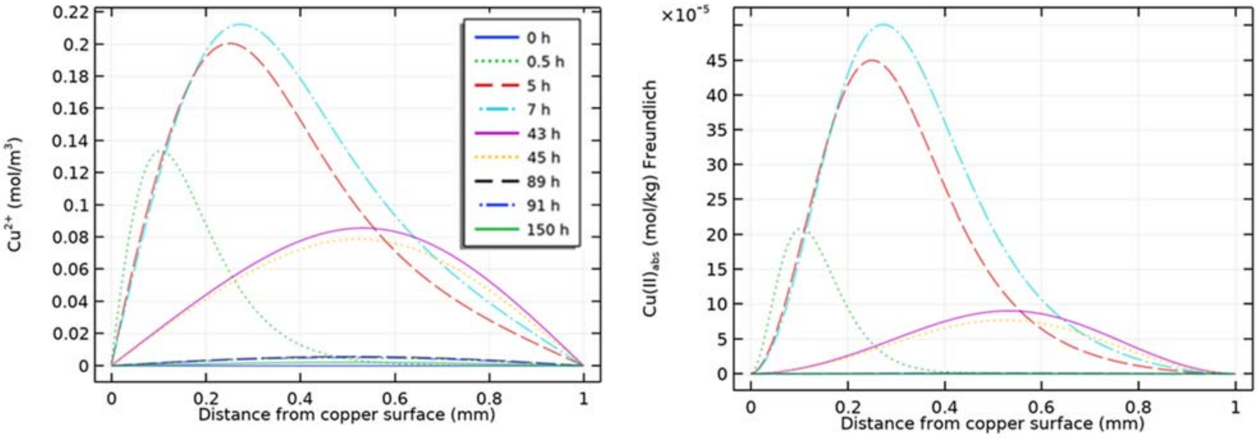

(a) Dissolved Cu^{2+} **(b) Adsorbed Cu(II)**

Figure 45: Comparison of the Predicted Concentration Profiles for Dissolved and Adsorbed Cu(II) for the Step 3d Model with a Freundlich Adsorption Isotherm. Profile times apply to both figures.

Figure 46 shows a comparison of the Langmuir and Freundlich isotherms for the adsorption of Cu^{2+} on Avonlea bentonite based on the data of Ryan and King (1994) for the range of dissolved copper concentrations relevant to the Step 3d model. These data confirm the linear nature of the Langmuir isotherm, but also show considerably more adsorbed copper compared with the Freundlich isotherm. This is confirmed by a comparison of the dissolved and adsorbed copper concentration profiles from the Step 3d model for the two isotherms (Figure 47). The Freundlich isotherm (dashed curves) results in higher dissolved Cu^{2+} concentrations and lower adsorbed amounts than the Langmuir isotherm (solid curves). The maximum adsorbed Cu(II) concentration for the Freundlich isotherm is equivalent to only approximately 0.1% of the CEC.

While the different isotherms affect the distribution of cupric species throughout the clay layer, the effect on E_{CORR} is determined by the concentration of dissolved Cu^{2+} and/or the Cu^{2+} concentration gradient at the copper surface. Figure 48 shows a comparison of the time dependence of both the interfacial $[Cu^{2+}]$ and of the concentration gradient for the Freundlich and Langmuir isotherms. For times up to 60 hrs, both the interfacial concentration and concentration gradient are higher for the Freundlich isotherm than the corresponding values for the Langmuir isotherm, corresponding to the period that the E_{CORR} for the Freundlich isotherm is more-positive than that for the Langmuir model (compare Figure 42 and Figure 43). At longer times the Langmuir interfacial concentrations and concentration gradients are higher (Figure 48) and the E_{CORR} becomes more-positive than for the Freundlich isotherm model. Thus, it is apparent that E_{CORR} is dependent on the interfacial $[Cu^{2+}]$ (or, possibly, the concentration gradient), but it is not clear why the relative values for the two isotherms should change mid-way through the experiment.

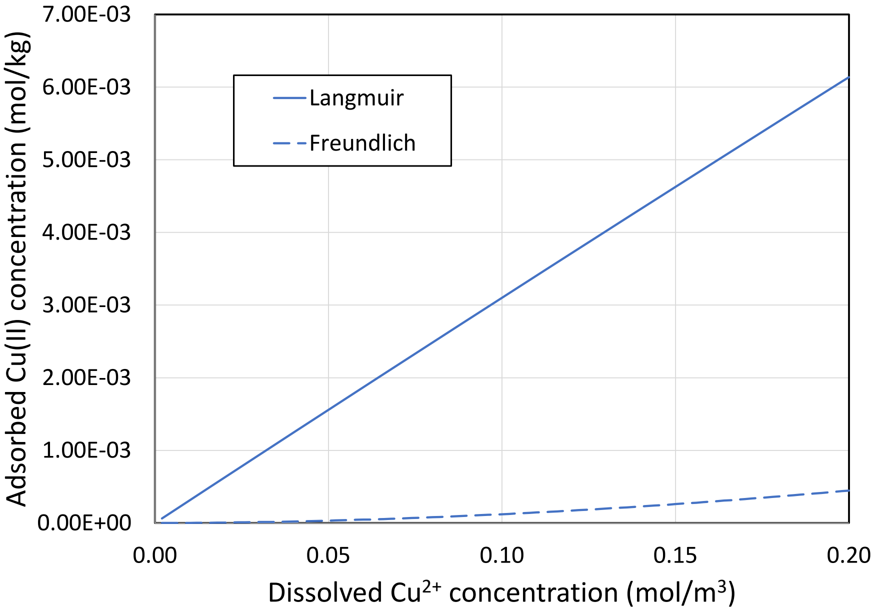

Figure 46: Comparison of the Langmuir and Freundlich Adsorption Isotherms for the Dissolved Cu^{2+} Concentration Range Applicable to the Step 3d Model.

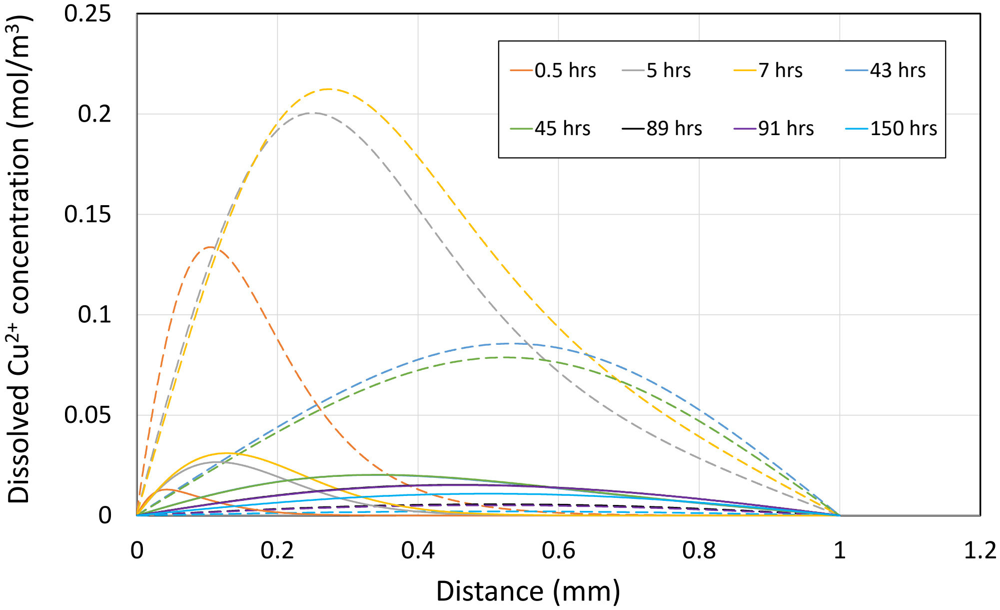

(a) Comparison of dissolved Cu^{2+} concentration profiles

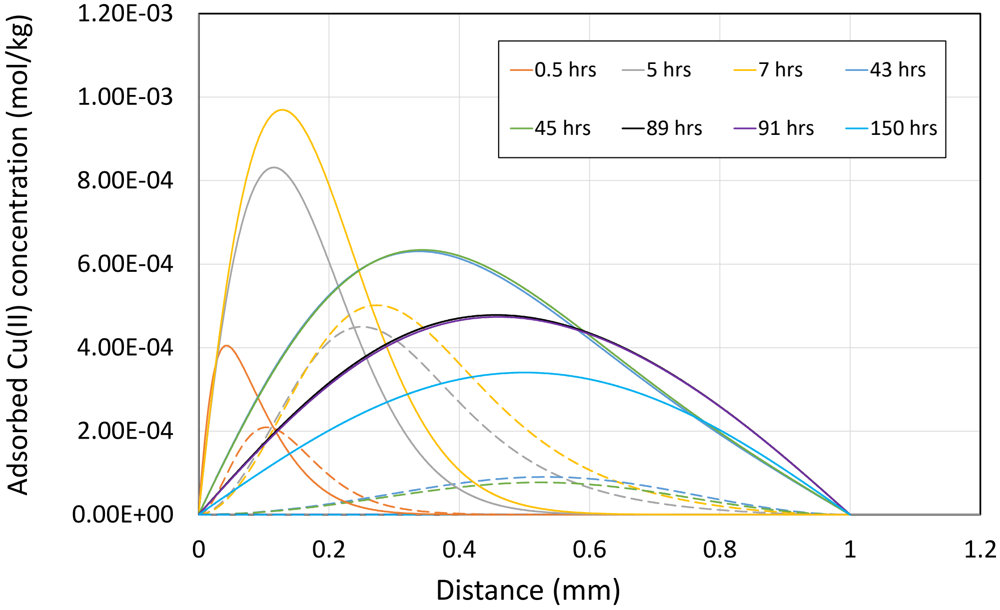

(b) Comparison of adsorbed Cu(II) concentration profiles

Figure 47: Comparison of the Predicted Dissolved and Adsorbed Cu(II) Concentration Profiles for Langmuir and Freundlich Isotherms for Various Times for the Step 3d COMSOL Model. Langmuir isotherm – solid curves, Freundlich isotherm – dashed curves. Based on data from Figure 44 and Figure 45.

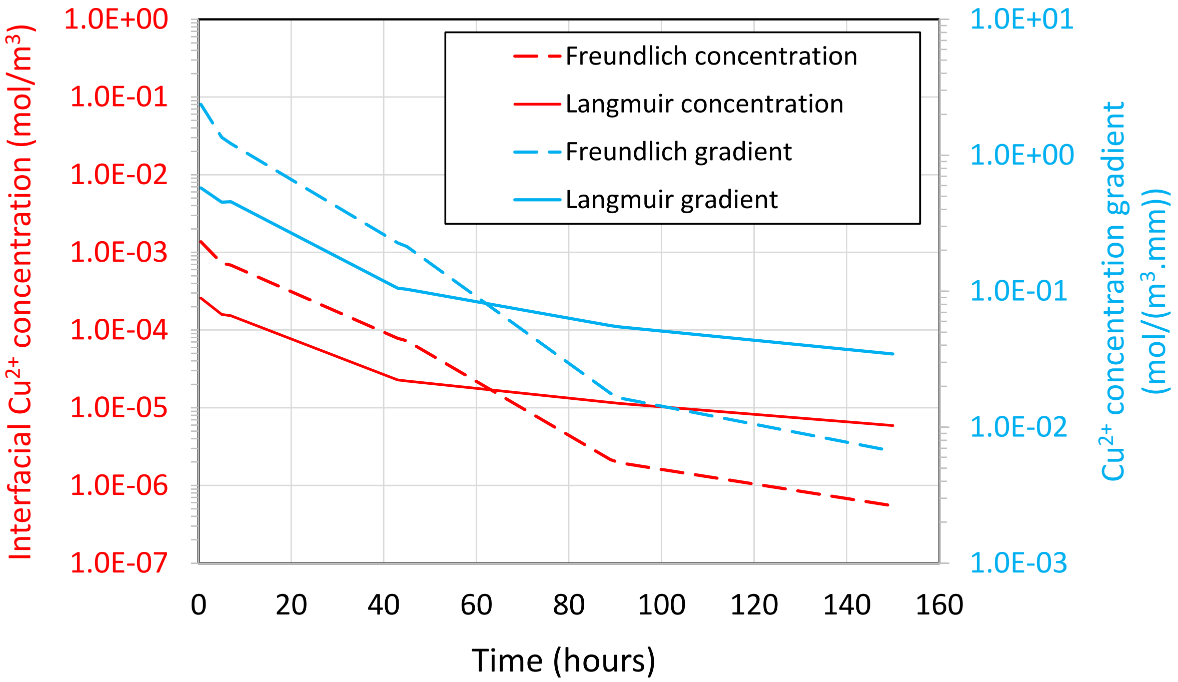

Figure 48: Comparison of the Predicted Time Dependence of the Interfacial Cu^{2+} Concentration (in red) and of the Interfacial Cu^{2+} Concentration Gradient (in blue) for Freundlich and Langmuir Isotherms for the Step 3d Model. Freundlich isotherm – dashed lines, Langmuir isotherm – solid lines. The interfacial Cu^{2+} concentration gradient was determined from the points within a distance of 0.01 mm of the copper surface.

4.1.7 Step 3e Aerobic Respiration

The next change to the model was the incorporation of a kinetic expression for the microbial aerobic respiration of O_2 (Appendix A.3.5)

$$O_2 \xrightarrow{\text{aerobes}} 2H_2O \tag{40}$$

and described by an assumed first-order kinetic expression (rate constant k_9, Figure 3). If microbial activity is feasible in the compacted bentonite, aerobic respiration would act as a sink for O_2 in competition with the corrosion reaction itself. The default value of k_9 (2.2×10^{-9} s^{-1}) is equivalent to a half-life for dissolved O_2 of 10 yrs and was selected based on observations of O_2-loss from a large-scale *in situ* experiment (see Appendix B). Development of the Step 3e model was based on the version of the Step 3d model with a kinetic treatment of Cu(II) adsorption/desorption with the optimized values for k_4/k_{-4} used for the simulation shown in Figure 40.

Figure 49 shows the prediction for the Step 3e model, superimposed on both the experimental E_{CORR} values and the predictions from the Steps 2-3d models. The predicted time dependence of E_{CORR} for the Step 3e model is indistinguishable from that for the prior Steps 3b-3d. The absence of any effect of including aerobic respiration is not surprising since the value of the corresponding rate constant is so small that this reaction would have an insignificant effect on the O_2 concentration within the timescale of the experiment. Furthermore, microbial activity of any sort would not generally be expected to occur in highly compacted bentonite, although the relatively low dry density of the clay layer in the experiment (1.2 g/cm^3, Section 3.4.1) would not have been sufficient to prevent all microbial activity in this case.

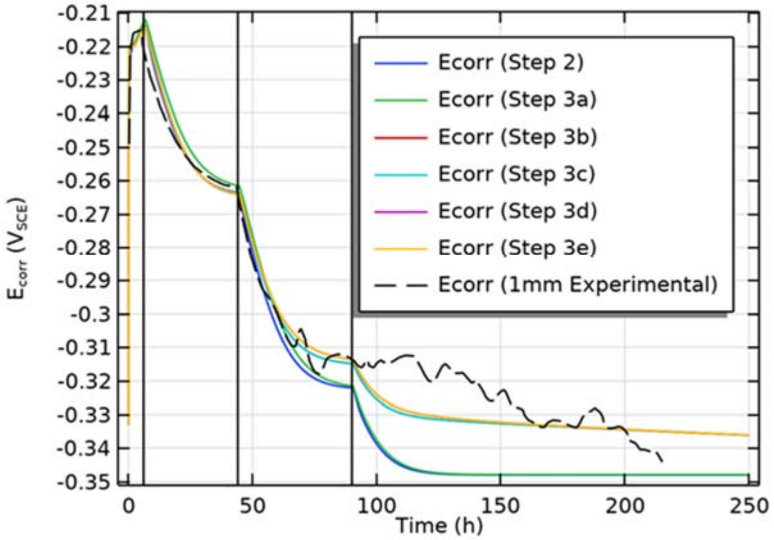

Figure 49: Comparison of the Experimental Corrosion Potential and the Predicted Values for the Step 2, and Step 3a to Step 3e COMSOL Models. The Step 3e model prediction is indistinguishable from that for Steps 3b, 3c, and 3d. The vertical lines indicate the times at which the purge gas was changed.

4.1.8 Step 3f Reactions Involving Iron(II) Species

The last stepwise modification to the reaction scheme for the COMSOL model involves the incorporation of reactions involving Fe(II), including (Appendix A.3.6):

- Dissolution of an Fe(II)-containing phase present in the bentonite, such as pyrite (FeS_2) or siderite ($FeCO_3$).
- Redox reaction between the released Fe(II) and O_2.
- Redox reaction between the released Fe(II) and Cu^{2+}.
- Precipitation of a secondary Fe(II)-containing phase if the concentration of dissolved Fe(II) exceeds the solubility of the secondary phase in the bentonite porewater.

The kinetic expressions for these processes are described in Appendix A.3.6 and the corresponding empirical rate constants are given in Appendix B.

Although the reactions were implemented in the Step 3f model, it was assumed that no Fe(II)-containing accessory minerals were present in the Avonlea bentonite. Hence, the time-dependent E_{CORR} for Step 3f is exactly the same as for Step 3e (Figure 50.

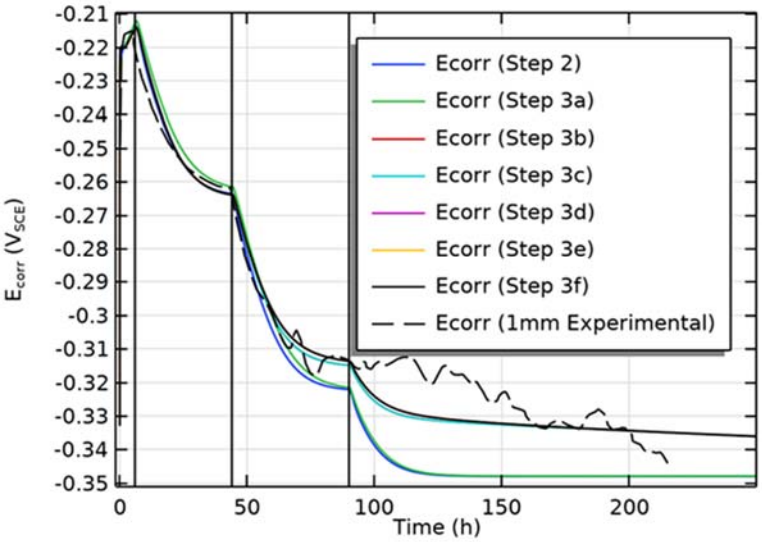

Figure 50: Comparison of the Experimental Corrosion Potential and the Predicted Values for the Step 2, and Step 3a to Step 3f COMSOL Models. The Step 3f model prediction is indistinguishable from that for Steps 3b-3e. The vertical lines indicate the times at which the purge gas was changed.

4.2 VALIDATION AGAINST THE CONVENTIONAL CCM

At an early stage of the development of the COMSOL model, a comparison was made between the results from Steps 2 and 3a of the stepwise COMSOL model and a version of the conventional CCM code modified to simulate the 1-mm-clay electrode experiment. At the time of this comparison, some of the input parameter values differed slightly from those used in the subsequent COMSOL validation steps described above, specifically:

- The activity coefficient for Cl^- ions was taken to be 0.7 instead of 0.657.
- A total porosity of 0.41 was used instead of 0.52.
- There were minor differences in the timing of the transitions in O_2 purge gas and of the dissolved O_2 concentration for the simulated experiment.

For the purposes of this inter-model validation exercise, both the COMSOL and conventional CCM models were run using these slightly modified values. All other input parameter values were the same as those used for the validation of the stepwise COMSOL model against the experimental data described above.

In general, the agreement between the predictions from the two models was very good. The validation was based on a visual comparison of the time dependence of (i) E_{CORR}, (ii) the different current densities and charge densities, (iii) the inventories of O_2 and the different dissolved copper species, and (iv) the integrated flux of O_2 across the right-hand boundary. In addition the concentration profiles for the different species at different times were compared. As shown below, the agreement between the COMSOL and conventional CCM models was especially good for Step 3a, with poorer agreement for Step 2.

Figure 51 shows a comparison of the predicted time dependence of E_{CORR} for the 1-mm-clay electrode experiment (experimental data not shown) for the conventional and COMSOL versions of the CCM. The agreement between the two versions of the CCM is excellent for both the Step 2 and Step 3a models, with the only discrepancies occurring at times less than 2 minutes for Step 3a and less than 2 hours for Step 2. These short-term differences are most likely the result of differences in the estimation of interfacial gradients of electroactive species using finite-difference and finite-element techniques. At very short times, these gradients are very steep as the initially uniform distribution of O_2 is depleted at the interface and dissolved copper is produced. In order to capture these steep concentration gradients with sufficient

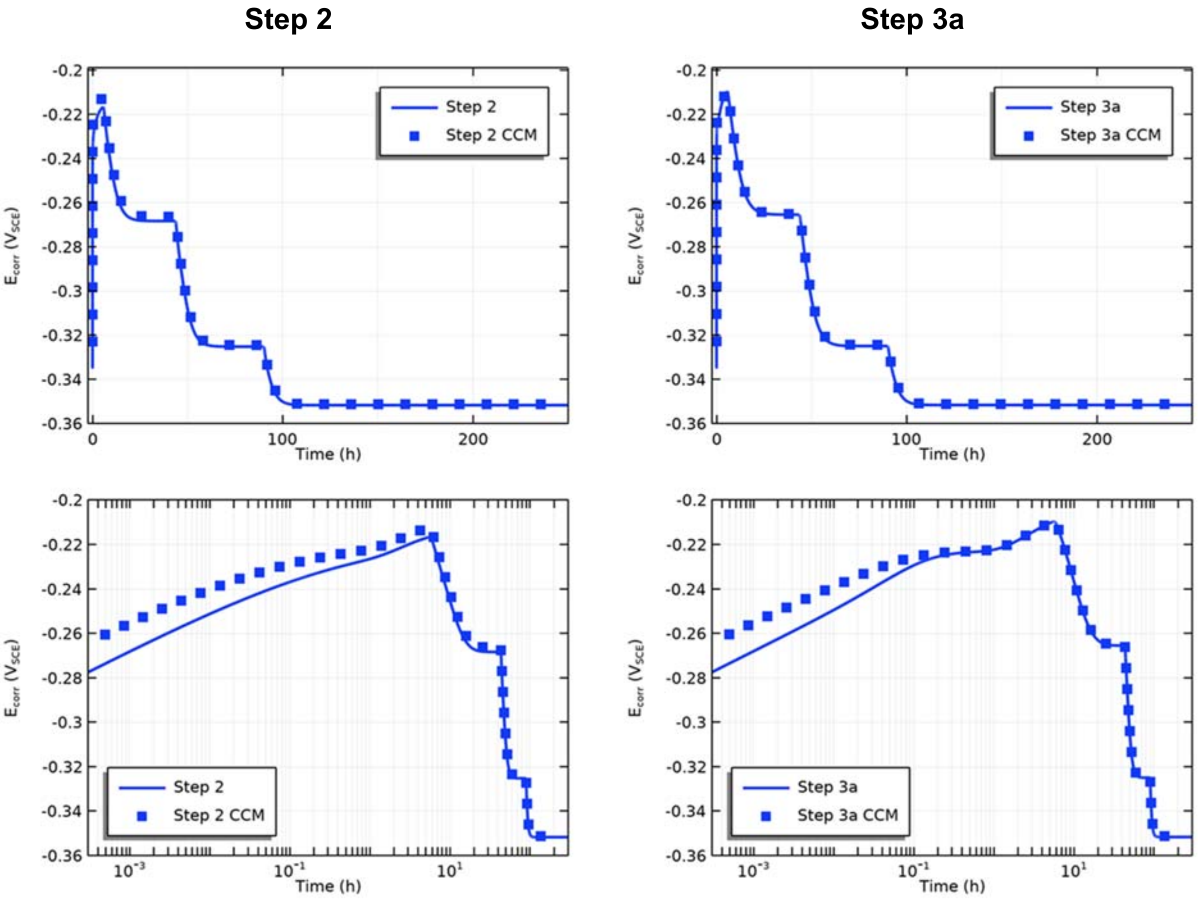

Figure 51: Comparison of the Predicted Time Dependence of the Corrosion Potential E_{CORR} Using the Conventional and COMSOL Versions of the CCM for the Step 2 (Left) and Step 3a (Right) Models on Linear and Logarithmic Time Scales. Conventional CCM – symbols, COMSOL CCM – solid line.

accuracy, the interfacial grid spacing for the conventional CCM is typically of the order of 4×10^{-8} m, whereas the element size for the COMSOL model is 6.7×10^{-7} m. As the steepness of the concentration gradients decrease with time, the effect of the difference in grid spacing/element size does not affect the accuracy of the prediction to the same degree and there is agreement between the two numerical solution methods.

This discrepancy at short times between the predictions from the conventional and COMSOL versions of the CCM is also seen in the predicted current densities (Figure 52, upper). However, the discrepancy seems to be mainly associated with the O_2 reduction reaction, because if the reduction of Cu^{2+} is the primary cathodic reaction, as in the Step 3a model, there is better agreement between the two versions of the CCM. This agreement is most clearly seen in the time dependence of the charge density (Figure 52, lower), where there is a discrepancy of up to approximately 10% for both the anodic and cathodic charge densities for the Step 2 model, but much better agreement for the Step 3a model for both the cathodic (reduction of Cu^{2+}) and anodic (dissolution as $CuCl_2^-$) reactions.

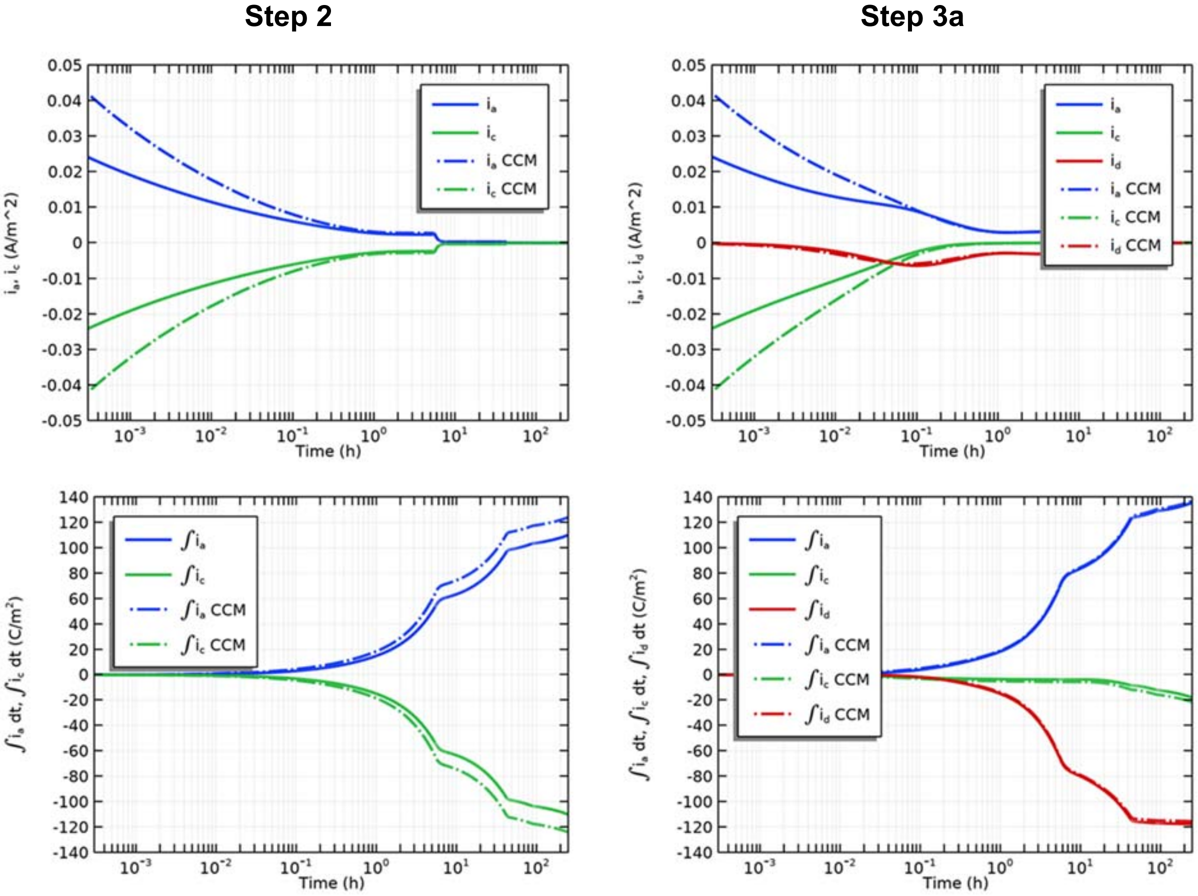

Figure 52: Comparison of the Predicted Time Dependence of the Current Densities (Upper) and Charge Densities (Lower) Using the Conventional and COMSOL Versions of the CCM for the Step 2 (Left) and Step 3a (Right) Models. Conventional CCM– dashed curves, COMSOL CCM – solid curves.

The better agreement between the two versions of the CCM for the Step 3a model is also apparent from the time dependent inventories of O_2 and dissolved copper (Figure 53). These inventories are calculated from the amount initially present (in the case of O_2) and the net fluxes of the respective species across the left-hand (electrode surface) and right-hand (clay/solution interface) boundaries. The agreement between the conventional and COMSOL models is good for both O_2 and total dissolved copper for Step 3a, but again there is a discrepancy for the Step 2 model of up to 10%. Comparison of the time dependence of the inventories of O_2 and dissolved Cu for the Step 2 model shows that the conventional CCM predicts a faster consumption of O_2 than the COMSOL model, which in turn leads to a faster production of dissolved copper. Because the anodic current density is constrained by the mixed-potential principle to be equal to the cathodic current density, an increased rate of O_2 reduction will automatically lead to an increased rate of copper dissolution. Thus, the apparent discrepancies for both O_2 and dissolved copper for the Step 2 model could both result from the same source; namely, a difference in the estimation of the O_2 flux at the copper surface between the conventional and COMSOL CCM's. These differences are not observed for the Step 3a model because the reduction of Cu^{2+} is the primary cathodic reaction, with the production of Cu^{2+} occurring away from the copper surface. Hence, the estimation of the flux of Cu^{2+} to the copper surface is less sensitive to the grid spacing at the left-hand boundary (i.e., the copper surface).

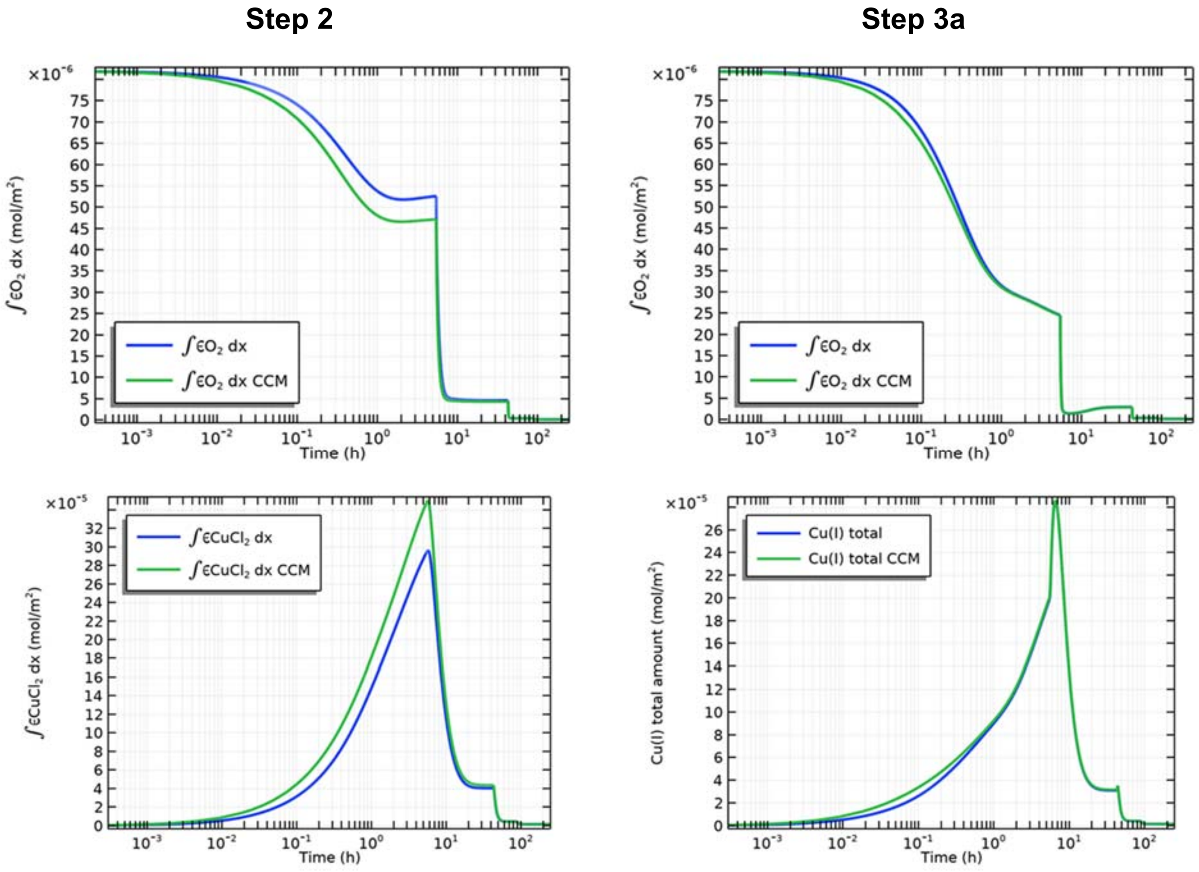
Step 2

Step 3a

Figure 53: Comparison of the Predicted Time Dependence of the Oxygen (Upper) and Total Copper (Lower) Inventories Using the Conventional and COMSOL Versions of the CCM for the Step 2 (Left) and Step 3a (Right) Models. Conventional CCM– green curves, COMSOL CCM – blue curves.

In addition to differences between the conventional and COMSOL models due to the treatment of the left-hand boundary, there are also differences in the extent of mass transport across the right-hand boundary, i.e., the clay/solution interface. Figure 54 shows a comparison of the cumulative net flux of O_2 (upper) and of the time-dependent flux of dissolved copper (lower) across this right-hand boundary for the two versions of the CCM. Again, comparisons are shown for the Step 2 (left) and Step 3a (right) models. There is a significant discrepancy in the cumulative flux of O_2 between the two CCM versions for both Steps 2 and 3a, with more O_2 predicted to enter the clay layer for the COMSOL model. (A negative cumulative flux indicates that O_2 enters the clay layer during the course of the simulation). The absolute difference in the cumulative fluxes for the Step 2 and Step 3a models are similar, but more O_2 enters the clay layer for the Step 3a model because the consumption of O_2 by the homogeneous oxidation of $CuCl_2^-$ to Cu^{2+} maintains a higher O_2 concentration gradient which acts as a driving force for O_2 entry. The agreement between the models is better for the time-dependence flux of dissolved copper out of the clay layer, with excellent agreement in the case of the Step 3a model.

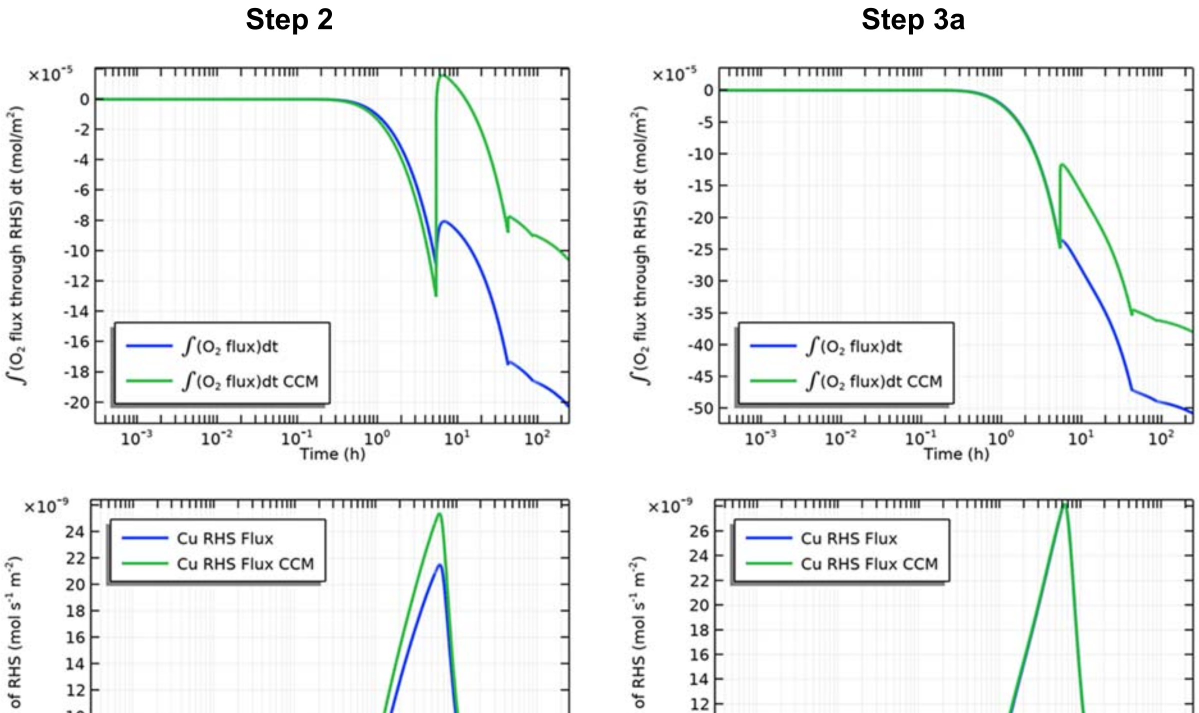

Figure 54: Comparison of the Predicted Time Dependence of the Cumulative Flux of Oxygen (Upper) and Instantaneous Flux of All Copper Species (Lower) Across the Clay/Solution Boundary Using the Conventional and COMSOL Versions of the CCM for the Step 2 (Left) and Step 3a (Right) Models. Conventional CCM– green curves, COMSOL CCM – blue curves.

Figure 55 shows a comparison of the concentration profiles for O_2, $CuCl_2^-$, and (for the Step 3a) model Cu^{2+} at various selected times for the two versions of the CCM. Excellent agreement is observed between the conventional and COMSOL models for Step 3a, with poorer agreement for Step 2. The discrepancies for Step 2 are consistent with those described above for the current and charge densities (Figure 52). The conventional CCM predicts higher current densities, which results in lower O_2 concentrations (as O_2 is consumed in the cathodic reaction) but higher dissolved Cu concentrations (as $CuCl_2^-$ is the product of the anodic reaction). Thus, all of the discrepancies for the Step 2 model stem from the same cause. Furthermore, the fact that discrepancies are smaller for the Step 3a model suggests that the root cause of the disagreement is a difference in the rate of the cathodic reduction of O_2, which is only a minor contributor to the overall cathodic current density for Step 3a but is the only oxidant for Step 2.

Given these discrepancies for the Step 2 model, the question is why (after the first several hours) are the predicted E_{CORR} values in good agreement (Figure 51). The E_{CORR} is determined by the relative kinetics of the anodic and cathodic reactions which, due to the mixed-potential requirement that the sum of the currents is zero, are coupled. Thus, for the Step 2 model, if the rate of O_2 reduction is higher for a given model, then so too is the rate of anodic dissolution. Thus, the relative rates remain the same and the value of E_{CORR} is unchanged.

It is apparent from the discussion above that the discrepancies observed between the two models are related to the predicted rates of O_2 reduction. In the presence of compacted, saturated bentonite, the overall rate of O_2 reduction is likely to be transport controlled, and the predicted rates will be dependent on the interfacial flux at the copper surface. Thus, the predicted currents will depend on how accurately the O_2 concentration gradient is predicted which, in turn, depends on the discretization at the interface (either the grid spacing for the conventional CCM or the element size for the COMSOL model).

The effect of the size of the COMSOL elements or conventional CCM grid spacing on the O_2 flux across the right-hand boundary was investigated in some detail. The conventional CCM was run using both the usual variable grid spacing, with smaller spacings at the two interfaces, and with a constant grid spacing of 10^{-7} m (Figure 56). Similarly the COMSOL model was run with constant element sizes of either 6.7×10^{-7} m or 4×10^{-8} m, the latter value corresponding to the smallest grid spacing used for the conventional CCM at either interface. Figure 57 shows the effect of grid/element discretization on the predicted cumulative O_2 flux across the clay/solution boundary for the Step 2 model. While the grid spacing has a significant effect on the predicted cumulative O_2 flux for the conventional CCM, there is no effect of a 17-fold change in element size for the COMSOL version of the CCM. The absence of any effect of spatial discretization is generally an indication of the reliability of the results, suggesting the COMSOL predictions are more reliable than those of the conventional CCM.

This inter-model comparison suggests, however, that careful attention has to be paid to the discretization of the mesh size for future COMSOL models, especially at interfaces between material as well as at the external boundaries.

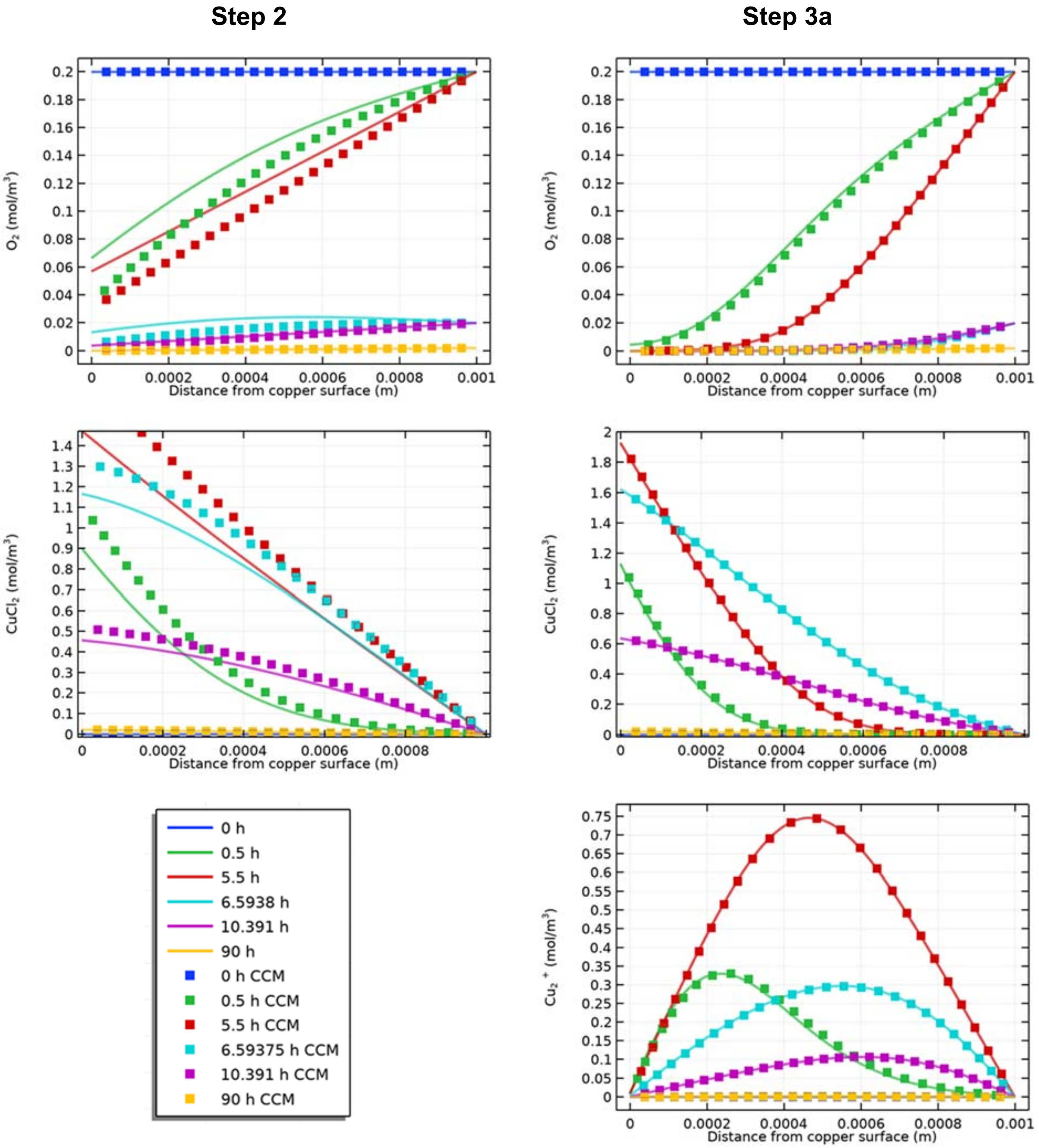

Figure 55: Comparison of the Predicted Concentration Profiles in the Clay Layer for Oxygen (Upper), $CuCl_2^-$ (Middle), and Cu^{2+} (Lower) Using the Conventional and COMSOL Versions of the CCM for the Step 2 (Left) and Step 3a (Right) Models. Conventional CCM– symbols, COMSOL CCM – solid line. Profiles correspond to the times shown in the legend in the lower left.

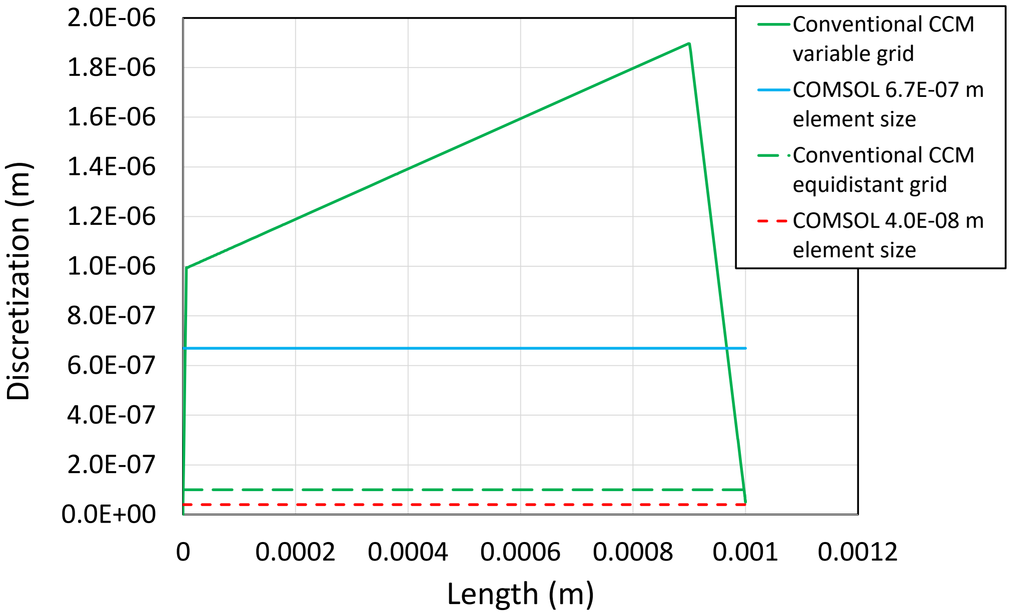

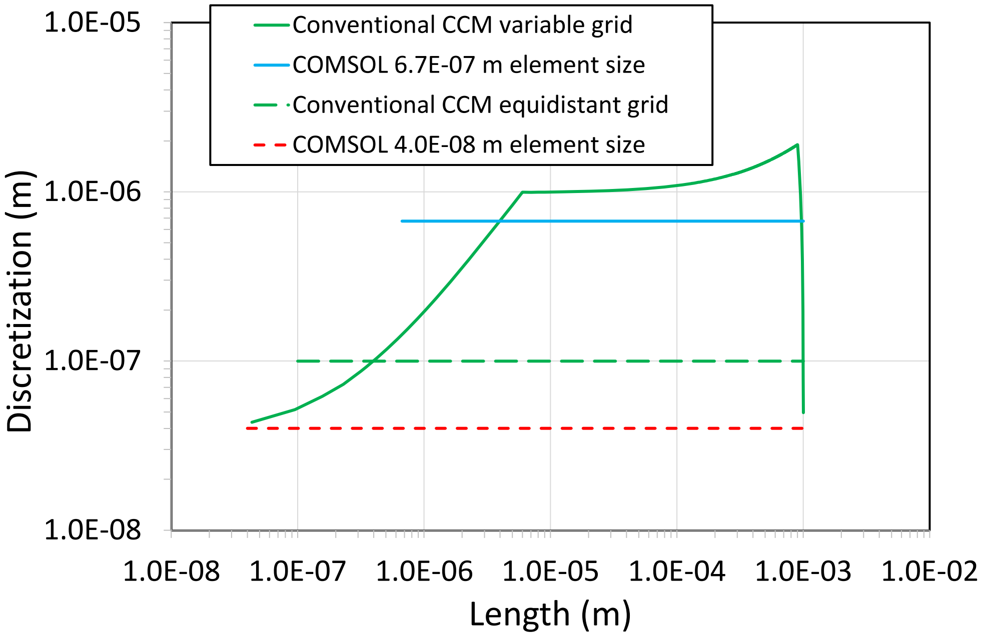

Figure 56: Comparison of the Variation in Discretization with Distance from the Copper Surface for the Grid Spacing of the Conventional CCM and the Element Size of the COMSOL CCM. The data are shown on both linear (upper) and logarithmic (lower) length scales.

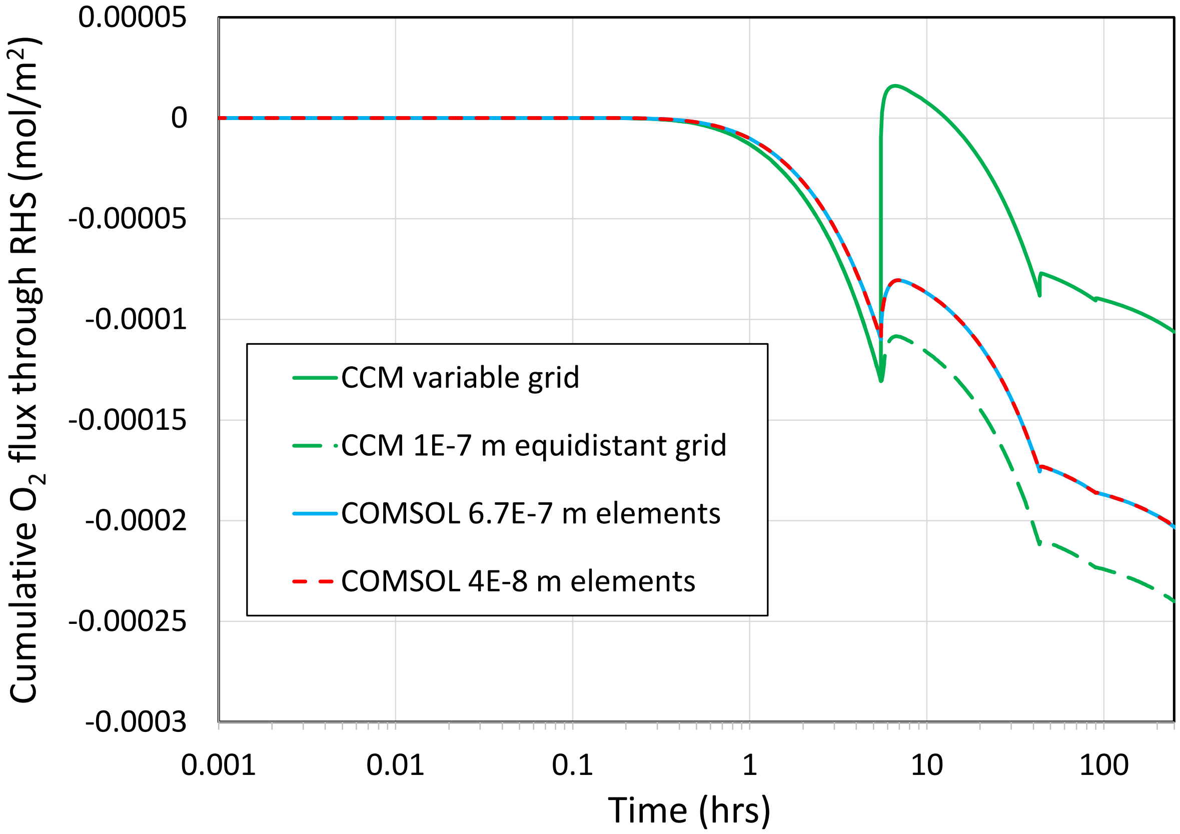

Figure 57: Effect of Grid Spatial or Element Size for the Conventional and COMSOL Versions of the CCM on the Cumulative Flux of O_2 Across the Right-hand Boundary for the Step 2 Model.

4.3 VALIDATION AGAINST THE 10-mm CLAY LAYER EXPERIMENT

Following the step-wise development of the COMSOL model and the validation against the results of the 1-mm-clay-layer experiment, the validated model was then applied to the prediction of the time-dependent E_{CORR} for the 10-mm clay layer. The experiment followed a similar format to the 1-mm experiment described in Section 3.4.1 with periodic changes in the purge-gas composition and ever-decreasing [O_2], except that the experiment lasted approximately 10 times longer because of the longer diffusion distance (King et al. 1995c).

Figure 58 shows a comparison of the measured and predicted E_{CORR} values for the 10-mm clay experiment, with the predictions made on the basis of the simple Step 2 model using the same parameter values as used for the earlier validation for the 1-mm clay experiment. Although the model adequately predicts the initial rise in E_{CORR} and the steady-state value in aerated solution, the predicted rate of decrease in potential once the purge-gas composition is changed is much slower than observed experimentally. The fit to the experimental data is no better for any of the Step 3 sub-models (Figure 59).

It is apparent from Figure 58 and Figure 59 that the predicted E_{CORR} changes too slowly with time, possibly because the effective diffusivities of O_2 and $CuCl_2^-$ (the only two diffusing species for the Step 2 model) are too small. A similarly poor fit was observed for the Step 2 model and the 1-mm clay electrode experiment, on the basis of which the value of the tortuosity factor τ (COMSOL symbol tau) was modified to improve the fit (Section 4.1.2). Figure 60 shows the results of varying the value of tau using the Step 2 model for the 10-mm clay experiment. While larger values of tau do indeed increase the rate of change of the predicted E_{CORR}, none of the values accurately represent the rate of change of E_{CORR} and the steady-state values for the various O_2-containing purge gases. The possibility that the poor correlation is due to multi-dimensional diffusion effects is explored in the next section.

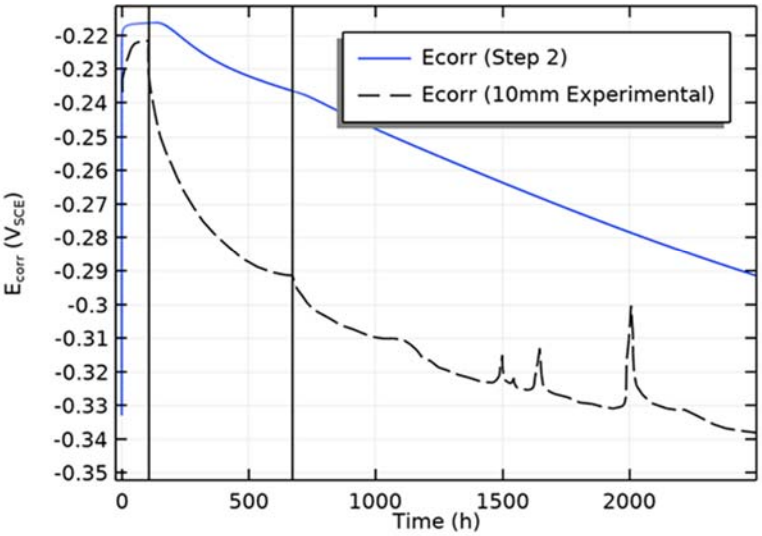

Figure 58: Comparison of the Predicted and Experimental Time Dependences of E_{CORR} for the 10-mm Clay-layer Experiment. Model predictions were made using the Step 2 COMSOL model. The vertical lines indicate the times at which the purge gas was changed.

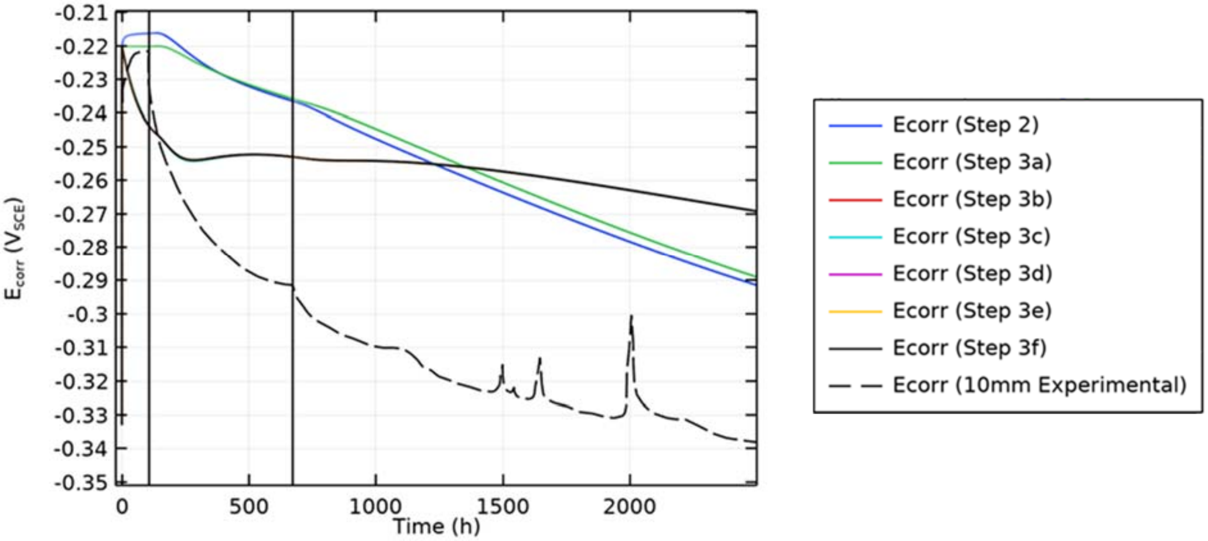

Figure 59: Comparison of the Predicted and Experimental Time Dependences of E_{CORR} for the 10-mm Clay-layer Experiment. Model predictions were made using the Step 2 and Steps 3a to 3f COMSOL models. The predicted curves for the Step 3b to 3f models are coincident. The vertical lines indicate the times at which the purge gas was changed.

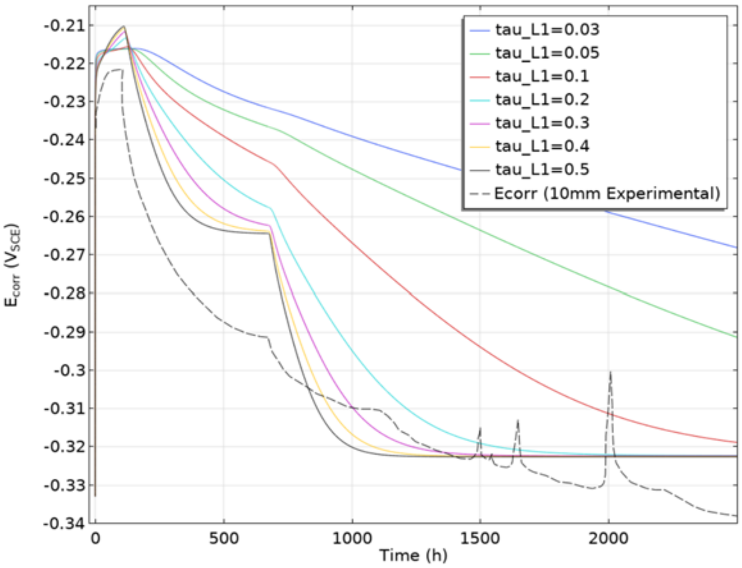

Figure 60: Effect of Tortuosity Value on the Predicted Time Dependence of E_{CORR} for the 10-mm Clay Electrode Experiment Based on the Step 2 COMSOL Model.

Notwithstanding the generally poor correlation between model and experiment in Figure 60, it is interesting that the effective diffusivity that was found to adequately fit the E_{CORR} profiles for the 1-mm clay electrode do not fit the 10-mm clay electrode data. Based on the sensitivity analysis in the figure, the rate of decrease of E_{CORR} observed experimentally is best represented in the model using a tau value of between 0.2 and 0.3. Figure 61 compares the measured and predicted time dependence of E_{CORR}, with predicted values based on the Step 2 model and the "best-fit" value of tau of 0.25. This is a factor of five times larger than the tau of 0.05 fitted to the 1-mm clay electrode data, suggesting that the effective diffusivities for the 10-mm clay layer are larger by the same amount. The question is why should the effective diffusivity be larger for the thicker clay layer. One possibility is that the thicker clay plug was not properly compacted and that the density was lower than that of the smaller, better-compacted, 1-mm clay layer.

It should also be noted that the original steady-state mixed-potential model of King et al. (1995c) could not successfully account for the steady-state E_{CORR} with 2 vol.% O_2/N_2 of -0.291 V_{SCE}, predicting a value of -0.263 V_{SCE} instead. This predicted value from the original steady-state model is identical to that predicted by the Step 2 COMSOL model. The experimental decrease in steady-state E_{CORR} of 68 mV when switching from air to a 2 vol.% O_2/N_2 purge gas is greater than would be predicted theoretically for any combination of anodic and cathodic rate-determining steps, and suggests that some other factor was responsible for the greater-than-expected decrease in E_{CORR}. In that context, no further attempt was made to validate the 1-D COMSOL model against the experimental 10-mm clay electrode data.

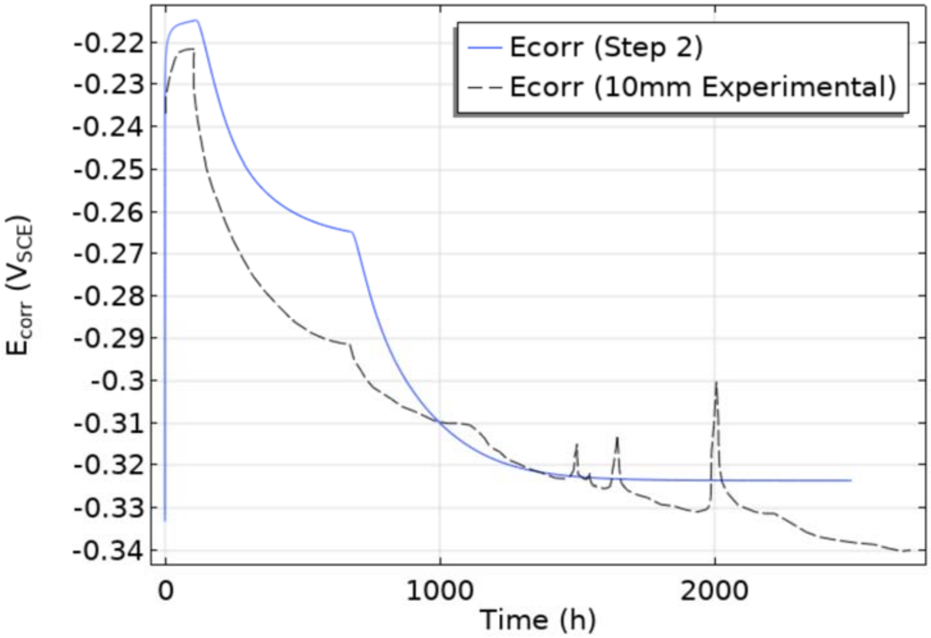

Figure 61: Predicted Time Dependence of E_{CORR} for the 10-mm Clay Electrode Experiment for the Step 2 COMSOL Model and a Value of Tau of 0.25.

4.4 DEVELOPMENT OF 2-D AXISYMMETRIC MODEL

It is apparent from the relatively poorer fit of the model predictions to the experimental data for the 10-mm clay layer experiment compared with that for the 1-mm clay layer, that there is a significant effect of increasing the diffusion path length. In addition to a greater diffusion path length, there may also be differences between the two experiments based on the radial geometry of the electrode. As noted in Section 3.4.1, the diameters of the copper electrode, clay layer, and of the opening to the bulk solution are not the same (Figure 13). The longer diffusive path length of the 10-mm clay electrode may result in significant radial components of the diffusive flux. In order to explore this possibility, 2-D axisymmetric versions of the Step 2 and Step 3a models were developed.

4.4.1 1-mm Clay Layer Experiment

4.4.1.1 E_{CORR} and Average Current and Charge Densities

The dimensionality of the COMSOL model has relatively little effect on the time dependence of the E_{CORR} (Figure 62). The 2-D axisymmetric model predicts a slightly faster attainment of steady state, but the differences between the 1-D and 2-D models for both Steps 2 and 3a are minor. A more significant difference is observed between the predicted average current and charge densities, with the 2-D models predicting 20-30% higher charge densities than the 1-D models by the end of the experiment (Figure 63). These current and charge densities are averaged over the entire electrode surface (or, more correctly, over the entire radius of the electrode for the 2-D axisymmetric model). Figure 63(b) also shows the sums of the average current densities for the two models which, apart from some fluctuating values at short times, are <<10^{-9} A/m^2 or less than 0.0001-0.01% of the individual current densities.

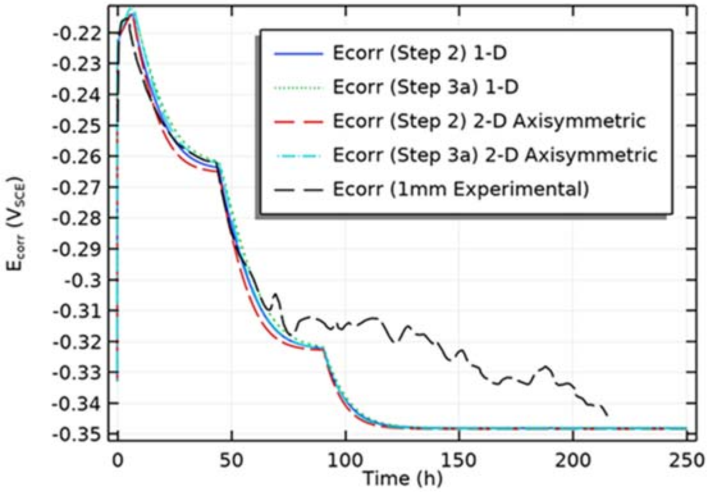

Figure 62: Comparison of the Predicted Time Dependence of E_{CORR} for the 1-mm Clay Electrode Experiment for the 1-D and 2-D Axisymmetric Versions of the Step 2 and Step 3a Models.

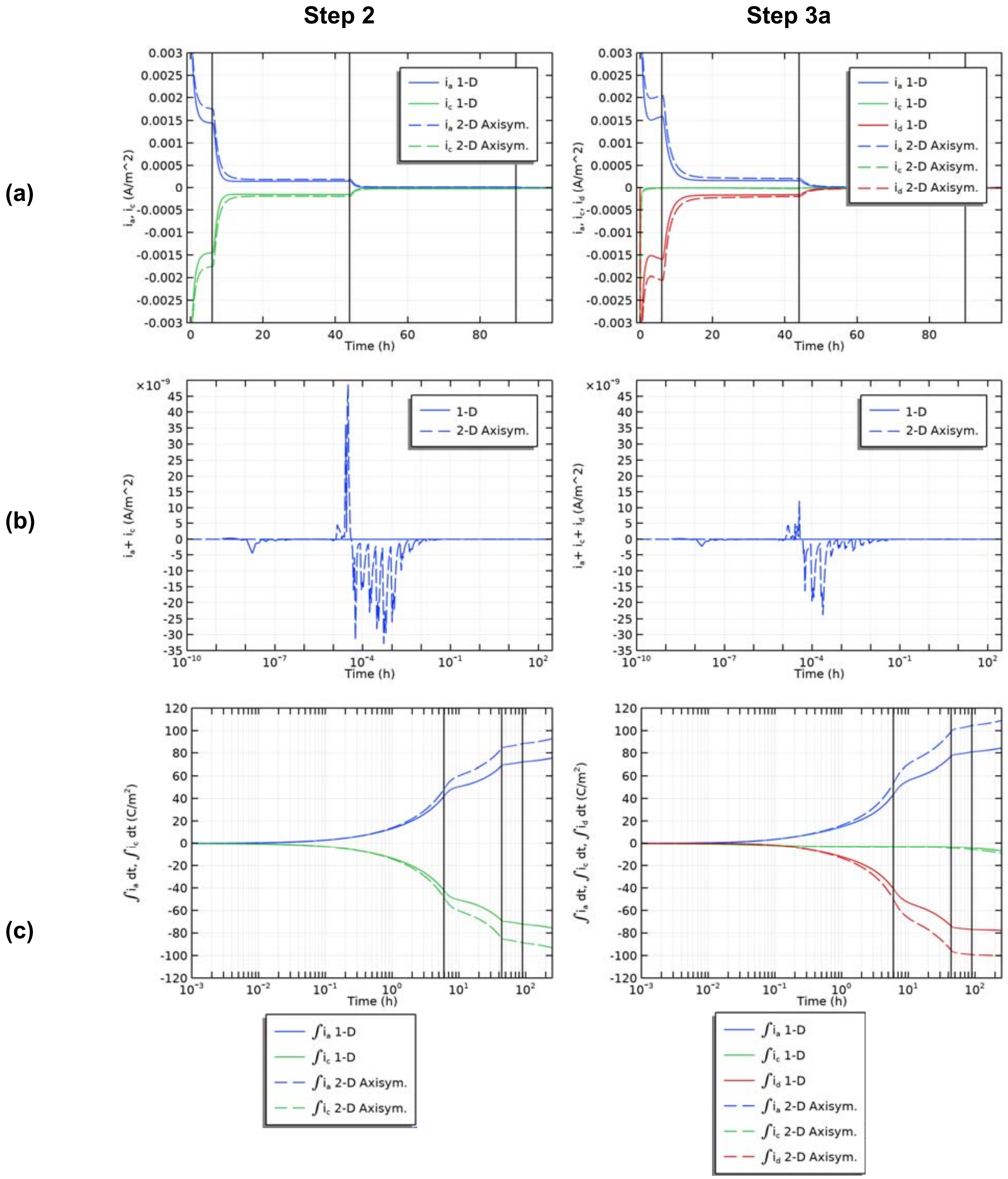

Figure 63: Comparison of the Predicted Time Dependence of (a) the Average Current Densities, (b) the Sum of the Average Current Densities, and (c) Charge Densities for the 1-mm Clay Electrode Experiment for the 1-D and 2-D Axisymmetric Versions of the Step 2 and Step 3a Models.

4.4.1.2 Concentration Profiles

Figure 64 to Figure 66 show the distributions of dissolved O_2, $CuCl_2^-$, and Cu^{2+}, respectively, in the (half) clay layer for the Steps 2 and 3a models, for the three times corresponding to the change of purge gas composition and at the end of the experiment. The O_2 concentration profiles are similar for the two models, suggesting that there is little oxidation of Cu(I) to Cu(II) around the periphery of the clay disc in the Step 3a model. The greatest depletion of O_2 is clearly close to the copper disc, although O_2 is also consumed (or is lost by diffusion out of the clay layer) further away from the centre. The diameter of the opening in the Plexiglas electrode holder was 16 mm and a steep O_2 concentration gradient is observed at a radius of 0.008 m after 44 hours and 90 hours in Figure 64.

There are more differences between the $CuCl_2^-$ profiles for the Step 2 and Step 3a model (Figure 65). Although the distribution of dissolved copper is largely limited to the approximate radius of the copper electrode in both cases, the $CuCl_2^-$ diffuses further away from the electrode in the Step 2 case because it is oxidized by O_2 to Cu^{2+} in the Step 3a model. Only at longer times does Cu(I) approach the outer edge of the clay layer for the Step 3a model because, by that time, the rate of oxidation to Cu(II) is much diminished because of the lower $[O_2]$. In terms of the lateral distribution of $CuCl_2^-$, very little dissolved Cu(I) diffuses outside of the radius of the copper disc.

The distribution of Cu^{2+} in the clay layer is shown in Figure 66 for the Step 3a model. As illustrated in Figure 26(c), the maximum Cu^{2+} concentration occurs at some distance away from the copper electrode in Figure 66 because it is at this location that the combination of the product of the concentrations of dissolved O_2 and $CuCl_2^-$, and hence the rate of Cu(I) oxidation, is at a maximum. Since the predominant cathodic reaction in this model is the reduction of Cu^{2+}, the interfacial concentration of Cu(II) species is close to zero, as illustrated in the figure.

A notable feature of the concentration profiles for $CuCl_2^-$ and Cu^{2+} (and, to some degree, also for O_2) is that these species are confined to a volume of the clay of the same radius as the copper disc. Overall, therefore, the concentration profiles from the 2-D axisymmetric model for the 1-mm clay experiment suggest that a 1-D approximation is reasonable for this electrode geometry.

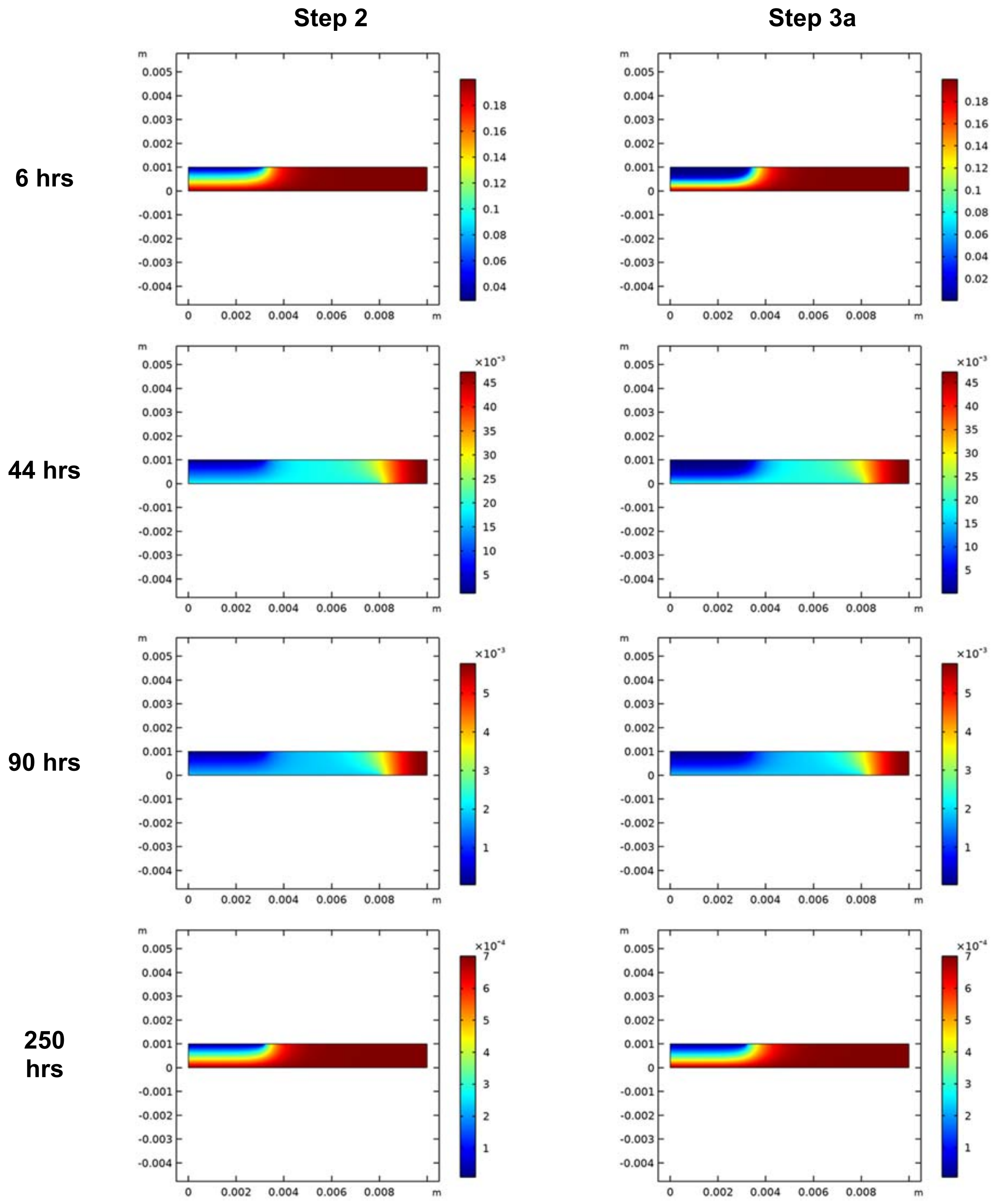

Figure 64: Distribution of Dissolved Oxygen in the 1-mm Clay Layer at Various Times for the Step 2 and Step 3a 2-D Axisymmetric Models. The radii of the copper electrode, clay disc, and opening to the bulk solution were 0.003175, 0.010, and 0.008 m, respectively. The four times correspond to the times at which the external purge gas was changed from (i) air to 2 vol.% O_2/N_2 (6 hrs), (ii) 2 vol.% to 0.2 vol.% O_2/N_2 (44 hrs), (iii) 0.2 vol.% O_2/N_2 to N_2 (90 hrs), and (iv) the end of the experiment (250 hrs). The scale bars indicate the concentration in mol/m^3.

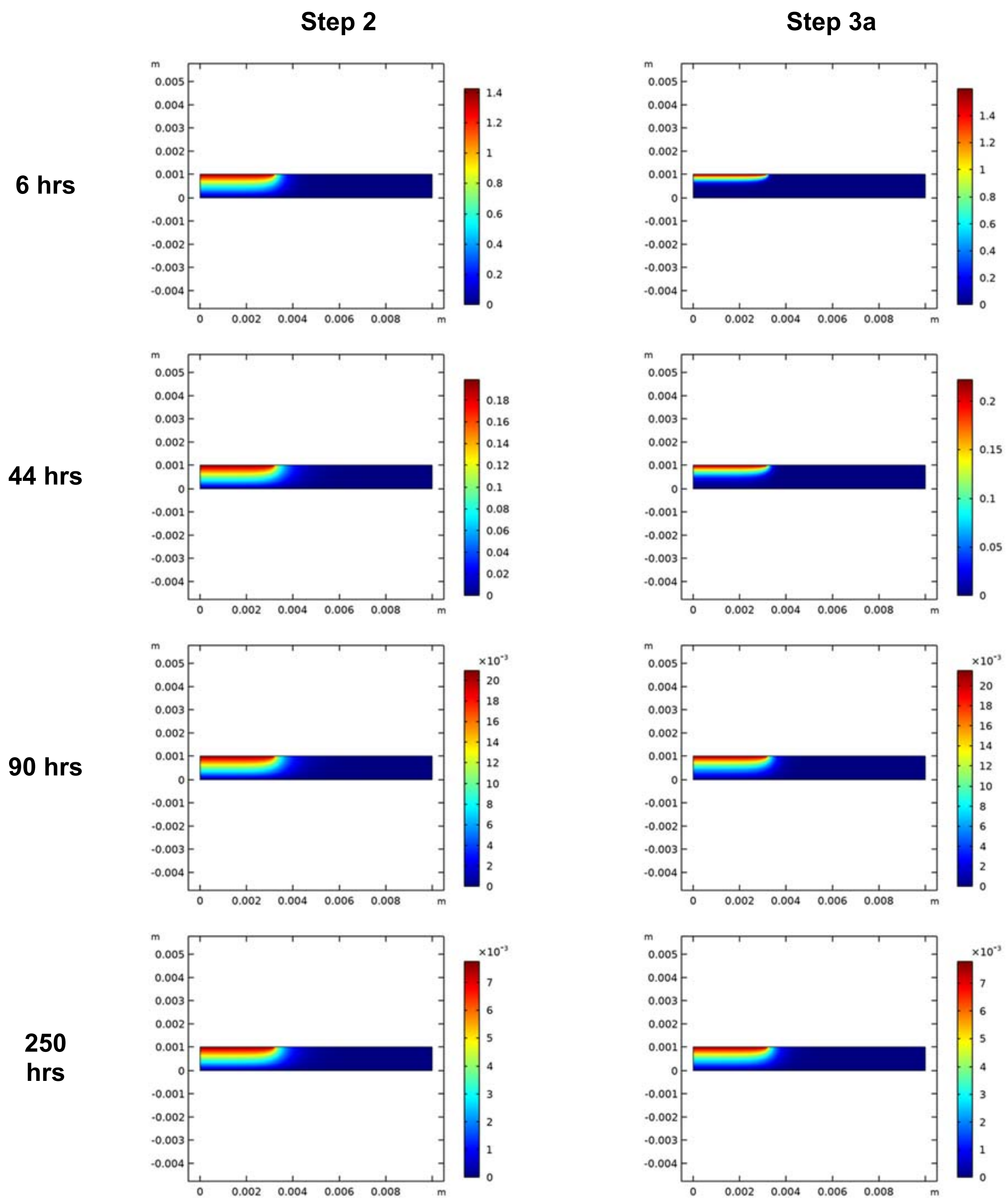

Figure 65: Distribution of $CuCl_2^-$ in the 1-mm Clay Layer at Various Times for the Step 2 and Step 3a 2-D Axisymmetric Models. The radii of the copper electrode, clay disc, and opening to the bulk solution were 0.003175, 0.010, and 0.008 m, respectively. The four times correspond to the times at which the external purge gas was changed from (i) air to 2 vol.% O_2/N_2 (6 hrs), (ii) 2 vol.% to 0.2 vol.% O_2/N_2 (44 hrs), (iii) 0.2 vol.% O_2/N_2 to N_2 (90 hrs), and (iv) the end of the experiment (250 hrs). The scale bars indicate the concentration in mol/m^3.

	Step 2	Step 3a
6 hrs	**n/a**	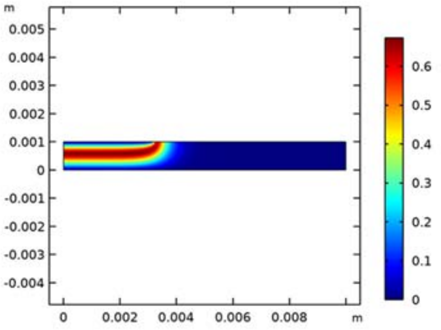
44 hrs	**n/a**	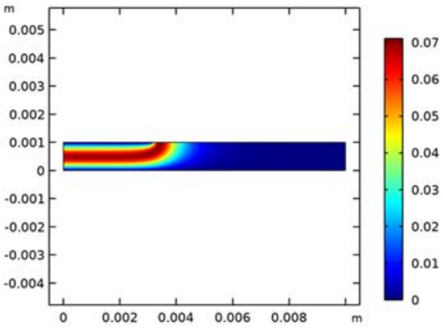
90 hrs	**n/a**	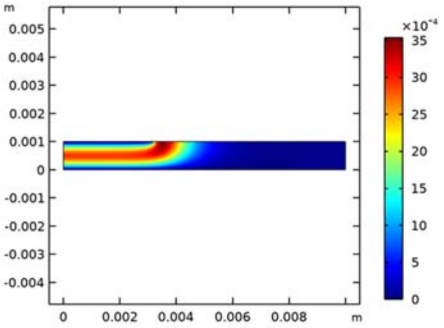
250 hrs	**n/a**	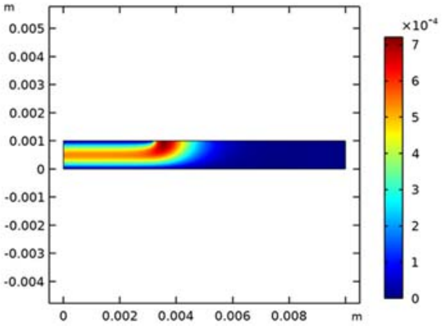

Figure 66: Distribution of Dissolved Cu^{2+} in the 1-mm Clay Layer at Various Times for the Step 3a 2-D Axisymmetric Model. The radii of the copper electrode, clay disc, and opening to the bulk solution were 0.003175, 0.010, and 0.008 m, respectively. The four times correspond to the times at which the external purge gas was changed from (i) air to 2 vol.% O_2/N_2 (6 hrs), (ii) 2 vol.% to 0.2 vol.% O_2/N_2 (44 hrs), (iii) 0.2 vol.% O_2/N_2 to N_2 (90 hrs), and (iv) the end of the experiment (250 hrs). The scale bars indicate the concentration in mol/m^3.

4.4.1.3 Radial Distribution of Current and Charge Densities

As shown in Figure 63(b), the sum of the average current densities is close to zero at all times for both models, indicating that the requirement of a net-zero current is maintained throughout the simulation. However, there is significant radial variation of the individual anodic and cathodic reactions as a result of spatial variation in the rates of mass transport of reactants towards, and of corrosion products away from, the copper surface.

Figure 67 shows the radial distribution of (a) the individual current densities, (b) the sum of the current densities, and (c) the charge density at the end of the experiment (simulation) for the Step 2 and Step 3a models. The spatial distributions of the anodic and cathodic current densities are similar, albeit that the reduction of O_2 is the (only) cathodic reaction for the Step 2 model, whereas the reduction of Cu^{2+} is the predominant cathodic reaction for the Step 3a model (Figure 67(a)). For both models, the current densities increase at the outer edge of the electrode, since this is where the rates of mass transport (of O_2 or Cu^{2+} towards and of $CuCl_2^-$ away from the electrode) are greatest and diffusion tends towards being spherical in nature (Figure 68). Towards the centre of the electrode, where the diffusion will be close to planar (Figure 68), the current densities are more uniform (Figure 67(a)).

However, the radial distribution of the sum of the current densities shows that the anodic and cathodic reactions are not uniformly distributed over the electrode surface and the distributions differ for the Step 2 and Step 3a models (Figure 67(b)). At short times (6 hours), much of the electrode is predicted to act as a net cathode based on the Step 2 model, with the anodic reaction preferred at the very outer edge. However, the degree of separation of anodic and cathodic reactions is not large, with the net cathodic current in the centre of the electrode only amounting to approximately 4% of the total rate of reduction of O_2. Even at the peak net cathodic current at a radial position of 3 mm, the net cathodic current only amounts to 11% of the total cathodic current density. Thus, even though the cathodic reaction is favoured towards the centre of the electrode, there is still substantial anodic activity in this area. Likewise, copper dissolution is favoured around the outer edge of the electrode, but O_2 reduction also occurs in this region.

In contrast to the behaviour for Step 2, the centre of the electrode at short times acts as a net anode for the Step 3a model, with the periphery acting as a net cathode (Figure 67(a)). Again, the spatial separation of anodic and cathodic reactions is relatively minor as the net anodic current in the centre of the electrode is only approximately 4% of the total dissolution current. As shown in Figure 63(a) and (c), the cathodic reaction for the Step 3a model is predominantly the reduction of Cu^{2+}, which is produced by the homogeneous oxidation of $CuCl_2^-$ by O_2.

During the early stages of the experiment, the concentration gradients of O_2 and of dissolved Cu species are strongly affected by the initial distribution of these species. Initially, the concentration of dissolved O_2 in the clay layer is uniform and equal to the concentration in the bulk solution. At the same time, the clay layer is free of dissolved Cu species. Thus, especially at the edges of the electrode where diffusion is rapid, the rate of transport of Cu species will be high initially. Thus, if O_2 reduction is that cathodic reaction, as in the Step 2 model, the higher flux of copper species around the periphery will result in that region being a net anode and, conversely, the centre will be a net cathode. For the Step 3a model in which the reduction of Cu^{2+} is the predominant cathodic reaction, the rapid diffusion of Cu^{2+} back towards the periphery of the electrode makes this region a net cathode and the centre a net anode.

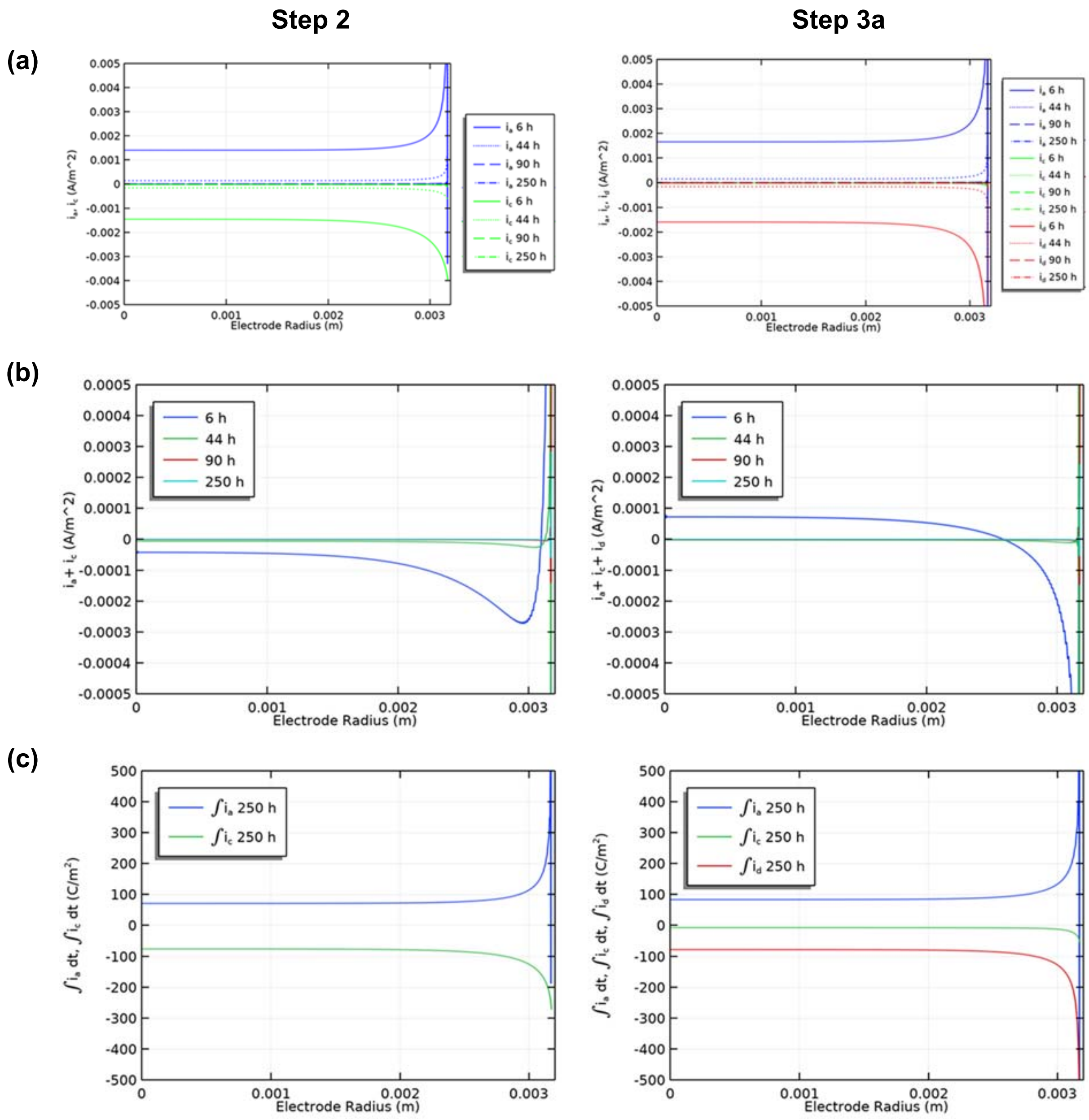

Figure 67: Radial Distribution of (a) the Individual Current Densities and (b) the Sum of the Current Densities at Various Times, and (c) the Charge Density at the End of the Experiment for the Step 2 and Step 3a COMSOL Models for the 1-mm Clay Electrode Experiment.

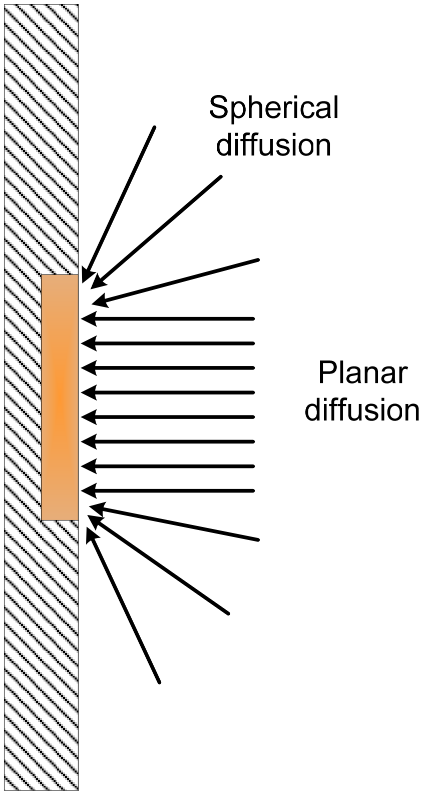

Figure 68: Schematic Illustrating the Different Diffusion Regimes at the Centre and Around the Edges of a Circular Electrode in an Inert Mount.

The charge densities (Figure 67(c)) are proportional to the depth of corrosion which, as the figure shows, varies radially, with the deepest corrosion predicted at the edge of the electrode. Although the predicted currents (and current densities) are subject to the largest potential error at the edge of the electrode which represents a discontinuity in the model, the charge densities suggest that the depth of corrosion at the edge of the electrode could be approximately five times that at the centre. Unfortunately, no corrosion rates measurements or surface profilometry was conducted during the original experiments.

4.4.2 10-mm Clay Layer Experiment

4.4.2.1 E_{CORR} and Average Current and Charge Densities

The 2-D axisymmetric COMSOL model was also used to simulate the results of the 10-mm clay electrode experiment. As for the 1-mm clay layer, there was relatively little effect of the model dimensionality on the predicted time dependence of E_{CORR} for the 10-mm clay electrode, except in the case of the Step 2 model which shows some difference between the 1-D and 2-D models (Figure 69). However, the discrepancy between the measured and predicted E_{CORR} values for the 10-mm-clay layer is not resolved by taking into account possible multi-dimensional diffusion effects using the 2-D axisymmetric model.

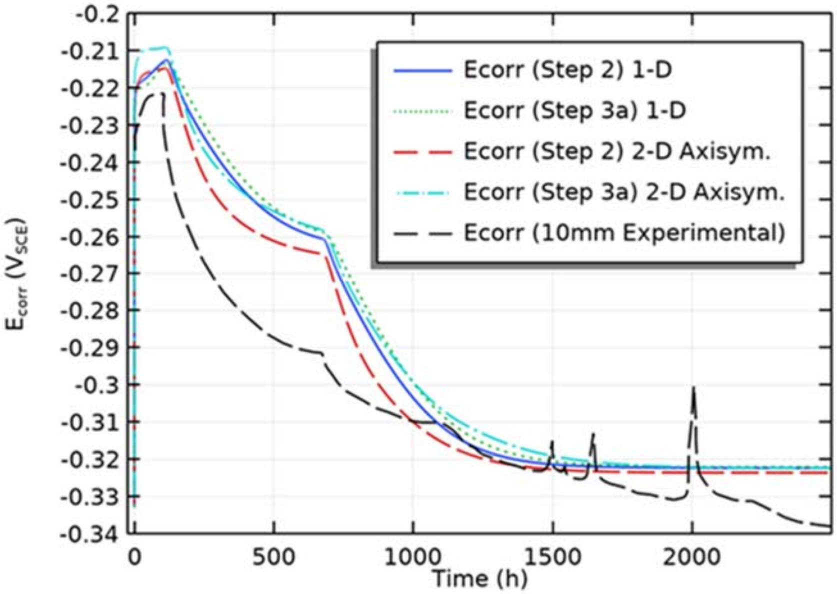

Figure 69: Comparison of the Predicted Time Dependence of E_{CORR} for the 10-mm Clay Electrode Experiment for the 1-D and 2-D Axisymmetric Versions of the Step 2 and Step 3a Models.

Figure 70 compares the predicted current densities and charge densities for the Step 2 and Step 3a models for the 10-mm clay electrode for both the 1-D and 2-D axisymmetric models. Although the 2-D axisymmetric model predicted slightly higher current and charge densities for the 1-mm clay electrode (by a factor of 20-25%, Figure 63), the effect of the model dimensionality is much greater for the 10-mm clay electrode, with up to a factor of 10 difference in the charge density after 2500 hours for the Step 3a model. The reason for the much higher charge densities for the 2-D axisymmetric model of the 10-mm clay electrode will be discussed in more detail later.

As for the 2-D axisymmetric simulation of the 1-mm clay experiment, the sum of the average current densities was close to zero for the Step 2 and Step 3a 2-D axisymmetric models of the 10-mm clay electrode (not shown). Apart from some initial fluctuations, the sum of the current densities was $<<10^{-9}$ A/m^2, representing less than 0.0001-0.01% of the individual current densities.

4.4.2.2 Concentration Profiles

The spatial dependence of the concentrations of dissolved O_2, $CuCl_2^-$, and (for Step 3a) Cu^{2+} for different times are shown as 3-D cut-away images in Figure 71 to Figure 73. Unlike the corresponding profiles for the 1-mm clay electrode, there are significant differences in the predicted spatial distribution of the three species for the 10-mm clay electrode between the Step 2 and Step 3a models.

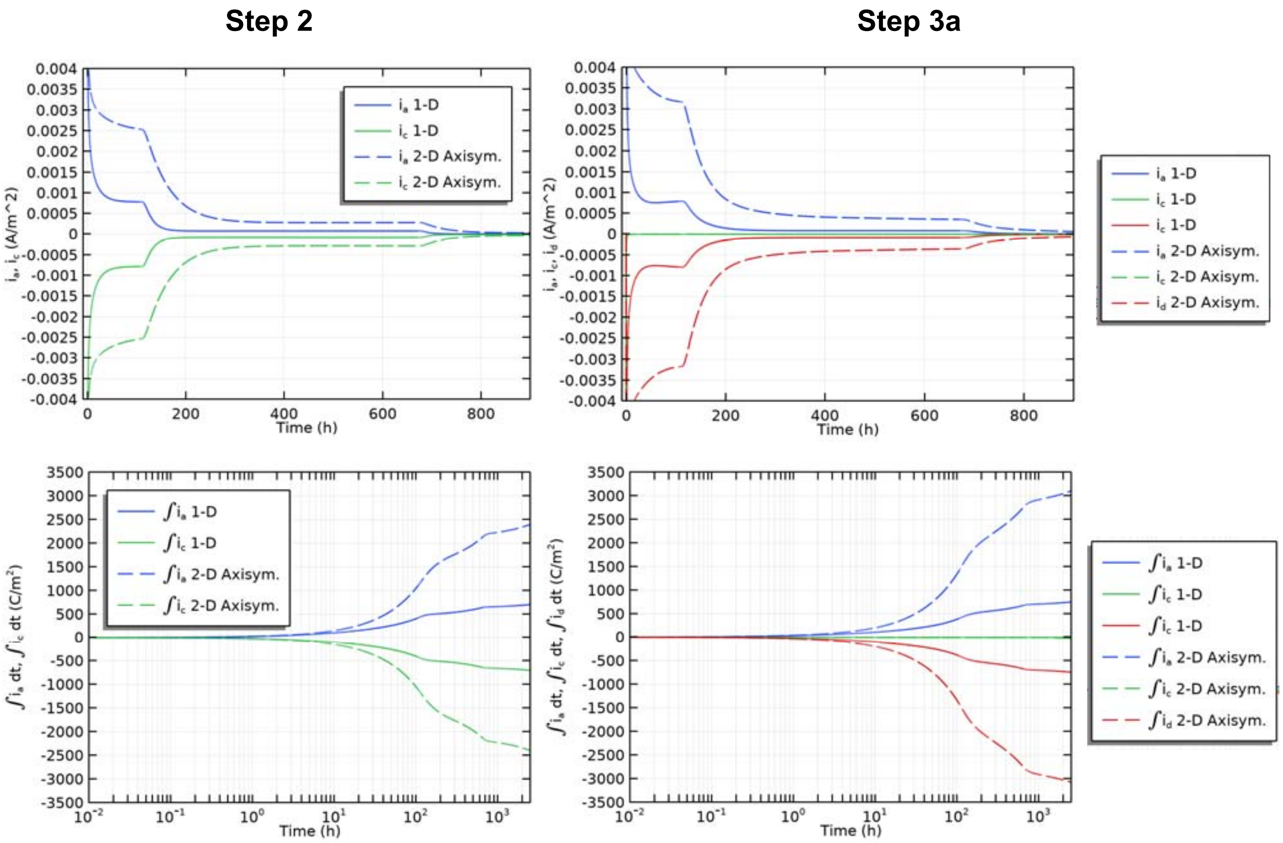

Figure 70: Comparison of the Predicted Time Dependence of the Current Densities (Upper) and Charge Densities (Lower) for the 10-mm Clay Electrode Experiment for the 1-D and 2-D Axisymmetric Versions of the Step 2 and Step 3a Models.

At all times, there is greater consumption of O_2 in the Step 3a model, as indicated by the predominance of green and blue tones, compared with the red and yellow tones indicative of higher concentrations for the Step 2 simulation. It is also noteworthy that the dissolved O_2 concentration is depleted across the entire diameter of the clay plug, especially for the Step 3a model, whereas the concentration changes tended to be limited to regions closer to the copper disc for the 1-mm clay electrode (Figure 64). This tendency for greater radial variations in concentration for the 10-mm electrode are highlighted by the differences in distribution of $CuCl_2^-$ for the Step 2 model for the 10-mm (Figure 72) and 1-mm clay electrodes (Figure 65). This greater extent of radial diffusion for the 10-mm clay electrode is a consequence of (i) the longer duration of the experiment and (ii) the longer diffusion path to the bulk solution compared with that for the 1-mm clay electrode.

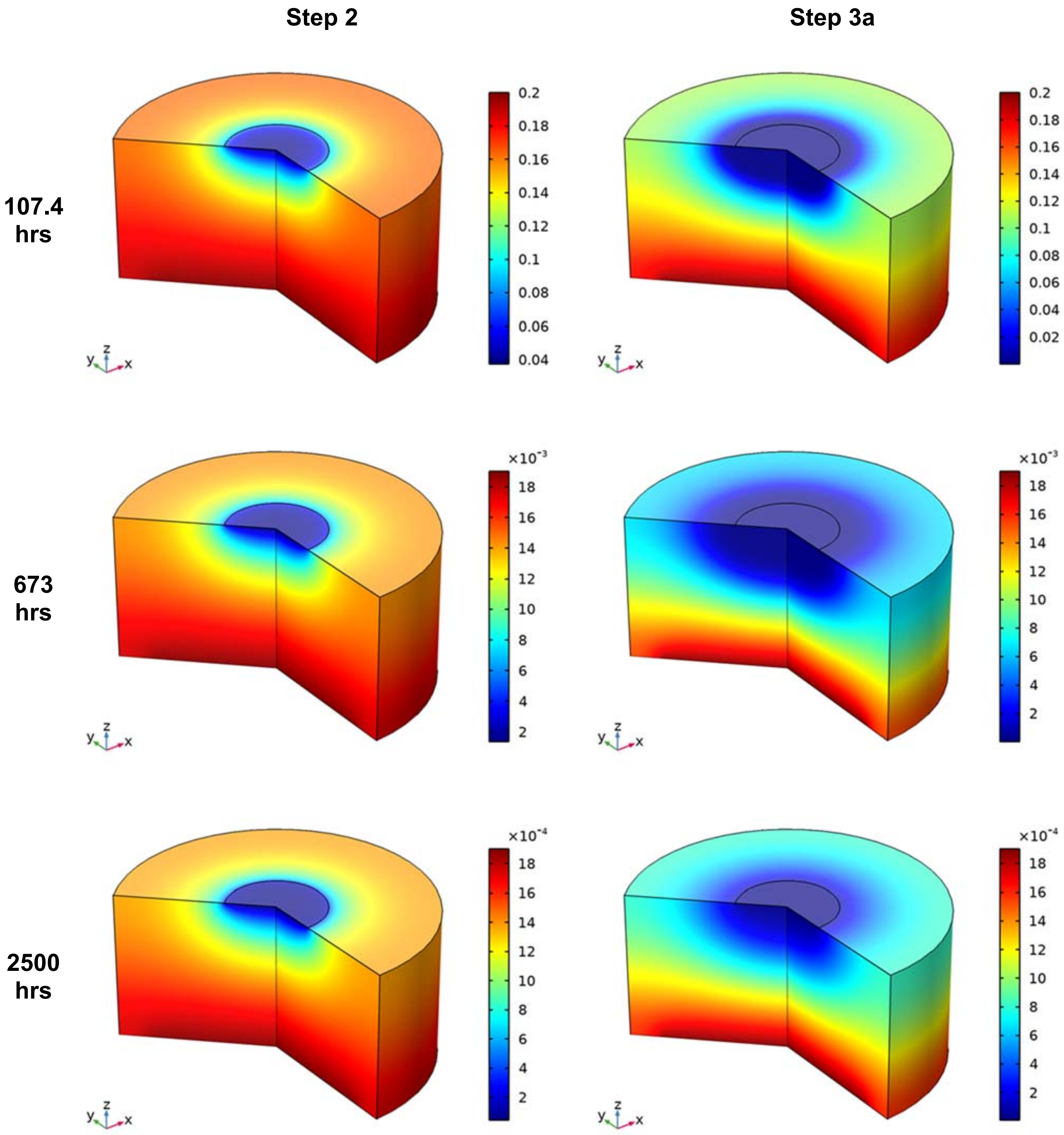

Figure 71: Distribution of Dissolved Oxygen in the 10-mm Clay Layer at Various Times for the Step 2 and Step 3a 2-D Axisymmetric Models. The radii of the copper electrode, clay disc, and opening to the bulk solution were 0.003175, 0.010, and 0.008 m, respectively. The central black circle on the upper face represents the edge of the copper electrode. The three times correspond to the times at which the external purge gas was changed from (i) air to 2 vol.% O_2/N_2 (107.4 hrs), (ii) 2 vol.% to 0.2 vol.% O_2/N_2 (673 hrs), and (iii) the end of the experiment (2500 hrs). The scale bars indicate the concentration in mol/m^3.

In contrast to the radial diffusion of $CuCl_2^-$ for the Step 2 model, the dissolved Cu(I) species is confined to regions close to the copper electrode for the Step 3a model (Figure 72). Instead, Cu(I) is oxidized to Cu^{2+}, with the oxidized species then diffusing radially towards the outer edges of the clay plug, and axially towards the bulk solution (Figure 73). As noted earlier during the discussion of the 1-D model and the 1-mm clay 2-D axisymmetric Step 3a model, the maximum Cu^{2+} concentration is observed some distance from the copper electrode at a location that corresponds to the maximum product of the O_2 and $CuCl_2^-$ concentrations (and, hence, of the rate of Cu(I) oxidation to Cu(II)). In the cut-away 3-D image for Step 3a in Figure 73, it can be seen that the Cu^{2+} concentration attains a maximum in a “halo” or “hemispherical dome” that spreads both radially and axially away from the copper electrode. Thus, as might be expected, the dissolved $CuCl_2^-$ is oxidized by both O_2 diffusing into the clay plug from the bulk solution and also from that around the periphery of the plug initially.

4.4.2.3 Radial Distribution of Current and Charge Densities

Figure 74 and Figure 75 show (a) the radial distribution of the individual current densities, (b) the sum of the current densities, and (c) the charge densities for the Step 2 and Step 3a models, respectively. As for the 1-m clay electrode, the predicted radial distribution of current densities for the 10-mm-clay electrode indicate higher corrosion rates around the edge of the electrode for both the Step 2 and Step 3a models (Figure 74(a) and Figure 75(a), respectively).

Unlike the 1-mm-clay electrode, however, the sums of the current densities for the 10-mm electrode indicates the centre of the electrode is a net cathode and the periphery a net anode for both Step 2 and Step 3a models (Figure 74(b) and Figure 75(b), respectively). The degree of spatial separation is somewhat greater for the 10-mm electrode, with the net cathodic current density at the centre of the electrode for the Step 2 model approximately 30% of the total cathodic current density. In the case of the Step 3a model, the net anodic region is not visible on the scale used in the figure, but is presumably very close to the edge of the electrode, suggesting a significant spatial separation of anodic and cathodic reactions in this case.

Again, the radial variation in the charge density (Figure 74(c) and Figure 75(c)) indicates that the edge of the electrode corrodes more than the centre. The charge densities are not shown at the very edge of the electrode (radius 0.003175 m) because of the numerical uncertainty associated with the discontinuity at the edge, but the ratio of corrosion depths between the centre and edge is at least a factor of five, as it was for the 1-mm-clay electrode.

As noted above in connection with Figure 70, the predicted charge densities for the 2-D axisymmetric model of the 10-mm-clay electrode are approximately a factor of ten higher than those predicted using the 1-D linear model. This difference is believed to be due to the differences in the initial inventories of O_2 for the two models. For the 1-D model, only that O_2 in the clay column of the same diameter as the copper electrode is included in the model. However, for the 2-D axisymmetric model, the entire O_2 inventory in the clay is included. The relative inventories are given by the ratio of the copper and clay diameters squared, or $(20\ \mathrm{mm}/6.35\ \mathrm{mm})^2 = 9.92$. The fact that the ratio of the predicted charge densities for the 2-D axisymmetric and 1-D models is the same as the ratio of the initial O_2 inventories suggests that the overall extent of corrosion is determined by the availability of O_2.

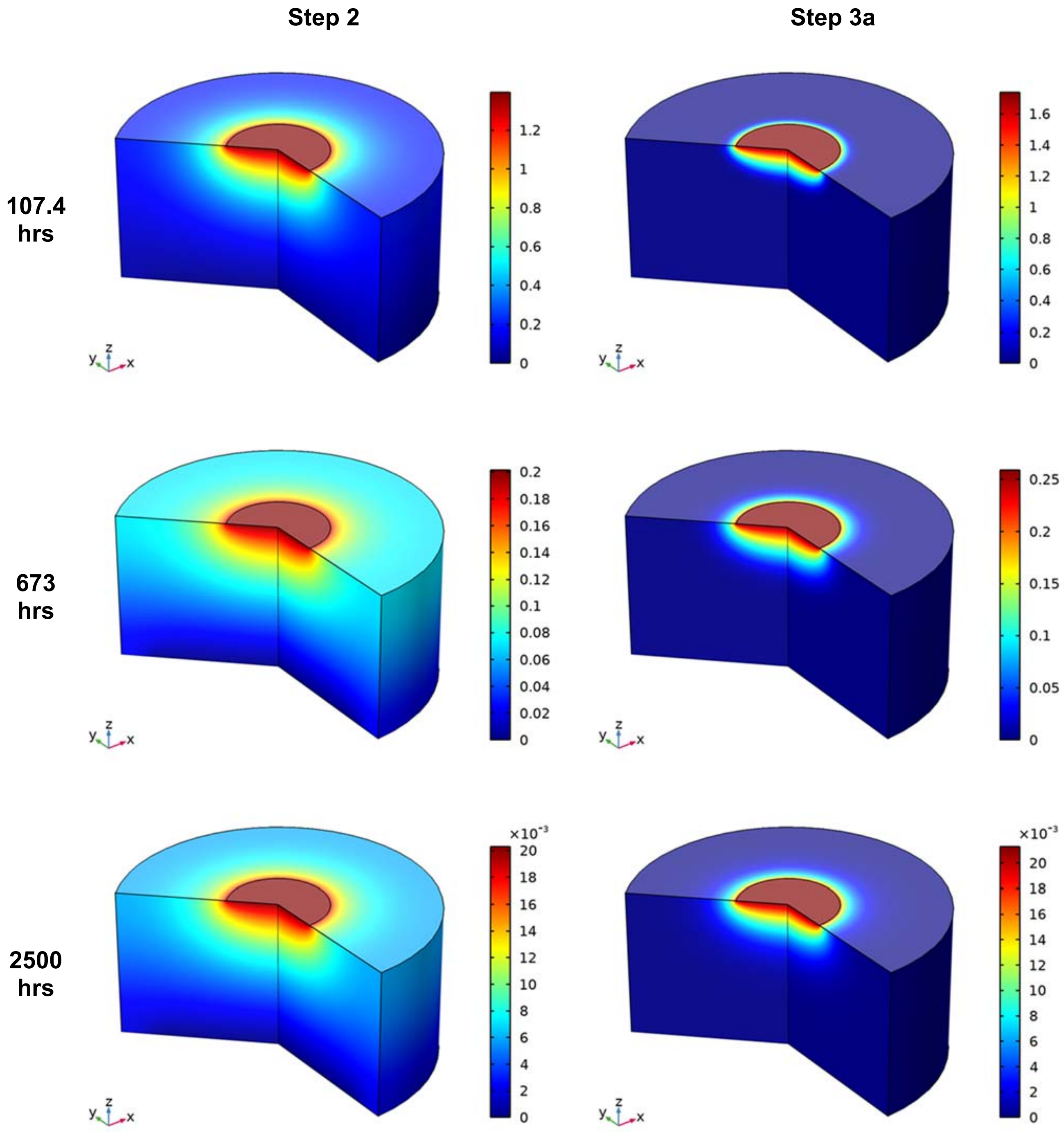

Figure 72: Distribution of Dissolved CuCl$_2^-$ in the 10-mm Clay Layer at Various Times for the Step 2 and Step 3a 2-D Axisymmetric Models. The radii of the copper electrode, clay disc, and opening to the bulk solution were 0.003175, 0.010, and 0.008 m, respectively. The central black circle on the upper face represents the edge of the copper electrode. The three times correspond to the times at which the external purge gas was changed from (i) air to 2 vol.% O$_2$/N$_2$ (107.4 hrs), (ii) 2 vol.% to 0.2 vol.% O$_2$/N$_2$ (673 hrs), and (iii) the end of the experiment (2500 hrs). The scale bars indicate the concentration in mol/m^3.

	Step 2	**Step 3a**
107.4 hrs	n/a	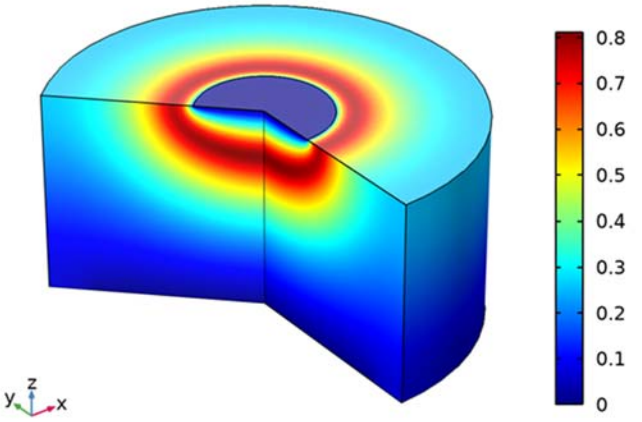
673 hrs	n/a	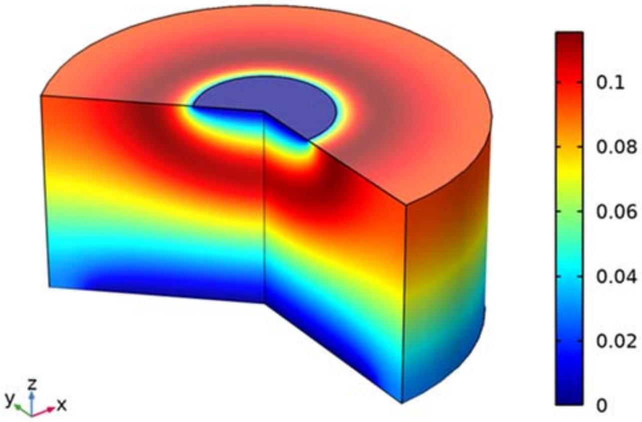
2500 hrs	n/a	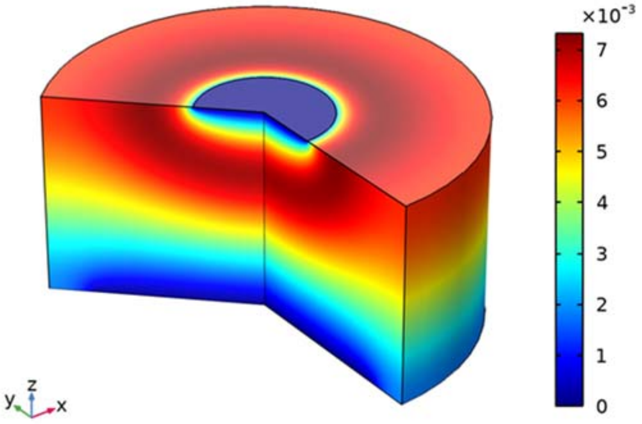

Figure 73: Distribution of Dissolved Cu^{2+} in the 10-mm Clay Layer at Various Times for the Step 3a 2-D Axisymmetric Models. The radii of the copper electrode, clay disc, and opening to the bulk solution were 0.003175, 0.010, and 0.008 m, respectively. The central black circle on the upper face represents the edge of the copper electrode. The three times correspond to the times at which the external purge gas was changed from (i) air to 2 vol.% O_2/N_2 (107.4 hrs), (ii) 2 vol.% to 0.2 vol.% O_2/N_2 (673 hrs), and (iii) the end of the experiment (2500 hrs). The scale bars indicate the concentration in mol/m^3.

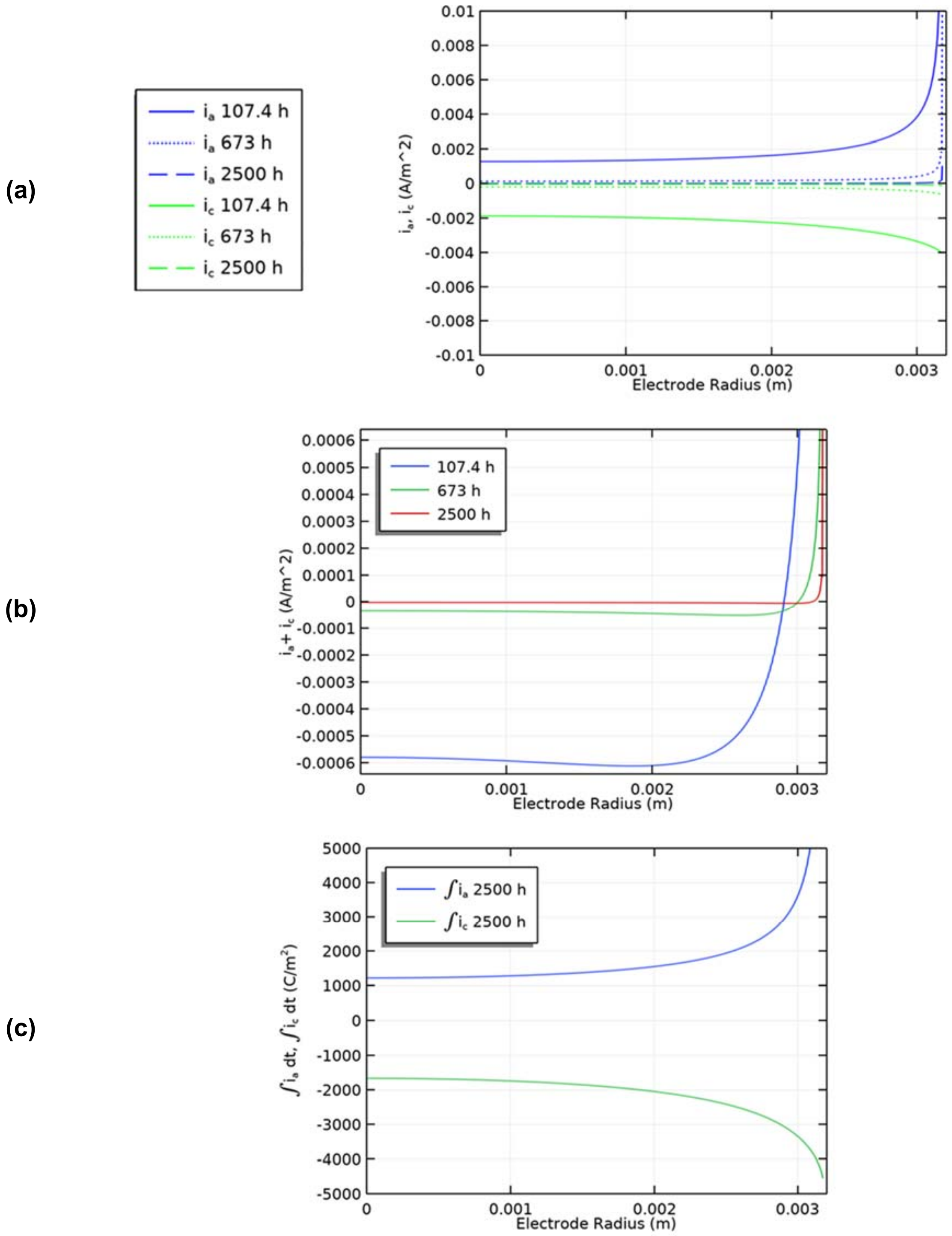

Figure 74: Radial distribution of (a) the individual current densities and (b) the sum of the current densities at various times, and (c) the charge density at the end of the experiment for the Step 2 COMSOL model of the 10-mm clay electrode experiment.

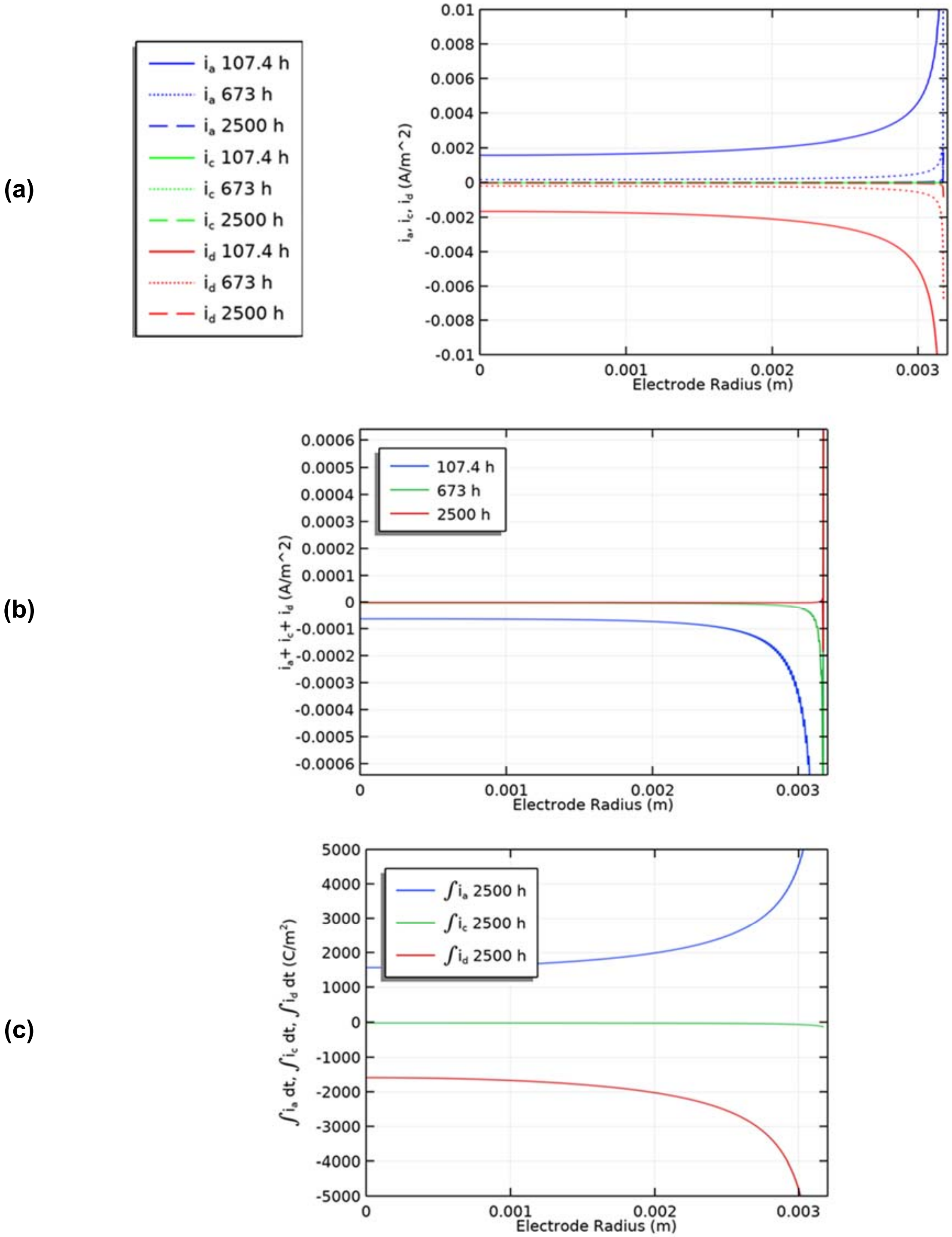

Figure 75: Radial distribution of (a) the individual current densities and (b) the sum of the current densities at various times, and (c) the charge density at the end of the experiment for the Step 3a COMSOL model of the 10-mm clay electrode experiment.

The ratio of O_2 inventories would, of course, be the same for the 1-mm-clay electrode 1-D and 2-D axisymmetric models, although in that case the charge densities only differed by a factor 20-30% (Figure 63(c)). However, for the thinner clay layer, the diffusion path length to the bulk solution is shorter than from the edge of the clay layer to the copper disc, so a significant fraction of the O_2 in the outer periphery of the clay layer diffuses into the bulk environment before it can diffuse to the copper surface. In this regard, the 1-mm-clay layer experiment resembles a 1-D geometry much more closely than the 10-mm-clay electrode, for which 3-D effects are more significant.

5. SUMMARY AND CONCLUSIONS

A stepwise approach to the conversion of the custom-designed Copper Corrosion Model (CCM) to the commercial COMSOL platform has been defined. The CCM accounts for the effects of the evolution of the near- and far-fields of a deep geological repository (DGR) on the corrosion behaviour of copper used-fuel containers (UFC). An important feature of the model is the coupling of the interfacial electrochemical reactions, representing the overall corrosion process, to the mass-transport, redox, microbiological, adsorption/desorption, and precipitation/dissolution processes occurring in the near- and far-fields. The coupled anodic and cathodic interfacial electrochemical reactions represent a mixed-potential model within the larger reactive-transport model, enabling the time dependence of both the corrosion potential (E_{CORR}) and of the corrosion rate to be predicted.

The stepwise CCM conversion involves the development of a number of interim versions of the COMSOL code of increasing mechanistic, dimensional, and functional complexity. In the work reported here, both steady-state and transient versions of a 1-D linear COMSOL CCM have been developed, with the complete mechanistic description of the original model incorporated in the new code. A key component of the stepwise development of the model has been the validation of each interim version of the code against experimental data. A 2-D axisymmetric version of the code has also been developed to aid in the interpretation of the experimental data. Various checks have been made for each interim version of the model to ensure the quality of the output. Whenever possible, all input parameter values have been taken from independent measurements or studies and have not been calibrated using the fit of the output to the experimental data. Future code developments will address the effects of spatial and temporal variations in the temperature and degree of saturation of the repository environment and of the complex 3-D geometry of the DGR.

Conversion of the conventional model to COMSOL provides several advantages. First, the COMSOL code can be implemented in 2- and 3-D with greater ease than the conventional model, in order to better represent the complex geometry of the DGR. The accompanying post-processing and graphical output capabilities of the commercial software are also superior. There are also advantages to the use of COMSOL in terms of the built-in quality assurance and model updates provided by the supplier, as well as by the broader user-community. Finally, it is easier to maintain the code and to pass it on to other users when it is based on a supported, widely-used software package, as opposed to the custom-written conventional CCM.

As noted above, an important aspect of the work described in this report has been the validation of the 1-D COMSOL model predictions against experimental measurements of the E_{CORR} of a copper electrode. The electrode was contacted by a 1-mm-thick layer of compacted clay saturated with initially aerated 1 mol/L NaCl solution, with measurement of the time-dependent E_{CORR} as the dissolved O_2 concentration was progressively reduced to simulate the evolution of redox conditions in the DGR. Both steady-state (Step 1) and transient (Step 2) versions of the COMSOL code were developed based on a simplified mechanism involving a single anodic reaction (the dissolution of Cu as $CuCl_2^-$) and a single cathodic reaction (the reduction of O_2). Validation of the Step 1 and Step 2 COMSOL codes was based on a comparison of the experimental and predicted steady-state and time-dependent E_{CORR} values, respectively. The steady-state E_{CORR} values were in good agreement (generally within 20 mV) and, following adjustment of the value for the tortuosity factor of the compacted clay, the predicted time-dependent evolution of E_{CORR} was in excellent agreement with that observed experimentally. All other input parameter values were derived from independent studies of the individual anodic and cathodic reactions are were not modified in order to obtain a better fit between experiment and prediction.

A further series of code modifications were made (Steps 3a to 3f) in order to introduce increasing degrees of mechanistic complexity. For the Step 3a model, the homogeneous oxidation of $CuCl_2^-$ to Cu^{2+} by O_2 was introduced, along with the reduction of Cu^{2+} as a second cathodic reaction. Surprisingly, the inclusion of a second cathodic reaction had relatively little impact on the evolution of E_{CORR}, primarily because the overall rate-determining process is the supply of O_2, and the precise nature and kinetics of the interfacial cathodic process are of less importance. Similarly, the inclusion in the underlying mechanism of (i) the precipitation and dissolution of $CuCl_2{\cdot}3Cu(OH)_2$ (Step 3b), (ii) the precipitation and dissolution of Cu_2O (Step 3c), (iii) the consumption of O_2 by aerobic microbial activity (Step 3e), or (iv) the consumption of O_2 by reactions with Fe(II) (Step 3f), all had relatively little impact on the predicted E_{CORR} values. The one mechanistic feature that did have a significant impact on E_{CORR} was the adsorption/desorption of Cu^{2+} by the bentonite clay (Step 3d). Agreement between the experimental and predicted E_{CORR} could only be obtained for the Step 3d model if either (a) a combination of adsorption and desorption rate constants were used which resulted in low adsorbed Cu(II) concentrations or (b) adsorption/desorption was modelled using an equilibrium Freundlich isotherm (but, interestingly, not an equilibrium Langmuir isotherm). Adsorption of Cu(II) by bentonite is known to be an important process in the corrosion of copper in contact with compacted clay based on earlier experimental studies, and the modelling of this process within the COMSOL code is an area of ongoing investigation.

The predictions from the 1-D COMSOL model were also compared with those from a version of the conventional model developed to predict the results from the experimental studies. This comparison is an alternative method for validating the COMSOL model and is useful for comparing predictions using finite-difference (conventional code) and finite-element schemes (COMSOL code). Comparisons were made for the Step 2 and Step 3a models. Predictions from the two models were generally in good agreement, with the predicted time dependence of E_{CORR} and of the concentration profiles for the various dissolved species. The agreement between the two techniques was better for the Step 3a model, in which the predominant cathodic reaction is the reduction of Cu^{2+}, than for the Step 2 model, where O_2 reduction is the only cathodic process. All of the observed discrepancies were associated with the treatment of the O_2 reduction reaction and of the flux of O_2 across the solution/clay interface. These differences highlight the importance of using sufficiently fine discretization at interfaces in numerical models, especially at the copper surface and at the right-hand boundary of the 1-D model.

Although the COMSOL model could replicate the results from the 1-mm clay electrode, the same validated model was less successful at predicting the time-dependent E_{CORR} from a similar experiment with a 10-mm-thick clay layer. Although there was some lack of agreement in terms of the steady-state E_{CORR} values, the most notable discrepancy was the slower response in the predicted E_{CORR} to changes in the O_2 concentration. This disagreement may indicate that the transport porosity and/or tortuosity of the thicker layer were different from those of the 1-mm clay layer, possibly due to differences in the degree of compaction of the thin and thick clay layers in the original experiments.

A 2-D axisymmetric COMSOL model was also developed in order to explain possible multi-dimensional diffusion effects in the experiments. The diameters of the copper electrode and clay layer in the experiments were 6.35 mm and 20 mm, respectively, with a 16-mm diameter opening to the bulk solution in the base of the electrode mount. While the differences between the 1-D linear and 2-D axisymmetric models of the 1-mm clay electrode were relatively minor, significant differences were observed for the 10-mm clay layer. With a relatively short 1-mm diffusion distance, the predominant diffusion path was perpendicular to the electrode surface, i.e., approximately 1-D. For the 10-mm-thick clay layer, however, the diffusion distance to the bulk solution is similar to that from the periphery of the clay layer to the centre of the copper electrode, so that O_2 from the edge of the clay is predicted to diffuse to the copper electrode in the 2-D axisymmetric model rather than being lost to the bulk solution. As a result, the average depth of corrosion for the 10-mm clay experiment was predicted to be ten times higher using the 2-D axisymmetric model than for the 1-D linear code, a ratio that is equal to the relative amounts of O_2 initially present in the modelled clay layers. The 2-D axisymmetric model also predicts that the depth of corrosion is deeper around the edge of the copper disc than at the centre due to the hemi-spherical diffusion profiles around the periphery. Unfortunately, neither the average corrosion rate nor the surface profile of the corroded copper electrode were determined in the original experiments.

Future development of the COMSOL CCM code will include the incorporation of the effects of variable temperature (Step 4) and of variable saturation (Step 5), as well as a fully 3-D version of the model (Step 6) to simulate the stacked buffer box arrangement in the DGR.

ACKNOWLEDGEMENTS

The authors wish to thank Mohd Moinuddin and Professor Magdalena Krol, York University, Toronto for the initial COMSOL simulations and for useful discussions.

Dr. Miroslav Kolář, LS Computing Ltd performed the conventional CCM simulations used in the validation of the COMSOL model described in Section 4.2.

REFERENCES

Birgesson, M. and O. Karnland. 2009. Ion equilibrium between montmorillonite interlayer space and an external solution – consequences for diffusional transport. Geochim. Cosmochim. Acta 73, 1908-1923.

Bradbury, M.H. and B. Baeyens. 2003. Porewater chemistry in compacted re-saturated MX-80 bentonite. J. Contam. Hydrol. 61, 329-338.

Brown, D.A. 1990. Microbial Water Stress Physiology. John Wiley, Chichester.

Choi,J.-W. and D.W. Oscarson. 1996. Diffusive transport through compacted Na- and ca-bentonite. J. Contam. Hydrol. 22, 189-202.

Johnson, L.H., D.M. LeNeveu, D.W. Shoesmith, D.W. Oscarson, M.N. Gray, R.J. Lemire, and N.C. Garisto. 1994. The disposal of Canada's nuclear fuel waste: the vault model for postclosure assessment. Atomic Energy of Canada Limited Report, AECL-10714, COG-93-4.

Johnson, L.H., D.M. LeNeveu, F. King, D.W. Shoesmith, M. Kolar, D.W. Oscarson, S. Sunder, C. Onofrei, and J.L. Crosthwaite. 1996. The disposal of Canada's nuclear fuel waste: a study of postclosure safety of in-room emplacement of used CANDU fuel in copper containers in permeable plutonic rock. Volume 2: vault model. Atomic Energy of Canada Limited Report, AECL-11494-2, COG-96-552-2.

Kear, G., B.D. Barker, and F.C. Walsh. 2004. Electrochemical corrosion of unalloyed copper in chloride media – a critical review. Corros. Sci. 46, 109-135.

King, F. 1987. A technique to investigate the mechanism of uniform corrosion in the presence of a semi-permeable membrane. Atomic Energy of Canada Limited Report, AECL-9064.

King, F. 2008a. Theory manual for the copper corrosion model for uniform corrosion in sedimentary rock CCM-UC.1.1. Nuclear Waste Management Organization Technical Report, NWMO TR-2008-07.

King, F. 2008b. Mixed-potential modelling of the corrosion of copper in the presence of sulphide. Posiva Working Report, WR 2007-63.

King, F. 2014. Predicting the lifetimes of nuclear waste containers. JOM 66, 526-537.

King, F. and S. Briggs. 2016. Validation of the COMSOL Step 1 simple copper mixed-potential model. Nuclear Waste Management Organization Technical Memorandum.

King, F. and M. Kolář. 1995. Prediction of the lifetimes of copper nuclear waste containers under restrictive mass-transport and evolving redox conditions. CORROSION/95, NACE International, Houston, TX, Paper #425.

King, F. and M. Kolář. 1996a. A numerical model for the corrosion of copper nuclear fuel waste containers. In Scientific Basis for Nuclear Waste Management XIX, (W.M. Murphy and D. Knecht, Editors), Material Research Society Proceedings, Volume 412, Pittsburgh, PA, 555-562.

King, F. and M. Kolář. 1996b. Mechanistic modelling of the corrosion behaviour of copper nuclear fuel waste containers. In Proc. Int. Conf. Deep Geological Disposal of Radioactive Waste, Canadian Nuclear Society, Toronto, ON, p. 5-39 to 5-50. (Also published as Atomic Energy of Canada Limited Report, AECL-11644, COG-96-327).

King, F. and M. Kolář. 1997a. Corrosion of copper containers prior to saturation of a nuclear fuel waste disposal vault. Atomic Energy of Canada Limited Report, AECL-11718, COG-96-566.

King, F and M. Kolář. 1997b. The effect of geosphere conditions on the lifetimes of copper containers. Atomic Energy of Canada Limited Report, AECL-11717, COG-96-565.

King, F. and M. Kolář. 2000. The copper container corrosion model used in AECL's second case study. Ontario Power Generation, Nuclear Waste Management Division Report 06819-REP-01200-10041-R00.

King, F. and M. Kolář. 2004. Theory manual for the copper corrosion model for stress corrosion cracking of used fuel disposal containers CCM-SCC.0. Ontario Power Generation, Nuclear Waste Management Division Report 06819-REP-01300-10095-R00.

King, F. and M. Kolář. 2005. Preliminary assessment of the stress corrosion cracking of used fuel disposal containers using the CCM-SCC.0 model. Ontario Power Generation, Nuclear Waste Management Division Report 06819-REP-01300-10103-R00.

King, F. and M. Kolář. 2006a. Simulation of the consumption of oxygen in long-term *in situ* experiments and in the third case study repository using the copper corrosion model CCM-UC.1.1. Ontario Power Generation, Nuclear Waste Management Division Report, 06819-REP-01300-10084-R00.

King, F. and M. Kolář. 2006b. Consequences of microbial activity for corrosion of copper used fuel containers – analyses using the CCM-MIC.0.1 code. Ontario Power Generation, Nuclear Waste Management Division Report 06819-REP-01300-00120-R00. Toronto, Ontario.

King, F. and M. Kolář. 2019a. Lifetime predictions for nuclear waste disposal containers. Corrosion 75, 309-323.

King, F. and M. Kolář. 2019b. Copper Sulfide Model (CSM) – model improvements, sensitivity analyses, and results from the Integrated Sulfide Project inter-model comparison exercise. Swedish Nuclear Fuel and Waste Management Co, SKB Technical Report TR-18-08.

King, F. and Y. Tang. 1998. The anodic dissolution of copper in chloride-sulphate groundwaters. Ontario Hydro, Nuclear Waste Management Division Report 06819-REP-01200-0058-R00.

King, F., C.D. Litke, and S.R. Ryan. 1992. A mechanistic study of the uniform corrosion of copper in compacted Na-montmorillonite/sand mixtures. Corros. Sci. 33, 1979-1995.

King, F., C.D. Litke and Y. Tang. 1995a. Effect of interfacial pH on the reduction of oxygen on copper in neutral NaClO4 solution. J. Electroanal. Chem. 384, 105-113.

King, F., M.J. Quinn and C.D. Litke. 1995b. Oxygen reduction on copper in neutral NaCl solution. J. Electroanal. Chem. 385, 45-55.

King, F., C.D. Litke, M.J. Quinn and D.M. LeNeveu. 1995c. The measurement and prediction of the corrosion potential of copper in chloride solutions as a function of oxygen concentration and mass-transfer coefficient. Corros. Sci. 37, 833-851.

King, F., Y. Tang, M.J. Quinn and C.D. Litke. 1995d. The effects of dissolved oxygen concentration and mass-transport conditions on the dissolution behaviour of copper nuclear waste containers. In Proc. CORROSION/95, NACE International, Houston, TX, paper #424.

King, F., M. Kolář, and D.W. Shoesmith. 1996. Modelling the effects of porous and semi-permeable layers on corrosion processes. In Proc. CORROSION/96, NACE International, Houston, TX, paper #380.

King, F., M. Kolář and S. Stroes-Gascoyne. 2002. Theory manual for the microbiological copper corrosion model CCM-MIC.0. Ontario Power Generation, Nuclear Waste Management Division Report 06819-REP-01200-10091-R00. Toronto, Ontario.

King, F., M. Kolář, and S. Stroes-Gascoyne. 2003. Preliminary simulations of the long-term activity of microbes in a deep geologic repository using CCM-MIC.0 and the implications for corrosion of copper containers. Ontario Power Generation Nuclear Waste Management Division Report No: 06819-REP-01200-10116.

King, F., M. Kolář, S. Stroes-Gascoyne, and P. Maak. 2004. Model for the microbiological corrosion of copper containers in a deep geologic repository. In Scientific Basis for Nuclear Waste Management XXVII, (V.M. Oversby and L.O. Werme, Editors), Mat. Res. Soc. Symp. Proc. 807, Materials Research Society, (Warrendale, PA), 811-816.

King, F., M. Kolář, and P. Maak. 2008. Reactive-transport model for the prediction of the uniform corrosion behaviour of copper used fuel containers. J. Nucl. Mater. 379, 133-141.

King, F., M. Kolář, M. Vähänen, and C. Lilja. 2011a. Modelling the long-term corrosion behaviour of copper canisters in a KBS-3 repository. Corros. Eng. Sci. Technol., 46, 217-222.

King, F., M. Kolář, and M, Vähänen. 2011b. Reactive-transport modelling of the sulphide-assisted corrosion of copper nuclear waste containers. In Sulphur-Assisted Corrosion in Nuclear Disposal Systems, B. Kursten, D. Feron, and F,. Druyts (eds.), European Federation of Corrosion Volume 59 (Maney Publishing, Leeds, UK), Chap. 9, pp. 152-164.

Kolář, M. 2020. TRANSIENT - A C package for the numerical solution of systems of partial differential equations of parabolic type. http://transient.mkolar.org/.

Kolář, M. and F. King. 1996. Modelling the consumption of oxygen by container corrosion and reaction with Fe(II). Mats. Res. Soc. Symp. Proc. Vol. 412, Materials Research Society, Pittsburgh, PA, p. 547-554.

Litke, C.D., S.R. Ryan, and F. King. 1992. A mechanistic study of the uniform corrosion of copper in compacted clay-sand soil. Atomic Energy of Canada Limited Report, AECL-10397, COG-91-304.

Macdonald, D.D. 1999. Passivity – the key to our metals-based civilization. Pure Appl. Chem. 71, 951-978.

Macdonald, D.D. 2003. The Holy Grail: Deterministic prediction of corrosion damage thousands of years into the future. In Prediction of Long Term Corrosion Behaviour in Nuclear Waste Systems, D. Féron and D.D. Macdonald (eds.), European Federation of Corrosion Green Book, Number 36, Chap. 6, pps. 75-90.

Man, A. and J.B. Martino. 2009. Thermal, hydraulic and mechanical properties of sealing materials. Nuclear Waste Management Organization Report, NWMO TR-2009-20.

Power, G.P. and I.M. Ritchie. 1981. Mixed potential measurements in the elucidation of corrosion mechanisms – I. Introductory theory. Electrochim. Acta 26, 1073-1078.

Ryan, S.R. and F. King. 1994. The adsorption of Cu(II) on sodium bentonite in a synthetic saline groundwater. Atomic Energy of Canada Limited Report, AECL-11062, COG-I-94-125.

Shaw, D.J. 1970. Introduction to Colloid and Surface Chemistry. 2nd edition, Butterworth, London.

Shoesmith, D.W. 2003. Kinetics of aqueous corrosion. In Corrosion: Fundamentals, Testing, and Protection. ASM Handbook, Volume 13A, ASM International (Materials park, OH), pp. 42-51.

Stroes-Gascoyne, S., C.J. Hamon, C. Kohle, and D.A. Dixon. 2006. The effects of dry density and porewater salinity on the physical and microbiological characteristics of highly compacted bentonite. Ontario Power Generation, Nuclear Waste Management Division Report 06819-REP-01200-10016.

Stroes-Gascoyne, S., C.J. Hamon, D.A. Dixon, C. Kohle, and P. Maak. 2007. The effects of dry density and porewater salinity on the physical and microbiological characteristics of highly compacted bentonite. In Scientific Basis for Nuclear Waste Management XXX, edited by Darrell Dunn, Christophe Poinssot, Bruce Begg (Mater. Res. Soc. Symp. Proc. 985, Warrendale, PA, 2007), paper 0985-NN13-02.

Wersin, P. 2003. Geochemical modelling of bentonite porewater in high-level waste repositories. J. Contam. Hydrol. 61, 405-422.

APPENDIX A: STEPWISE DEVELOPMENT OF COMSOL VERSION OF THE CCM

In this Appendix, the information required to implement the Step 1 to Step 3f COMSOL models identified in Table 2 is defined. The following information is provided for each step:

- Summary of changes from the immediately prior version of the code.
- The reaction scheme for the particular code version.
- A description of the model geometry and dimensionality.
- A description of any additional homogeneous reactions or processes from the immediately prior version of the code.
- Description of any changes to the near-field (UFC surface) and far-field (a user-defined location in the intact host) boundary conditions.
- Definition of the initial conditions.
- Description of the treatment of thermal effects (if any).
- Description of the treatment of saturation effects (if any).
- Listing of the reaction-diffusion equations for all species in that model version.

For each Step, only the changes to the code are defined below. Unless explicitly stated, all reactions and processes included in prior versions of the code remain unchanged for the new, higher version.

The following description applies to the stepwise development of the COMSOL CCM as it would be applied to simulate the corrosion behaviour of a copper-coated UFC in a DGR. However, the same approach is also applicable to the simulation of the clay-covered copper electrode experiments of King et al. (1995c) that are used for validation purposes. In the latter case, the near-field boundary represents the copper electrode rather than the UFC and the far-field boundary represents the clay/solution interface rather than a location in the DGR host rock.

A.1 STEP 1: STEADY-STATE MODEL WITH SIMPLIFIED REACTION SCHEME

A.1.1 Summary of Changes from Prior Version

Since this is the first step in the development of the CCM COMSOL code, there are no changes from prior versions of the code.

A.1.2 Reaction Scheme

A simplified reaction scheme is simulated in Step 1 comprising three species, namely dissolved O_2, Cl^-, and $CuCl_2^-$. These species are free to diffuse to and from the left-hand boundary which represents the container surface. All three species participate in one of two electrochemical reactions that together constitute the corrosion reaction.

Corrosion of the copper container is supported by the cathodic reduction of dissolved O_2 which diffuses to the surface from a source at the right-hand boundary.

Dissolution of the copper also consumes Cl^- ions (in the form of $CuCl_2^-$ complex ions). Chloride is generally in excess (i.e., the concentration of Cl^- is much greater than the concentration of $CuCl_2^-$), but in general is also supplied by diffusion from the source at the right-hand boundary.

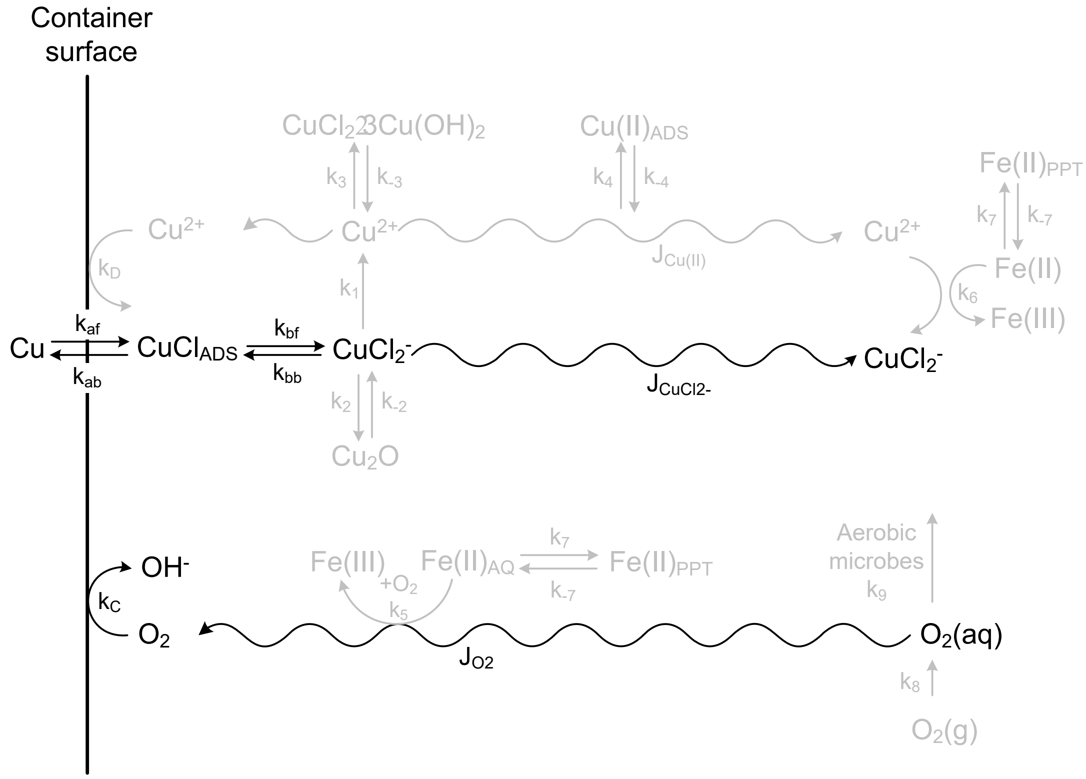

Figure A-1: Reaction Scheme for Step 1 in the Development of the CCM COMSOL code. The species and processes shown in black font are those included in the model. Those shown greyed out are those from the reaction scheme for the custom-designed CCM Version 1.1 which will be progressively introduced in further developments of the COMSOL code.

The $CuCl_{ADS}$ species shown in the figure is a surface intermediate that is consumed in the interfacial reaction and is not specifically modelled.

The OH^- species that is the product of the cathodic reduction of O_2 is not included in the model as that reaction is irreversible (i.e., the rate does not depend on the reverse reaction involving the oxidation of OH^-).

A.1.3 Geometry

A simple one dimensional (1-D), single layer geometry is used for Step 1.

The length of the layer (L) will vary depending upon the system being modelled. As for the custom-designed CCM, and in order to increase accuracy, the size of the finite element mesh should be smaller close to the left-hand boundary as this is where the steepest concentration gradients occur (Figure A-2).

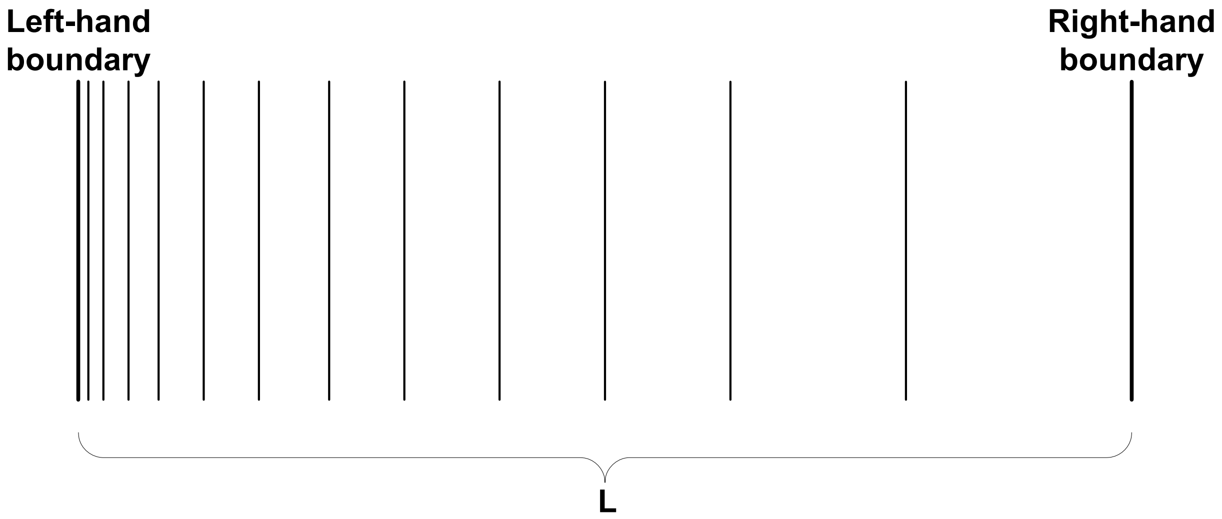

Figure A-2: Illustration of the Decreasing Element Size near the Left-hand Boundary Designed to Improve Accuracy of the Code.

Mass transport across the layer is by diffusion only, described using an effective diffusion coefficient (D_{EFF}) for each species. For Step 1, values of D_{EFF} for each species are inputted directly. In later steps, D_{EFF} is defined in terms of the corresponding diffusion coefficient for bulk solution modified by suitable porosity and/or tortuosity terms (e.g., $D_{EFF} = \varepsilon\tau D_0$). Table A-1 lists the effective diffusion coefficients for testing Step 1 of the COMSOL model.

Table A-1: Effective Diffusion Coefficients for Testing Step 1 Model.

System	**L (m)**	**D_{EFF} (m^2/s)**			**Comments**
		O_2	**Cl^-**	**$CuCl_2^-$**	
Bulk solution	10^{-5}-10^{-3}	1.7×10^{-9}	2.0×10^{-9}	6.0×10^{-10}	Parametric sweep on L
Compacted bentonite	0.2	1.7×10^{-11}	2.0×10^{-11}	6.0×10^{-12}	

A.1.4 Homogeneous Reactions

There are no homogeneous reactions included in Step 1.

A.1.5 Boundary Conditions

A.1.5.1 Near Field

The two interfacial electrochemical reactions are:

- the anodic dissolution of copper

$$\mathrm{Cu} + \mathrm{Cl}^- \underset{k_{ab}}{\overset{k_{af}}{\rightleftharpoons}} \mathrm{CuCl_{ADS}} + e^-$$

$$\mathrm{CuCl_{ADS}} + \mathrm{Cl}^- \underset{k_{bb}}{\overset{k_{bf}}{\rightleftharpoons}} \mathrm{CuCl_2^-} \qquad \text{(A-1)}$$

- the cathodic reduction of dissolved O_2

$$O_2 + 2H_2O + 4e^- \xrightarrow{k_c} 4OH^- \qquad \text{(A-2)}$$

The left-hand boundary represents the copper surface and it is on this boundary that we impose a zero net current condition:

$$\sum_j i_j = 0 \qquad \text{(A-3)}$$

where the current density i_j (A/m^2) corresponds to either the anodic current density i_a for Reaction (A-1) or the cathodic current density i_c for Reaction (A-2). The corresponding electrochemical expressions are:

$$i_a = n_a F \left\{ k_a [\mathrm{Cl}^-]_0^2 \exp\left[\frac{F}{RT}(E - E_a^0) \right] - k_{bb} [\mathrm{CuCl_2^-}]_0 \right\} \qquad \text{(A-4)}$$

and

$$i_c = -n_0 F k_c [O_2]_0 \exp\left[-\frac{\alpha_c F}{RT}(E - E_c^0) \right] \qquad \text{(A-5)}$$

where the various symbols are defined below:

F	Faraday constant (96 485 C·mol^{-1}).
R	Gas constant (8.314 J·K^{-1}·mol^{-1}).
n_0	Number of electrons transferred in the reduction of O_2 (4).
α_c	Cathodic transfer coefficient for the reduction of O_2 (0.37).
k_c	Electrochemical rate constant for the reduction of O_2 (1.7 x 10^{-10} m·s^{-1} at 25°C).
E_c^0	Standard potential for the reduction of O_2 (0.16 V_{SCE} at 25°C at pH 7).
n_a	Number of electrons transferred during the oxidation of Cu (1).
E_a^0	Standard potential for the dissolution of Cu as CuCl (-0.105 V_{SCE} at 25°C).
k_a	Combined electrochemical rate constant for the anodic dissolution of Cu (3.3 x 10^{-8} m^4·mol^{-1}·s^{-1} at 25°C). k_a is a combined rate constant, equivalent to $k_{af}k_{bf}/k_{ab}$.
k_{bb}	Rate constant for the conversion of $\mathrm{CuCl_2^-}$ to CuCl (1.42 x 10^{-4} m·s^{-1} at 25°C).

In general, a number of the parameters are temperature (T) dependent, but isothermal conditions are assumed for Step 1 using parameter values at 298.15 K, as defined in Appendix B.

The concentrations of Cl^-, $CuCl_2^-$, and O_2 in Equations (A-4) and (A-5) are those at the copper surface. In the conventional custom-designed CCM, we take these interfacial concentrations as the mean value over the first three finite-difference grid points because the interfacial concentration of O_2 drops to very low values at the interface and because the first grid location is only a few nm from the left-hand boundary. In COMSOL, we simply equate these concentrations to those in the first element next to the boundary, but it is worthwhile checking the dependency of the results on the coarseness of the mesh.

As a minor point, we are using concentrations instead of the more-rigorous activities for dissolved species.

The rates of the interfacial electrochemical reactions depend on the potential (E). There is a unique potential at which the values of Equations (A-4) and (A-5) are equal and of opposite sign and, hence, satisfy Equation (A-3). This is the corrosion potential (E_{CORR}), which is one of the main parameters that we are seeking to determine.

A.1.5.2 Far Field

We use constant- (or zero-) concentration boundary conditions for all three species:

- $[O_2]_{x=L}$ = constant
- $[Cl^-]_{x=L}$ = constant
- $[CuCl_2^-]_{x=L} = 0$

In separate runs, or in a parametric sweep, we can determine the steady-state E_{CORR} for the following $[O_2]$ and $[Cl^-]$:

- $[O_2]$: 2×10^{-4}, 2×10^{-3}, 2×10^{-2}, 0.2 mol/m^3
- $[Cl^-]$: 100, 1000 mol/m^3

A.1.6 Initial Conditions

The initial conditions for the dissolved species are:

- $0 \leq x \leq L$, $[O_2]$ = constant
- $0 \leq x \leq L$, $[Cl^-]$ = constant
- $0 \leq x \leq L$, $[CuCl_2^-] = 0$

We do not define an initial value for E_{CORR} for the custom-designed CCM. If we need to for the COMSOL version, then we should use a value of -0.25 V_{SCE}.

A.1.7 Temperature Effects

The Step 1 model is isothermal with a constant temperature of 25°C (298.15 K).

A.1.8 Saturation Effects

The single layer is assumed to be completely saturated at all times.

A.1.9 Reaction-Diffusion Equations

No formal reaction-diffusion equations are required for the Step 1 model.

A.2 STEP 2: TRANSIENT MODEL WITH SIMPLIFIED REACTION SCHEME

A.2.1 Summary of Changes from Prior Version

The Step 2 model is exactly the same as the steady-state model described in Step 1 except that a transient solution is required.

A.2.2 Reaction Scheme

As for Step 1.

A.2.3 Geometry

As for Step 1.

A.2.4 Homogeneous Reactions

As for Step 1.

A.2.5 Boundary Conditions

A.2.5.1 Near Field

As for Step 1.

A.2.5.2 Far Field

As for Step 1.

A.2.6 Initial Conditions

As for Step 1.

A.2.7 Temperature Effects

As for Step 1.

A.2.8 Saturation Effects

As for Step 1.

A.2.9 Reaction-Diffusion Equations

As for Step 1.

A.3 STEP 3: TRANSIENT MODELS WITH INCREASING MECHANISTIC COMPLEXITY

A.3.1 Step 3a: Homogeneous Oxidation of Cu(I) and Interfacial Reduction of Cu(II)

A.3.1.1 Summary of Changes from Prior Version

In the various Step 3 models, increasingly complex reaction mechanisms are progressively introduced involving additional chemical species, reactions, and/or processes. Step 3a involves the introduction of:

- One additional species, namely Cu^{2+} (concentration c_3)
- Diffusive transport of Cu^{2+} towards and away from the container surface
- One homogeneous reaction, involving the oxidation of $CuCl_2^-$ (concentration c_1) by dissolved O_2 (concentration c_0), with an associated rate constant k_1, the value of which is dependent on the Cl^- concentration (concentration c_6)
- An additional cathodic interfacial reaction, involving the reduction of Cu^{2+} to $CuCl_2^-$

A.3.1.2 Reaction Scheme

The reaction scheme for Step 3a is shown in Figure A-3. In the figure, the red fonts highlights the new species and processes that, together with the existing species and processes from Steps 1 and 2 illustrated in black, constitute the full reaction scheme for the CCMC-D3a model.

The notation for all of the species introduced in Steps 3-5 is summarized in Table A-2.

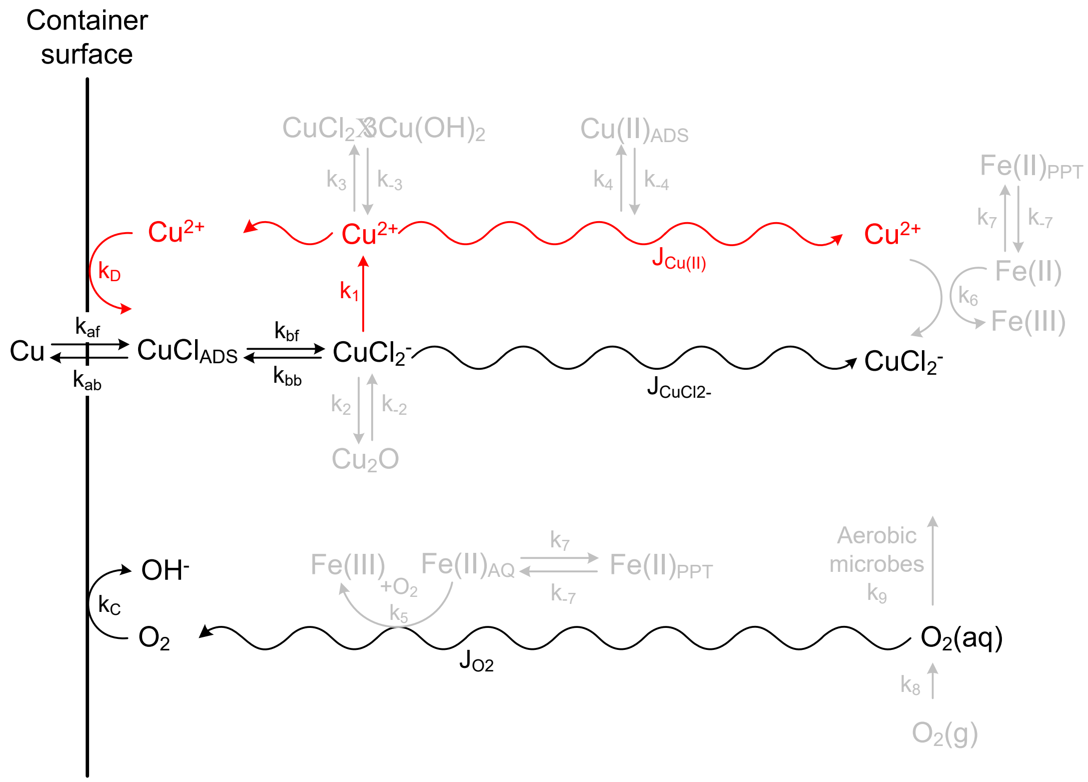

Figure A-3: Reaction Scheme for Step 3a in the Development of the CCM COMSOL code. The red font shows the additional species and processes that together with the species and processes in black font constitute the new model. Those shown greyed out are those from the reaction scheme for the custom-designed CCM Version 1.1 which will be progressively introduced in further developments of the COMSOL code.

A.3.1.3 Geometry

The geometry to be used for all sub-models in Step 3 is a 1-D, multi-layer geometry. In general, the code should be capable of handling an arbitrary number of layers since the precise geometry will depend on the system being modelled. For example, when simulating a complex DGR layout containing both buffer and backfill materials with temporally and spatially varying saturation (S(x,t)), we may need to incorporate up to eight separate layers comprising:

- Three layers of highly compacted bentonite (HCB)
- Two layers of dense backfill
- An excavation-damaged zone (EDZ)
- An excavation-disturbed zone (EdZ)
- Host rock

Table A-2: Notation for the Concentration of Each of the Chemical Species and Temperature Used in the Copper Corrosion Model.

Species	Notation
Gaseous O_2	c_A
Dissolved O_2	c_0
Dissolved $CuCl_2^-$	c_1
Precipitated Cu_2O	c_2
Dissolved Cu^{2+}	c_3
Precipitated $CuCl_2 \cdot 3Cu(OH)_2$	c_4
Adsorbed Cu(II)	c_5
Dissolved Cl^-	c_6
Dissolved Fe(II)	c_7
Precipitated Fe(II)	c_8
Temperature	T

Here, the layers representing the HCB and dense backfill are sub-divided into three and two sub-layers, respectively, so that the (externally defined) S(x,t) can better represent the expected variation in saturation within the repository. For other examples, for instance for a simpler repository design under saturated conditions or when simulating laboratory experiments, a smaller number of layers may be sufficient.

Each layer is treated as an equivalent porous medium in which the transport of species occurs by diffusion only. Thus, the pore structure in each layer is described by the porosity (ε) and tortuosity factor (τ_f). Historically, we have implicitly assumed a multi-porosity model in which the total porosity is divided into accessible (ε_a) and non-accessible (ε_{na}) porosity, representing connected and isolated pores, respectively.[1] The accessible porosity is further divided into a storage porosity (ε_s) and the effective porosity for mass transport (ε_e). Thus, the total porosity (ε_t) is given by:

$$\varepsilon_t = \varepsilon_{na} + \varepsilon_s + \varepsilon_e \tag{A-6}$$

Using this multi-porosity approach, the effective diffusion coefficient is given by:

$$D_{EFF} = \varepsilon_e \tau_f D_0 \tag{A-7}$$

where D_0 is the species-specific diffusion coefficient in bulk solution. For unsaturated systems (Step 5), the pore structure is further divided into saturated and vapour-filled components.

---

[1] Even though the non-accessible porosity is included here for completeness, we have tended to set ε_{na} to zero in order to properly account for all of the O_2 initially trapped in the pores of the HCB. Otherwise, O_2 trapped in isolated pores would logically not contribute to corrosion of the UFC, which could result in a non-conservative assessment.

This description of the pore network was derived on the basis of diffusion experiments in HCB, and may not be appropriate for other materials such as the host rock. In those cases, the description of the pore structure can be simplified by setting the values of certain types of pore to zero.

Furthermore, although the multi-porosity approach described above has been that traditionally adopted for the conventional CCM code, there may be a need in the future to consider the effects of other pore models, such as the Donnan equilibrium approach (Birgersson and Karnland 2008).

When the COMSOL code is fully developed, each of the porous layers will be characterized by the properties listed in Table A-3. Not all of these parameters will need to be defined for the Step 3 model. In particular, those parameters relating to the time-dependent degree of saturation are not required until the development of the Step 5 model.

The grid spacing for the multi-layer 1-D model should be adjusted to optimize the accuracy and speed of execution. For the custom-designed code, a geometric progression was used to increase the grid spacing from the left-hand boundary (at which concentration gradients are the steepest) to the right-hand boundary where concentration gradients are shallow and change only slowly with time.

A.3.1.4 Homogeneous Reactions

The Step 3a code includes a single homogeneous reaction, namely the oxidation of $CuCl_2^-$ by O_2:

$$4CuCl_2^- + O_2 + 2H_2O \rightarrow 4Cu^{2+} + 8Cl^- + 4OH^- \qquad \text{(A-8)}$$

for which the rate of O_2 consumption is given by

$$-\frac{\partial c_0}{\partial t} = \frac{k_1}{4} c_0 c_1 \qquad \text{(A-9)}$$

where k_1 is the overall second-order rate constant (Figure A-3). The reaction is first-order with respect to both $[O_2]$ and $[CuCl_2^-]$ and the rate constant k_1 is a function of temperature (to be included in Step 4) and $[Cl^-]$ and, therefore, varies in space and time. The value of k_1 is given by (Sharma and Millero 1988):

$$\log k_1 = 11.38 - \frac{2064}{T} - 3.69\left(\frac{c_6}{1-0.1103\,c_6}\right)^{1/2} + 0.73\left(\frac{c_6}{1-0.1103\,c_6}\right) \qquad \text{(A-10)}$$

Table A-3: Media-dependent Parameters in the CCM.

Symbol	Definition
L	Layer thickness
ε_{na}	Non-accessible porosity[1]
ε_a	Accessible (total) porosity, $\varepsilon_a = \varepsilon_e + \varepsilon_s$
ε_e	Effective porosity for mass transport
ε_s	Storage porosity. Equivalent to that part of the connected porosity that does not participate directly in diffusion, e.g., the dead-end pores, but is still accessible to the dissolved species.
τ_f	Tortuosity factor
$\rho(S)$	Bulk density
$c_A(x,0)$	Initial concentration of gaseous O_2
$c_0(x,0)$	Initial concentration of dissolved O_2
$c_6(x,0)$	Initial concentration of Cl^- ions
$c_7(x,0)$	Initial concentration of dissolved Fe(II)
c_5^{max}	Maximum concentration of adsorbed Cu^{2+}
A_F	Surface area of exposed biotite
C(S)	Bulk specific heat
K(S)	Bulk thermal conductivity
S(t)	Time-dependent degree of saturation
S_{MIC}	Minimum degree of saturation at which microbial activity can occur

[1] Typically set to zero (see footnote 1)

The homogeneous oxidation Reaction (A-8) not only results in the loss of O_2, but also the loss of $CuCl_2^-$ and the gain of both Cu^{2+} and Cl^- ions. Neither the H_2O molecules consumed nor the OH^- ions produced by Reaction (A-8) are tracked in the CCM code, and are not discussed further.[2] Thus, the rate expression Equation (A-9) can be extended to include the gain/loss terms for all species considered in the model:

$$-\frac{\partial c_0}{\partial t} = -\frac{1}{4}\frac{\partial c_1}{\partial t} = \frac{1}{4}\frac{\partial c_3}{\partial t} = \frac{1}{8}\frac{\partial c_6}{\partial t} = \frac{k_1}{4}c_0 c_1 \qquad \text{(A-11)}$$

It is important to remember that this reaction only occurs in the accessible porosity since, by definition, $CuCl_2^-$ cannot enter non-accessible (isolated) pores. Furthermore, since the oxidation reaction occurs in solution, this reaction will be limited to the saturated accessible pore space in Step 5.

---

[2] In future developments of the CCM, we may want to track both H_2O and OH^- (pH), which will require including these species in the model.

A.3.1.5 Boundary Conditions

The nature of the near- and far-field boundary conditions for Step 3a are defined in Table A-4, along with those for species to be introduced in Steps 3b-5. Non-diffusing species do not require the specification of boundary conditions.

Table A-4: Nature of the Boundary Conditions for the Diffusing Species for Steps 3-5.*

Species	Near-field boundary condition	Far-field boundary condition
$O_2(g)$	Zero flux	Zero flux
$O_2(aq)$	Electrochemical	Constant concentration
$CuCl_2^-$	Electrochemical	Zero concentration
Cu^{2+}	Electrochemical	Zero concentration
Cl^-	Electrochemical	Constant concentration
Fe(II)(aq)	Zero flux	Constant concentration
T	Time dependent	Time dependent

* Non-diffusing species are $Cu_2O(s)$, $CuCl_2.3Cu(OH)_2(s)$, Cu(II)(ads) and Fe(II)(s).

A.3.1.5.1 Near Field

Electrochemical expressions are used as the near-field boundary condition for those species that react on the container surface, namely; $O_2(aq)$, $CuCl_2^-$, Cu^{2+}, and Cl^-. The respective electrochemical reactions are:

$$\begin{aligned} Cu + Cl^- &\underset{k_{ab}}{\overset{k_{af}}{\rightleftharpoons}} CuCl_{ADS} + e^- \\ CuCl_{ADS} + Cl^- &\underset{k_{bb}}{\overset{k_{bf}}{\rightleftharpoons}} CuCl_2^- \end{aligned} \qquad \text{(A-12a)}$$

$$O_2 + 2H_2O + 4e^- \xrightarrow{k_c} 4OH^- \qquad \text{(A-12b)}$$

$$Cu^{2+} + 2Cl^- + e^- \xrightarrow{k_d} CuCl_2^- \qquad \text{(A-12c)}$$

The rate of the anodic dissolution of Cu as $CuCl_2^-$ (Reaction (A-12a)) is given by

$$i_a = n_a F\left(k_a[Cl^-]^2 \exp\left(\frac{F}{RT}(E - E_a^0)\right) - k_{bb}[CuCl_2^-]\right) \qquad \text{(A-13)}$$

where the various symbols have been defined previously.

The equivalent expressions for the reduction of O_2 (Reaction (A-12b)) and of Cu^{2+} (Reaction (A-12c)) are

$$i_c = -n_c F k_c [O_2] \exp\left(-\frac{\alpha_c F}{RT}(E - E_c^0) \right) \tag{A-14}$$

and

$$i_d = -n_d F k_d [Cu^{2+}] \exp\left(-\frac{\alpha_d F}{RT}(E - E_d^0) \right) \tag{A-15}$$

The expressions for the anodic dissolution of Cu as $CuCl_2^-$ and of the cathodic reduction of O_2 are exactly the same as used in Steps 1 and 2.

The rate of the anodic reaction must equal the sum of the rates of the two cathodic reactions

$$i_a(t) + i_c(t) + i_d(t) = 0 \tag{A-16}$$

A.3.1.5.2 Far Field

The far-field boundary physically represents a location in the host rock at which conditions are either invariant with time or their time dependence can be explicitly defined by the user (for example, as in the case of the time-dependent temperature of the host rock in the treatment of thermal effects). Logical physical locations for the far-field boundary are a major water-bearing fracture in crystalline rock (where constant concentration conditions exist for the various chemical species) or the boundary between different sequences in sedimentary rock (where there could be a significant change in local hydraulic conductivity). It is recommended that the ground surface should not be defined as the far-field boundary as this is likely to result in increased computation times with no added benefit since it is unlikely that the surface conditions will either influence, or be influenced by, the performance of the DGR.

Either constant or zero concentration boundary conditions are used for the four species in the Step 3a model, $O_2(aq)$, $CuCl_2^-$, Cu^{2+}, and Cl^- (see Table A-4).

A.3.1.6 Initial Conditions

The initial conditions for the four species included in the Step 3a model (as well as those for subsequent versions of the model) are defined in Table A-5.

Table A-5: Initial Conditions for Each of the Species Included in the CCM.

Notation	Species	Initial Condition
c_A	$O_2(g)$	$c_A(x,0) = c_{AINIT}$
c_0	$O_2(aq)$	$c_0(x,0) = c_{0INIT}$
c_1	$CuCl_2^-$	$c_1(x,0) = 0$
c_2	Cu_2O	$c_2(x,0) = 0$
c_3	Cu^{2+}	$c_3(x,0) = 0$
c_4	$CuCl_2{\cdot}3Cu(OH)_2$	$c_4(x,0) = 0$
c_5	Cu(II)(ads)	$c_5(x,0) = 0$
c_6	Cl^-	$c_6(x,0) = c_{6INIT}$
c_7	Fe(II)(aq)	$c_7(x,0) = c_{7INIT}$
c_8	Fe(II)(ppt)	$c_8(x,0) = 0$
T	-	$T(x,0) = T_{INIT}$

A.3.1.7 Temperature Effects

For Step 3a the system is treated as being isothermal with a temperature of 25°C.

A.3.1.8 Saturation Effects

Fully saturated conditions are assumed for Step 3a.

A.3.1.9 Reaction-Diffusion Equations

The custom-designed code is based on the solution of a series of 1-D reaction-diffusion equations, one for each of the chemical species in the model plus a heat-conduction equation to solve for the temperature.

The 1-D reaction-diffusion equations for dissolved O_2, $CuCl_2^-$, Cu^{2+}, and Cl^- for Step 3a are:[3]

$$\varepsilon_a \frac{\partial c_0}{\partial t} = \tau_f \varepsilon_e D_0 \frac{\partial^2 c_0}{\partial x^2} - \varepsilon_a \frac{k_1}{4} c_0 c_1 \tag{A-17}$$

$$\varepsilon_a \frac{\partial c_1}{\partial t} = \tau_f \varepsilon_e D_1 \frac{\partial^2 c_1}{\partial x^2} - \varepsilon_a k_1 c_0 c_1 \tag{A-18}$$

---

[3] Note that the reaction-diffusion equations for these four species will be different for subsequent steps as additional species and reactions are introduced.

$$\varepsilon_a \frac{\partial c_3}{\partial t} = \tau_f \varepsilon_e D_3 \frac{\partial^2 c_3}{\partial x^2} + \varepsilon_a k_1 c_0 c_1 \tag{A-19}$$

and

$$\varepsilon_a \frac{\partial c_6}{\partial t} = \tau_f \varepsilon_e D_6 \frac{\partial^2 c_6}{\partial x^2} + 2\varepsilon_a k_1 c_0 c_1 \tag{A-20}$$

A.3.2 Step 3b: Precipitation/dissolution of Solid Cu(II)

A.3.2.1 Summary of Changes from Prior Version

In Step 3b, a second homogenous reaction is introduced, namely the precipitation and dissolution of the solid Cu(II) species paratacamite ($CuCl_2 \cdot 3Cu(OH)_2$). As in Step 3a, the homogeneous reaction is treated kinetically rather than being at equilibrium, although the reaction is reversible with precipitation resulting in the loss of Cu^{2+} and dissolution resulting in a gain.

Because we track the concentration and the spatial and temporal distribution of $CuCl_2 \cdot 3Cu(OH)_2$, it is included as a new species in the model (concentration c_4).

A.3.2.2 Reaction Scheme

The reaction scheme for Step 3b is shown in Figure A-4. The updated scheme results in the addition of one species ($CuCl_2 \cdot 3Cu(OH)_2$) and two reactions (denoted by rate constants k_3 and k_{-3}) to the reaction scheme used for the prior Step 3a.

A.3.2.3 Geometry

The model geometry is the same as that for Step 3a.

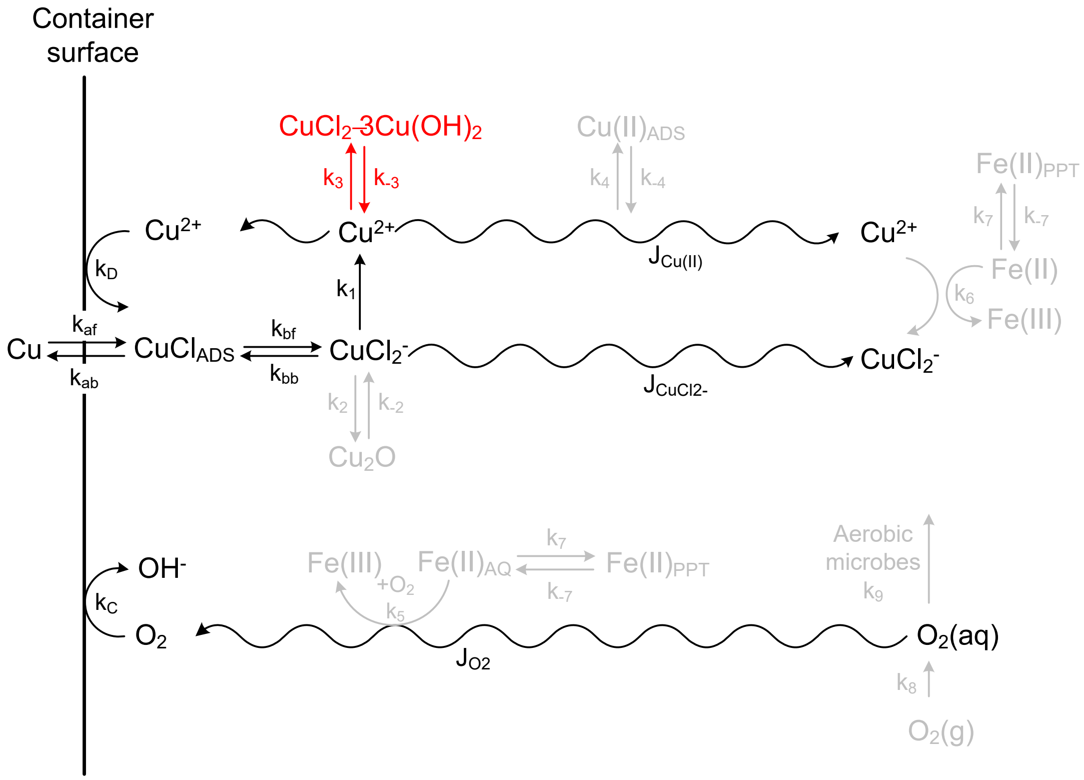

Figure A-4: Reaction Scheme for Step 3b in the Development of the COMSOL CCM Code. The species and reactions shown in red font are those added to the reaction scheme from Step 3a.

A.3.2.4 Homogeneous Reactions

Precipitation of $CuCl_2 \cdot 3Cu(OH)_2$ occurs from a supersaturated solution of dissolved Cu(II) (King et al. 2001, 2002b). Dissolution of $CuCl_2 \cdot 3Cu(OH)_2$ is most likely to occur chemically, rather than via a reductive dissolution mechanism, because the high electrical resistivity of geological specimens of atacamite suggests that the surface would not mediate electron-transfer reactions (King and Standlund, unpublished work). Thus, the precipitation and dissolution of $CuCl_2 \cdot 3Cu(OH)_2$ can be described by the reversible reaction

$$4Cu^{2+} + 6OH^{-} + 2Cl^{-} \underset{k_{-3}}{\overset{k_3}{\rightleftharpoons}} CuCl_2 \cdot 3Cu(OH)_2 \quad \text{(A-21)}$$

The rate of precipitation is given by

$$\frac{\partial c_4}{\partial t} = \frac{k_3}{4} \max(0, c_3 - c_3^{sat}) \quad \text{(A-22)}$$

where c_3^{sat} is the concentration of Cu^{2+} in a saturated solution in equilibrium with $CuCl_2{\cdot}3Cu(OH)_2$ and k_3 is the first-order rate constant for the precipitation reaction. The "max" term in Equation (A-22) ensures that precipitation does not occur from a solution that is not super-saturated with respect to dissolved Cu^{2+}. The "max" term takes the value of the maximum of the two terms in the argument.

The rate of dissolution of $CuCl_2{\cdot}3Cu(OH)_2$ is given by

$$-\frac{\partial c_4}{\partial t} = k_{-3}c_4 \tag{A-23}$$

where c_4 is the "concentration of $CuCl_2{\cdot}3Cu(OH)_2$" in units of moles per unit volume of buffer, backfill or host rock and k_{-3} is the corresponding first-order rate constant.

The precipitation and dissolution of $CuCl_2{\cdot}3Cu(OH)_2$ also results in the loss and gain, respectively, of Cl^-. These gain and loss terms are reflected in the reaction-diffusion equations for Cl^- (species c_6) given below.

A.3.2.5 Boundary Conditions

A.3.2.5.1 Near Field

The near-field boundary conditions for Step 3b are the same as those for Step 3a.

A.3.2.5.2 Far Field

The far-field boundary conditions for Step 3b are the same as those for Step 3a.

A.3.2.6 Initial Conditions

The initial conditions for the five species included in Step 3b (along with those for other species to be introduced in subsequent versions of the code) are defined in Table A-5.

A.3.2.7 Temperature Effects

As for previous steps, the Step 3b is an isothermal code with a temperature of 25°C.

A.3.2.8 Saturation Effects

As for previous steps, the domains in the Step 3b model are treated as being fully saturated.

A.3.2.9 Reaction-Diffusion Equations

The reaction-diffusion equations for the five species in the Step 3b model are as follows:

$$\varepsilon_a \frac{\partial c_0}{\partial t} = \tau_f \varepsilon_e D_0 \frac{\partial^2 c_0}{\partial x^2} - \varepsilon_a \frac{k_1}{4} c_0 c_1 \tag{A-24}$$

$$\varepsilon_a \frac{\partial c_1}{\partial t} = \tau_f \varepsilon_e D_1 \frac{\partial^2 c_1}{\partial x^2} - \varepsilon_a k_1 c_0 c_1 \tag{A-25}$$

$$\varepsilon_a \frac{\partial c_3}{\partial t} = \tau_f \varepsilon_e D_3 \frac{\partial^2 c_3}{\partial x^2} + \varepsilon_a \left[k_1 c_0 c_1 - k_3 \max(0, c_3 - c_3^{sat}) \right] + 4k_{-3} c_4 \tag{A-26}$$

$$\frac{\partial c_4}{\partial t} = \varepsilon_a \frac{k_3}{4} \max(0, c_3 - c_3^{sat}) - k_{-3} c_4 \tag{A-27}$$

$$\varepsilon_a \frac{\partial c_6}{\partial t} = \tau_f \varepsilon_e D_6 \frac{\partial^2 c_6}{\partial x^2} + \varepsilon_a \left[2k_1 c_0 c_1 - \frac{k_3}{2} \max(0, c_3 - c_3^{sat}) \right] + 2k_{-3} c_4 \tag{A-28}$$

The reaction-diffusion equations for dissolved O_2 (species c_0) and $CuCl_2^-$ (species c_1) are exactly the same for Step 3b as for Step 3a. The reaction-diffusion equations for dissolved Cu^2 (species c_3) and Cl^- (species c_6) are different, with the additional terms shown in red font. Equation (A-27) is the reaction-diffusion equation for the new species $CuCl_2 \cdot 3Cu(OH)_2$ (species 4).

By convention, the “concentration” of solid species are referred to unit volume of the entire medium (pores plus solids) in the custom-designed CCM, as opposed to per unit volume of pore solution for dissolved species. As a result, reactions involving the precipitation from solution of a dissolved species include the accessible porosity term ε_a, whereas those involving dissolution of a solid phase do not.

A.3.3 Step 3c: Precipitation/dissolution of Solid Cu_2O

A.3.3.1 Summary of Changes from Prior Version

The incremental change for Step 3c is similar to that for Step 3b, except in this case we are simulating the precipitation and dissolution of a Cu(I) solid, namely Cu_2O (species c_2).

As before, therefore, the changes for Step 3c result in the addition of one species and two reactions (rate constants k_2 and k_{-2}).

A.3.3.2 Reaction Scheme

The reaction scheme for Step 3c is shown in Figure A-5.

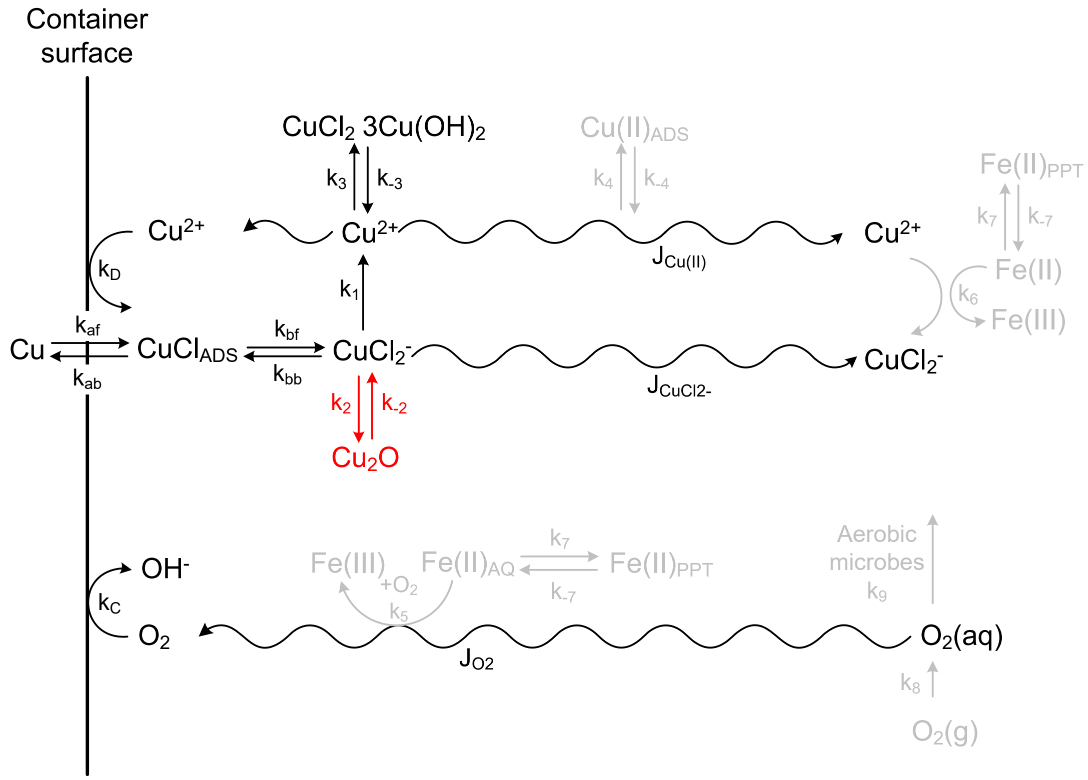

Figure A-5: Reaction Scheme for Step 3c in the Development of the COMSOL CCM Code. The species and reactions shown in red font are those added to the reaction scheme from Step 3b.

A.3.3.3 Geometry

The model geometry is the same as that for Steps 3a and 3b.

A.3.3.4 Homogeneous Reactions

The precipitation and dissolution of Cu_2O are treated in an analogous fashion to the corresponding reactions for $CuCl_2{\cdot}3Cu(OH)_2$ in Step 3b.

The detailed mechanism by which the Cu_2O forms is not completely understood, but may involve the dehydration of a $Cu(OH)_{ADS}$ intermediate species or the hydrolysis of dissolved $CuCl_2^-$ (King and Kolar 2000; King et al. 1995a,b, 2001, 2002b). The former process typically is responsible for the formation of the first monolayer or two of Cu_2O, but is unlikely to be responsible for the majority of the relatively thick Cu_2O layer observed experimentally (King et al. 2001, 2002b). Therefore, the most likely reaction for the precipitation of Cu_2O is

$$2CuCl_2^- + H_2O \underset{k_{-2}}{\overset{k_2}{\rightleftharpoons}} Cu_2O + 4Cl^- + 2H^+ \qquad \text{(A-29)}$$

Given that water is generally present in excess in the system, the rate of Cu_2O precipitation is taken to be first order with respect to the concentration of $CuCl_2^-$ and is given by

$$\frac{\partial c_2}{\partial t} = \frac{k_2}{2}\max(0, c_1 - c_1^{sat}) \tag{A-30}$$

where c_1^{sat} is the concentration of $CuCl_2^-$ in a saturated solution in equilibrium with Cu_2O and k_2 is the first-order rate constant for the precipitation reaction. As before, the $\max(0, c_1 - c_1^{sat})$ term in Equation (A-30) prevents Cu_2O from precipitating from an under-saturated solution in the model.

King and Légère (unpublished work) studied the dissolution of Cu_2O powder as a function of pH and Cl^- concentration. The rate was found to be independent of $[Cl^-]$, but to be a function of pH. The rate expression for the dissolution of Cu_2O derived from this work and used in the CCM is

$$-\frac{\partial c_2}{\partial t} = k_{-2}c_2 \tag{A-31}$$

where c_2 is the concentration of Cu_2O in units of moles per unit volume of buffer, backfill or host rock, and k_{-2} is the corresponding first-order dissolution rate constant.

The precipitation and dissolution of Cu_2O also results in the gain and loss, respectively, of Cl^-. These gain and loss terms are reflected in the reaction-diffusion equations for Cl^- (species c_6) given below.

A.3.3.5 Boundary Conditions

A.3.3.5.1 Near Field

The near-field boundary conditions for Step 3c are the same as those for Steps 3a and 3b.

A.3.3.5.2 Far Field

The far-field boundary conditions for Step 3c are the same as those for Steps 3a and 3b.

A.3.3.6 Initial Conditions

The initial conditions for the six species included in Step 3c (along with those for other species to be introduced in subsequent versions of the code) are defined in Table A-5.

A.3.3.7 Temperature Effects

As for previous steps, the Step 3c model is an isothermal code with a temperature of 25°C.

A.3.3.8 Saturation Effects

As for previous steps, the domains in the Step 3c model are treated as being fully saturated.

A.3.3.9 Reaction-Diffusion Equations

The reaction-diffusion equations for the six species in the Step 3c model are as follows:

$$\varepsilon_a \frac{\partial c_0}{\partial t} = \tau_f \varepsilon_e D_0 \frac{\partial^2 c_0}{\partial x^2} - \varepsilon_a \frac{k_1}{4} c_0 c_1 \tag{A-32}$$

$$\varepsilon_a \frac{\partial c_1}{\partial t} = \tau_f \varepsilon_e D_1 \frac{\partial^2 c_1}{\partial x^2} - \varepsilon_a \left[k_1 c_0 c_1 + k_2 \max(0, c_1 - c_1^{sat}) \right] + 2k_{-2} c_2 \tag{A-33}$$

$$\frac{\partial c_2}{\partial t} = \varepsilon_a \frac{k_2}{2} \max(0, c_1 - c_1^{sat}) - k_{-2} c_2 \tag{A-34}$$

$$\varepsilon_a \frac{\partial c_3}{\partial t} = \tau_f \varepsilon_e D_3 \frac{\partial^2 c_3}{\partial x^2} + \varepsilon_a \left[k_1 c_0 c_1 - k_3 \max(0, c_3 - c_3^{sat}) \right] + 4k_{-3} c_4 \tag{A-35}$$

$$\frac{\partial c_4}{\partial t} = \varepsilon_a \frac{k_3}{4} \max(0, c_3 - c_3^{sat}) - k_{-3} c_4 \tag{A-36}$$

$$\varepsilon_a \frac{\partial c_6}{\partial t} = \tau_f \varepsilon_e D_6 \frac{\partial^2 c_6}{\partial x^2} + \varepsilon_a \left[2k_1 c_0 c_1 + 2k_2 \max(0, c_1 - c_1^{sat}) - \frac{k_3}{2} \max(0, c_3 - c_3^{sat}) \right] + 2k_{-3} c_4 - 4k_{-2} c_2 \tag{A-37}$$

For Step 3c, the reaction-diffusion equations for O_2 (Equation (A-32)), Cu^{2+} (Equation (A-35)), and $CuCl_2{\cdot}3Cu(OH)_2$ (Equation (A-36)) are the same as for Step 3b. Incremental changes to the reaction-diffusion equations for $CuCl_2^-$ (Equation (A-33)) and Cl^- (Equation (A-37)) are shown in red font.

As for Step 3b, reactions involving the precipitation from solution of a dissolved species include the accessible porosity term ε_a, whereas those involving dissolution of a solid phase do not.

A.3.4 Step 3d: Adsorption/desorption of Cu(II)

A.3.4.1 Summary of Changes from Prior Version

The adsorption/desorption of Cu^{2+} provides an alternative reaction for this species, in addition to diffusion and cathodic reduction on the copper surface (Step 3a) and/or precipitation as $CuCl_2{\cdot}3Cu(OH)_2$ (Step 3b).

These changes introduce one additional species (adsorbed Cu(II), species c_5) and two additional reactions for the adsorption and desorption of Cu^{2+} (rate constants k_4 and k_{-4}, respectively).

Adsorption/desorption is most important for HCB, although it is assumed that all porous materials can adsorb Cu(II) to some degree. A maximum adsorption capacity (c_5^{max}) is defined for each material.

A.3.4.2 Reaction Scheme

The reaction scheme for Step 3d is illustrated in Figure A-6.

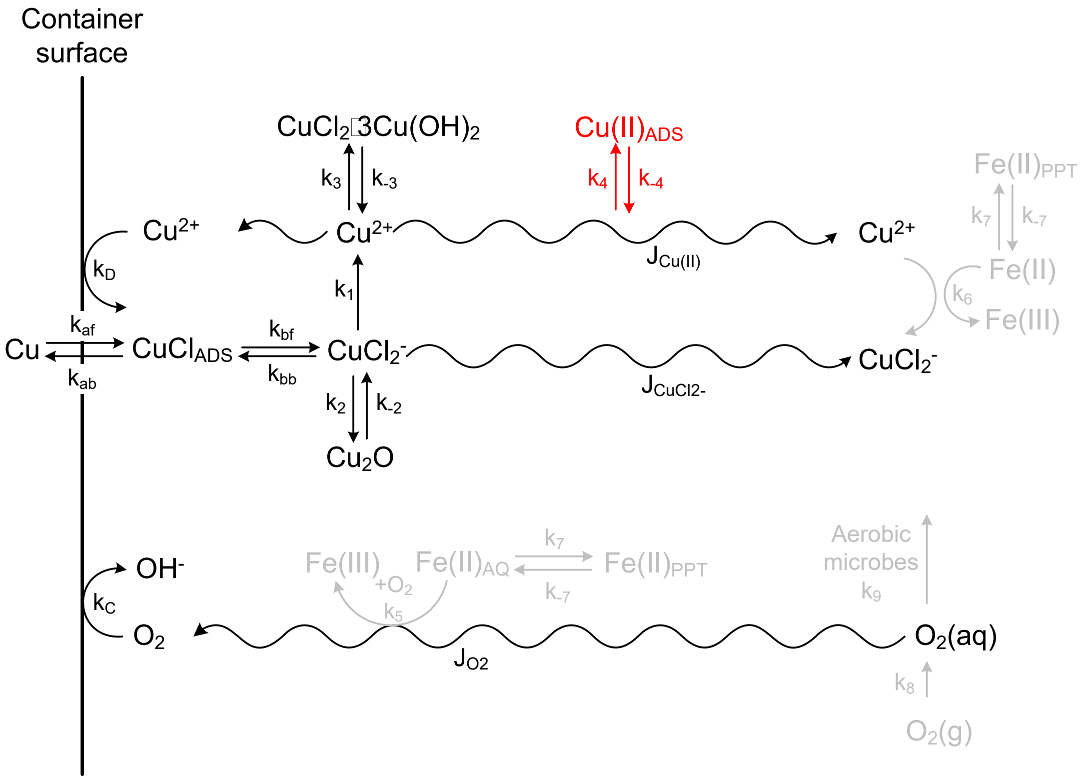

Figure A-6: Reaction Scheme for Step 3d in the Development of the COMSOL CCM Code. The species and reactions shown in red font are those added to the reaction scheme from Step 3c.

A.3.4.3 Geometry

The model geometry is the same as that for Steps 3a-3c.

A.3.4.4 Homogeneous Reactions

Dissolved Cu(II) adsorbs strongly on sodium bentonite (Ryan and King 1994) and could adsorb on other mineral surfaces within the repository and geosphere. On the other hand, cuprous species in the form of anionic $CuCl_2^-$ species do not adsorb (King et al. 1992, 2001, 2002b).

It is common to model the adsorption of radionuclides on clay using equilibrium linear isotherms (Cook 1988), since the concentration of species is small compared with the cation-exchange capacity of the clay and sorption and desorption are assumed to be fast relative to the rate of diffusion. In the case of the corrosion of copper in buffer material, however, experimental studies have shown that the total concentration of copper in the buffer close to the corroding surface equals or exceeds the cation-exchange capacity of Na-bentonite (King et al. 1992, Litke et al. 1992). Consequently, it is unlikely that the adsorption behaviour is linear (i.e., the ratio of dissolved to adsorbed concentrations of Cu^{2+} is constant) over the entire concentration range of interest. Equilibrium adsorption studies on loose and compacted Na-bentonite suggest that a Langmuir or Freundlich-type isotherms are more appropriate (Ryan and King 1994). In addition, the rate of desorption of Cu^{2+} from Na-bentonite is much slower than its rate of adsorption. Modelling studies suggest that the adsorption/desorption of diffusing Cu^{2+} on compacted Na-bentonite may not be at equilibrium (King et al. 1996).

The adsorption and desorption of Cu^{2+} on bentonite, and other mineral surfaces can be described by

$$Cu^{2+} + 2Y^{-} \underset{k_{-4}}{\overset{k_4}{\rightleftharpoons}} CuY_2 \qquad \text{(A-38)}$$

where Y^- represents a singly charged adsorption site and CuY_2 an adsorbed species. Mathematically, this process is modelled using a kinetic Langmuir expression, with the rate of adsorption given by

$$\frac{\partial c_5}{\partial t} = k_4 c_3 (c_5^{max} - c_5) \quad \text{for} \quad c_5 < c_5^{max} \qquad \text{(A-39)}$$

where, for the Langmuir expression, the rate of adsorption is proportional to both the concentration of dissolved Cu^{2+} (c_3) and the concentration of vacant surface sites ($c_5^{max} - c_5$), where c_5^{max} is the maximum surface coverage of adsorbed copper, and k_4 is the second-order adsorption rate constant. The rate of desorption is proportional to the concentration of adsorbed Cu(II)

$$-\frac{\partial c_5}{\partial t} = k_{-4} c_5 \qquad \text{(A-40)}$$

where k_{-4} is the desorption rate constant.

Note that the adsorption expression is only valid for $c_5 < c_5^{max}$. If c_5 exceeds c_5^{max} then adsorbed Cu(II) will desorb (as the term ($c_5^{max} - c_5$) will be negative), but at an incorrect rate that also depends on the concentration of Cu^{2+} (c_3). This should not be an issue provided that c_5 approaches the value of c_5^{max} asymptotically and never exceeds c_5^{max}.

A.3.4.5 Boundary Conditions

A.3.4.5.1 Near Field

The near-field boundary conditions for Step 3d are the same as those for Steps 3a-3c.

A.3.4.5.2 Far Field

The far-field boundary conditions for Step 3d are the same as those for Steps 3a-3c.

A.3.4.6 Initial Conditions

The initial conditions for the seven species included in Step 3d (along with those for other species to be introduced in subsequent versions of the code) are defined in Table A-5.

A.3.4.7 Temperature Effects

As for previous steps, Step 3d is an isothermal code with a temperature of 25°C.

A.3.4.8 Saturation Effects

As for previous steps, the domains in the Step 3d model are treated as being fully saturated.

A.3.4.9 Reaction-Diffusion Equations

The reaction-diffusion equations for the seven species in the Step 3d model are as follows:

$$\varepsilon_a \frac{\partial c_0}{\partial t} = \tau_f \varepsilon_e D_0 \frac{\partial^2 c_0}{\partial x^2} - \varepsilon_a \frac{k_1}{4} c_0 c_1 \tag{A-41}$$

$$\varepsilon_a \frac{\partial c_1}{\partial t} = \tau_f \varepsilon_e D_1 \frac{\partial^2 c_1}{\partial x^2} - \varepsilon_a \left[k_1 c_0 c_1 + k_2 \max(0, c_1 - c_1^{sat})\right] + 2k_{-2} c_2 \tag{A-42}$$

$$\frac{\partial c_2}{\partial t} = \varepsilon_a \frac{k_2}{2} \max(0, c_1 - c_1^{sat}) - k_{-2} c_2 \tag{A-43}$$

$$\varepsilon_a \frac{\partial c_3}{\partial t} = \tau_f \varepsilon_e D_3 \frac{\partial^2 c_3}{\partial x^2} + \varepsilon_a \left[k_1 c_0 c_1 - k_3 \max(0, c_3 - c_3^{sat}) - k_4 c_3 (c_5^{max} - c_5) \rho_d\right] + 4k_{-3} c_4 + k_{-4} c_5 \rho_d \tag{A-44}$$

$$\frac{\partial c_4}{\partial t} = \varepsilon_a \frac{k_3}{4} \max(0, c_3 - c_3^{sat}) - k_{-3} c_4 \tag{A-45}$$

$$\rho_d \frac{\partial c_5}{\partial t} = \varepsilon_a k_4 c_3 (c_5^{max} - c_5) \rho_d - k_{-4} c_5 \rho_d \tag{A-46}$$

$$\varepsilon_a \frac{\partial c_6}{\partial t} = \tau_f \varepsilon_e D_6 \frac{\partial^2 c_6}{\partial x^2} + \varepsilon_a \left[2k_1 c_0 c_1 + 2k_2 \max(0, c_1 - c_1^{sat}) - \frac{k_3}{2} \max(0, c_3 - c_3^{sat})\right] + 2k_{-3} c_4 - 4k_{-2} c_2$$

(A-47)

The reaction-diffusion equations for Step 3d for dissolved O_2 (Equation (A-41)), $CuCl_2^-$ (Equation (A-42)), Cu_2O (Equation (A-43)), $CuCl_2{\cdot}3Cu(OH)_2$ (Equation (A-45)), and Cl^- (Equation (A-47)) are the same as those for Step 3c. Only the reaction-diffusion equation for Cu^{2+} (Equation (A-44)) has been updated.

Because the concentration of adsorbed Cu^{2+} (c_5) is expressed per unit mass of the adsorbate, it is necessary to include the dry density of the material (ρ_d) in the reaction-diffusion equation.

A.3.5 Step 3e: Aerobic Respiration

A.3.5.1 Summary of Changes from Prior Version

The inclusion of aerobic microbial respiration introduces an additional sink by dissolved O_2. If microbes are active within the system then aerobic bacteria will consume a fraction of the initially trapped O_2

$$O_2 \xrightarrow{\text{aerobes}} 2H_2O \tag{A-48}$$

where the rate of reaction is assumed to be first-order with respect to the concentration of dissolved O_2

$$-\frac{dc_0}{dt} = k_9 c_0 \theta (1 - S_{MIC}) \tag{A-49}$$

where the S_{MIC} is the threshold degree of saturation below which microbes are not active, k_9 is the corresponding first-order rate constant, and the operator θ takes the value of 1 if the argument is positive and zero if the argument has a value of ≤ 0.

There is strong evidence to indicate that microbes are only active above a given water activity a_W (Brown 1990). In compacted clay systems, it has been found that microbial activity is suppressed below an a_W of approximately 0.96, a value that can be achieved either by using a sufficient HCB density or by using a pore-water solution of sufficient salinity (Stroes-Gascoyne et al. 2006, 2007). Due to the suction properties of HCB, an a_W of 0.96 is also achieved at low water contents, and the threshold can be expressed as a threshold degree of saturation (S_{MIC}) below which microbial activity does not occur based on the Van Genuchten-type soil-water characteristic curve for the clay material (Man and Martino 2009).

A.3.5.2 Reaction Scheme

The reaction scheme for Step 3e is shown in Figure A-7.

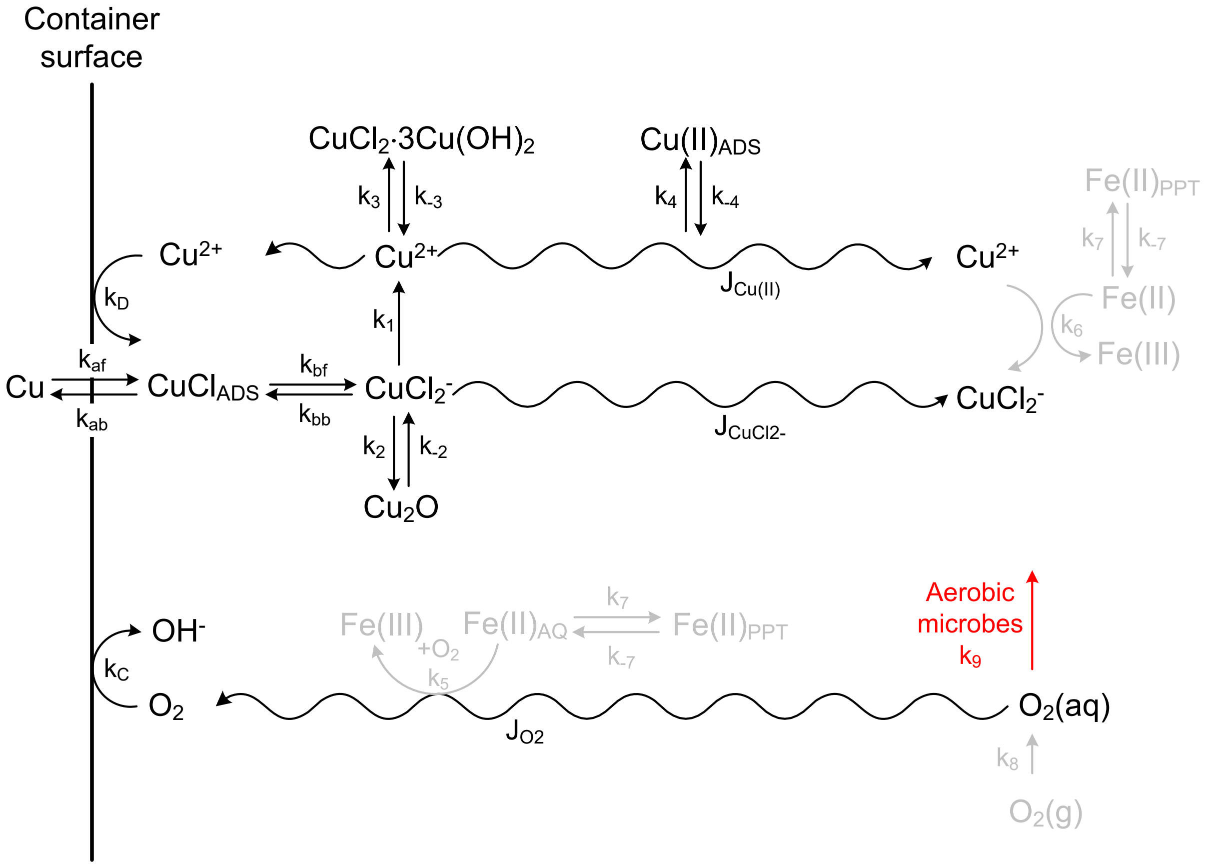

Figure 76: Reaction scheme for Step 3e in the development of the COMSOL CCM code. The species and reactions shown in red font are those added to the reaction scheme from Step 3d.

A.3.5.3 Geometry

The model geometry is the same as that for Steps 3a-3d.

A.3.5.4 Homogeneous Reactions

The single additional homogeneous reaction is given above in Equations (A-48) and (A-49).

A.3.5.5 Boundary Conditions

A.3.5.5.1 Near Field

The near-field boundary conditions for Step 3e are the same as those for Step 3d. No additional diffusing species requiring the definition of left-hand and right-hand boundary conditions are introduced in Step 3e.

A.3.5.5.2 Far Field

The far-field boundary conditions for Step 3e are the same as those for Step 3d. No additional diffusing species requiring the definition of left-hand and right-hand boundary conditions are introduced in Step 3e.

A.3.5.6 Initial Conditions

The initial conditions for the seven species included in Step 3e (along with those for other species to be introduced in subsequent versions of the code) are defined in Table A-5.

A.3.5.7 Temperature Effects

As for previous steps, the Step 3e model is an isothermal code with a temperature of 25°C.

A.3.5.8 Saturation Effects

As for previous steps, the domains in the Step 3e model are treated as being fully saturated.

A.3.5.9 Reaction-Diffusion Equations

$$\varepsilon_a \frac{\partial c_0}{\partial t} = \tau_f \varepsilon_e D_0 \frac{\partial^2 c_0}{\partial x^2} - \varepsilon_a \left[\frac{k_1}{4} c_0 c_1 + k_9 c_0 \theta (1 - S_{MIC}) \right] \tag{A-50}$$

A.3.6 Step 3f: Reactions Involving Fe(II)/Fe(III)

A.3.6.1 Summary of Changes from Prior Version

Redox processes involving Fe(II)/Fe(III) species are treated in the CCM Version 1.1 by the introduction of two new species representing dissolved Fe(II) (concentration c_7, Table A-2) and a secondary precipitated Fe(II) phase (c_8, Table A-2). The dissolved Fe(II) participates in redox reactions with both dissolved O_2 and Cu^{2+}.

The source of dissolved Fe(II) is the dissolution or alteration of an Fe(II)-bearing mineral phase, such as biotite or pyrite, present either as an accessory mineral in the buffer or backfill or as a component of the host rock.

If more dissolved Fe(II) is formed by dissolution of the pyrite or biotite than is consumed in the subsequent redox reaction, as might occur under anaerobic conditions in the absence of oxidized species, then excess dissolved Fe(II) can precipitate as a secondary Fe(II) solid phase (c_8), subject to solubility constraints.

The ferric species formed by the reaction between dissolved Fe(II) and either O_2 or Cu^{2+} is not specifically treated in the model as it is assumed to irreversibly precipitate as a low-solubility Fe(III) solid.

A.3.6.2 Reaction Scheme

The reaction scheme for Step 3f is shown in Figure A-8.

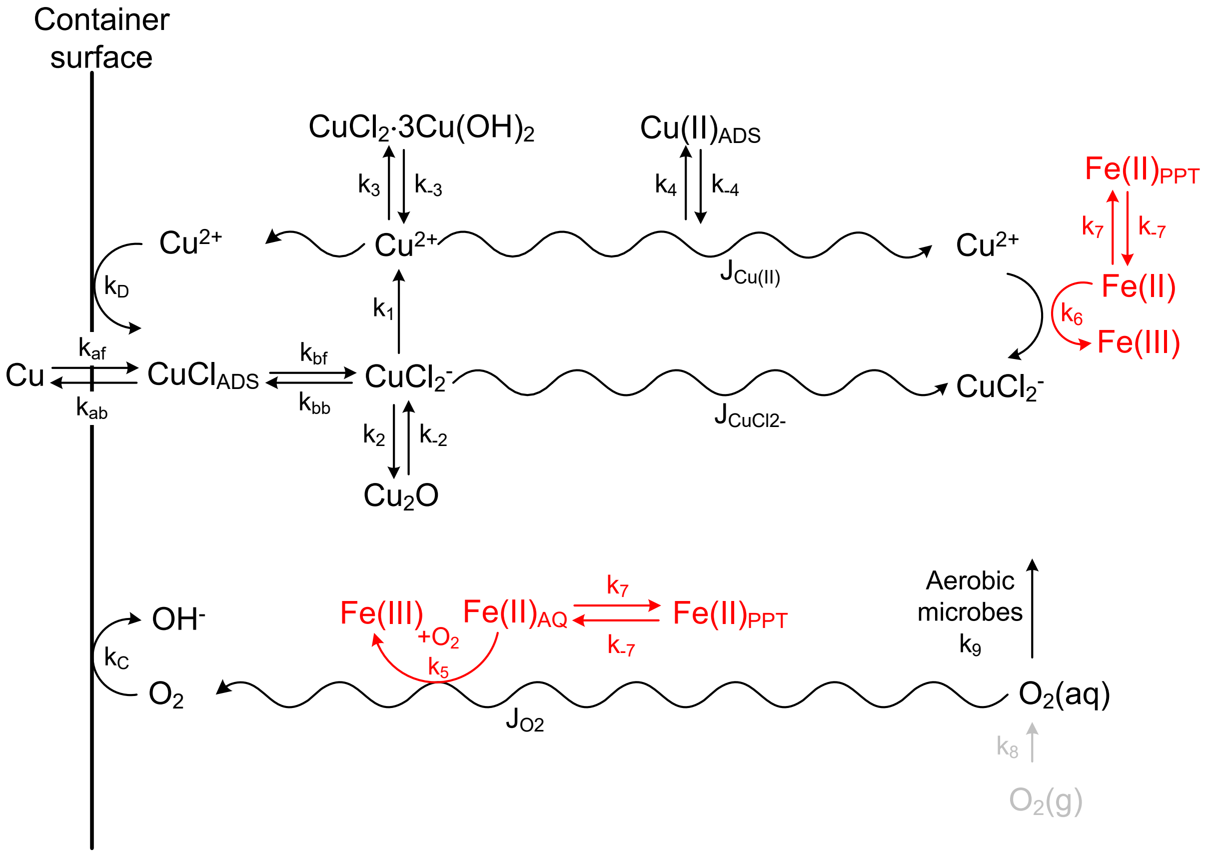

Figure A-8: Reaction scheme for Step 3f in the development of the COMSOL CCM code. The species and reactions shown in red font are those added to the reaction scheme from Step 3e.

A.3.6.3 Geometry

The model geometry is the same as that for Steps 3a-3e.

A.3.6.4 Homogeneous Reactions

The dissolution of the Fe(II) mineral phase (typically pyrite or biotite) is treated kinetically according to a "shrinking-core" model, in which an altered layer depleted in the element of interest precipitates as the mineral dissolves. The kinetics of such reactions are described by

$$\frac{d[\mathrm{Fe(II)}]}{dt} = A_F [R_0 \exp(-\alpha_F t) + R_1] \qquad \text{(A-51)}$$

where A_F is the area of exposed mineral per unit volume of buffer, backfill or rock, R_0 and R_1 are the initial and steady-state Fe(II) dissolution rate, and α_F determines the rate at which the steady-state dissolution rate is attained. A steady state is eventually established in which the dissolution rate of Fe(II) is governed by the dissolution rate of the least-soluble component of the mineral lattice. The values of α_F, R_0 and R_1 will vary from mineral to mineral.

In the CCM Version 1.1, A_F is treated as a user-defined constant that varies only from layer to layer (i.e., from material to material). Implicit in this treatment is the assumption that the Fe(II) mineral is present to excess. This is an important assumption that was modified in the Copper Sulphide Model (CSM) derived from the CCM. In the CSM, the initial quantity of the Fe(II) mineral phase is specified, and the formation of dissolved Fe(II) stops once all of the initial inventory has been consumed.

Following dissolution, Fe(II) is oxidized in solution by O_2, according to

$$4\text{Fe(II)} + O_2 + 2H_2O \rightarrow 4\text{Fe(III)} + 4OH^- \tag{A-52}$$

followed by irreversible precipitation of $Fe(OH)_3$, at the pH of interest in natural waters. The kinetics of Reaction (A-52) are strongly pH-dependent (Stumm 1992), with (at pH > 5)

$$-\frac{d[\text{Fe(II)}]}{dt} = k[\text{Fe(II)}][OH^-]^2[O_2] \tag{A-53}$$

where the rate constant k_5 defined in the model is the term $k[OH^-]^2$.

At low $[O_2]$, the rate of Fe(II) oxidation (Equation (A-53)) may become smaller than the rate of Fe(II) dissolution (Equation (A-51)). Under those circumstances, Fe(II) will accumulate in the system and may ultimately precipitate (see below).

Dissolved Fe(II) may also react with Cu^{2+} via the overall reaction

$$Cu^{2+} + 2Cl^- + \text{Fe(II) (aq)} \rightarrow \text{Fe(III)} + CuCl_2^- \tag{A-54}$$

This reaction is assumed here to be first order with respect to both $[Cu^{2+}]$ and [Fe(II)]

$$-\frac{d[\text{Fe(II)}]}{dt} = -\frac{d[Cu^{2+}]}{dt} = k_6\,[Cu^{2+}][\text{Fe(II)}] \tag{A-55}$$

where k_6 is the corresponding second-order rate constant.

The precipitation of Fe(II) is also included in the model as an Fe(II) secondary phase (Fe(II)_{ppt}). If the rate of dissolution of Fe(II) from ferrous mineral phases in the repository exceeds the rate at which the Fe(II) is subsequently oxidized by reaction with O_2 or Cu^{2+}, the secondary Fe(II) phase will precipitate if the dissolved ferrous ion concentration exceeds the solubility of the secondary phase, as given by

$$\text{Fe(II)}_{aq} = \text{Fe(II)}_{ppt} \tag{A-56}$$

The kinetic expressions for the rates of precipitation and dissolution are given by

$$-\frac{d[\mathrm{Fe(II)_{aq}}]}{dt} = k_7 \max\left[0, ([\mathrm{Fe(II)_{aq}}] - [\mathrm{Fe(II)_{aq}}]_{sat}\right] \tag{A-57}$$

and

$$-\frac{d[\mathrm{Fe(II)_{ppt}}]}{dt} = k_{-7}[\mathrm{Fe(II)_{ppt}}] \tag{A-58}$$

where $[\mathrm{Fe(II)_{aq}}]_{sat}$ (c_7^{sat}) is the concentration of $\mathrm{Fe(II)_{aq}}$ in a saturated solution in equilibrium with the $\mathrm{Fe(II)_{ppt}}$ phase and k_7 and k_{-7} are the respective first-order rate constants.

A.3.6.5 Boundary Conditions

Left-hand and right-hand boundary conditions must be specified for the dissolved Fe(II) (c_7). Boundary conditions do not need to be specified for the Fe(II) secondary-phase precipitate (c_8) as it is a solid species.

A.3.6.5.1 Near Field

A zero-flux condition is used for the left-hand boundary for dissolved Fe(II) c_7 (Table A-4).

A.3.6.5.2 Far Field

A constant-concentration condition is used for the right-hand boundary for dissolved Fe(II) c_7 (Table A-4), with the concentration equivalent to that in the ground water.

A.3.6.6 Initial Conditions

The initial conditions for the nine species included in Step 3f are defined in Table A-5.

A.3.6.7 Temperature Effects

As for previous steps, the Step 3f model is an isothermal code with a temperature of 25°C.

A.3.6.8 Saturation Effects

As for previous steps, the domains in the Step 3f model are treated as being fully saturated.

A.3.6.9 Reaction-Diffusion Equations

The updated reaction-diffusion equation for dissolved O_2 (c_0) is given by

$$\varepsilon_a \frac{\partial c_0}{\partial t} = \frac{\partial}{\partial x}\left(\tau_f \varepsilon_e D_0 \frac{\partial c_0}{\partial x}\right) - \varepsilon_a \left[\frac{k_1}{4} c_0 c_1 + k_5 c_0 c_7 + k_9 c_0 \theta (S - S_{MIC})\right] \tag{A-59}$$

The updated reaction-diffusion equation for Cu^{2+} (c_3) is given by

$$\varepsilon_a \frac{\partial c_3}{\partial t} = \frac{\partial}{\partial x}\left(\tau_f \varepsilon_e D_3 \frac{\partial c_3}{\partial x}\right) + \varepsilon_a \left[k_1 c_0 c_1 - k_6 c_3 c_7 - k_3 \max(0, c_3 - c_3^{sat}) - k_4 c_3 (c_5^{max} - c_5) \rho_d\right] + 4k_{-3} c_4 + k_{-4} c_5 \rho_d \tag{A-60}$$

The reaction-diffusion equation for dissolved Fe(II) (c_7) is given by

$$\begin{aligned} \varepsilon_a \frac{\partial c_7}{\partial t} &= \frac{\partial}{\partial x}\left(\tau_f \varepsilon_e D_7 \frac{\partial c_7}{\partial x}\right) + \varepsilon_a A_F [R_0 e^{-\alpha_F t} + R_1] \\ &\quad - \varepsilon_a [4k_5 c_0 c_7 + k_6 c_3 c_7 + k_7 \max(0, c_7 - c_7^{sat})] + k_{-7} c_8 \end{aligned} \tag{A-61}$$

The reaction-diffusion equation for the precipitated Fe(II) secondary phase (c_8) is given by

$$\frac{\partial c_8}{\partial t} = \varepsilon_a k_7 \max(0, c_7 - c_7^{sat}) - k_{-7} c_8 \tag{A-62}$$

APPENDIX B: INPUT PARAMETER VALUES

B.1 LAYER (DOMAIN) SPECIFIC PROPERTIES

The layer-dependent properties will depend on the system being modelled. Here, input data are provided for layers of highly compacted bentonite (HCB) and gapfill (Table B.1). The HCB properties apply to both the shaped buffer components of the buffer box and the spacer blocks between buffer boxes (Dixon 2019). The gapfill is used to fill the spaces between the HCB blocks and the tunnel walls. Data are taken from Dixon (2019) and Gobien et al. (2016).

The basis for each of the values in Table B.1 is as follows:

L	Layer thickness (m). Based on the buffer volume:UFC surface area ratio for HCB of 657 m^3 for 338 buffer boxes and 4.455 m^2 (calculated) (Table 6.1 and Figure 6.2, Gobien et al. 2016) and actual dimension of 0.1 m for gapfill (Figure 6.2, Gobien et al. 2016).
ε_e, ε_s	Effective and storage porosities (unitless). Based on assumption that 100% of total porosity of 0.382 for HCB and 0.486 for gapfill (Table 6.4, Gobien et al. 2016) is accessible, and is equally divided between interconnected through pores and dead-end pores, respectively.
τ_f	Tortuosity factor (unitless). Assumed value for both HCB and gapfill based on value of 0.1 for 50:50 sand:bentonite buffer material (Oscarson et al. 1992).
ρ_d	Dry density (kg/m^3). Values of 1700 kg/m^3 and 1410 kg/m^3 for HCB and gapfill, respectively, taken from Table 6.4 of Gobien et al. 2016).
ρ_b	Bulk (saturated) porosity (kg/m^3). Values of 1955 kg/m^3 and 1439 kg/m^3 for HCB and gapfill, respectively, taken from Table 6.4 of Gobien et al. 2016).
$c_{A,INIT}$	Initial concentration gaseous O_2 (8.54×10^{-3} mol/dm^3). Based on the volume of an ideal gas at 25°C of 24.5 $dm^3\cdot mol^{-1}$ and the mole fraction of O_2 in air of 0.209 (CRC 2019).
$c_{0,INIT}$	Initial concentration dissolved O_2 (2.3×10^{-4} mol/dm^3). Based on the solubility of O_2 in water in contact with air at 25°C (0.00025 $mol\cdot dm^{-3}$) with some salting-out due to the salinity of the pore water.
$c_{6,INIT}$	Initial concentration Cl^- ions (0.03 mol/dm^3). Based on analysis of King et al. (2017).
$c_{7,INIT}$	Initial concentration Fe(II) ions (0 mol/dm^3). The HCB and gapfill porewater are assumed to be initially free of dissolved Fe(II) since these materials have been assembled and exposed to air for some time.
c_5^{max}	Maximum Cu(II) adsorption capacity (0.4 mol/kg). Based on typical cation exchange capacity for MX-80 bentonite of 80 meq/100g (Table 4-3, Dixon 2019).

A_F	Specific surface area of biotite or other Fe(II)-containing solid phase (0 m^{-1}). In the absence of a specific accessory mineral content, the HCB and gapfill are assumed not to contain any Fe(II)-containing soluble mineral phases.
C	Heat capacity (845 $J \cdot kg^{-1} \cdot K^{-1}$). Generic value for clay/rock/sand (King and Kolář 2000).
K	Thermal conductivity ($W \cdot m^{-1} \cdot K^{-1}$). The thermal conductivity is saturation-dependent, with the exact dependence specified by the user.
S	Degree of saturation (unitless). The time-dependent degree of saturation of the HCB and gapfill will depend on the thermal and hydraulic boundary conditions in the DGR. The dependence if supplied as a user-defined external input.
S_{MIC}	Threshold degree of saturation for microbial activity (unitless). A default value of 1 is specified for both HCB and gapfill. There is strong evidence that microbial activity only occurs above a threshold water activity or, for porous media, a threshold degree of saturation (King 2009, Stroes-Gascoyne et al. 2010). Since the degree of saturation cannot exceed 1, the default parameter value is equivalent to assuming that no microbial activity occurs in the HCB or gapfill at any time. This assumption is reasonable for HCB, but microbial activity may be possible in the gapfill due to the lower density, in which case a value for S_{MIC} <1 would be specified.

Table B.1: Layer-specific Properties for the Implementation of the NWMO Buffer Box Concept in the COMSOL Version of the CCM.

Symbol	Definition	Units	Highly compacted bentonite	Gapfill
L	Layer thickness[1]	m	0.436	0.1
ε_e	Effective porosity for mass transport[2]	Unitless	0.191	0.243
ε_s	Storage porosity[2]	Unitless	0.191	0.243
τ_f	Tortuosity factor	Unitless	0.1	0.1
ρ_d	Dry density	kg/m^3	1700	1410
ρ_b	Bulk density	kg/m^3	1955	1439
$c_{A,INIT}$	Initial concentration of gaseous O_2	mol/dm^3	8.54×10^{-3}	8.54×10^{-3}
$c_{0,INIT}$	Initial concentration of dissolved O_2	mol/dm^3	2.3×10^{-4}	2.3×10^{-4}
$c_{6,INIT}$	Initial concentration of Cl^- ions	mol/dm^3	0.03	0.03
$c_{7,INIT}$	Initial concentration of dissolved Fe(II)	mol/dm^3	0	0
c_5^{max}	Maximum concentration of adsorbed Cu^{2+}	mol/kg	0.4	0.4
A_F	Surface area of exposed biotite	m^{-1}	0	0
C	Heat capacity	$J\cdot kg^{-}\cdot K^{-1}$	845	845
K	Thermal conductivity	$W\cdot m^{-1}\cdot K^{-1}$	User-defined	User-defined
S	Time-dependent degree of saturation	Unitless	User-defined	User-defined
S_{MIC}	Minimum degree of saturation at which microbial activity can occur	Unitless	1	1

B.2 KINETIC, THERMODYNAMIC, AND TRANSPORT PROPERTIES

k_1	Rate constant for the homogeneous oxidation of $CuCl_2^-$ by O_2, a function of T and $[Cl^-]$ according to Equation (A-8) and calculated within the model, rather than being inputted as a distinct input parameter. The temperature dependence is taken directly from Sharma and Millero (1988) and is equivalent to an activation energy of 39.5 $kJ \cdot mol^{-1}$. This value was used by these authors for pure NaCl solutions in the pH range 6-9 and for Cl^- solutions with additions of HCO_3^- and Mg^{2+} (or Ca^{2+}), and is valid over the temperature range 5-45°C. For seawater, they used an activation energy of 45.4 $kJ \cdot mol^{-1}$, valid over the same pH and T ranges. We have taken the expression for pure NaCl solutions for k_1 ([Cl-], T, pH), which may underestimate the effect of Ca^{2+} on k_1. The derived expression (Equation (A-10)) is for a constant pH of 7.
k_2	Rate constant for the hydrolysis of $CuCl_2^-$ (1 s^{-1} at 25°C). The mechanism for the formation of Cu_2O is unknown, but is assumed here to result from the hydrolysis of $CuCl_2^-$. The value of k_2 is set a factor of 10 larger than k_{-2} in order to simulate the experimentally observed formation of Cu_2O.
ΔH_2	Temperature dependence of k_2 (60 $kJ \cdot mol^{-1}$). Estimated value based on a typical ΔH for chemical processes.
k_{-2}	Rate constant for the dissolution of Cu_2O (0.1 s^{-1} at 25°C). Some experimental data are available on the dissolution rate of Cu_2O in Cl^- solutions as a function of pH (King and Legere, unpublished data), including an activation energy, the dependence on pH and $[Cl^-]$ and estimated values for the rate constant in units of $mol \cdot cm^{-2} \cdot s^{-1}$. The reaction is pH-dependent, but independent of $[Cl^-]$. However, k_{-2} is expressed in terms of the rate of Cu_2O dissolution per unit volume. Consequently, a value for the specific surface area of Cu_2O ($cm^2 \cdot mol^{-1}$) is required to convert the experimentally accessible rate constant to k_{-2}. The specific surface area of Cu_2O is unknown and will depend on the environmental conditions under which precipitation occurs. Therefore, the value of k_{-2} of 0.1 s^{-1} is an assumed value.
ΔH_{-2}	Temperature dependence of k_{-2} (40 $kJ \cdot mol^{-1}$). Based on experimental data on Cu_2O dissolution at pH 5 (King and Legere, unpublished data).
k_3	Rate constant for the precipitation of $CuCl_2 \cdot 3Cu(OH)_2$ ($1 \times 10^{-5} \cdot s^{-1}$ at 25°C). There are no kinetic data for the rate of precipitation of $CuCl_2 \cdot 3Cu(OH)_2$. The precipitation rate constant is 10 times higher than the dissolution rate constant to account for the experimental observation of precipitated $CuCl_2 \cdot 3Cu(OH)_2$. The value of k_3 of 1×10^{-5} s^{-1} is assumed.
ΔH_3	Temperature dependence of k_3 (60 $kJ \cdot mol^{-1}$). Estimated value based on a typical ΔH for chemical processes.
k_{-3}	Rate constant for the dissolution of $CuCl_2 \cdot 3Cu(OH)_2$ (1×10^{-6} s^{-1} at 25°C). There are a limited number of measurements on the dissolution rate of $CuCl_2 \cdot 3Cu(OH)_2$

	(King and Strandlund, unpublished data). However, as in the case of the dissolution of Cu_2O (k_{-2}), k_{-3} contains a term for the specific surface area of precipitated $CuCl_2 \cdot 3Cu(OH)_2$, an unknown parameter. Therefore, an assumed value of k_{-3} is used.
ΔH_{-3}	Temperature dependence of k_{-3} (60 $kJ \cdot mol^{-1}$). Estimated value based on a typical ΔH for chemical processes.
k_4	Rate constant for the adsorption of Cu^{2+} on Na-bentonite (2×10^{-3} $dm^3 \cdot mol^{-1} \cdot s^{-1}$ at 25°C). The rate of Cu^{2+} adsorption is based on unpublished data (King and Ryan) from studies on loose clay. The form of the kinetic adsorption expression is consistent with the equilibrium Langmuir isotherm observed experimentally (Ryan and King 1994).
ΔH_4	Temperature dependence of k_4 (0 $kJ \cdot mol^{-1}$). Various equilibrium sorption studies of Cu^{2+} on loose montmorillonite clay report both positive and negative enthalpies (Ryan and King 1994). Therefore, in the absence of other data, the adsorption of Cu^{2+} will be assumed to be independent of temperature.
k_{-4}	Rate constant for the desorption of Cu^{2+} (1×10^{-6} s^{-1} at 25°C). The desorption rate constant is an estimated value based on the observation of extremely slow desorption in loose clay systems (King and Ryan, unpublished data).
ΔH_{-4}	Temperature dependence of k_{-4} (0 $kJ \cdot mol^{-1}$). Various equilibrium sorption studies of Cu^{2+} on loose montmorillonite clay report both positive and negative enthalpies (Ryan and King 1994). Therefore, in the absence of other data, the desorption of Cu^{2+} will be assumed to be independent of temperature.
k_5	Rate constant for the reaction between O_2 and dissolved Fe(II) (2.9 $dm^3 \cdot mol^{-1} \cdot s^{-1}$ at 25°C). This reaction is highly pH dependent. The value is derived from the estimated pseudo-first-order (with respect to [Fe(II)]) rate constant in oxygenated solution at pH 7, 3.7×10^{-3} s^{-1} (Wehrli 1990). This corresponds to a value of k_5 of 2.9 $dm^3 \cdot mol^{-1} \cdot s^{-1}$ for an $[O_2]$ of 1.26×10^{-3} $mol \cdot dm^{-3}$, on the assumption that the reaction is first order with respect to $[O_2]$. Wehrli (1990) does not quote a temperature, which is assumed to be 25°C.
ΔH_5	Temperature dependence of k_5 (40 $kJ \cdot mol^{-1}$). Activation energy assumed to be the same as that for k_1.
k_6	Rate constant for the reaction between Cu^{2+} and Fe(II) (10 $dm^3 \cdot mol^{-1} \cdot s^{-1}$ at 25°C). No experimental data are available. The value is based on the assumption that the homogeneous kinetics are rapid, as is the case for the redox reactions involving O_2 and $CuCl_2^-$ and O_2 and Fe(II) discussed above.
ΔH_6	Temperature dependence of k_6 (40 $kJ \cdot mol^{-1}$). Activation energy assumed to be the same as that for k_1.
R_0	Instantaneous rate of the anaerobic dissolution of biotite (expressed as the Fe(II) release rate) ($R_0 = 2 \times 10^{-14}$ $mol \cdot dm^{-2} \cdot s^{-1}$ at 25°C). The model used for predicting the release rate of Fe(II) from biotite dissolution is based on the experimental

	observation that an Fe(II)-depleted layer of constant thickness forms on the biotite surface. During the transient period, the thickness of this layer grows. At steady-state (i.e., once a constant film thickness has been achieved), the dissolution rate of the film (and, hence, the release rate of Fe(II)) is determined by the dissolution rate of the least soluble component. The value of R_0 is based on the data of Malmstrom et al. (1995) at pH 7.
ΔH_{R_O}	Temperature dependence of R_0 (59 kJ/mol). An activation energy of 59 $kJ \cdot mol^{-1}$ was suggested by Johnson et al. (1994) to describe the general dissolution behaviour of biotite. Here the same value is used for the temperature dependence of R_0, R_1, and α_F.
R_1	Steady-state dissolution rate of the Fe(II) mineral phase (7.4×10^{-15} $mol \cdot dm^{-2} \cdot s^{-1}$). Taken from the study of Malmstrom et al. (1995) for biotite at pH 7.
ΔH_{R_1}	Temperature dependence of R_1 (59 kJ/mol). See comment for ΔH_{R_O}.
α_F	Time constant for the dissolution of the Fe(II) mineral phase 1×10^{-6} s^{-1}). Taken from Malmstrom et al. (1995).
ΔH_{α_F}	Temperature dependence of α_F (59 kJ/mol). See comment for ΔH_{R_O}.
k_7	Rate constant for the rate of precipitation of an unidentified Fe(II) solid (1.0 s^{-1} at 25°C). Rate constants k_7 and k_{-7} are included in the model to simulate the precipitation and subsequent re-dissolution of a secondary Fe(II) solid phase. This phase forms if the rate of dissolution of Fe(II) from the initially present Fe(II) phase exceeds the rate at which it is consumed in redox reactions with either O_2 or Cu^{2+}. Under these conditions, Fe(II) will accumulate in the system and could eventually exceed the solubility of a secondary Fe(II) solid. These processes simulate the transformation of the original Fe(II) phase to a more stable Fe(II) solid. In the absence of experimental evidence for this process, k_7 is assumed to have the same value as that for the precipitation of Cu_2O.
ΔH_7	Temperature dependence of k_7 (60 $kJ \cdot mol^{-1}$). Estimated value based on a typical ΔH for chemical processes.
k_{-7}	Rate constant for the dissolution of a Fe(II) secondary phase (0.1 s^{-1} at 25°C). See comments above for k_7. Value of k_{-7} assumed to be the same as that for the dissolution rate of Cu_2O.
ΔH_{-7}	Temperature dependence of k_{-7} (60 $kJ \cdot mol^{-1}$). Estimated value based on a typical ΔH for chemical processes.
k_8	Rate constant for the dissolution of gaseous O_2 (0.0122 s^{-1} at 25°C). Equivalent to a half-life for gaseous O_2 of approximately 1 minute.
ΔH_8	Temperature dependence of k_8 (60 $kJ \cdot mol^{-1}$). Activation energy based on typical value for a chemical reaction.

k_9	Rate constant for microbial aerobic respiration (2.2×10^{-10} s^{-1} at 25°C). If the degree of saturation exceeds the threshold value of microbial activity, then the consumption of O_2 by aerobic respiration is permitted. The value for the rate constant is derived from the Isothermal test (ITT) at AECL's Underground Research Laboratory (Dixon et al. 2001). Over the 6.5 yr duration of the test, the composition of the atmosphere in the test was observed to decrease from an initial O_2:Ar ratio of 20.2 to between 16.4 and 18.3. Microbial activity was known to have occurred in the test (Stroes-Gascoyne et al. 2000) and the decrease in O_2 content was ascribed to aerobic microbial respiration at a rate equivalent to an O_2 half-life of 10 a (King and Kolář 2006), resulting in a first-order rate constant of 2.2×10^{-9} s^{-1}. Simulations of various large-scale *in situ* tests using this value suggested the rate of O_2 consumption was over-estimated (King and Kolář 2006), so the value used for the CSM was decreased by one order of magnitude.
ΔH_9	Temperature dependence of k_9 (60 $kJ\cdot mol^{-1}$). Activation energy based on typical value for a chemical reaction.
D_A	Diffusion coefficient of gaseous O_2 in air (0.00165 $dm^2\cdot s^{-1}$ at 25°C). Based on the value of 0.00178 $dm^2\cdot s^{-1}$ at 0°C (CRC 2019), corrected for temperature based on the value of ΔH_{D_A}.
ΔH_{D_A}	Temperature dependence of D_A (-2.06 $kJ\cdot mol^{-1}$ at 25°C), based on the temperature dependence of the increase in viscosity of air with temperature for temperatures between 0°C and 74°C (CRC 2019). By analogy with the temperature-dependence of aqueous diffusion coefficients which is determined by the effect of temperature on viscosity.
D_0	Bulk-solution diffusion coefficient of O_2 (1.7×10^{-7} $dm^2\cdot s^{-1}$ at 25°C). From data of King et al. (1995a).
ΔH_{D_0}	Temperature dependence of D_0 (15 $kJ\cdot mol^{-1}$). In the absence of other data, the activation energy for the diffusion of dissolved species is taken to be the same as that for the temperature dependence of the viscosity of H_2O.
D_1	Bulk-solution diffusion coefficient of $CuCl_2^-$ (6×10^{-8} $dm^2\cdot s^{-1}$ at 25°C). From data of Smyrl (1985).
ΔH_{D_1}	Temperature dependence of D_1 (18.8 $kJ\cdot mol^{-1}$). From Bacarella and Griess (1973).
D_3	Bulk-solution diffusion coefficient of Cu^{2+} (6×10^{-8} $dm^2\cdot s^{-1}$ at 25°C). From data of Miller et al. (1980) in $CuSO_4$ solutions and Peters and Cruser (1965) in Cl^- solution.
ΔH_{D_3}	Temperature dependence of D_3 (15 $kJ\cdot mol^{-1}$). In the absence of other data, the activation energy for the diffusion of dissolved species is taken to be the same as that for the temperature dependence of the viscosity of H_2O.

D_6	Bulk-solution diffusion coefficient of Cl^- (2×10^{-7} $dm^2\cdot s^{-1}$ at 25°C). From Fontana et al. (1985).
ΔH_{D_6}	Temperature dependence of D_6 (15 $kJ\cdot mol^{-1}$). In the absence of other data, the activation energy for the diffusion of dissolved species is taken to be the same as that for the temperature dependence of the viscosity of H_2O.
D_7	Bulk-solution diffusion coefficient of Fe(II) (5×10^{-8} $dm^2\cdot s^{-1}$ at 25°C). From International Critical Tables (ICT 1926).
ΔH_{D_7}	Temperature dependence of D_7 (15 $kJ\cdot mol^{-1}$). In the absence of other data, the activation energy for the diffusion of dissolved species is taken to be the same as that for the temperature dependence of the viscosity of H_2O.
c_1^{sat}	Concentration of $CuCl_2^-$ in equilibrium with Cu_2O (3.4×10^{-3} $mol\cdot dm^{-3}$ at 25°C in 1 $mol\cdot dm^{-3}$ Cl^-, pH 7). The concentration of $CuCl_2^-$ in equilibrium with Cu_2O is equated to the total concentration of dissolved Cu(I) species (Cu^+, $CuCl_2^-$, Cu(OH) and $Cu(OH)_2^-$). No Cu(II) species are included in the equilibrium calculations. The solubility of Cu_2O is a function of $[Cl^-]$ and temperature. Since, in the pH and $[Cl^-]$ ranges of interest (King and Kolář 2000), $CuCl_2^-$ is the dominant species, the solubility of Cu_2O is proportional to $[Cl^-]^2$. The pH is assumed to be constant in the model.
ΔH_1^{sat}	Temperature dependence of c_1^{sat} (24 $kJ\cdot mol^{-1}$). Determined from the effect of temperature on the solubility of Cu_2O (D.J. Jobe, private communication).
c_3^{sat}	Concentration of Cu^{2+} in equilibrium with $CuCl_2\cdot 3Cu(OH)_2$ (4.3×10^{-7} $mol\cdot dm^{-3}$ at 25°C, pH 7). The concentration of Cu^{2+} in equilibrium with $CuCl_2\cdot 3Cu(OH)_2$ is equated to the sum of the concentrations of all major dissolved species, namely; Cu^{2+}, $Cu(OH)^+$, $Cu(OH)_2$, $Cu(OH)_4^{2-}$ and $CuCl^+$ (D.J. Jobe, private communication). No Cu(I) species are considered in the equilibrium calculations. The relative proportions of these various species is a function of T, $[Cl^-]$ and pH. At $[Cl^-] < 0.1$ $mol\cdot dm^{-3}$, the solubility of $CuCl_2\cdot 3Cu(OH)_2$ is proportional to $[Cl^-]^{-0.5}$, as would be expected from the stoichiometry. At higher $[Cl^-]$ ($0.1 < [Cl^-] < 1.0$ $mol\cdot dm^{-3}$), the solubility is approximately independent of $[Cl^-]$. Therefore, c_3^{sat} is assumed to be independent of $[Cl^-]$ for the present calculations.
ΔH_3^{sat}	Temperature dependence of c_3^{sat} (19 $kJ\cdot mol^{-1}$). The temperature dependence of c_3^{sat} varies with temperature. The value quoted is a mean of several values determined between 25°C and 100°C (D.J. Jobe, private communication).
c_7^{sat}	Concentration of dissolved Fe(II) in equilibrium with a precipitated Fe(II) secondary phase (1×10^{-5} $mol\cdot dm^{-3}$ at 25°C). Malmstrom et al. (1995) cited an observed [Fe(II)] in a fracture of 1×10^{-5} $mol\cdot dm^{-3}$, which will be used here in the absence of other data.
ΔH_7^{sat}	Temperature dependence of c_7^{sat} (30 $kJ\cdot mol^{-1}$). An assumed value.

B.3 BOUNDARY CONDITIONS

B.3.1 NEAR-FIELD (CONTAINER SURFACE)

n_0	Number of electrons transferred in the reduction of O_2 (4). From King et al. (1995b).
α_{c1}	Cathodic transfer coefficient for the reduction of O_2 (0.5). The transfer coefficient is a function of $[O_2]$ (King et al. 1995b). The value used is that used for the steady-state mixed-potential model of King et al. (1995a).
k_c	Electrochemical rate constant for the reduction of O_2 (1.7×10^{-9} dm·s^{-1} at 25°C). From King et al. (1995a).
ΔH_c	Temperature dependence of k_c (60 kJ·mol^{-1}). From Kinoshita (1992).
$E^0{}_c$	Standard potential for the cathodic reduction of O_2 (0.16 V_{SCE} at 25°C). $E^0{}_c$ is corrected to pH 7, so that the exponential term in the expression for the equilibrium potential of Reaction (A-5) is not pH-dependent.
$\Delta E^0{}_c$	Temperature dependence of $E^0{}_c$ (-1.23×10^{-4} V·K^{-1}). Calculated on the assumption of a linear temperature dependence of $E^0{}_c$ between 298.2 K and 368.2 K. The values of $E^0{}_c$ at these temperatures was calculated using the convention that the free energy of the standard hydrogen electrode (SHE) is zero only at 298.2 K. Therefore, the standard potential of the SHE changes with temperature.
n_a	Number of electrons transferred during the oxidation of Cu (1). From King et al. (1995a).
$E_a{}^0$	Standard potential for anodic dissolution of copper as $CuCl_2^-$ (-0.105 V_{SCE} at 25°C). From King et al. (1995a).
$\Delta E_a{}^0$	Temperature dependence of $E_a{}^0$ (-6.35×10^{-4} V·K^{-1}). From Bertocci and Turner (1974).
k_a	Combined electrochemical rate constant for the anodic dissolution of Cu (3.3×10^{-4} dm·s^{-1} at 25°C). k_a is a combined rate constant, equivalent to $k_{af}k_{bf}/k_{ab}$. The value of k_a is a mean value from 0.1 mol·dm^{-3} and 1.0 mol·dm^{-3} Cl^- solution (King et al. 1995a).
ΔH_a	Temperature dependence of k_a (60 kJ·mol^{-1}). Assumed value.
k_{bb}	Rate constant for the reverse reaction involving $CuCl_2^-$ (1.42×10^{-3} dm·s^{-1} at 25°C). From King et al. (1995a).
ΔH_{bb}	Temperature dependence of k_{bb} (60 kJ·mol^{-1}). Assumed value.
n_2	Number of electrons transferred for the reduction of Cu^{2+} (1).

k_d	Electrochemical rate constant for the reduction of Cu^{2+} (2×10^{-8} $dm \cdot s^{-1}$ at 25°C). Value derived from i/E curves of Hurlen (1961).
ΔH_d	Temperature dependence of k_d (45 $kJ \cdot mol^{-1}$). From Astakhova and Krasikov (1971).
α_d	Transfer coefficient for the reduction of Cu^{2+} (0.5). Assumed value based on facile electron transfer reaction.
E^0_d	Standard potential for the reduction of Cu^{2+} (0.223 V_{SCE} at 25°C). From Van Muylder et al. (1961) and Peters and Cruser (1965).
ΔE^0_d	Temperature dependence of E^0_d (0 $V \cdot K^{-1}$). Temperature dependence unknown.
h_k	Time-dependent humidity at the container surface.
h_k^{min}	Minimum threshold humidity for electrochemical reactions (0.6).
h_k^{max}	Maximum threshold humidity for electrochemical reactions (0.7).

B.3.2 FAR-FIELD (HOST ROCK)

The far-field boundary conditions for mobile species will be determined by the composition of the groundwater at the site being simulated.

B.4 INITIAL CONDITIONS

Examples of values for the initial concentrations of various species in the various layers are given in Table B.1 above.

B.5 PHYSICAL, CHEMICAL, AND ELECTROCHEMICAL CONSTANTS

Farad	Faraday constant (96 485 $C \cdot mol^{-1}$).
R	Gas constant (8.314 $J \cdot K^{-1} \cdot mol^{-1}$).

REFERENCES FOR APPENDIX B

Astakhova, R.K. and B.S. Krasikov. 1971. Electrochemical behaviour of copper in chloride electrolytes. Applied Chemistry USSR 44, 356-362.

Bacarella, A.L. and J.C. Griess Jr. 1973. The anodic dissolution of copper in flowing sodium chlroide solutions from 25°C and 175°C. Electrochemical Society 120, 459-465.

Bertocci, U. and D.R. Turner. 1974. Copper. In Encyclopedia of the Electrochemistry of the Elements, (Editor, A.J. Bard), Volume II. Marcel Dekker, New York, NY, Ch. II-6, Table 1.1.2.

Fontana, A., J. Van Muylder and R. Winand. 1985. Etablissement de diagrammes tension-pH cinetiques du cuivre en milieu de chlorures. Electrochimica Acta 30, 641-647.

Hurlen, T. 1961. Dissolution of copper by oxidation agents in acid chloride solution. Acta Chem. Scand. 15, 1239-1245.

ICT. 1926. International Critical Tables of Numerical Data, McGraw-Hill, New York, NY.

King, F. and M. Kolar. 2000. The copper container corrosion model used in AECL's second case study. Ontario Power Generation, Nuclear Waste Management Division Report 06819-REP-01200-10041-R00. Toronto, Ontario.

King, F., C.D. Litke, M.J. Quinn and D.M. LeNeveu. 1995a. The measurement and prediction of the corrosion potential of copper in chloride solutions as a function of oxygen concentration and mass-transfer coefficient. Corrosion Science 37, 833-851.

King, F., M.J. Quinn and C.D. Litke. 1995b. Oxygen reduction on copper in neutral NaCl solution. Electroanalysis Chemistry 385, 45-55.

Kinoshita, K. 1992. Electrochemical Oxygen Technology. Wiley, New York, NY, Table 2.3.

Kolar, M. 2020. TRANSIENT - A C package for the numerical solution of systems of partial differential equations of parabolic type. http://transient.mkolar.org/.

Malmström, M., S. Banwart, L. Duro, P. Wersin and J. Bruno. 1995. Biotite and chlorite weathering at 25°C. Swedish Nuclear Fuel and Waste Management Company Technical Report, TR 95-01.

Miller, D.G., J.A. Rard, L.B. Eppstein and R.A. Robinson. 1980. Mutual diffusion coefficients, electrical conductances, osmotic coefficients, and ionic transport coefficients l_{ij} for aqueous $CuSO_4$ at 25°C. Solution. Chem. 9, 467-496.

Peters, D.G. and S.A. Cruser. 1965. Cathodic chronopotentiometry of copper(I) and copper(II) in chloride media. Electrochemical Society 9, 27-40.

Ryan, S.R. and F. King. 1994. The adsorption of Cu(II) on sodium bentonite in a synthetic saline groundwater. Atomic Energy of Canada Limited Report, AECL-11062, COG-I-94-125.

Sharma, V.K. and F.J. Millero. 1988. The oxidation of Cu(I) in electrolyte solutions. Solution Chemistry 17, 581-599.

Smyrl, W.H. 1985. Digital impedance for Faradaic analysis. Part II. Electrodissolution of Cu in HCl. Electrochemical Society 132, 1555-1562.

Van Muylder, J., N. de Zoubov and M. Pourbaix. 1961. Diagrammes d'equilibres tension-pH des systemes Cu-H_2O et Cu-Cl^--H_2O a 25°C. CEBELCOR Report (Centre Belges D'Etudes de la Corrosion, Brussels), Report No. 755.

Wehrli, B. 1990. Redox reactions of metal ions at mineral surfaces. In Aquatic Chemical Kinetics, (Editor, W. Stumm), Wiley-Interscience, New York, NY, Chapter 11.

APPENDIX C: COPPER ADSORPTION ON, AND DESORPTION FROM, BENTONITE

C.1 KINETIC TREATMENT OF COPPER ADSORPTION BY BENTONITE

A sensitivity analysis was performed to determine the optimum values for the adsorption (k_4) and desorption (k_{-4}) rate constants for Cu(II) on bentonite. The default values for these rate constants are $k_4 = 2\times10^{-3}$ $dm^3\cdot mol^{-1}\cdot s^{-1}$ and $k_{-4} = 10^{-6}$ s^{-1}, the basis for which is given in Section B.2.

Table C.1 summarizes all of the sensitivity analyses that were performed, as well as the results of the simulations. The latter were judged based on the visual "goodness-of-fit" of the predictions to the experimental data, and were classified as either poor (P), good (G), very poor (VP), or very good (VG). The adsorption rate constant (k_4) was systematically varied by a factor of 0.001× to 1000 × the default value, whereas the desorption rate constant (k_{-4}) was systematically varied by a factor of 0.002× to 10^{-7}× the default value. For the various simulations, the ratio of the rate constants for adsorption:desorption varied from 0.00002 to 200, compared with a ratio of 2000 for the default values. Thus, based on the results of the initial simulations, the focus of the sensitivity analysis was on slowing the rate of adsorption (compared with the rate of desorption) compared to the situation for the default values of k_4 and k_{-4}. Simulations were also performed in which either adsorption or desorption were switched off (by setting the value of the respective rate constant to zero). Figure C.1 shows the results of the sensitivity analyses, where the plots are grouped based on a given value of k_4. In each plot, the results of the sensitivity analyses are compared with the experimental E_{CORR} values and to the predicted value for Step 3c and for Step 3d using the default values for the adsorption and desorption rate constants.

Based on the visual comparison of predicted and experimental E_{CORR} values, very good (VG) fits to the experimental data were obtained for the following conditions (highlighted in green font in Table C.1):

- No adsorption or desorption, equivalent to Step 3c.
- If the rate of desorption is fast compared with the rate of adsorption (a k_4/k_{-4} ratio of 0.0002).
- Regardless of the rate of desorption, a slow rate of adsorption ($k_4 = 2\times10^{-9}$ $m^3\cdot mol^{-1}\cdot s^{-1}$).

The selection of the optimum values for k_4 and k_{-4} from the combinations that produced VG fits to the experimental data is arbitrary, but for the purposes of further model development a combination of $k_4 = 2\times10^{-9}$ $dm^3\cdot mol^{-1}\cdot s^{-1}$ and $k_{-4} = 10^{-5}$ s^{-1} was selected for the optimum values (highlighted in green italic font in Table C.1).

Based on the optimum value of k_4, the half-life of dissolved Cu(II) is estimated to be 192,500 hrs (Table C.1). Thus, within the timescale of the experiments, Cu(II) essentially does not adsorb based on the selected value of k_4.

Table C.1: Summary of Simulations Performed to Determine Optimal Values for Adsorption and Desorption Rate Constants.

Run #	Ratio k_4/k_{-4}	Multipliers		k_4 ($m^3 \cdot mol^{-1} \cdot s^{-1}$)	Half-life dissolved Cu(II) (hrs)	k_{-4} (s^{-1})	Half-life adsorbed Cu(II) (hrs)	Fit to expt. E_{CORR}
		k_4	k_{-4}					
1	0	0	1	0.00E+00	infinite	1.00E-06	193	
2	200	1000	10	2.00E-03	0	1.00E-05	19	VP
3	20	1000	100	2.00E-03	0	1.00E-04	2	VP
4	2	1000	1000	2.00E-03	0	1.00E-03	0	VP
5	0.2	1000	10000	2.00E-03	0	1.00E-02	0	VP
6	0.02	1000	100000	2.00E-03	0	1.00E-01	0	VP
7	0.002	1000	1000000	2.00E-03	0	1.00E+00	0	G
8	0.0002	1000	10000000	2.00E-03	0	1.00E+01	0	VG
9	20	100	10	2.00E-04	2	1.00E-05	19	VP
10	2	100	100	2.00E-04	2	1.00E-04	2	VP
11	0.2	100	1000	2.00E-04	2	1.00E-03	0	VP
12	0.02	100	10000	2.00E-04	2	1.00E-02	0	P
13	0.002	100	100000	2.00E-04	2	1.00E-01	0	G
14	0.0002	100	1000000	2.00E-04	2	1.00E+00	0	VG
15	2	10	10	2.00E-05	19	1.00E-05	19	VP
16	0.2	10	100	2.00E-05	19	1.00E-04	2	VP
17	0.02	10	1000	2.00E-05	19	1.00E-03	0	P
18	0.002	10	10000	2.00E-05	19	1.00E-02	0	G
19	0.0002	10	100000	2.00E-05	19	1.00E-01	0	VG
20		1	0	2.00E-06	193	0.00E+00	infinite	VP
21	1	1	2	2.00E-06	193	2.00E-06	96	VP
22	0.2	1	10	2.00E-06	193	1.00E-05	19	VP
23	0.02	1	100	2.00E-06	193	1.00E-04	2	P
24	0.002	1	1000	2.00E-06	193	1.00E-03	0	G
25	0.0002	1	10000	2.00E-06	193	1.00E-02	0	VG

Run #	Ratio k_4/k_{-4}	Multipliers		k_4 ($m^3 \cdot mol^{-1} \cdot s^{-1}$)	Half-life dissolved Cu(II) (hrs)	k_{-4} (s^{-1})	Half-life adsorbed Cu(II) (hrs)	Fit to expt. E_{CORR}
		k_4	k_{-4}					
26		0.1	0	2.00E-07	1925	0.00E+00	infinite	V
27	1	0.1	0.2	2.00E-07	1925	2.00E-07	963	VP
28	0.2	0.1	1	2.00E-07	1925	1.00E-06	193	VP
29	0.02	0.1	10	2.00E-07	1925	1.00E-05	19	P
30	0.002	0.1	100	2.00E-07	1925	1.00E-04	2	G
31	0.0002	0.1	1000	2.00E-07	1925	1.00E-03	0	VG
32		0.01	0	2.00E-08	19250	0.00E+00	infinite	G
33	1	0.01	0.02	2.00E-08	19250	2.00E-08	9625	G
34	0.2	0.01	0.1	2.00E-08	19250	1.00E-07	1925	G
35	0.02	0.01	1	2.00E-08	19250	1.00E-06	193	G
36	0.002	0.01	10	2.00E-08	19250	1.00E-05	19	G
37	0.0002	0.01	100	2.00E-08	19250	1.00E-04	2	VG
38		0.001	0	2.00E-09	192500	0.00E+00	infinite	VG
39	1	0.001	0.002	2.00E-09	192500	2.00E-09	96250	VG
40	0.2	0.001	0.01	2.00E-09	192500	1.00E-08	19250	VG
41	0.02	0.001	0.1	2.00E-09	192500	1.00E-07	1925	VG
42	0.002	0.001	1	2.00E-09	192500	1.00E-06	193	VG
43	*0.0002*	*0.001*	*10*	*2.00E-09*	*192500*	*1.00E-05*	*19*	*VG*
44	0.00002	0.001	100	2.00E-09	192500	1.00E-04	2	VG

(a)

$k_4 = 2\times10^{-3}\ \mathrm{m^3{\cdot}mol^{-1}{\cdot}s^{-1}}$

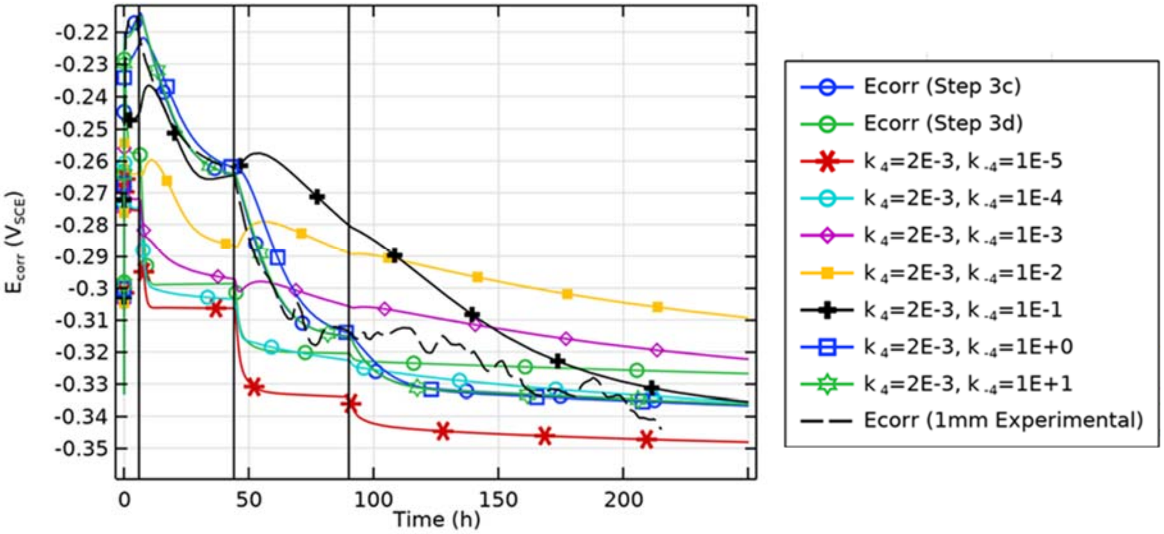

(b)

$k_4 = 2\times10^{-4}\ \mathrm{m^3{\cdot}mol^{-1}{\cdot}s^{-1}}$

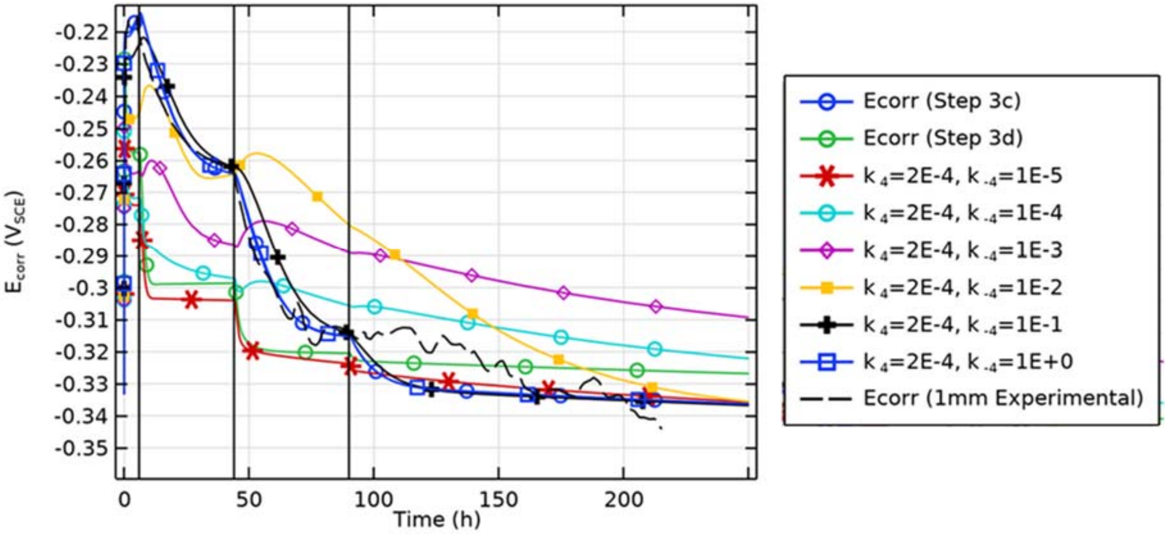

(c)

$k_4 = 2\times10^{-5}\ m^3\cdot mol^{-1}\cdot s^{-1}$

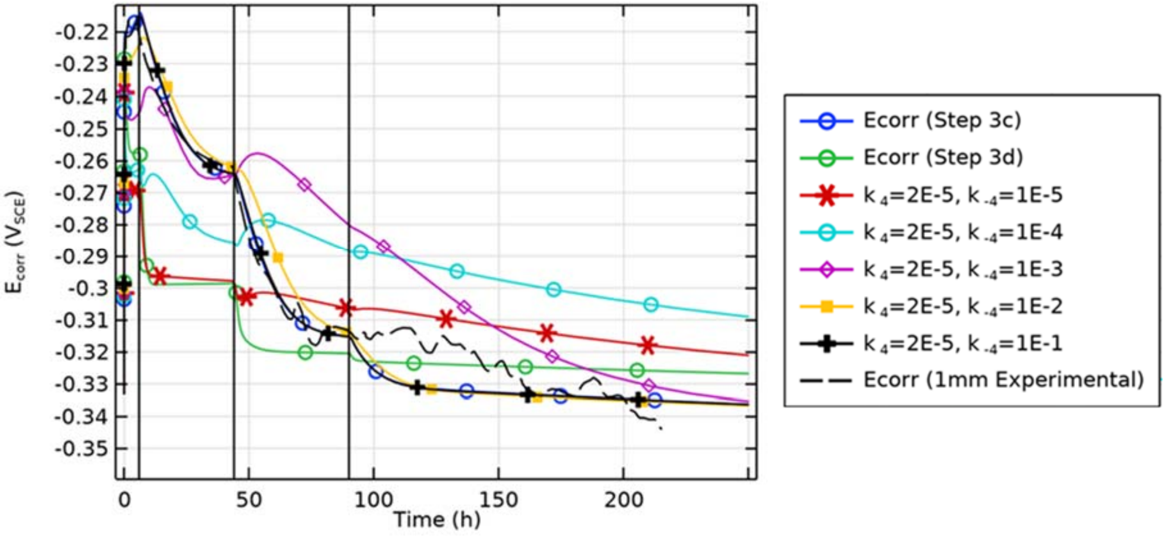

(d)

$k_4 = 2\times10^{-6}\ m^3\cdot mol^{-1}\cdot s^{-1}$

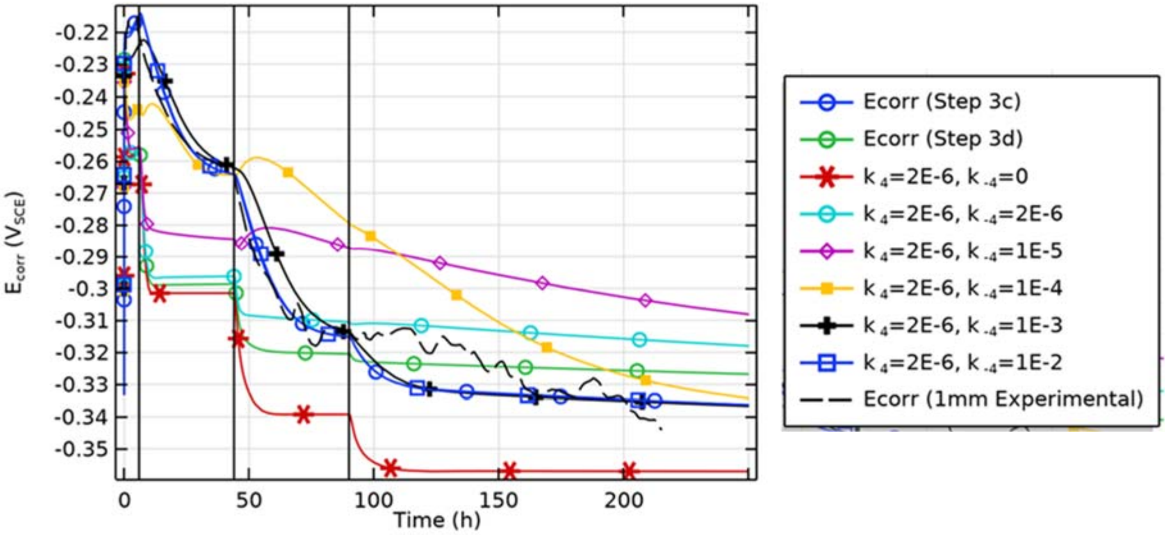

(e)

$k_4 = 2\times10^{-7}$ m^3·mol^{-1}·s^{-1}

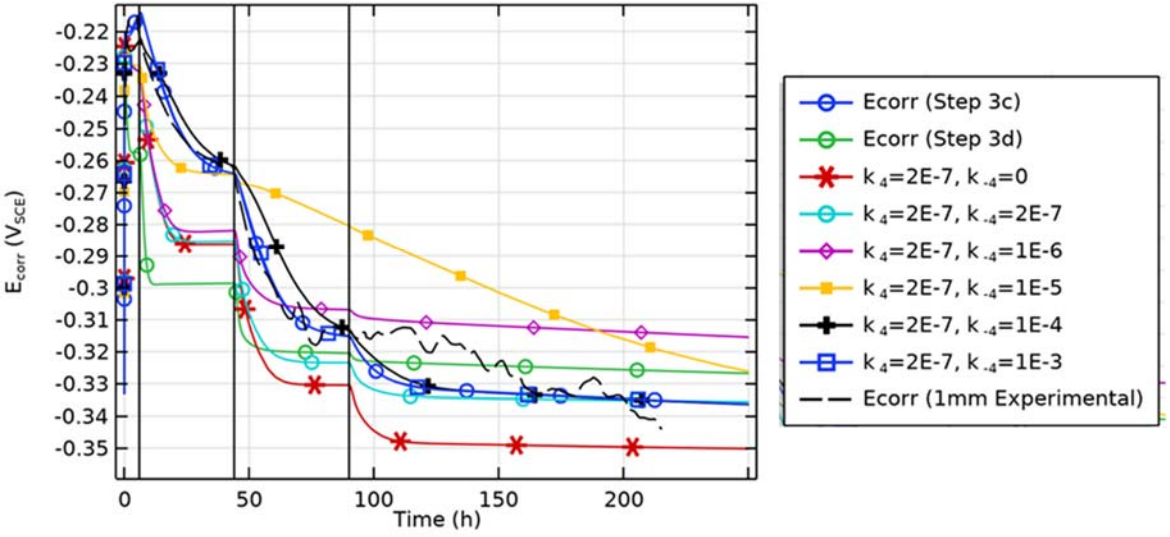

(f)

$k_4 = 2\times10^{-8}$ m^3·mol^{-1}·s^{-1}

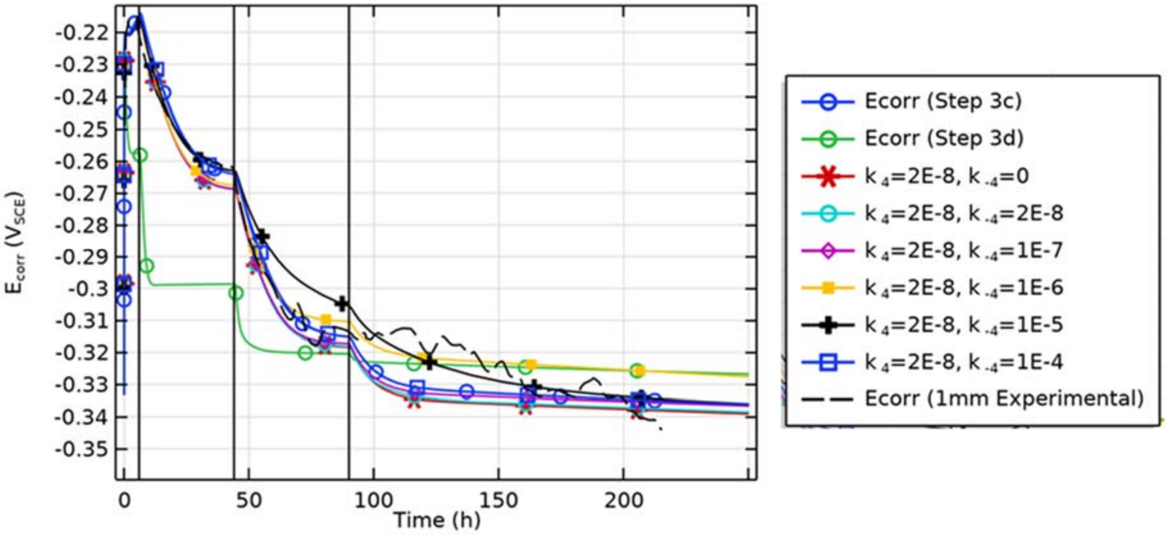

(g)

$k_4 = 2\times10^{-9}$ $m^3\cdot mol^{-1}\cdot s^{-1}$

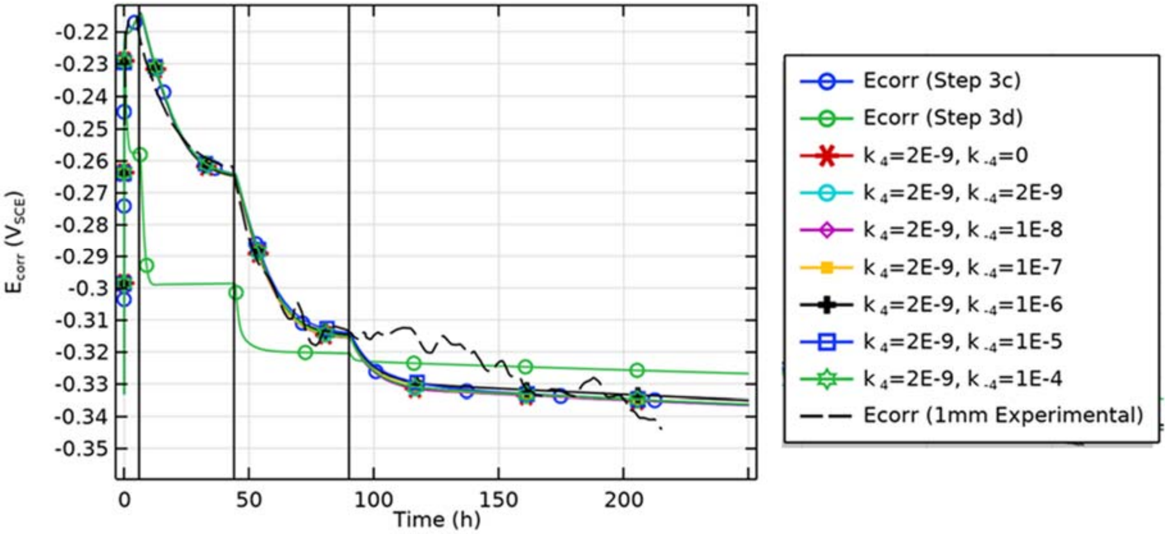

Figure C.1: Results of Sensitivity Analyses on Values for the Adsorption and Desorption Rate Constants. Plots (a) to (g) are grouped based on a given value for the adsorption rate constant k_4, as indicated.

C.2 EQUILIBRIUM TREATMENT OF COPPER ADSORPTION BY BENTONITE

Ryan and King (1994) studied the adsorption of Cu(II) on bentonite under steady state (equilibrium) conditions. Experiments were performed with both loose and compacted Avonlea bentonite (the same type used for the E_{CORR} measurements of King et al. (1995c) with the same dry density of 1.2 g/cm^3) using Saturated Canadian Shield Saline Solution (SCSSS, a Ca^{2+}/Na^+-based Cl^- solution with a [Cl^-] of 0.97 mol/L) as a supporting electrolyte. Experiments were performed at temperatures of 25, 50, and 95 °C.

For loose clays, the adsorption behaviour followed a Langmuir isotherm. The maximum adsorbate surface coverage increased with temperature, and exceeded the cation exchange capacity for Cu^{2+} at temperatures of 50 °C and 95 °C. For compacted clays, the data followed a Freundlich-type isotherm, and exhibited no apparent temperature dependence. At a given pore-water copper concentration, the extent of adsorption on compacted clay was less than on loose clay. The difference between the behaviour of loose and compacted clays was explained in terms of the inaccessibility of some of the adsorption sites in compacted media.

Reanalysis of the original data gives values for the Langmuir constant K_L and maximum adsorption concentration s_{MAX} at 25°C of 0.101 m^3/mol and 0.31 mol/kg, respectively for the loose clay. Similarly, analysis of the data produced value for the Freundlich constant K_F and exponent n at 25 °C of 0.00933 mol/kg and 0.53, respectively, for compacted Avonlea bentonite.